EERC Publication ER10-05

In-Situ Compaction Measurements for Geosynthetic Stabilized Subbase: Weirton, West Virginia

October, 2010

Authors
White, D.J., Gieselman, H.H., Douglas, C., Zhang, J., Vennapusa, P.

EERC
EARTHWORKS ENGINEERING
RESEARCH CENTER

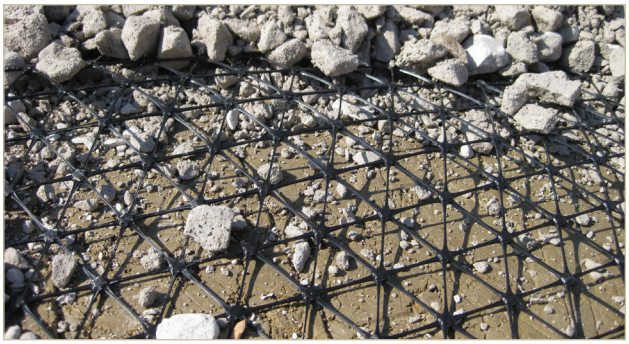

IOWA STATE UNIVERSITY
Institute for Transportation

Sponsored by
Tensar International Corporation
5883 Glenridge Drive, Suite 200
Atlanta, GA, 30328

About the EERC

The mission of the Earthworks Engineering Research Center at Iowa State University is to be the nation's premier institution for developing fundamental knowledge of earth mechanics, and creating innovative technologies, sensors, and systems to enable rapid, high quality, environmentally friendly, and economical construction of roadways, aviation runways, railroad embankments, dams, structural foundations, fortifications constructed from earth materials, and related geotechnical applications.

Disclaimer Notice

The contents of this report reflect the views of the authors, who are responsible for the facts and the accuracy of the information presented herein. The opinions, findings and conclusions expressed in this publication are those of the authors and not necessarily those of the sponsors.

The sponsors assume no liability for the contents or use of the information contained in this document. This report does not constitute a standard, specification, or regulation.

The sponsors do not endorse products or manufacturers. Trademarks or manufacturers' names appear in this report only because they are considered essential to the objective of the document.

Non-discrimination Statement

Iowa State University does not discriminate on the basis of race, color, age, religion, national origin, sexual orientation, gender identity, sex, marital status, disability, or status as a U.S. veteran. Inquiries can be directed to the Director of Equal Opportunity and Diversity, (515) 294-7612.

Technical Report Documentation Page

1. Report No. ER10-05	2. Government Accession No.	3. Recipient's Catalog No.
4. Title and Subtitle In-Situ Compaction Measurements for Geosynthetic Stabilized Subbase: Weirton, West Virginia		5. Report Date October 24, 2010 6. Performing Organization Code
7. Author(s) White, D.J., Gieselman, H.H., Douglas, C., Zhang, J., Vennapusa, P.		8. Performing Organization Report No.
9. Performing Organization Name and Address Institute for Transportation Earthworks Engineering Research Center Iowa State University 2711 South Loop Drive, Suite 4700 Ames, IA 50010-8664		10. Work Unit No. (TRAIS) 11. Contract or Grant No.
12. Sponsoring Organization Name and Address Tensar International Corporation 5883 Glenridge Drive, Suite 200 Atlanta, GA, 30328		13. Type of Report and Period Covered 14. Sponsoring Agency Code

15. Supplementary Notes

Visit www.eerc.iastate.edu for color PDF files of this and other research reports.

16. Abstract

This study documents the performance of controlled test sections of unpaved geosynthetic reinforced aggregate base overlying soft subgrade. The tests were conducted in Weirton, West Virginia from March 17 to 20, 2009. The test sections included a control section with no geosynthetic and sections incorporating a woven geotextile (14.5 osy), Tensar BX1200 geogrid, or Tensar TX 160 geogrid. Case/Ammann and Caterpillar roller with integrated compaction monitoring systems, in-ground piezoelectric earth pressure cells (EPCs), and in-situ point measurement techniques (i.e., dynamic cone penetrometer, light weight deflectometer, plate load test, and nuclear density gauge test) were used to evaluate the conditions of the test sections after selected roller and trafficking passes. The roller measurement values showed that results were repeatable between passes, but primarily reflected the conditions of the underlying weak subgrade due to the high compaction stresses and one the dimensional nature of the test strips. The underlying subgrade was considered to be weak and variable. The in-situ point measurements showed unique compaction curves for density, elastic modulus, and CBR not previously documented. Rut depth measurements under trafficking from a heavy vehicle, layer compaction measurements, and in-ground stress measurements under compaction and trafficking passes, provide information on the reinforcement provided by the different geosynthetics. Key findings from this study are that rut depth and compaction measurements showed better performance in the TX160 geogrid section compared to other test sections, while the elastic modulus and CBR measurements were variable between sections. In-ground stress cell measurements showed that the "locked-in" horizontal stress in the subgrade after trafficking was lower in the TX160 section compared to other test sections. Improved performance in the TX160 section can in part be explained by higher lateral restraint of the subbase layer following compaction and trafficking and reduced horizontal stresses in the soft subgrade layer under loading, compared to the control and other geosynthetic sections. Additional research is needed to verify these results for different subgrade and aggregate materials.

17. Key Words Geosynthetic, Geogrid, subbase, subgrade, earth pressure cells		18. Distribution Statement No restrictions.	
19. Security Classification (of this report) Unclassified.	20. Security Classification (of this page) Unclassified.	21. No. of Pages	22. Price NA

Form DOT F 1700.7 (8-72) **Reproduction of completed page authorized**

IN-SITU COMPACTION MEASUREMENTS FOR GEOSYNTHETIC STABILIZED SUBBASE: WEIRTON, WEST VIRGINIA

Final Report
October 2010

Principal Investigators
David J. White
Associate Professor of Civil Engineering, Geotechnical/Materials Division
Iowa State University

Heath Gieselman
Assistant Scientist
Iowa State University

Research Assistants
Jiake Zhang, S. Caleb Douglas, Pavana Vennapusa

Authors
White, D.J., Gieselman, H.H., Douglas, C., Zhang, J., Vennapusa, P.

Sponsored by
Tensar International Corporation

A report from
Earthworks Engineering Research Center Iowa State University
2901 South Loop Drive, Suite 3100
Ames, IA 50010-8664
Phone: 515-294-8103
Fax: 515-294-0467

TABLE OF CONTENTS

ACKNOWLEDGMENTS XI

INTRODUCTION 1

Tasks 1

TEST METHODS 3

Laboratory Test Procedures 3
In-Situ Testing Methods 4
Roller-Integrated Compaction Monitoring Technology 6
Roller-Integrated Stiffness (k_s) measurement Value 6
Roller-Integrated Compaction Meter Value (CMV) 7
Roller Positioning 8
Piezoelectric Earth Pressure Cells 8
Load Test Truck 12
Elevation Profiling 12
Transit Survey 12
RTK-GPS 12
Ruler Measurement 13
Post-Trafficking Excavation 13

MATERIALS 14

Soils and Aggregates 14
Geosynthetic Materials 20

EXPERIMENTAL PLAN AND TEST BED CONSTRUCTION 21

Description of Test Sections 22
Construction/ Testing Process and Photo Log 24

RESULTS AND DISCUSSION 44

Roller-Integrated Measurement Values 56
Rut Depth Measurements 65
Earth Pressure Cell Measurements 68

SUMMARY AND CONCLUSIONS 77

REFERENCES 78

APPENDIX A. IN-SITU DATA 1

APPENDIX B. EARTH PRESSURE CELL DATA 1

APPENDIX C. INDIVIDUAL CROSS SECTIONS 1

APPENDIX D. HISTOGRAMS 1

LIST OF FIGURES

Figure 1. In-situ testing methods used on the project: (a) 200-mm diameter plate Zorn LWD, (b) dynamic cone penetrometer, (c) calibrated nuclear moisture-density gauge, (d) 300-mm diameter static PLT, and (e) Iowa State University geotechnical mobile lab 5
Figure 2. E_{V1} and E_{V2} determination procedure from static PLT for subgrade and base materials.6
Figure 3. Case smooth drum roller used on the project 7
Figure 4. Lumped parameter two-degree-of-freedom spring dashpot model representing vibratory compactor and soil behavior (reproduced from Yoo and Selig 1980) 7
Figure 5. CAT smooth drum roller used on the project 8
Figure 6. Calibration of EPC in the lab 9
Figure 7. Obtaining stress cell data during traffic 9
Figure 8. Profile of EPC installation 10
Figure 9. Placing vertical earth pressure cell on Tensar BX1200 at base of subbase 1 10
Figure 10. Vertical and horizontal EPC during placement of subbase 1 in control section – cardboard is used as a temporary liner to contain the sand backfill 11
Figure 11. Placing horizontal earth pressure cell in subbase 1 11
Figure 12. Truck utilized for load testing 12
Figure 13. Cross section surveys of W-PP-GT section prior to traffic on subbase 1 13
Figure 14. Trenching sections after traffic 14
Figure 15. Crushed limestone subbase aggregate with maximum particle size = 1.5 inches 15
Figure 16. Grain-size distribution curve for subgrade 16
Figure 17. Grain-size distribution curve for subbase 16
Figure 18. Laboratory Proctor curve and field moisture and dry density measurements on subgrade 17
Figure 19. CBR test results (at 0.1 in penetration) in relationship with moisture and dry unit weight measurements and Proctor test results 18
Figure 20. UU tests results for both subgrade and subbase materials 19
Figure 21. View of site and test section locations 23
Figure 22. Test section layout and in-situ test locations 24
Figure 23. Transit survey and RTK-GPS survey locations 24
Figure 24. View of W-PP-GT and BX1200 sections during subgrade preparation 25
Figure 25. View of control and TX160 sections 25
Figure 26. Moisture conditioning of W-PP-GT and BX1200 sections 26
Figure 27. Compacting W-PP-GT and BX1200 sections 26
Figure 28. Compacting subgrade in control and TX160 sections 27
Figure 29. W-PP-GT and Tensar BX1200 27
Figure 30. Tensar TX160 and control sections 28
Figure 31. Placing subbase layer 1 on BX1200 section 28
Figure 32. Placing subbase layer 1 on Tensar TX160 section 29
Figure 33. Subgrade, Tensar TX160, and subbase layer 1 29
Figure 34. Point testing in W-PP-GT prior to compacting subbase 1 30
Figure 35. Point testing in BX1200 section after roller compaction 30
Figure 36. W-PP-GT and BX1200 sections after roller compaction of subbase 1 31
Figure 37. W-PP-GT and BX1200 subbase 1 after traffic 31
Figure 38. Point testing in TX160 during compaction of subbase 1 32
Figure 39. Point testing in TX160 section during compaction of subbase 1 and plate load testing

in BX1200 section 32
Figure 40. TX160 and control sections near completion of compaction of subbase 1 33
Figure 41. Traffic on subbase 1 in TX160 section 33
Figure 42. Rut depth measurements on subbase 1 in control section 34
Figure 43. Placing subbase 2 in control section and rut depth measurements on subbase 1 in control and TX160 sections 34
Figure 44. Point testing in W-PP-GT and BX1200 sections during compaction of subbase 2 35
Figure 45. Plate load testing in W-PP-GT section after compaction of subbase 2 35
Figure 46. Initial profiles W-PP-GT and BX1200 sections after compaction of subbase 2 prior to traffic 36
Figure 47. Initial profiles in section after compaction of subbase 2 prior to traffic 36
Figure 48. Traffic in BX1200 section on subbase 2 37
Figure 49. Traffic in W-PP-GT and BX1200 sections on subbase 2 37
Figure 50. Measuring rut depth 38
Figure 51. W-PP-GT and BX1200 sections subbase 2 during traffic 38
Figure 52. Control and TX sections subbase 2 during traffic 39
Figure 53. W-PP-GT and BX1200 sections nearing end of traffic 39
Figure 54. Control and TX160 sections nearing end of traffic 40
Figure 55. Control and TX160 sections nearing end of traffic 40
Figure 56. Full depth DCP testing after traffic 41
Figure 57. Trenching sections after traffic 41
Figure 58. View of deformation after traffic 42
Figure 59. W-PP-GT after excavation 42
Figure 60. Tensar BX1200 after excavation 43
Figure 61. Tensar TX160 after excavation 43
Figure 62. Dry unit weight compaction curves for W-PP-GT and BX1200 sections 48
Figure 63. Dry density compaction curves for control and TX160 sections 49
Figure 64. E_{LWD} compaction curves for W-PP-GT and BX1200 sections 50
Figure 65. E_{LWD} compaction curves for control and TX160 section 51
Figure 66. CBR compaction curves for W-PP-GT and BX1200 sections 52
Figure 67. CBR compaction curves for control and TX160 sections 53
Figure 68. Averaged E_{LWD}, γd and CBR compaction curves for each section 54
Figure 69. Comparison between CBR, γd and E_{LWD} of each layer 55
Figure 70. Average in-situ test measurements on subbase layer 2 after 0, 1, 2, 4, 10, and 21 roller passes (note data within 3 m from the start and end of each section not included) 56
Figure 71. Case/Ammann k_s results for W-PP-GT and BX1200 sections 58
Figure 72. Case/Ammann average k_s (error bar indicates one standard deviation) compaction growth with increasing pass for W-PP-GT and BX1200 sections 59
Figure 73. Case/Ammann k_s results for control and TX 160 sections 60
Figure 74. Case/Ammann average k_s (error bar indicates one standard deviation) compaction growth with increasing pass for control and TX160 sections 61
Figure 75. Caterpillar CMV results for W-PP-GT and BX1200 sections 62
Figure 76. Caterpillar average CMV (average value shown as circle and error bar indicates one standard deviation) compaction growth with increasing pass for W-PP-GT and TX160 .63
Figure 77. Caterpillar CMV results for W-PP-GT and TX160 sections 63
Figure 78. Caterpillar average CMV (average value shown as circle and error bar indicates one standard deviation) compaction growth with increasing pass for W-PP-GT and TX160 sections 64

Figure 79. Change in elevation during compaction passes on subbase layer 2 relative to pass 1 (note: negative Δelevation means settlement and +ve Δelevation means heave) 64
Figure 80. Average change in elevation during compaction on subbase layer 2 (with one standard deviation error bars) relative to pass 1 for different sections (note: negative Δelevation means settlement and +ve Δelevation means heave) 65
Figure 81. W-PP-GT and BX1200 section subbase 1 longitudinal rut depth after 4 trafficking passes 65
Figure 82. W-PP-GT and BX1200 sections subbase 2 longitudinal rut depth after 75 and 150 truck passes, subbase layer depths (interpreted from DCP profiles) after 150 trafficking passes, and CBR of the subgrade layer 66
Figure 83. Control and TX160 sections subbase 2 longitudinal rut depth after 75 and 150 truck passes and subbase layer depths (interpreted from DCP profiles) after 150 trafficking passes, and CBR of the subgrade layer 67
Figure 84. Bar chart comparing average longitudinal rut depth after 75 and 150 truck passes on subbase layer 2 68
Figure 85. Total vertical stress at interface between geosynthetic and subgrade after roller compaction and test vehicle passes 70
Figure 86. Total horizontal stress below geosynthetic in subgrade layer after roller compaction and test vehicle passes 70
Figure 87. Total horizontal stress above geosynthetic in subbase layer after roller compaction and test vehicle passes 71
Figure 88. Maximum total vertical stress at interface between geosynthetic and subgrade during roller compaction and test vehicle passes 71
Figure 89. Maximum total horizontal stress below geosynthetic in subgrade layer during roller compaction and test vehicle passes 72
Figure 90. Maximum total horizontal stress above geosynthetic in subbase layer during roller compaction and test vehicle passes 72
Figure 91. Lateral stress ratio (ratio of horizontal and vertical stresses) in subgrade and subbase layers after roller and test truck trafficking passes 73
Figure 92. Lateral stress ratio (ratio of horizontal and vertical stresses) under roller drum and test truck wheel loading in subgrade and subbase layers 74
Figure 93. Total stress at interface between geosynthetic and subgrade and horizontal stress in subbase during Case roller pass number 4 (W-PP-GT treatment) 74
Figure 94. Total stress at interface between geosynthetic and subgrade and horizontal stress in subbase during Case roller pass number 4 (BX1200 treatment) 75
Figure 95. Total stress at interface between geosynthetic and subgrade and horizontal stress in subbase during Case roller pass number 4 (Control treatment) 75
Figure 96. Total stress at interface between geosynthetic and subgrade and horizontal stress in subbase during Case roller pass number 4 (TX160 treatment) 76
Figure 97. Example dynamic EPC measurements on TX160 section (under a trafficking pass on subbase layer 2) 76
Figure 98. DCP profiles for W-PP-GT and BX1200 sections 11
Figure 99. DCP profiles for W-PP-GT and BX1200 sections – subbase layer 1 12
Figure 100. DCP profiles for W-PP-GT and BX1200 section – subbase layer 2 13
Figure 101. DCP profiles for W-PP-GT and BX1200 sections – final full depth test 14
Figure 102. DCP profiles for control and TX160 sections 15
Figure 103. DCP profiles for control and TX160 sections – subbase layer 1 16

Figure 104. DCP profiles for control and TX160 sections – subbase layer 2 17
Figure 105. DCP profiles for control and TX160 sections – final full depth test.....18
Figure 106. CBR profiles for subgrade layer for W-PP-GT and BX1200 sections.....19
Figure 107. CBR profiles for subgrade layer for control and TX160 sections.....19
Figure 108. CBR profiles for W-PP-GT and BX1200 sections – subbase layer 1 20
Figure 109. CBR profiles for W-PP-GT and BX1200 sections – subbase layer 2 20
Figure 110. CBR profiles for W-PP-GT and BX1200 sections – final full depth test 21
Figure 111. CBR profiles for control and TX160 sections – subbase layer 1 21
Figure 112. CBR profiles for control and TX160 sections – subbase layer 2 22
Figure 113. CBR profiles for control and TX160 sections – final full depth test 22
Figure 114. Plate load test results on control section – Subgrade 27
Figure 115. Plate load test results for section W-PP-GT – subbase 1 28
Figure 116. Plate load test results on section W-PP-GT – subbase 2 29
Figure 117. Plate load test results for BX1200 section – subbase 2 30
Figure 118. Plate load test results for control section – subbase 1 31
Figure 119. Plate load test results for TX160 section – subbase 1 32
Figure 120. Plate load test results for control section – subbase 2 33
Figure 121. Plate load test results for TX160 section – subbase 2 34
Figure 122. Earth pressure cell W-PP-GT and BX1200 sections layer 1 vertical (left) and horizontal (right) stress data at 0 passes 1
Figure 123. Earth pressure cell W-PP-GT and BX1200 sections layer 1 vertical (left) and horizontal (right) stress data Case roller pass 2 1
Figure 124. Earth pressure cell W-PP-GT and BX1200 sections layer 1 vertical (left) and horizontal (right) stress data Case roller pass 3 2
Figure 125. Earth pressure cell W-PP-GT and BX1200 sections layer 1 vertical (left) and horizontal (right) stress data Case roller pass 4 2
Figure 126. Earth pressure cell W-PP-GT and BX1200 sections layer 1 vertical (left) and horizontal (right) stress data Case roller pass 2
Figure 127. Earth pressure cell W-PP-GT and BX1200 sections layer 1 vertical (left) and horizontal (right) stress data Case roller 10 3
Figure 128. Earth pressure cell W-PP-GT and BX1200 sections layer 1 vertical (left) and horizontal (right) stress data Case roller 12 3
Figure 129. Earth pressure cell W-PP-GT and BX1200 sections layer 1 vertical (left) and horizontal (right) stress data truck traffic pass 1 3
Figure 130. Earth pressure cell W-PP-GT and BX1200 sections layer 1 vertical (left) and horizontal (right) stress data truck traffic pass 2 4
Figure 131. Earth pressure cell W-PP-GT and BX1200 sections layer 1 vertical (left) and horizontal (right) stress data truck traffic pass 3 4
Figure 132. Earth pressure cell Control and TX160 sections layer 1 vertical (left) and horizontal (right) stress data pass 0 4
Figure 133. Earth pressure cell Control and TX160 sections layer 1 vertical (left) and horizontal (right) stress data Case roller pass 1 5
Figure 134. Earth pressure cell Control and TX160 sections layer 1 vertical (left) and horizontal (right) stress data Case roller pass 2 5
Figure 135. Earth pressure cell Control and TX160 sections layer 1 vertical (left) and horizontal (right) stress data Case roller pass 3 5
Figure 136. Earth pressure cell Control and TX160 sections layer 1 vertical (left) and horizontal (right) stress data Case roller pass 4 6

Figure 137. Earth pressure cell Control and TX160 sections layer 1 vertical (left) and horizontal (right) stress data Case roller pass 5 6
Figure 138. Earth pressure cell Control and TX160 sections layer 1 vertical (left) and horizontal (right) stress data Case roller pass 6 6
Figure 139. Earth pressure cell Control and TX160 sections layer 1 vertical (left) and horizontal (right) stress data Case roller pass 7 7
Figure 140. Earth pressure cell Control and TX160 sections layer 1 vertical (left) and horizontal (right) stress data Case roller pass 8 7
Figure 141. Earth pressure cell Control and TX160 sections layer 1 vertical (left) and horizontal (right) stress data Case roller pass 10 7
Figure 142. Earth pressure cell Control and TX160 sections layer 1 vertical (left) and horizontal (right) stress data CAT roller pass 12 8
Figure 143. Earth pressure cell Control and TX160 sections layer 1 vertical (left) and horizontal (right) stress data truck traffic pass 1 8
Figure 144. Earth pressure cell Control and TX160 sections layer 1 vertical (left) and horizontal (right) stress data truck traffic pass 2 8
Figure 145. Earth pressure cell Control and TX160 sections layer 1 vertical (left) and horizontal (right) stress data truck traffic pass 3 9
Figure 146. Earth pressure cell Control and TX160 sections layer 1 vertical (left) and horizontal (right) stress data truck traffic pass 4 9
Figure 147. Earth pressure cell W-PP-GT and BX1200 sections layer 2 vertical (left) and horizontal (right) stress data Case roller pass 1 9
Figure 148. Earth pressure cell W-PP-GT and BX1200 sections layer 2 vertical (left) and horizontal (right) stress data Case roller pass 2 10
Figure 149. Earth pressure cell W-PP-GT and BX1200 sections layer 2 vertical (left) and horizontal (right) stress data Case roller pass 3 10
Figure 150. Earth pressure cell W-PP-GT and BX1200 sections layer 2 vertical (left) and horizontal (right) stress data Case roller pass 4 10
Figure 151. Earth pressure cell W-PP-GT and BX1200 sections layer 2 vertical (left) and horizontal (right) stress data Case roller pass 12 11
Figure 152. Earth pressure cell W-PP-GT and BX1200 sections layer 2 vertical (left) and horizontal (right) stress data Case roller high amplitude pass 13 11
Figure 153. Earth pressure cell W-PP-GT and BX1200 sections layer 2 vertical (left) and horizontal (right) stress data Case roller high amplitude pass 14 11
Figure 154. Earth pressure cell W-PP-GT and BX1200 sections layer 2 vertical (left) and horizontal (right) stress data CAT roller pass 16 12
Figure 155. Earth pressure cell W-PP-GT and BX1200 sections layer 2 vertical (left) and horizontal (right) stress data CAT roller high amplitude pass 17 12
Figure 156. Earth pressure cell W-PP-GT and BX1200 sections layer 2 vertical (left) and horizontal (right) stress data CAT roller high amplitude pass 18 12
Figure 157. Earth pressure cell W-PP-GT and BX1200 sections layer 2 vertical (left) and horizontal (right) stress data CAT roller pass 19 13
Figure 158. Earth pressure cell W-PP-GT and BX1200 sections layer 2 vertical (left) and horizontal (right) stress data CAT roller high amplitude pass 20 13
Figure 159. Earth pressure cell W-PP-GT and BX1200 sections layer 2 vertical (left) and horizontal (right) stress data CAT roller pass 21 13
Figure 160. Earth pressure cell W-PP-GT and BX1200 sections layer 2 vertical (left) and horizontal (right) stress data CAT roller static pass 22 14

Figure 161. Earth pressure cell W-PP-GT and BX1200 sections layer 2 vertical (left) and horizontal (right) stress data truck traffic pass 1 14
Figure 162. Earth pressure cell W-PP-GT and BX1200 sections layer 2 vertical (left) and horizontal (right) stress data truck traffic pass 2 14
Figure 163. Earth pressure cell W-PP-GT and BX1200 sections layer 2 vertical (left) and horizontal (right) stress data truck traffic pass 3 15
Figure 164. Earth pressure cell W-PP-GT and BX1200 sections layer 2 vertical (left) and horizontal (right) stress data truck traffic pass 4 15
Figure 165. Earth pressure cell W-PP-GT and BX1200 sections layer 2 vertical (left) and horizontal (right) stress data truck traffic pass 5 15
Figure 166. Earth pressure cell W-PP-GT and BX1200 sections layer 2 vertical (left) and horizontal (right) stress data truck traffic pass 10 16
Figure 167. Earth pressure cell W-PP-GT and BX1200 sections layer 2 vertical (left) and horizontal (right) stress data truck traffic pass 15 16
Figure 168. Earth pressure cell W-PP-GT and BX1200 sections layer 2 vertical (left) and horizontal (right) stress data truck traffic pass 35 16
Figure 169. Earth pressure cell W-PP-GT and BX1200 sections layer 2 vertical (left) and horizontal (right) stress data truck traffic pass 45 17
Figure 170. Earth pressure cell W-PP-GT and BX1200 sections layer 2 vertical (left) and horizontal (right) stress data truck traffic pass 50 17
Figure 171. Earth pressure cell W-PP-GT and BX1200 sections layer 2 vertical (left) and horizontal (right) stress data truck traffic pass 60 17
Figure 172. Earth pressure cell W-PP-GT and BX1200 sections layer 2 vertical (left) and horizontal (right) stress data truck traffic pass 75 18
Figure 173. Earth pressure cell W-PP-GT and BX1200 sections layer 2 vertical (left) and horizontal (right) stress data truck traffic pass 100 18
Figure 174. Earth pressure cell W-PP-GT and BX1200 sections layer 2 vertical (left) and horizontal (right) stress data truck traffic pass 126 18
Figure 175. Earth pressure cell W-PP-GT and BX1200 sections layer 2 vertical (left) and horizontal (right) stress data truck traffic pass 150 19
Figure 176. Earth pressure cell Control and TX160 sections layer 2 vertical (left) and horizontal (right) stress data Case roller pass 4 19
Figure 177. Earth pressure cell Control and TX160 sections layer 2 vertical (left) and horizontal (right) stress data Case roller high amplitude pass 5 19
Figure 178. Earth pressure cell Control and TX160 sections layer 2 vertical (left) and horizontal (right) stress data Case roller high amplitude pass 6 20
Figure 179. Earth pressure cell Control and TX160 sections layer 2 vertical (left) and horizontal (right) stress data Case roller pass 7 20
Figure 180. Earth pressure cell Control and TX160 sections layer 2 vertical (left) and horizontal (right) stress data Case roller pass 8 20
Figure 181. Earth pressure cell Control and TX160 sections layer 2 vertical (left) and horizontal (right) stress data Case roller pass 9 21
Figure 182. Earth pressure cell Control and TX160 sections layer 2 vertical (left) and horizontal (right) stress data Case roller pass 10 21
Figure 183. Earth pressure cell Control and TX160 sections layer 2 vertical (left) and horizontal (right) stress data CAT roller pass 13 21
Figure 184. Earth pressure cell Control and TX160 sections layer 2 vertical (left) and horizontal (right) stress data CAT roller pass 14 22

Figure 185. Earth pressure cell Control and TX160 sections layer 2 vertical (left) and horizontal (right) stress data CAT roller high amplitude pass 15 22
Figure 186. Earth pressure cell Control and TX160 sections layer 2 vertical (left) and horizontal (right) stress data CAT roller high amplitude pass 16 22
Figure 187. Earth pressure cell Control and TX160 sections layer 2 vertical (left) and horizontal (right) stress data CAT roller pass 17 23
Figure 188. Earth pressure cell Control and TX160 sections layer 2 vertical (left) and horizontal (right) stress data CAT roller pass 18 23
Figure 189. Earth pressure cell Control and TX160 sections layer 2 vertical (left) and horizontal (right) stress data CAT roller high amplitude pass 19 23
Figure 190. Earth pressure cell Control and TX160 sections layer 2 vertical (left) and horizontal (right) stress data CAT roller static pass 20 24
Figure 191. Earth pressure cell Control and TX160 sections layer 2 vertical (left) and horizontal (right) stress data truck traffic pass 1 24
Figure 192. Earth pressure cell Control and TX160 sections layer 2 vertical (left) and horizontal (right) stress data truck traffic pass 5 24
Figure 193. Earth pressure cell Control and TX160 sections layer 2 vertical (left) and horizontal (right) stress data truck traffic pass 10 25
Figure 194. Earth pressure cell Control and TX160 sections layer 2 vertical (left) and horizontal (right) stress data truck traffic pass 15 25
Figure 195. Earth pressure cell Control and TX160 sections layer 2 vertical (left) and horizontal (right) stress data truck traffic pass 35 25
Figure 196. Earth pressure cell Control and TX160 sections layer 2 vertical (left) and horizontal (right) stress data truck traffic pass 45 26
Figure 197. Earth pressure cell Control and TX160 sections layer 2 vertical (left) and horizontal (right) stress data truck traffic pass 50 26
Figure 198. Earth pressure cell Control and TX160 sections layer 2 vertical (left) and horizontal (right) stress data truck traffic pass 60 26
Figure 199. Earth pressure cell Control and TX160 sections layer 2 vertical (left) and horizontal (right) stress data truck traffic pass 75 27
Figure 200. Earth pressure cell Control and TX160 sections layer 2 vertical (left) and horizontal (right) stress data truck traffic pass 100 27
Figure 201. Earth pressure cell Control and TX160 sections layer 2 vertical (left) and horizontal (right) stress data truck traffic pass 126 27
Figure 202. Earth pressure cell Control and TX160 sections layer 2 vertical (left) and horizontal (right) stress data truck traffic pass 150 28
Figure 203. Cross section profiles, W-PP-GT section, points A1, A2 and A3 1
Figure 204. Cross section profiles W-PP-GT section, points A4 and A5 2
Figure 205. Cross section profiles BX1200 section, points A6, A7 and A8 3
Figure 206. Cross section profiles BX1200 section, points A9 and A10 4
Figure 207. Cross section profiles control section, points B1, B2 and B3 5
Figure 208. Cross section profiles control section, points B4 and B5 6
Figure 209. Cross section profiles TX160 section, points B6, B7 and B8 7
Figure 210. Cross section profiles TX160 section, points B9 and B10 8
Figure 211. W-PP-GT and BX1200 sections subgrade DPI histogram 1
Figure 212. W-PP-GT and BX1200 sections subbase 1 DPI histogram 1
Figure 213. W-PP-GT and BX1200 sections subbase 2 DPI histogram 2
Figure 214. Control and TX160 sections subgrade DPI histogram 2

Figure 215. Control and TX160 sections subbase 1 DPI histogram....3
Figure 216. Control and TX160 sections subbase 2 DPI histogram....3
Figure 217. Combined sections subbase 2 modulus histogram....4

LIST OF TABLES

Table 1. Summary of test methods used in this study....3
Table 2. Summary of material properties....15
Table 3. Laboratory CBR test results on subgrade material....18
Table 4. Laboratory CBR tests on subbase material....18
Table 4. Summary of geosynthetic treatments....20
Table 5. Summary of test beds and in-situ testing....21
Table 6. Average DPI and CBR of test sections after moisture conditioning....44
Table 7. Average DPI and CBR of test sections after compaction of subbase 1....44
Table 8. Average DPI and CBR of test sections after trafficking subbase 2....45
Table 9. Summary of average D_r, E_{LWD} and CBR for each section....46
Table 10. Case/Ammann roller pass summary....57
Table 11. Caterpillar roller pass summary....62
Table 12. Performance comparison between test sections....76
Table 13. Summary of point test data – subgrade....1
Table 14. Summary of point test data – subbase 1....2
Table 15. Summary of point test data – subbase 2....4
Table 16. Summary of point test data – subgrade....6
Table 17. Summary of point test data – subbase 1....7
Table 18. Summary of point test data – subbase 2....9
Table 19. Summary of DCP testing on subgrade....23
Table 20. Summary of DCP testing on subbase 1....24
Table 21. Summary of DCP testing on W-PP-GT and BX sections after trafficking subbase 2....25
Table 22. Summary of DCP testing on control and TX sections after trafficking subbase 2....26
Table 23. Summary of plate load tests results....35

ACKNOWLEDGMENTS

The authors would like to thank Tensar International Corporation for sponsoring this research. Stephen N. Valero, P.E. and Pinnacle Construction personnel provided support during construction of test sections.

INTRODUCTION

A field study at a site located in Weirton, West Virginia was conducted from March 17 to 20, 2009 to evaluate the support conditions of three different geosynthetics placed at the interface between soft clayey subgrade and crushed limestone. The project involved preparing and testing four different test sections. All four sections evaluated as part of this study included crushed limestone over a relatively weak, lean clay subgrade. One of the test sections included a control section where the crushed stone was placed directly on the subgrade. The remaining three sections included a woven geotextile (W-PP-GT), Tensar BX1200 geogrid, and Tensar TX 160 geogrid at the interface between the subgrade and crushed limestone. Case/Ammann and Caterpillar roller-integrated compaction monitoring systems, in-ground piezoelectric earth pressure cells (EPCs), and various in-situ point measurement techniques were used to evaluate the support conditions of the test sections. The Case/Ammann smooth drum roller was equipped with roller-integrated stiffness (k_s) measurement system and the Caterpillar smooth drum roller was equipped with roller-integrated CMV measurement system. The rollers were equipped with real time kinematic (RTK) global positioning system (GPS) and on-board visual display and documentation systems. The EPCs were installed to measure in-ground total stresses before, during, and after compaction and trafficking.

Goals of this field investigation were to:

- Obtain roller-integrated measurement values (MVs), in-ground instrumentation, and various in-situ point measurements to document performance of geosynthetic reinforcement of aggregate base material over relatively weak and non-uniform subgrade soils, and
- Develop relationships between measured deformations from truck traffic and the various in-situ measurements.

Tasks

The specific tasks completed during this research project are summarized below.

- Mobilized the rollers and geotechnical mobile lab to the project site in West Virginia.
- Obtained CMV and k_s roller-integrated compaction measurements for the underlying subgrade layer prior to placement of geogrid/geotextile.
- Worked with the contractor to layout the test strip locations, each with lengths of about 18.3 meters (60 feet).
- Placed in-ground earth pressure cells in the subgrade prior to placement of crushed stone fill and geotextile/geogrid.
- After placing the geogrid/geotextile, aggregate base layers were placed and compacted using the Case and Caterpillar rollers with variable machine operations (frequency, amplitude, and speed). Generated field compaction curves for each roller-integrated compaction measurements and test section.
- Performed in-situ point measurements and develop compaction curves for density, 300 mm plate load modulus, dynamic cone penetration index profile, and light weight

deflectometer measurements for each test section.

- Obtained samples of the aggregate material and underlying subgrade soil for laboratory classification including liquid limit, plasticity index, classification, moisture content, and compactability.
- Trafficking passes were made on the sections with a loaded truck to obtain deformations or rut depths beneath the wheels.
- Analyzed and synthesized the results.

Background information for the rollers, EPCs, and various in-situ point measurement techniques utilized in this field study are described in this report. This report documents the results and analysis from test bed field studies and the field demonstration activities. To the authors' knowledge, this is the first documented field study to report link all of the various measurements together. These results should be of significant interest to the pavement, geotechnical, and construction engineering community.

TEST METHODS

Laboratory Test Procedures

Laboratory testing was conducting on the subgrade and base materials used in this field study. A list of ASTM test methods used is provided in Table 1.

Table 1. Summary of test methods used in this study

Test Name	ASTM Standard
Particle size analysis of soils	ASTM D422
Liquid Limit, Plastic Limit, and Plasticity Index of Soils	ASTM D4318
Classification of Soils for Engineering Purposes (Unified Soil Classification System	ASTM D2487
Laboratory Compaction Characteristics of Soil Using Standard Effort (12,400 ft-lbf/ft^3 (600 kN-m/m^3))	ASTM D698
Maximum Index Density and Unit Weight of Soils Using a Vibratory Table	ASTM D4253
Standard Test Methods for Specific Gravity of Soil Solids by Water Pycnometer	ASTM D854
Unconsolidated-Undrained Triaxial Compression Test on Cohesive Soils	ASTM D2850
Use of the Dynamic Cone Penetrometer in Shallow Pavement Applications	ASTM D6951
CBR (California Bearing Ratio) of Laboratory-Compacted Soils	ASTM 1883*

* Tests performed on subbase material samples prepared using three different compaction energies: Substandard 300 kN-m/m^3, Standard 600 kN-m/m^3, Modified 2700 kN-m/m^3, and on subgrade material using one compaction energy: Substandard 570 kN-m/m^3 (i.e., about 95% of standard Proctor energy)

In-Situ Testing Methods

Six different in-situ testing methods were used in this study to evaluate the in-situ compaction properties (Figure 1): (a) 200-mm diameter Zorn light weight deflectometer (LWD) setup with 50 mm drop height to determine elastic modulus ($E_{LWD\text{-}Z2}$), (b) Dynamic Cone Penetrometer (DCP) to determine California bearing Ratio (CBR), (c) calibrated nuclear moisture-density gauge (NG), and (d) 300-mm diameter static PLT to determine initial (E_{V1}) and re-load modulus (E_{V2}). LWD, DCP, NG, and PLT tests were conducted by the ISU research team with aid of the geotechnical mobile lab (Figure 1e).

LWD tests were performed following manufacturer recommendations (Zorn 2003) and the $E_{LWD\text{-}Z2}$ value was determined using Equation 1, where E = elastic modulus (MPa), d_0 = measured settlement (mm), v = Poisson's ratio, σ_0 = applied stress (MPa), r = radius of the plate (mm), f = shape factor depending on stress distribution (assumed as 8/3 for aggregate base and $\pi/2$ for clay subgrade).

$$E = \frac{(1-v^2)\sigma_0 r}{d_0} \times f \tag{1}$$

DCP test was performed in accordance with ASTM D6951-03 to determine dynamic cone penetration index (DPI) and calculate CBR using Equation 2. The DCP test results are presented in this report as CBR point values or CBR profiles. When the data is presented as point values, the data represents an average CBR of the compaction layer or the depth specified (e.g., $CBR_{0\text{-}250}$ represents 0-250 mm depth).

$$CBR = \frac{292}{DPI^{1.12}} \tag{2}$$

Static PLT's were conducted by applying a static load on a 300 mm diameter plate against a 6.2kN capacity reaction force. The applied load was measured using a 90-kN load cell and deformations were measured using three 50-mm linear voltage displacement transducers (LVDTs). The load and deformation readings were continuously recorded during the test using a data logger. The E_{V1} and E_{V2} values were determined from Equation 1, using appropriate stress and deflection values as illustrated in Figure 2 depending on the material/layer type.

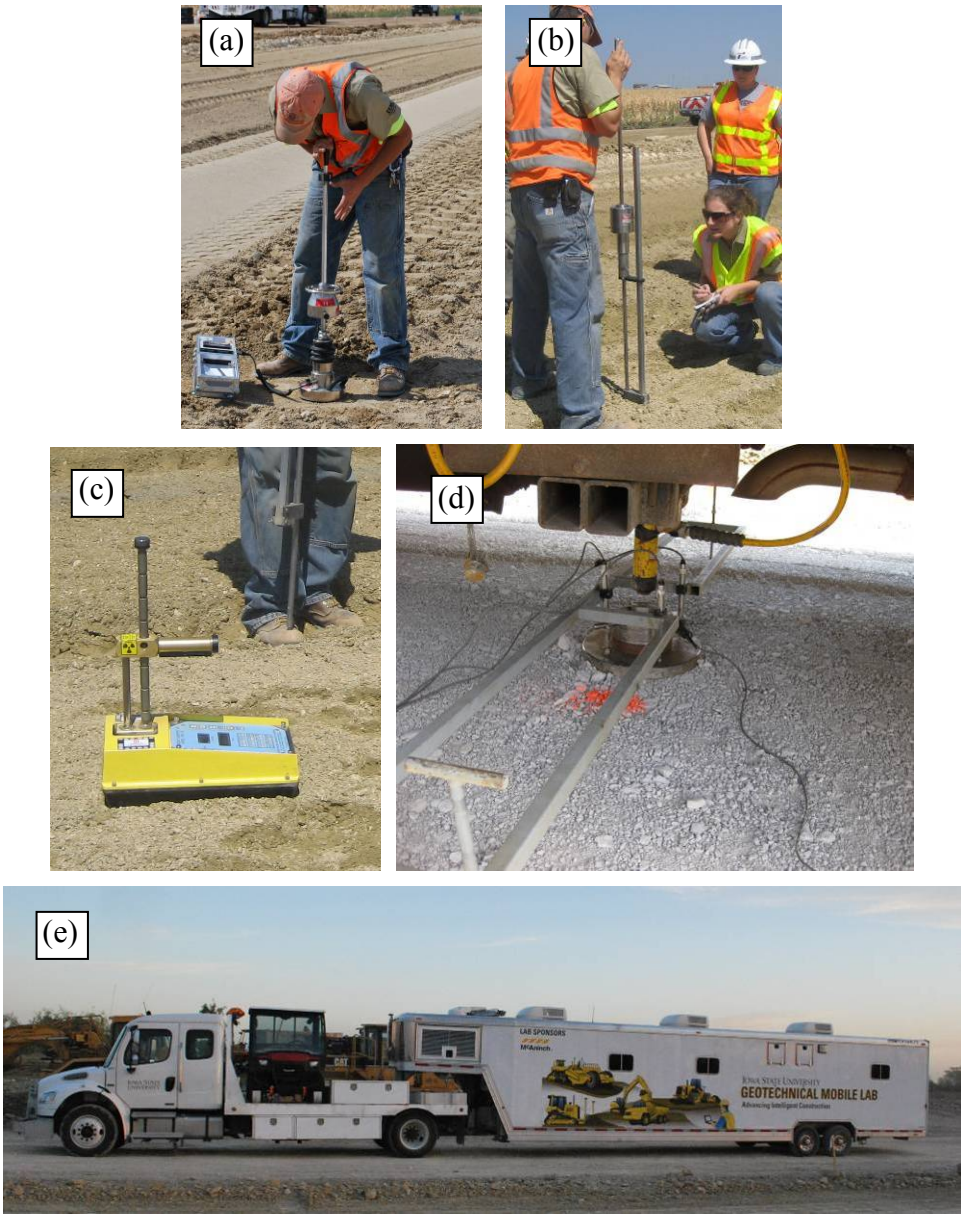

Figure 1. In-situ testing methods used on the project: (a) 200-mm diameter plate Zorn LWD, (b) dynamic cone penetrometer, (c) calibrated nuclear moisture-density gauge, (d) 300-mm diameter static PLT, and (e) Iowa State University geotechnical mobile lab

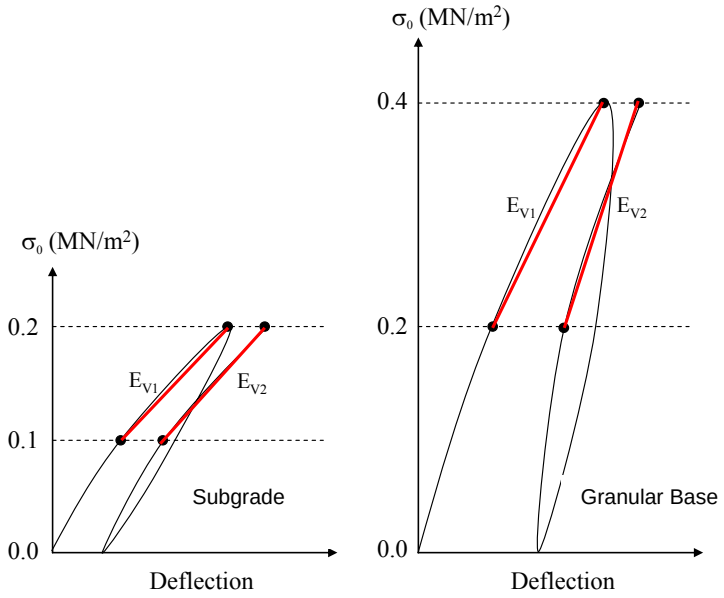

Figure 2. E_{V1} and E_{V2} determination procedure from static PLT for subgrade and base materials

Roller-Integrated Compaction Monitoring Technology

Roller-Integrated Stiffness (k_s) measurement Value

A smooth drum Case roller equipped with Ammann's roller-integrated stiffness k_s measurement value was used on this project (Figure 3). The k_s measurement system was introduced by Ammann during late 1990's considering a lumped parameter two-degree-of-freedom spring dashpot system illustrated in Figure 4 (Anderegg 1998). The spring dashpot model has been found effective in representing the drum-ground interaction behavior (Yoo and Selig 1980). The drum inertia force and eccentric force time histories are determined from drum acceleration and eccentric position (neglecting frame inertia). The drum displacement z_d is determined by double integrating the measured peak drum accelerations. The soil stiffness k_s is determined using Equation 3 when there is no loss of contact between drum and soil. The k_s value represents a quasi-static stiffness value and is independent of the excitation frequency between 25 to 40 Hz (Anderegg and Kaufmann 2004).

$$k_s = 4\pi^2 f^2 \left(m_d + \frac{m_e r_e \cos(\phi)}{a} \right) \tag{3}$$

where f is the excitation frequency, m_d is the drum mass, $m_e r_e$ is the eccentric moment of the unbalanced mass, φ is the phase angle, a is vibration amplitude. The machines used on this project reported a measurement value approximately every 0.5 m at the drum center along the direction of travel. The k_s measurement system has the capability to perform compaction in a manual mode (i.e., using constant amplitude setting) and in an automatic feedback control (AFC) mode. AFC mode operations, however, were not evaluated at this site.

Figure 3. Case smooth drum roller used on the project

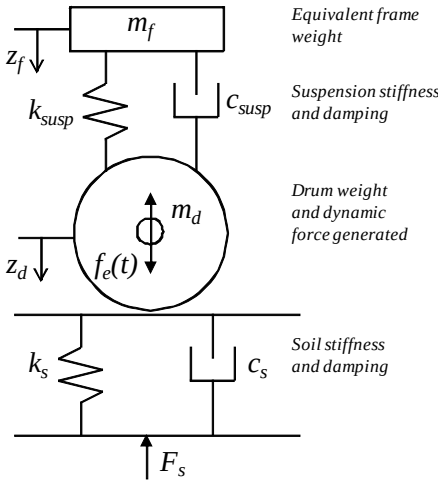

Figure 4. Lumped parameter two-degree-of-freedom spring dashpot model representing vibratory compactor and soil behavior (reproduced from Yoo and Selig 1980)

Roller-Integrated Compaction Meter Value (CMV)

A Caterpillar 563 smooth drum roller equipped with the Accugrade system was used on this project (Figure 5). The system measures compaction meter value (CMV) as an indicator of compaction quality. The CMV technology uses accelerometers to measure drum accelerations in response to soil behavior during compaction operations. The ratio between the amplitude of the first harmonic and the amplitude of the fundamental frequency provides an indication of the soil compaction level (Thurner and Sandström, 1980). An increase in CMV indicates increasing compaction. CMV is calculated using Equation 4.

$$CMV = C \cdot \frac{A_1}{A_0} \quad (4)$$

where C = constant , A_1 = acceleration of the first harmonic component of the vibration, and A_0 = acceleration of the fundamental component of the vibration (Sandström and Pettersson, 2004).

CMV is a dimensionless parameter that depends on roller dimensions (i.e., drum diameter, weight) and roller operation parameters (i.e., frequency, amplitude, speed). The machine used on this project reported a measurement value approximately every 0.5 m at the drum center along the direction of travel.

Roller Positioning

Both rollers were outfitted with RTK-GPS systems for collecting spatial data associated with roller measurement values. A base station was established on site to provide corrections. The Case/Ammann roller was equipped with a Trimble Zephyr Model 2 Rugged antenna and Trimble SPS GPS receiver. The Caterpillar roller was equipped with a MS 990 GPS receiver and radio.

Figure 5. CAT smooth drum roller used on the project

Piezoelectric Earth Pressure Cells

Geokon Model 3500 piezoelectric earth pressure cells (EPC) were installed to measure in-ground total stresses before, during, and after compaction and trafficking. These EPCs are designed to measure total stress in soil with a dynamic readout capability. The EPC consist of two thin metal plates separated by a small gap containing hydraulic fluid. As stress is applied to the cell a pressure transducer measures the change in pressure of the fluid. Calibration of these cells was conducted in the laboratory. For stress calibration the each was calibrated in standard silica sand in a pressure controlled chamber (Figure 6). Known stress was applied and measurements were recorded over the range of EPC. The hydraulic fluid volume is temperature dependant. To correct for this effect a correction factor must be applied. Correction factors were determine in a temperature controlled room by taking zero readings from 4.4° C to 37.8° C in 5.6° C increments. A National Instruments Compact DAQ system was used to interface a field rugged laptop computer with the EPC (Figure 7). Customized labview software was used for data acquisition.

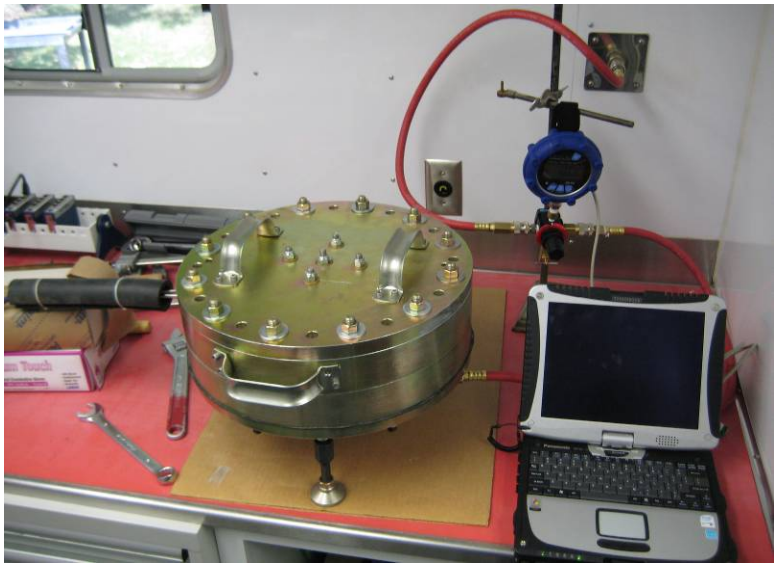

Figure 6. Calibration of EPC in the lab

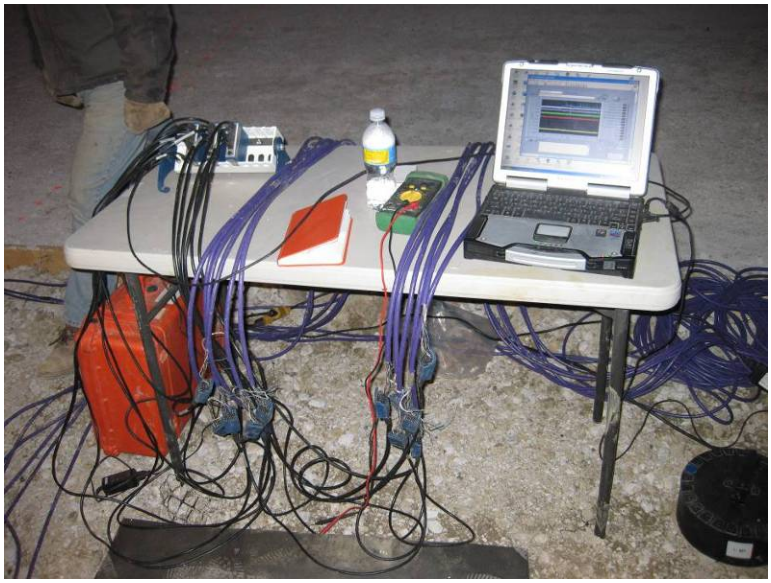

Figure 7. Obtaining stress cell data during traffic

Three EPCs were placed in each test section for field data collection. A summary profile of the test section with location of the EPCs is shown in Figure 8. Vertical stress measurements were taken at the subgrade/geotextile/subbase interface (Figure 9, Figure 10). Horizontal stress measurements were taken in the subgrade and layer 1 of the subbase material (Figure 11). During installation, EPCs were placed and surrounded by the same standard silica sand used during calibration. Use of the sand ensured a uniform stress was applied to the EPC surface. Measurements were taken at a frequency of 1613 Hz. Periodic temperature measurements for temperature correction were taken using thermistors mounted on the EPC.

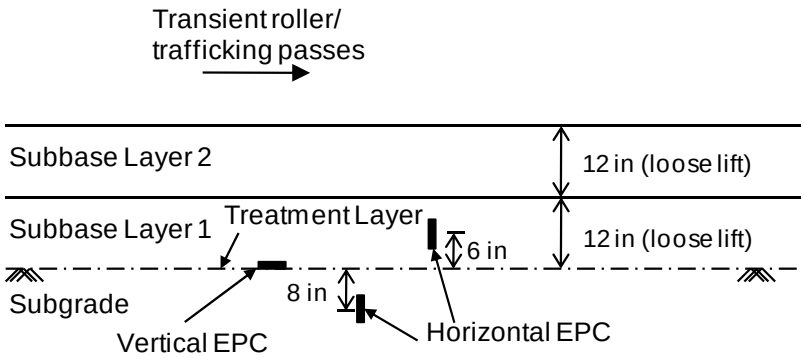

Figure 8. Profile of EPC installation

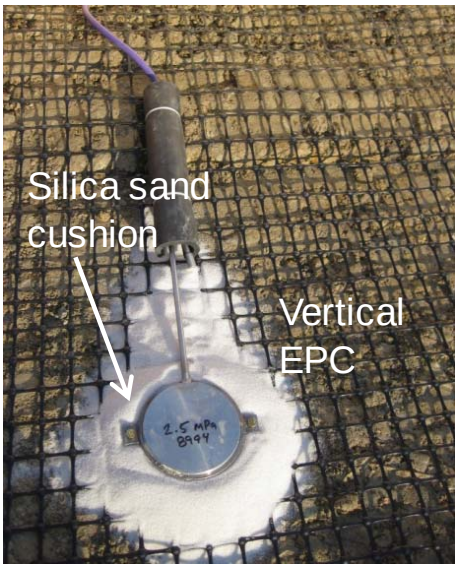

Figure 9. Placing vertical earth pressure cell on Tensar BX1200 at base of subbase 1

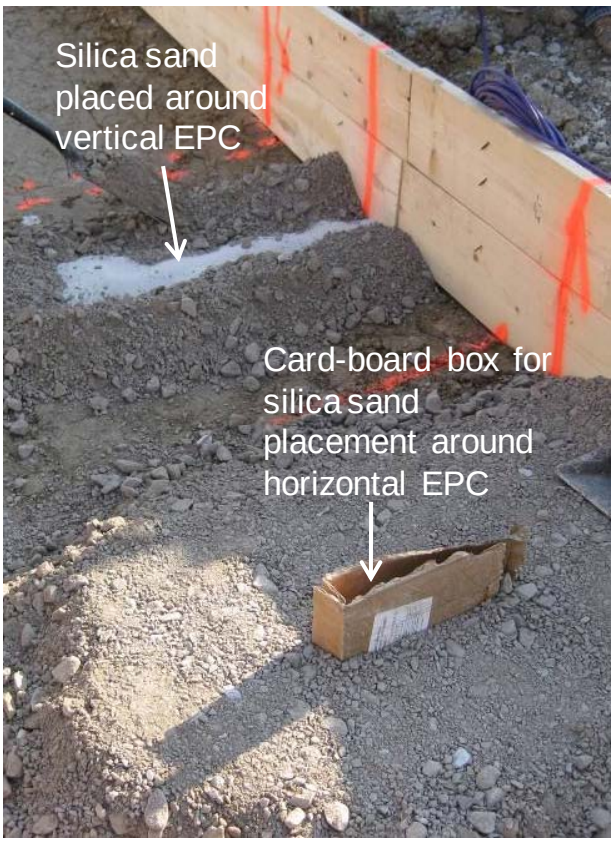

Figure 10. Vertical and horizontal EPC during placement of subbase 1 in control section – cardboard is used as a temporary liner to contain the sand backfill

Figure 11. Placing horizontal earth pressure cell in subbase 1

Load Test Truck

The Ford L8000 dump truck shown in Figure 12 was used for trafficking the constructed test sections. The vehicle was loaded to a gross vehicle weight of 18,370 kg (20 tons). The front tires were Goodyear G159 size 11R22.5 and rear dual tires were Continental HSR size 11R22.5. Both front and rear tire pressures were about 690 kPa (100 psi). The truck was operated at approximately 5 km/h (3 mph) during trafficking passes following the same wheel path during each pass and in the same direction.

Figure 12. Truck utilized for load testing

Elevation Profiling

Prior to compaction and trafficking profile surveys were conducted at locations in each treatment section. Profile surveys were also conducted at intervals during the trafficking and after final pass to evaluate changes in ground conditions. A variety of survey devices and techniques were used to collect data points as described below.

Transit Survey

Vertical profile measurements of rutting were collected using an auto level and rod measurements. The horizontal positions of these points were marked and the same locations surveyed at intervals during trafficking.

RTK-GPS

Vertical and horizontal survey data was acquired using RTK-GPS (Figure 13). A

Trimble SPS 881 receiver was used with base station correction provided from a Trimble SPS851 established on site. This survey system is capable of horizontal accuracies of less than 10 mm and vertical accuracies less than 20 mm.

Figure 13. Cross section surveys of W-PP-GT section prior to traffic on subbase 1

Ruler Measurement

At intervals between trafficking passes, rut depth measurements were recorded. A 1 m straight edge was placed perpendicularly across the rut and a tape measure was used to measure the depth from the straight edge to the bottom of the rut. Measurements were taken at the rut edges and every 10 cm across the rut.

Post-Trafficking Excavation

Trenches were excavated using a trenching machine (Figure 14) and a mini-excavator across the test sections after final trafficking was completed to inspect changes in the profile geometry. Transit survey and RTK-GPS survey was conducted. Measurements were focused on the subgrade/subbase interface zone to investigate the resulting deformation from trafficking. Excavations were initially planned at several locations within each test section, but limited to just one or a few in each section due to the amount of time to complete each excavation.

Figure 14. Trenching sections after traffic

MATERIALS

Soils and Aggregates

Two materials comprised the test beds in this study – clay subgrade and crushed limestone subbase. Index properties for both materials are summarized in Table 2. The clay subgrade was classified as CL and the crushed limestone subbase was classified as GP-GM with about 8 percent of fines passing the No. 200 sieve. The maximum particle size of the crushed limestone subbase was 1.5 inches. Figure 15 shows a picture of the subbase material. Grain-size distribution curves for the subgrade and subbase materials are provided in Figure 16 and Figure 17, respectively.

Standard Proctors curves for the subgrade material are provided in Figure 18. Results of Proctor tests conducted by the ISU research team and results provided by Contractor are included in Figure 18. The maximum dry unit weight (γ_{dmax}) and optimum moisture content (w_{opt}) for this material are listed in Table 2. Figure 18also shows the subgrade in-situ moisture density measurements in relation to the standard Proctor curves. In-situ test measurements were obtained from four to five test locations in each test section. The in-situ moisture content of the subgrade varied from about 15.8% to 24.0% with an average of about 20.4% which is about 3.2% wet of w_{opt}. The in-situ dry unit weight of the subgrade varied from about 100.4 pcf (15.77 kN/m^3) to 116.3 pcf (18.26 kN/m^3) with an average of about 107.5 pcf (16.88 kN/m^3) which is about 97% of standard Proctor γ_{dmax}.

Figure 15. Crushed limestone subbase aggregate with maximum particle size = 1.5 inches

Table 2. Summary of material properties

Parameter	Clay	Crushed stone
Layer	Subgrade	Subbase
Material Description	Lean clay	Poorly graded gravel with silt and sand
Standard Proctor maximum dry unit weight (kN/m^3) (based on tests conducted by ISU)	17.41	—
Optimum moisture content (%) (based on tests conducted by ISU)	17.2	
Maximum and minimum index density (kN/m^3)	—	22.4, 16.7
Percent Finer (1.5 inch)	—	100
Percent Finer (1.0 inch)	—	87
Percent Finer (0.75 inch)	—	77
Gravel Content (%) (> 4.75mm)	3	55
Sand Content (%) (4.75mm – 75μm)	20	37
Silt Content (%) (75μm – 2μm)	45	6
Clay Content (%) (< 2μm)	32	2
Coefficient of Uniformity (c_u)	—	29.2
Coefficient of Curvature (c_c)	—	3.2
Liquid Limit, LL (%)	45	NP
Plasticity Index, PI	21	NP
AASHTO	A-7-6(16)	A-1-a
USCS	CL	GP-GM
G_s	2.75	—

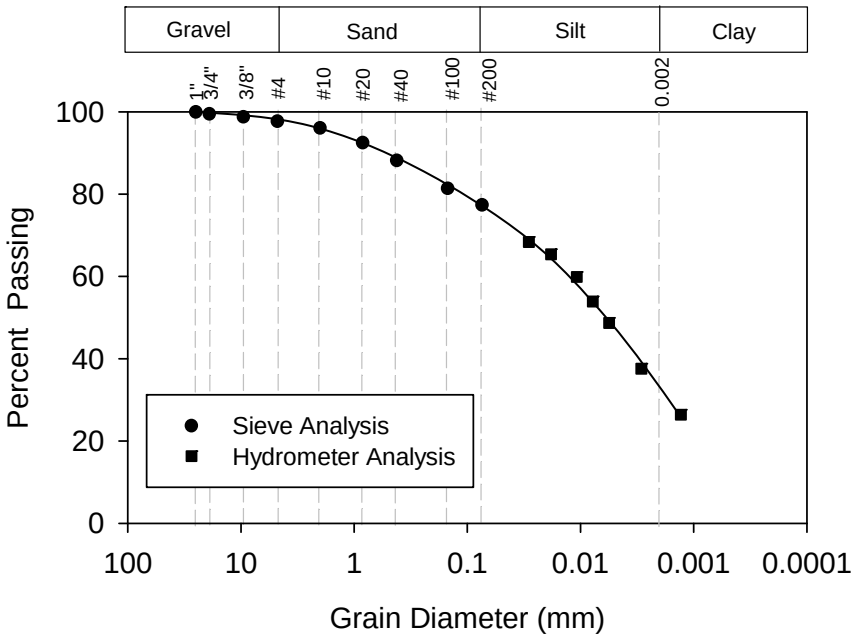

Figure 16. Grain-size distribution curve for subgrade

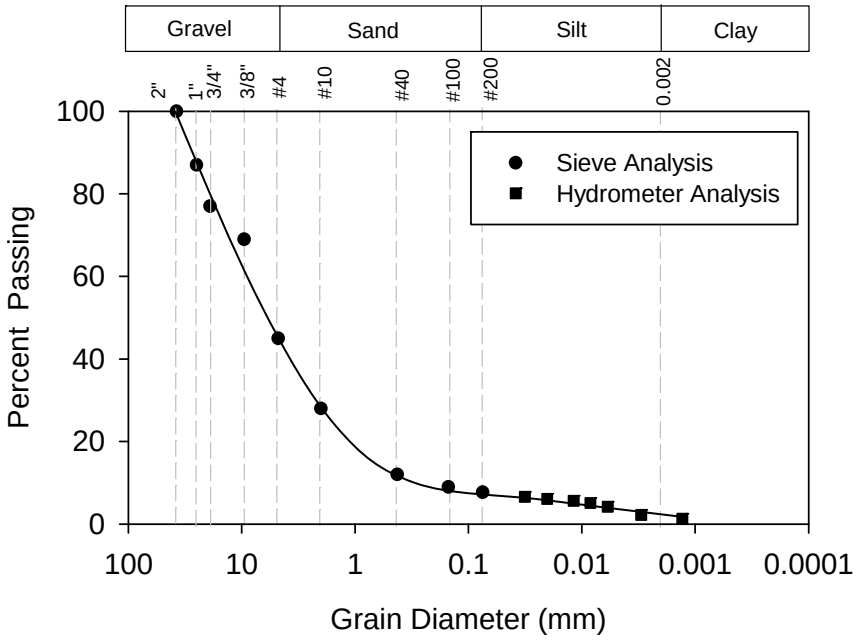

Figure 17. Grain-size distribution curve for subbase

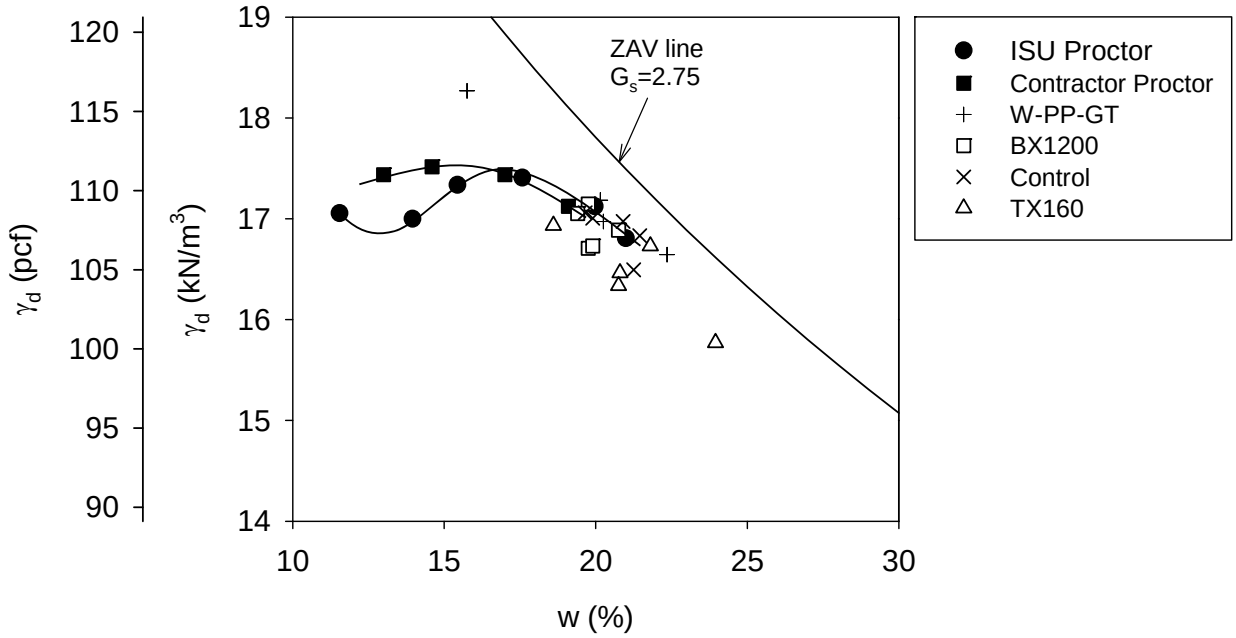

Figure 18. Laboratory Proctor curve and field moisture and dry density measurements on subgrade

Laboratory CBR testing was conducted on subgrade materials at six different moisture contents varying from about 14% to 26%. Samples were compacted to about 95% of the standard Proctor energy achieved by using 53 blows per each layer in three layers. The objective of using lower compaction energy was to achieve similar relative compaction values as measured in the test sections. CBR results along with moisture and dry unit weight measurements of the CBR samples in comparison with the laboratory standard Proctor test results are presented in Figure 19. The relative compaction of the CBR samples varied from about 86% to 96% of standard Proctor maximum dry unit weight. CBR values obtained for each sample are summarized in Table 3. Results indicate that the CBR values are sensitive to moisture content. The CBR value decreased from about 28 to 10 with an increase in moisture content from about 15% to 20%. The CBR value further decreased to about 3 at about 22% moisture content and 1 at about 26% moisture content. It believed that variable and low CBR values contributed to variable rut depth measurements presented later.

Laboratory CBR testing was also conducted on subbase material. Tests were conducted by preparing samples at three different compaction energies as summarized in Table 4. Moisture and dry unit weight measurements of the samples and CBR results are summarized in Table 4. Results indicate that CBR of the subbase material increase with increasing dry unit weight of the material.

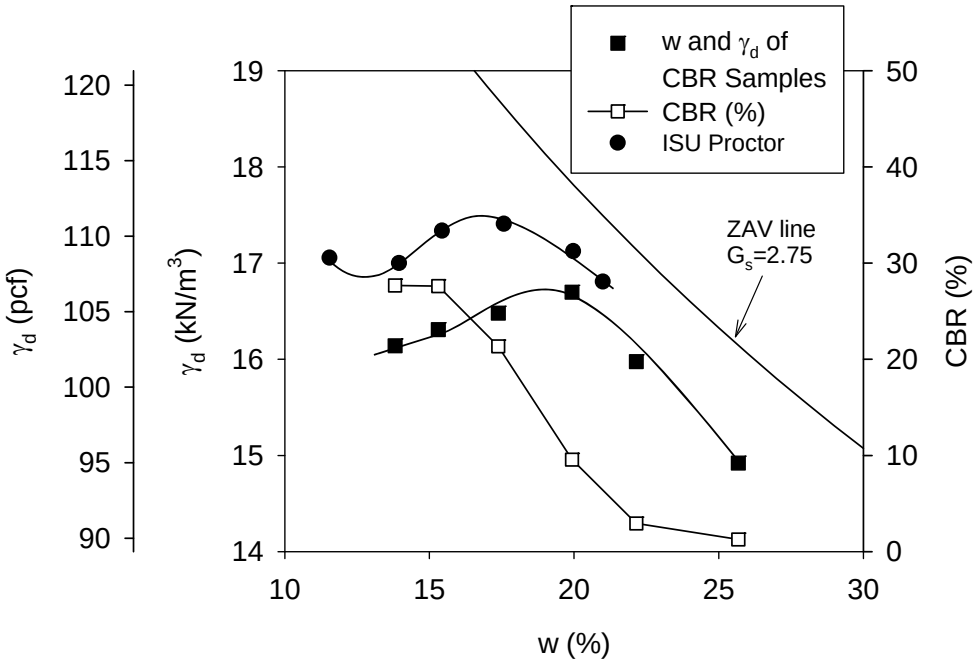

Figure 19. Subgrade CBR test results (at 0.1 in penetration) in relationship with moisture and dry unit weight measurements and Proctor test results

Table 3. Laboratory CBR test results on subgrade material

w (%)	γ_d (kN/m^3)	γ_d (pcf)	CBR at 0.1 in penetration	CBR at 0.2 in penetration
13.8	16.14	102.7	27.7	23.9
15.3	16.31	103.8	27.6	23.5
17.4	16.48	104.9	21.3	18.6
19.9	16.70	106.3	9.6	8.5
22.1	15.97	101.7	2.9	2.9
25.7	14.92	95.0	1.3	1.2

Table 4. Laboratory CBR tests on subbase material

Compaction Effort	Substandard*	Standard**		Modified ***
Moisture content (%)	3.8	3.7	3.9	3.6
Dry density (kN/m^3)	18.5	19.4	19.3	21.2
CBR at 0.1 in	21	38	31	108
CBR at 0.2 in	21	39	34	—

Notes: * Compaction energy = 300 kN-m/m^3, **Compaction energy = 600 kN-m/m^3, *** Compaction energy = 2700 kN-m/m^3

To characterize the shear strength properties of the compacted subgrade and subbase materials, reconstituted samples of materials were compacted and tested in the laboratory using UU triaxial test procedures at confining stresses up to 462 kPa (67 psi). The subgrade samples were compacted to a target relative compaction value of about 97% of standard Proctor γ_{dmax} at a moisture content of about 4.1% wet of standard Proctor w_{opt}. The subbase aggregate was compacted at 3.1 to 3.4 percent moisture content to two different target densities – 56% and 93% relative density (D_r) to represent different states of compaction in the field. Results obtained from UU triaxial testing on subgrade and subbase materials at different confining stresses are presented in Figure 20.

The undrained shear strength for the subgrade material varied from about 115 to 128 kPa (2400 to 2600 psf @ 21.3% moisture content). The shear strength of the subgrade material was not sensitive to change in confining stresses. Subbase materials on the other hand were highly confining stress dependent – increasing confining stresses increased the shear strength of the material. Subbase material samples tested at D_r = 56% relative density exhibited a strain hardening response, while the specimens at D_r = 93% exhibited a strain softening response (note that the samples were unsaturated). For both relative density conditions, peak shear strengths were achieved at about 1.5 to 2.5% strain.

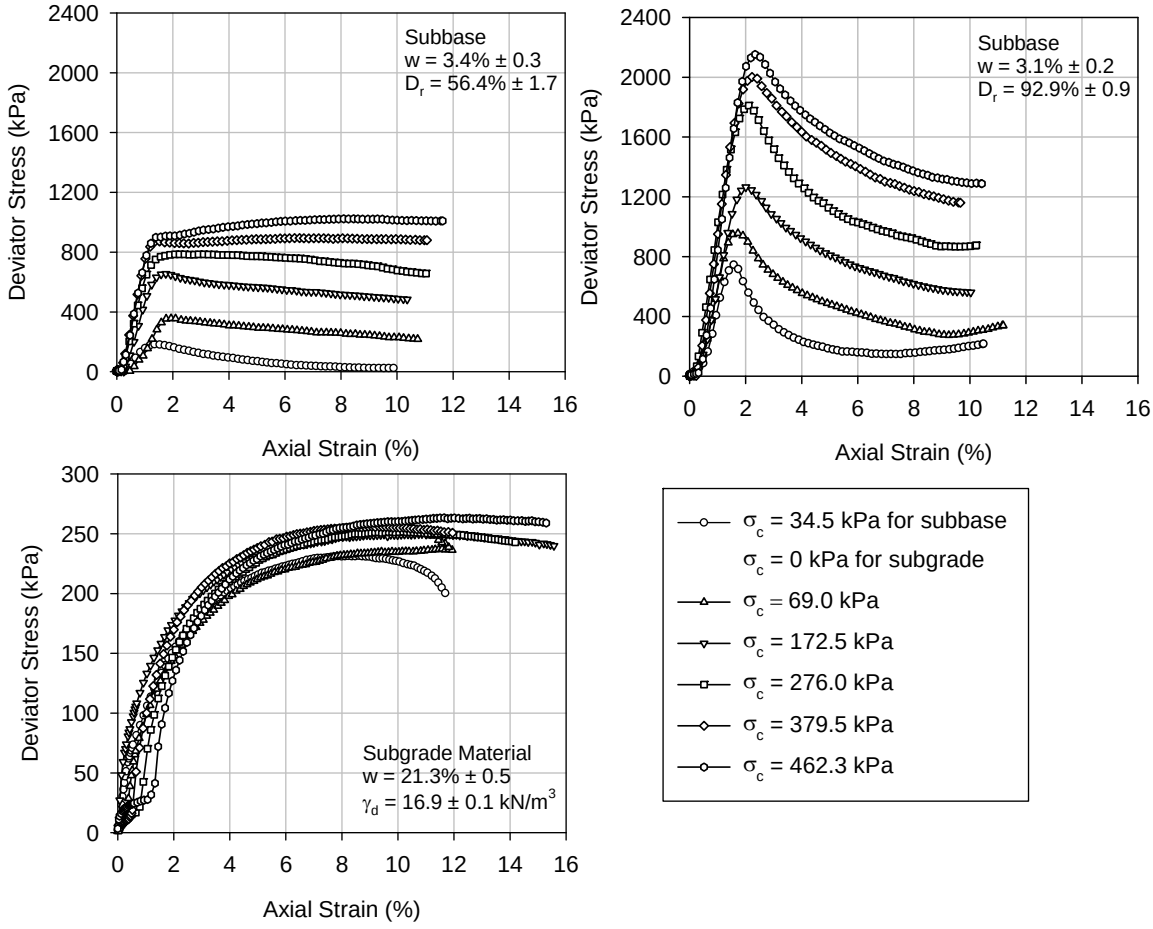

Figure 20. UU tests results for both subgrade and subbase materials

Geosynthetic Materials

Three geosynthetic materials were used during this investigation. Some physical properties of each geosynthetic material are summarized in Table 5. Each geosynthetic material was placed using the same technique whereby the subgrade was moisture conditioned, mixed, and rolled prior to rolling out the geosynthetic and pulling the edges tight to eliminate any folds in the geosynthetic. Next the aggregate material was carefully placed over the geosynthetic using a skid steer loader whereby the loader did not drive directly over the geosynthetic, but rather the aggregate being placed ahead of the machine.

Table 5. Summary of geosynthetic treatments

Designation	Type	Physical Properties
BX1200	Polypropylene Geogrid	Tensile Strength @ 2% strain 6.0 kN/m Ultimate Tensile strength 19.2 kN/m
TX160	Polypropylene Geogrid	Radial Stiffness = 300 kN/m @ 0.5% strain
W-PP-GT	Polypropylene 14.5 osy Geotextile	Tensile Strength @ 2% strain 14.0 kN/m Ultimate Tensile Strength 70.0 kN/m

EXPERIMENTAL PLAN AND TEST BED CONSTRUCTION

Table 6 provides a brief summary of the testing schedule and measurements on each test section and each layer of material.

Table 6. Summary of test beds and in-situ testing

Test Sections	Date	Material	In-situ Test Measurement	Comments
W-PP-GT, BX1200, Control, TX160	3/17/2009	Subgrade	w, γ_d, CBR, E_{LWD-Z2}	Initial Check
W-PP-GT, BX1200	3/17/2009	Subgrade	w, γ_d, CBR, E_{LWD-Z2}	Moisture Low
W-PP-GT, BX1200, Control, TX160	3/17/2009	Subgrade	w, γ_d, CBR, E_{LWD-Z2}	Point measurements on final subgrade after 2 Passes
W-PP-GT, BX1200, Control, TX160	3/18/2009	Subbase layer #1	w, γ_d, CBR, E_{LWD-Z2}	Point measurements after 0, 1, 2, 4 and 10 roller passes
W-PP-GT, BX1200	3/18/2009	Subbase layer #1	Rut depth profiles	Outside and inside wheel path longitudinal profiles after 4 trafficking passes
Control, TX160	3/18/2009	Subbase layer #1	E_{V1}, E_{V2}	Point measurements at two locations after 10 passes
W-PP-GT, BX1200, Control, TX160	3/19/2009	Subbase layer #2	w, γ_d, CBR, E_{LWD-Z2}	Point measurements after 0, 1, 2, 4, and 21 roller passes
W-PP-GT, BX1200, Control, TX160	3/19/2009	Subbase layer #2	E_{V1}, E_{V2}	Point measurements after 21 roller passes
W-PP-GT, BX1200, Control, TX160	3/19/2009 3/20/2009	Subbase layer #2	Rut depth profiles	Transverse rut profiles at one location in each section after 5, 10, 15, 25, 50, 75, 100, 126, 150 trafficking passes, outside and inside wheel path longitudinal profiles after 75 and 150 trafficking passes
W-PP-GT, BX1200, Control, TX160	3/20/2009	Subbase layer #2	CBR	Point measurements in outside and inside wheel paths after 150 trafficking passes
W-PP-GT, BX1200, Control, TX160	3/20/2009	Subbase layer #2	CBR, full depth cross-section	Outside and inside wheel paths after trafficking passes

Note: w – moisture content, γ_d – dry unit weight, CBR – California bearing ratio determined from dynamic cone penetrometer (DCP) test, E_{LWD-Z2} – elastic modulus determined using Zorn model light weight deflectometer (LWD) with a 200 millimeter plate, E_{V1} and E_{V2} – initial and reload moduli determined from 300 mm diameter static plate load test (PLT)

Description of Test Sections

Four test sections with three different layers (subgrade, subbase layer 1, and subbase layer 2) were tested during this field study. Figure 21 shows a photograph of the test site and labeled test sections.

Three test sections (W-PP-GT, BX1200, and TX160) consisted of a geosynthetic treatment layer at the interface of the subgrade and subbase layer 1, and one test section (control) did not have a treatment layer at the interface. A summary of each test bed with material conditions and tests performed is provided in Table 6. Figure 22 shows the proximity of the test sections and locations of the in-situ point measurements based on RTK-GPS position measurements. In-situ point measurements (e.g., w, γ_d, CBR, E_{LWD-Z2}, E_{V1}, E_{V2}) were mostly obtained from five test locations along the center lane in each test section. Longitudinal rut depth profiles were obtained along the outside and inside wheel paths trafficking lanes (as labeled in Figure 22) on subbase layers 1 and 2. Transverse rut depth profiles were obtained from one test location (point (3)) in each test section from multiple trafficking passes under outside and inside wheel paths. To assess variability across each test section, additional DCP tests were conducted in the outside and inside wheel paths after final trafficking pass on subbase layer 2. Transit survey and RTK-GPS survey was performed transversely at each test location on subgrade, subbase layer 1, and subbase layer 2 to obtain comparison elevation measurements. These measurement locations are shown in Figure 23.

Rut depth measurements obtained beneath the wheel following trafficking passes are presented in this report using the nomenclature – outside and inside wheel paths as indicated in Figure 22.

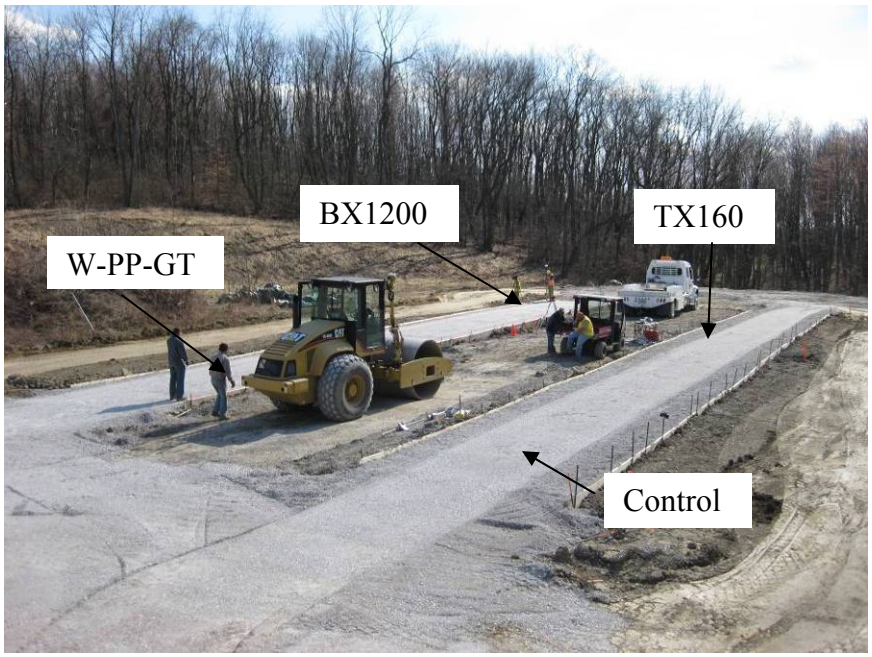

Figure 21. View of site and test section locations

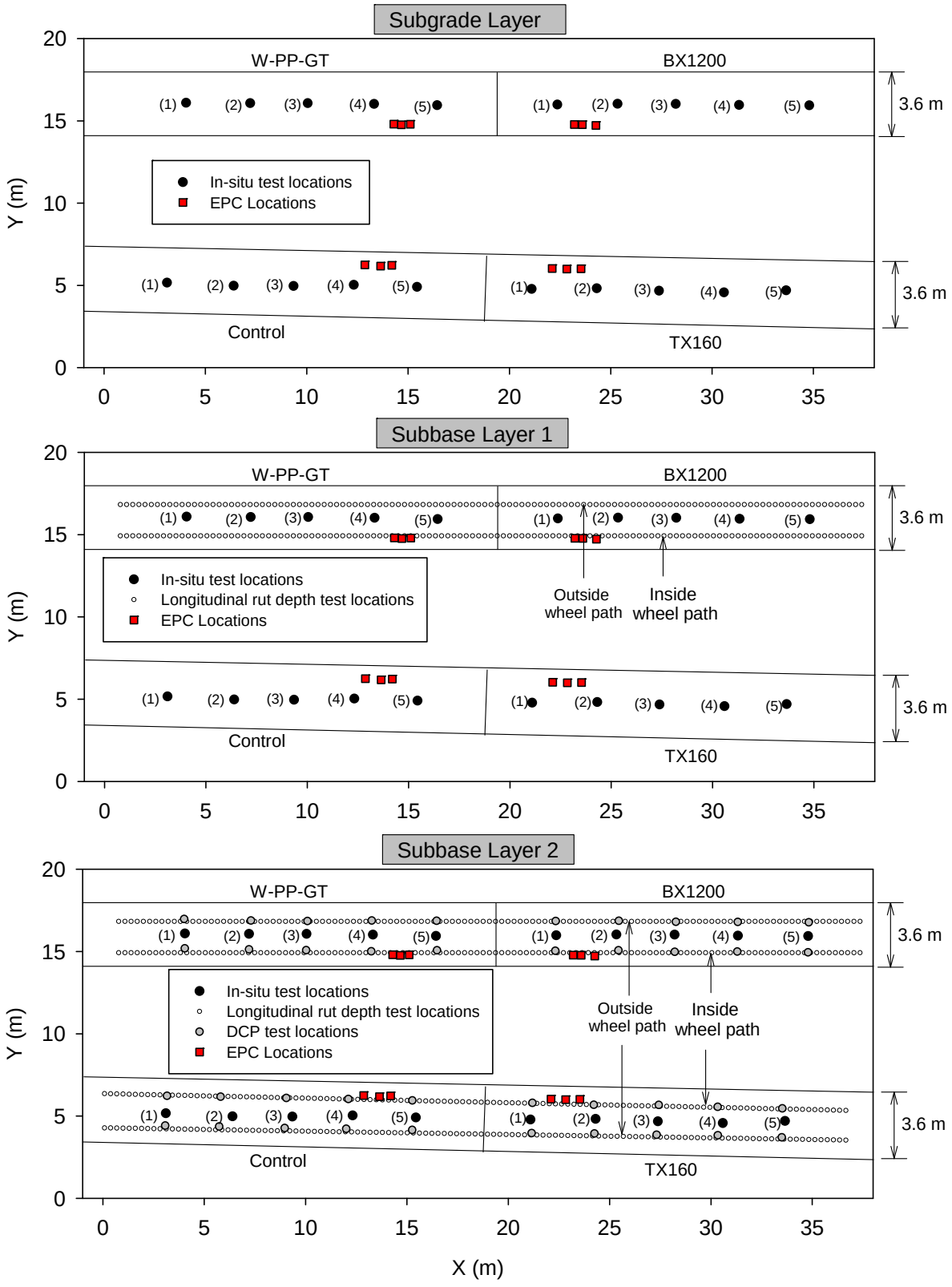

Figure 22. Test section layout and in-situ test locations

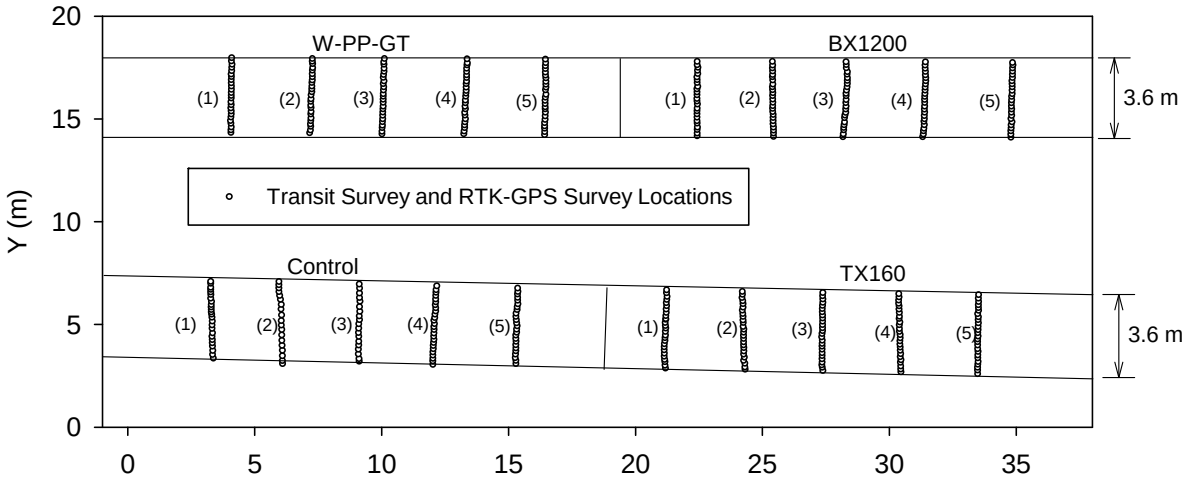

Figure 23. Transit survey and RTK-GPS survey locations

Construction/ Testing Process and Photo Log

Figure 24 through Figure 61 document key features of the construction and testing phases. The construction process was initiated by scarifying the clay subgrade material to a depth of 150 to 200 mm (6 to 8 inches) using a tiller mounted on a tractor. Water was added and several passes of the tiller were used to arrive at a moisture content that produced a subgrade CBR of about 2 to 3. Next the test sections were compacted with two passes of the smooth drum roller. The geosynthetic materials were rolled out and pulled tight. Boards were positioned along the edges of the test sections to contain the subbase layers. Subbase aggregate was then placed using a skid steer loader and advancing the aggregate placement ahead of the skid steer to avoid driving directly on the subgrade. Once the first layer of subbase was placed, in-situ testing was performed along with several roller passes.

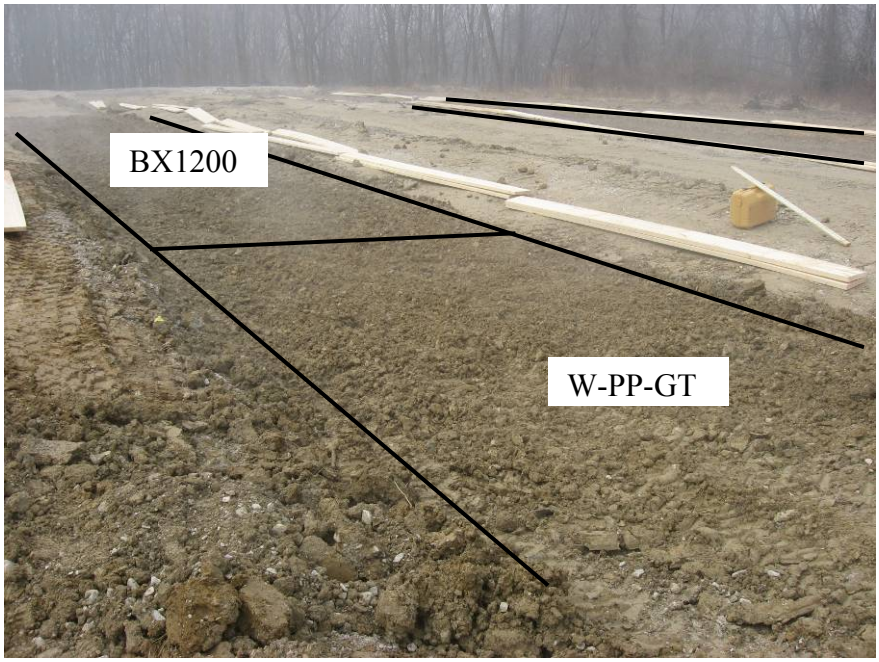

Figure 24. View of W-PP-GT and BX1200 sections during subgrade preparation

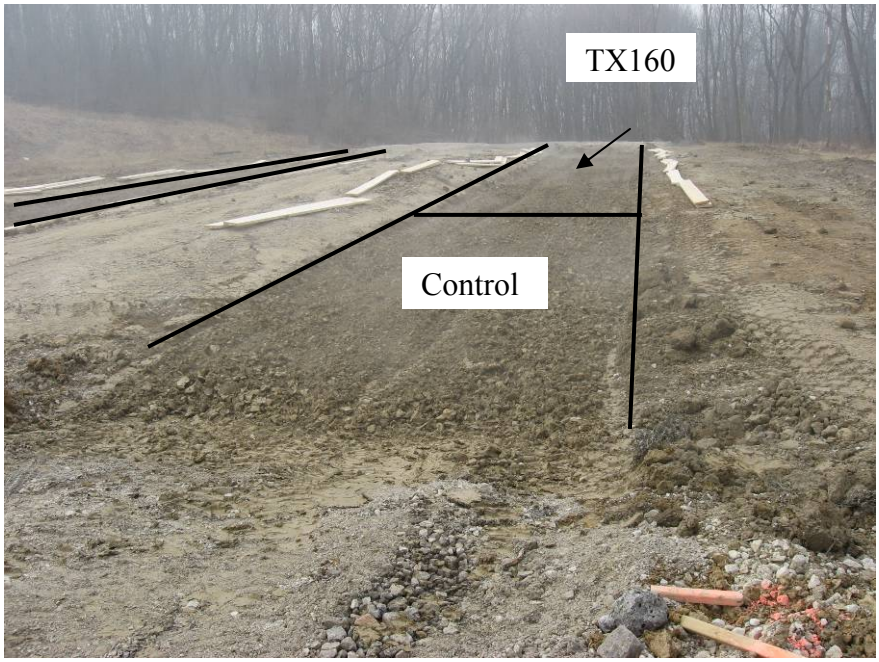

Figure 25. View of control and TX160 sections

Figure 26. Moisture conditioning of W-PP-GT and BX1200 sections

Figure 27. Compacting W-PP-GT and BX1200 sections

Figure 28. Compacting subgrade in control and TX160 sections

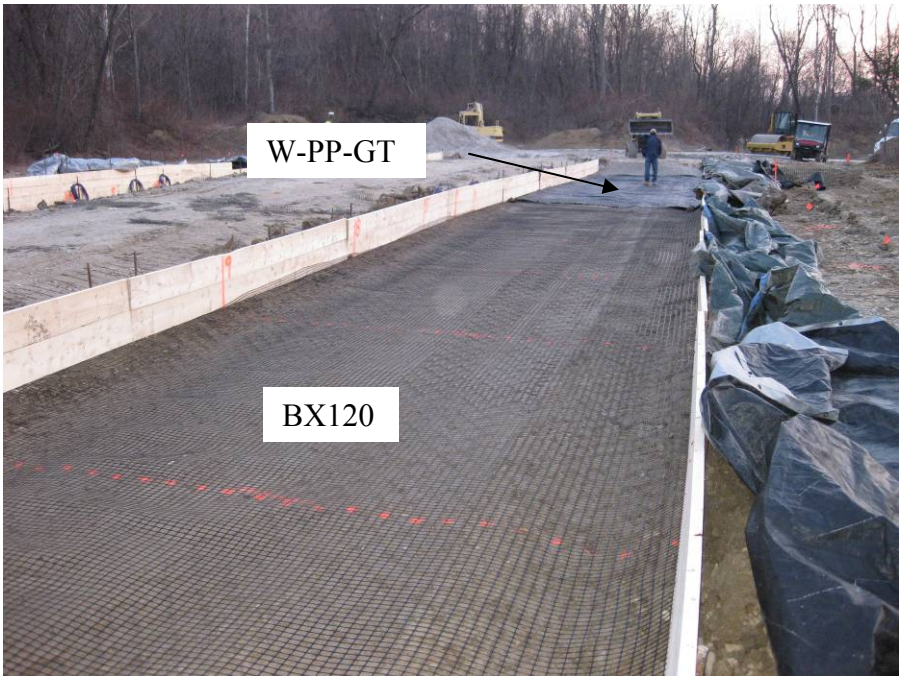

Figure 29. W-PP-GT and Tensar BX1200

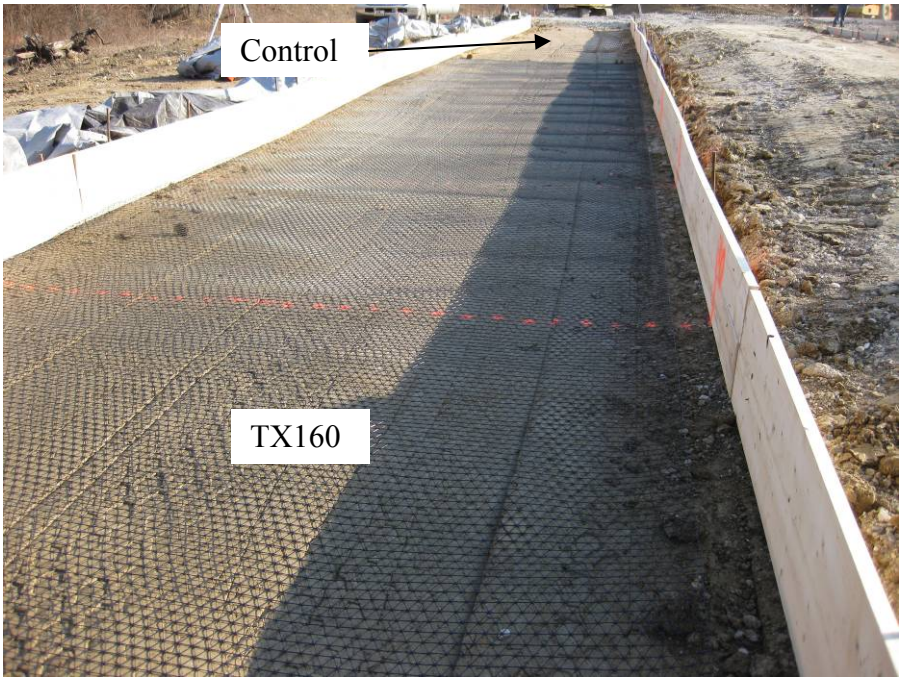

Figure 30. Tensar TX160 and control sections

Figure 31. Placing subbase layer 1 on BX1200 section

Figure 32. Placing subbase layer 1 on Tensar TX160 section

Figure 33. Subgrade, Tensar TX160, and subbase layer 1

Figure 34. Point testing in W-PP-GT prior to compacting subbase 1

Figure 35. Point testing in BX1200 section after roller compaction

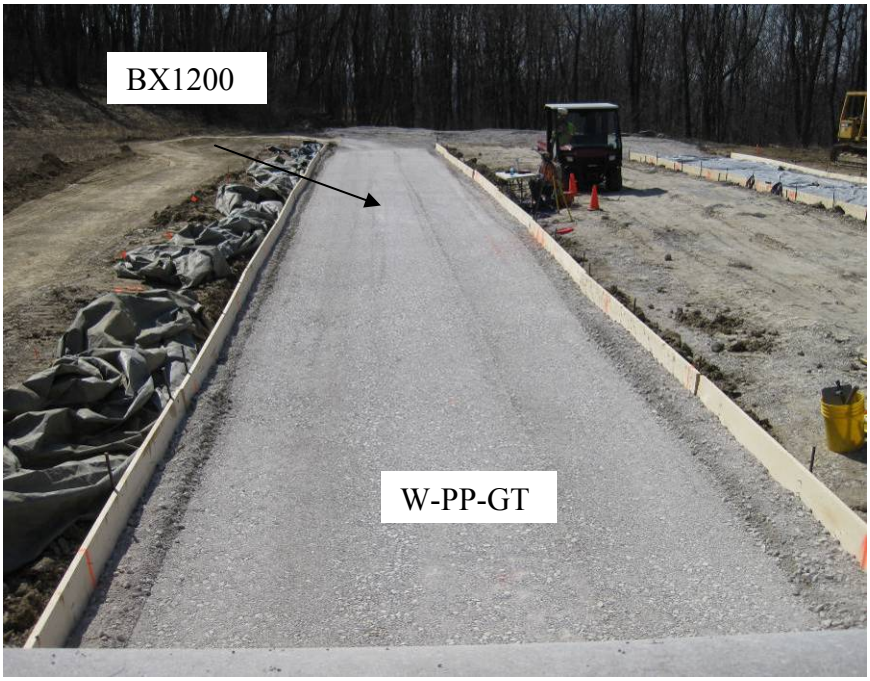

Figure 36. W-PP-GT and BX1200 sections after roller compaction of subbase 1

Figure 37. W-PP-GT and BX1200 subbase 1 after traffic

Figure 38. Point testing in TX160 during compaction of subbase 1

Figure 39. Point testing in TX160 section during compaction of subbase 1 and plate load testing in BX1200 section

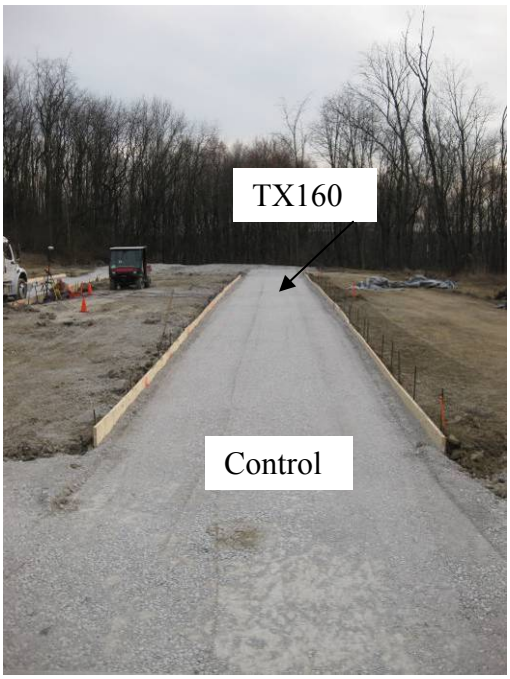

Figure 40. TX160 and control sections near completion of compaction of subbase 1

Figure 41. Traffic on subbase 1 in TX160 section

Figure 42. Rut depth measurements on subbase 1 in control section

Figure 43. Placing subbase 2 in control section and rut depth measurements on subbase 1 in control and TX160 sections

Figure 44. Point testing in W-PP-GT and BX1200 sections during compaction of subbase 2

Figure 45. Plate load testing in W-PP-GT section after compaction of subbase 2

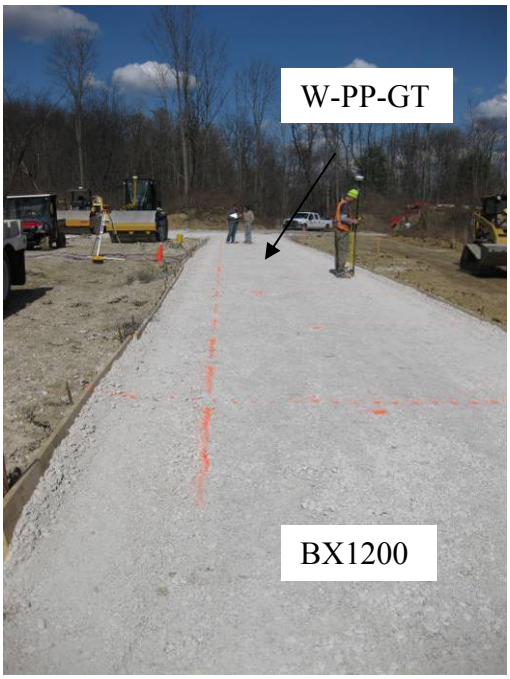

Figure 46. Initial profiles W-PP-GT and BX1200 sections after compaction of subbase 2 prior to traffic

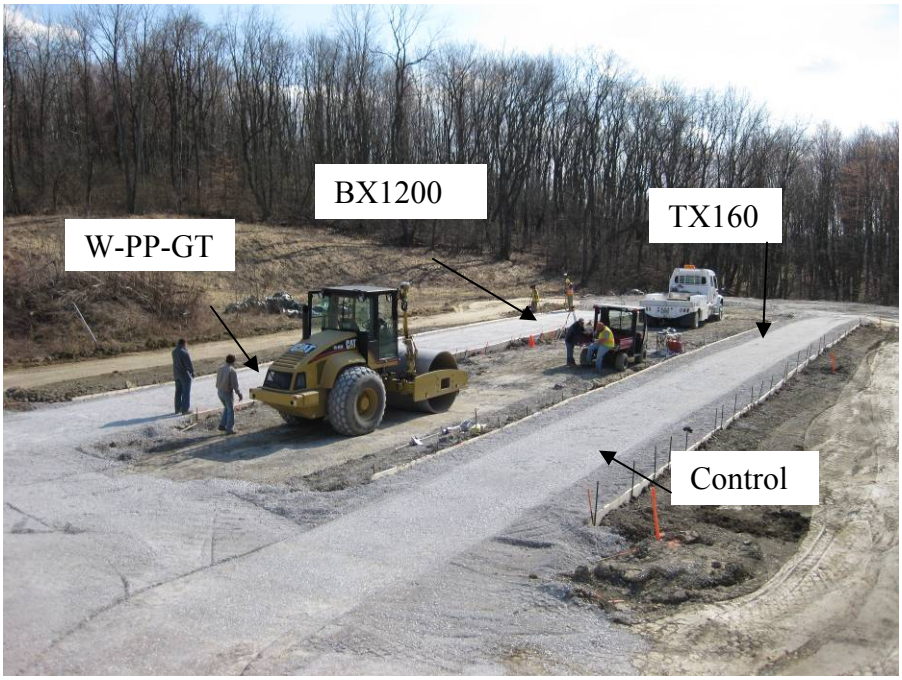

Figure 47. Initial profiles in section after compaction of subbase 2 prior to traffic

Figure 48. Traffic in BX1200 section on subbase 2

Figure 49. Traffic in W-PP-GT and BX1200 sections on subbase 2

Figure 50. Measuring rut depth

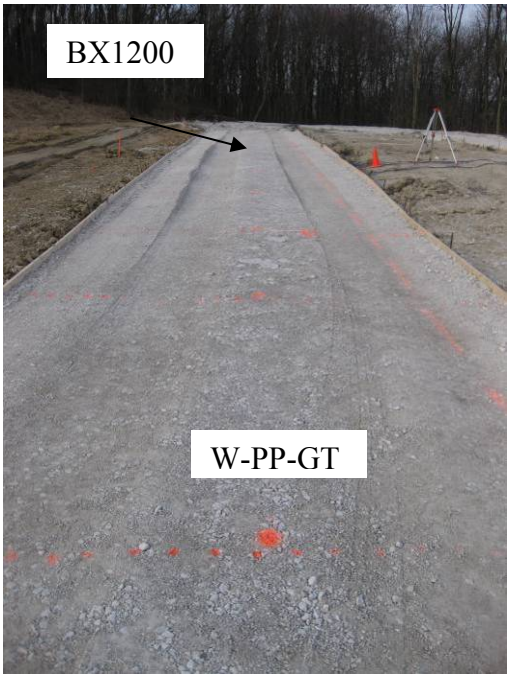

Figure 51. W-PP-GT and BX1200 sections subbase 2 during traffic

Figure 52. Control and TX sections subbase 2 during traffic

Figure 53. W-PP-GT and BX1200 sections nearing end of traffic

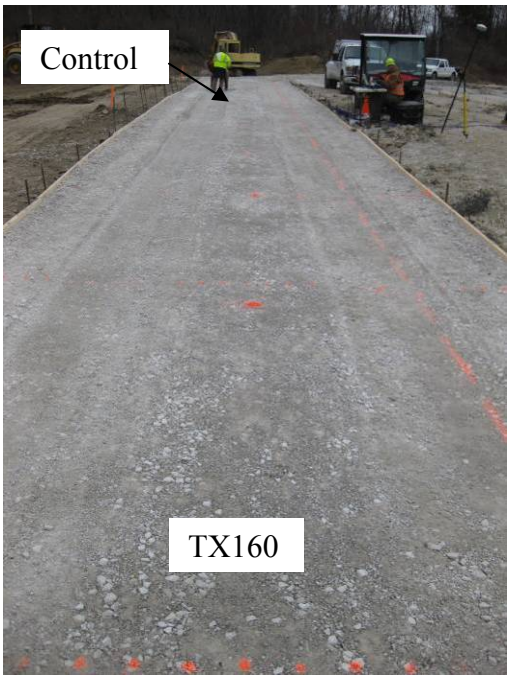

Figure 54. Control and TX160 sections nearing end of traffic

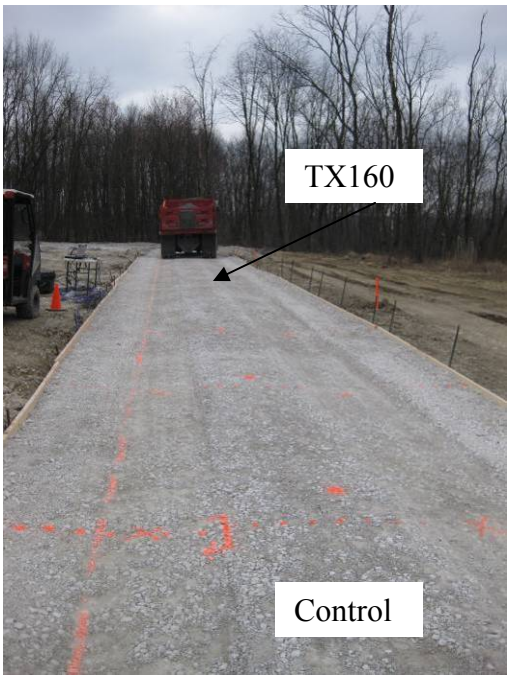

Figure 55. Control and TX160 sections nearing end of traffic

Figure 56. Full depth DCP testing after traffic

Figure 57. Trenching sections after traffic

Figure 58. View of deformation after traffic

Figure 59. W-PP-GT after excavation

Figure 60. Tensar BX1200 after excavation

Figure 61. Tensar TX160 after excavation

RESULTS AND DISCUSSION

In this section of the report, field measurements are presented and discussed. The detail and volume of testing provides new information on the response of these different test sections as a function of the number of roller passes applied during the compaction phase of testing and during the post compaction trafficking study.

Table 6 through Table 8 summarize the average CBR values for each of the test layers – subgrade, subbase layer 1, and subbase layer 2. The average CBR of the subgrade layer CBR was about 2, although it was expected to be variable based on observations of equipment trafficking during preparation. The average CBRs for subbase layers 1 and 2 were about 10 and 45 respectively, but were variable between the different test sections. Table 10 summarizes the average values for each of the test sections for several different roller passes including CBR, E_{LWD}, and D_r. Results show general trends of increasing values with increasing number of roller passes. An interesting observation for the BX1200 and TX160 sections was that the D_r values increased from about 70% to 90% with increasing roller passes from 10 to 21 suggesting a suitable platform for compaction and a benefit from high compaction energy.

Table 7. Average DPI and CBR of test sections after moisture conditioning

Section	Material	DPI	CBR
W-PP-GT	Subgrade	80.8	2.2
BX1200	Subgrade	77.5	2.4
Control	Subgrade	87.0	2.0
TX160	Subgrade	88.9	2.0

Table 8. Average DPI and CBR of test sections after compaction of subbase 1

Section	Material	DPI	CBR
W-PP-GT	Subbase 1	21.5	9.8
BX1200	Subbase 1	24.3	8.6
Control	Subbase 1	19.5	10.7
TX160	Subbase 1	21.3	9.8

Table 9. Average DPI and CBR of test sections after trafficking subbase 2

Section	Material	DPI	CBR
W-PP-GT	Subbase[1]	5.7	41.8
	Subgrade	77.6	2.4
BX1200	Subbase[1]	5.1	47.3
	Subgrade	76.6	2.6
Control	Subbase[1]	5.4	44.9
	Subgrade	63.7	2.9
TX160	Subbase[1]	4.9	49.6
	Subgrade	64.4	2.9

[1] Subbase includes subbase 1 and subbase 2 as included in depth ranges.

Table 10. Summary of average D_r, E_{LWD} and CBR for each section

Layers			Subbase 1				Subbase 2			
Sections			W-PP-GT	BX1200	Control	TX160	W-PP-GT	BX1200	Control	TX160
Passes	0	D_r	44.1	41.3	42.6	46.9	59.7	57.9	60.4	59.9
		E_{LWD} (MPa)	15.4	13.6	18.5	18.0	27.5	26.7	27.1	25.7
		CBR	6.4	5.1	6.5	7.2	8.7	7.6	11.9	8.8
	1	D_r	55.3	51.5	49.8	49.4	59.3	56.6	69.9	68.0
		E_{LWD} (MPa)	13.4	14.9	15.7	13.5	23.1	24.3	31.4	27.0
		CBR	5.8	5.0	6.9	6.5	8.7	8.1	11.2	9.5
	2	D_r	64.5	61.7	57.4	58.6	67.2	62.6	68.9	67.3
		E_{LWD} (MPa)	13.2	13.0	14.7	13.2	23.6	22.9	31.3	26.1
		CBR	8.0	6.1	7.1	7.0	8.9	6.9	10.6	10.1
	4	D_r	59.3	59.4	60.8	60.6	68.8	67.7	68.6	72.8
		E_{LWD} (MPa)	14.4	13.8	15.2	13.7	24.0	22.9	28.2	24.0
		CBR	7.6	6.7	8.1	8.4	9.6	7.0	12.1	10.4
	10	D_r	67.5	70.5	67.8	71.5	75.7	70.2	76.9	76.2
		E_{LWD} (MPa)	14.3	15.2	16.1	14.3	23.7	25.2	29.8	25.9
		CBR	9.7	8.5	11.4	9.5	13.7	10.7	14.6	14.6
	21	D_r	—*	—	—	—	84.5	90.1	90.2	98.5
		E_{LWD} (MPa)	—	—	—	—	31.4	33.8	31.3	28.5

*Note: — indicates no data

Figure 62 through Figure 67 show relationships between the various in-situ measurements and number of roller passes for each layer. On each plot, measurements from the subgrade and subbase layers are provided. The purpose of plotting the data in this manner was to identify trends in the measurement values as a function of the number of roller passes and to identify reflections in support condition in underlying layers to overlying layers (e.g. weak spot in lower layer resulting in poorer compaction in overlying layer, etc.). Figure 62 and Figure 63 show in general that the dry unit weight values achieved in subbase layer 1 can be empirically correlated to the density values in subbase layer 2 as evidenced by the coefficient of regression values, but the data is variable. Also density increases rapidly for the initial 3 to 4 passes and then at a slower rate after that.

Figure 64 and Figure 65 show compaction curves for the light weight deflectometer results. Results show new behavior not previously documented whereby the E_{LWD} values tend to decrease with the first few roller passes and then increase with addition roller passes. This behavior needs to be studied further but is likely linked to mobilization of stresses in the geosynthetic and surrounding subbase materials. Results also show that the modulus value increase by a factor of about two from the subgrade layer to subbase layer 1 and then double again between subbase layer 1 and 2.

Figure 66 and Figure 67 show the CBR values for each layer and each test point as a function of the number of roller passes. Results are similar to the E_{LWD} results, but show variability at a given point location. Figure 68 shows the average values of dry unit weight, E_{LWD}, and CBR plotted as a function of roller pass numbers. Presenting the data as an average for each individual test section has the affect of smoothing out variation in the point measurement plots and clearly shows repeatable trends in the measurement values. Here again the E_{LWD} values tend to initially decrease for subbase layer 1, while density and CBR tends to increase with increasing roller passes. The values measured for all parameter for subbase layer 2 where higher than subbase layer 1. Figure 69 shows relationships between the various in-situ measurements. It is interesting to note that as the density increases beyond 18 kN/m^3, the modulus values increase significantly. A key observation here would be that it might be more important to focus on achievement of a target modulus during QC/QA operations than density.

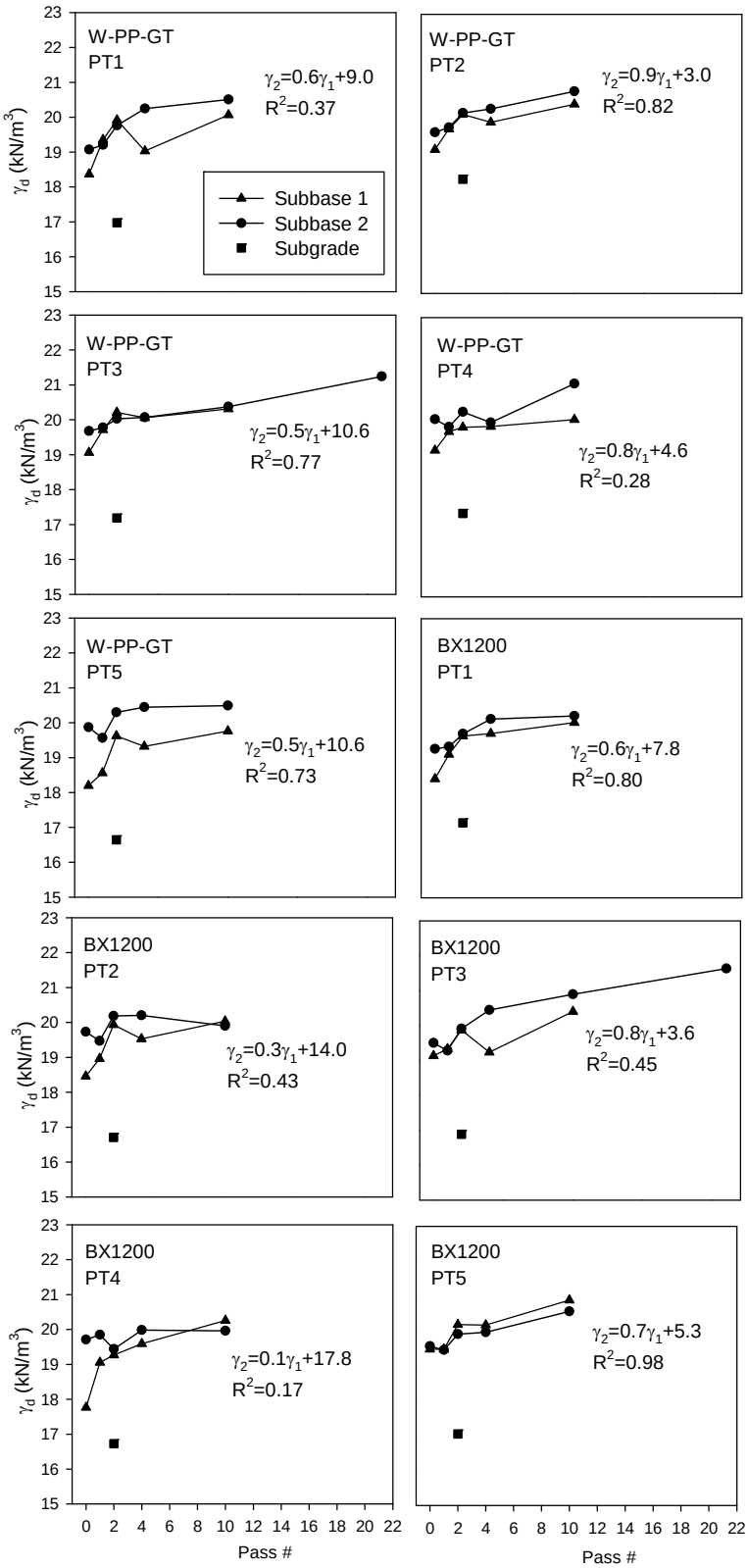

Figure 62. Dry unit weight compaction curves for W-PP-GT and BX1200 sections

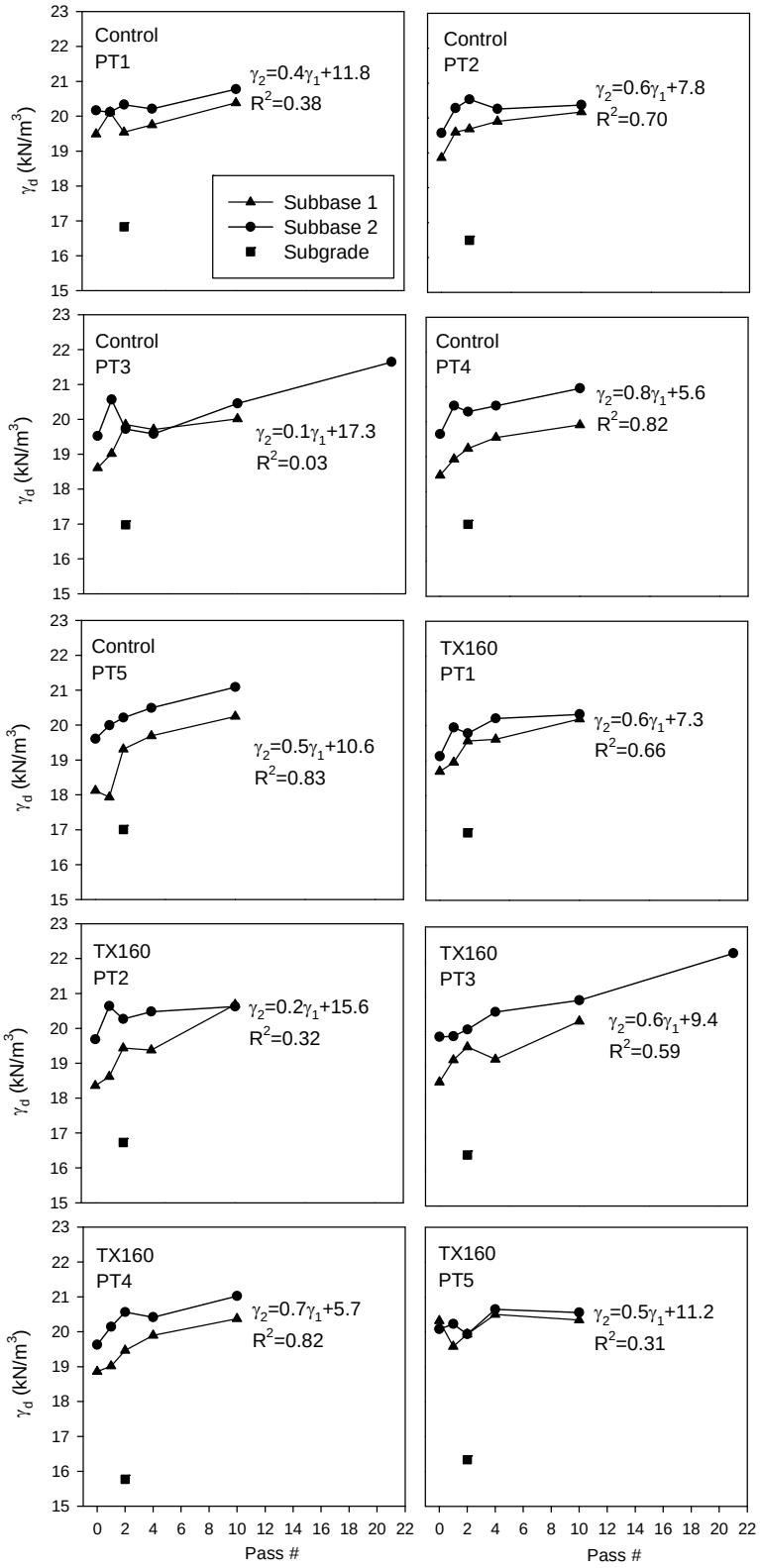

Figure 63. Dry density compaction curves for control and TX160 sections

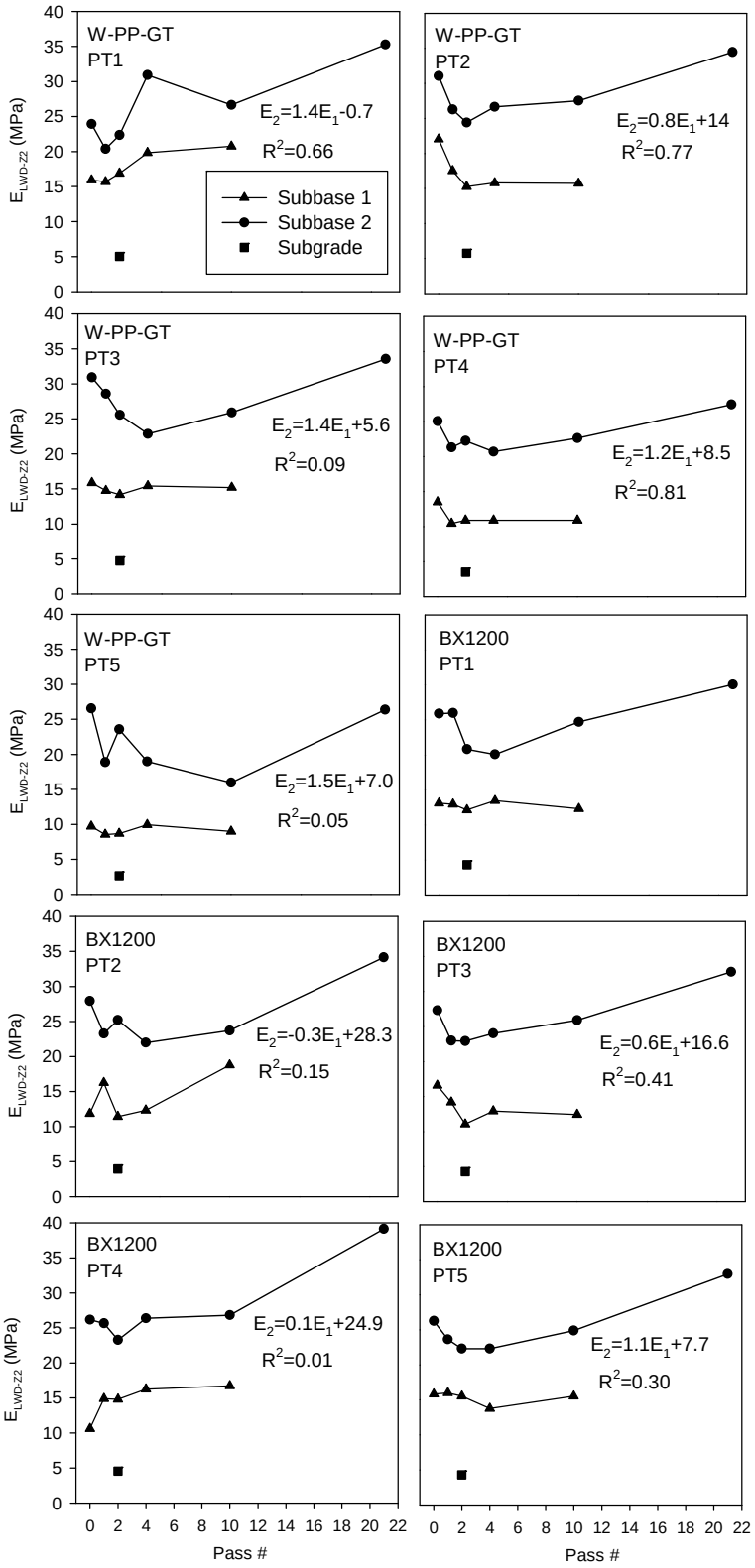

Figure 64. E_{LWD} compaction curves for W-PP-GT and BX1200 sections

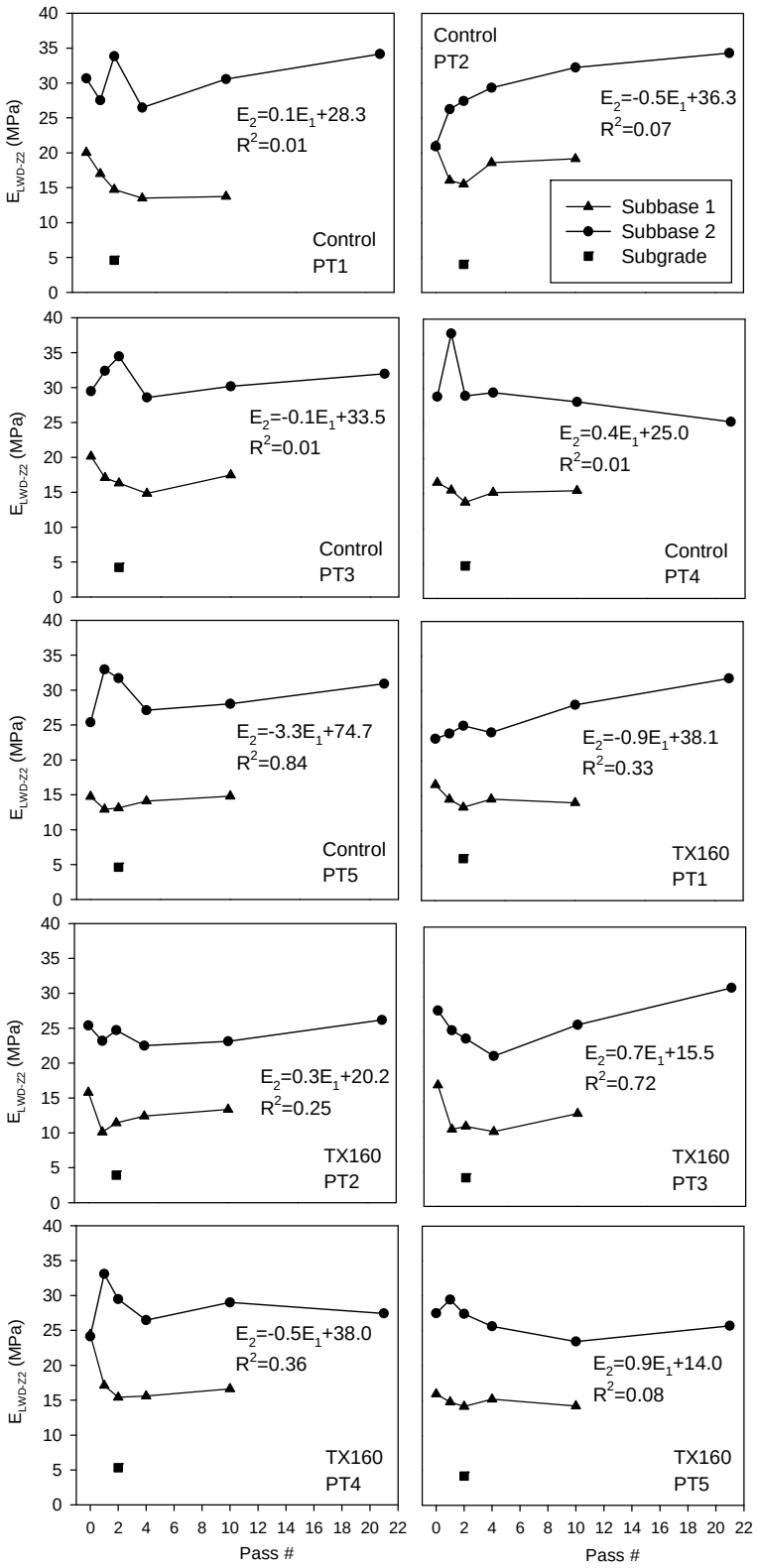

Figure 65. E_{LWD} compaction curves for control and TX160 section

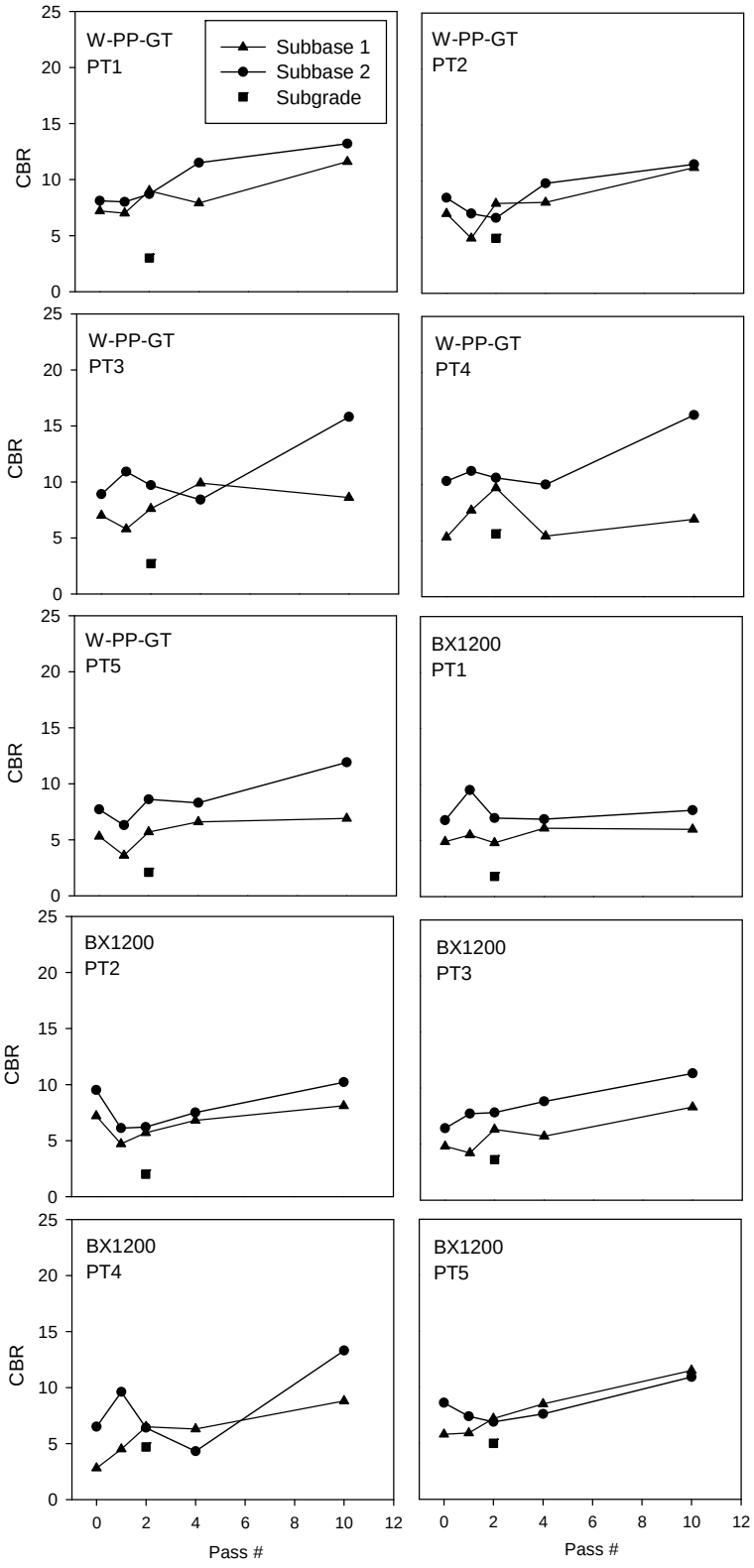

Figure 66. CBR compaction curves for W-PP-GT and BX1200 sections

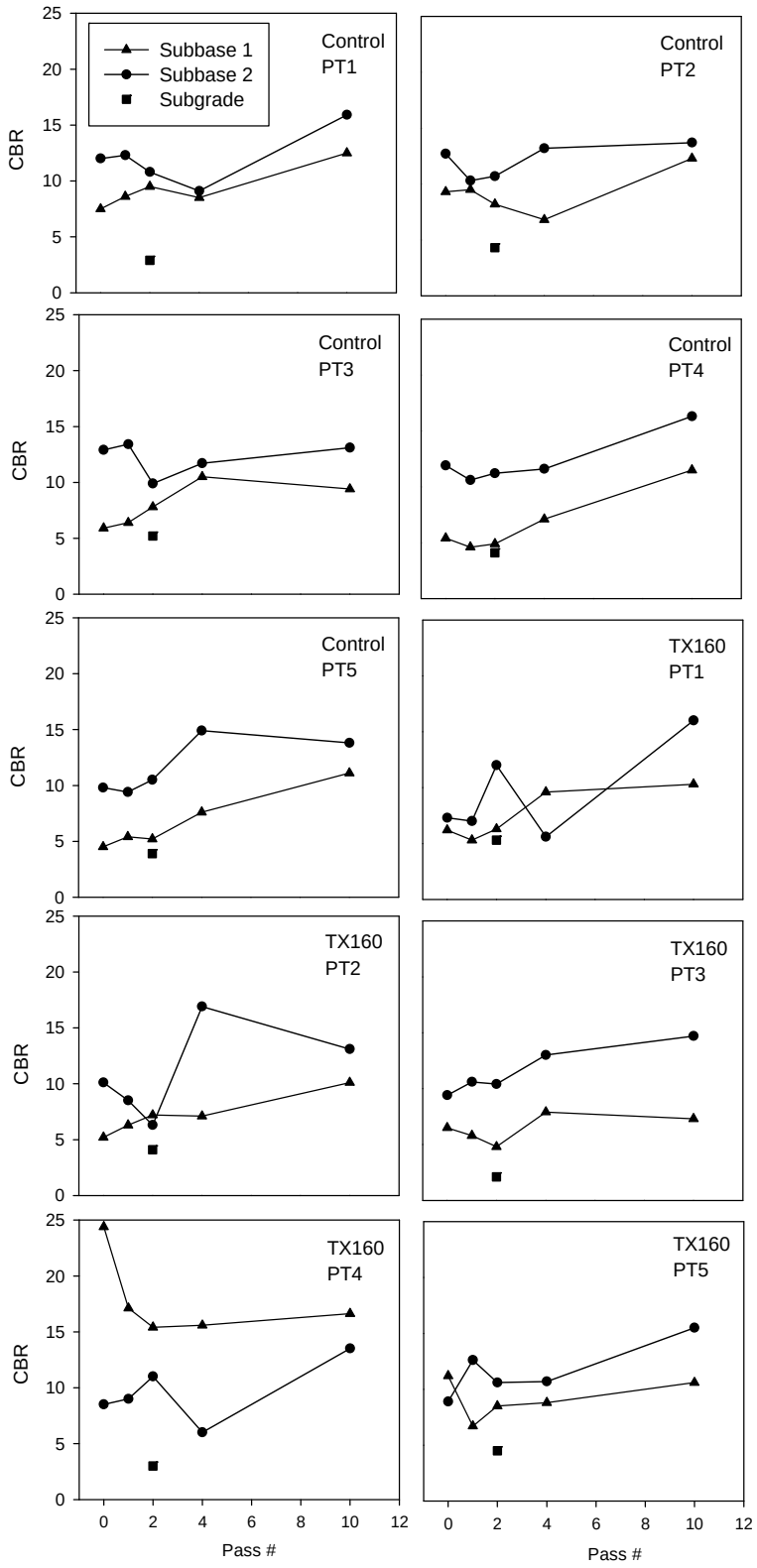

Figure 67. CBR compaction curves for control and TX160 sections

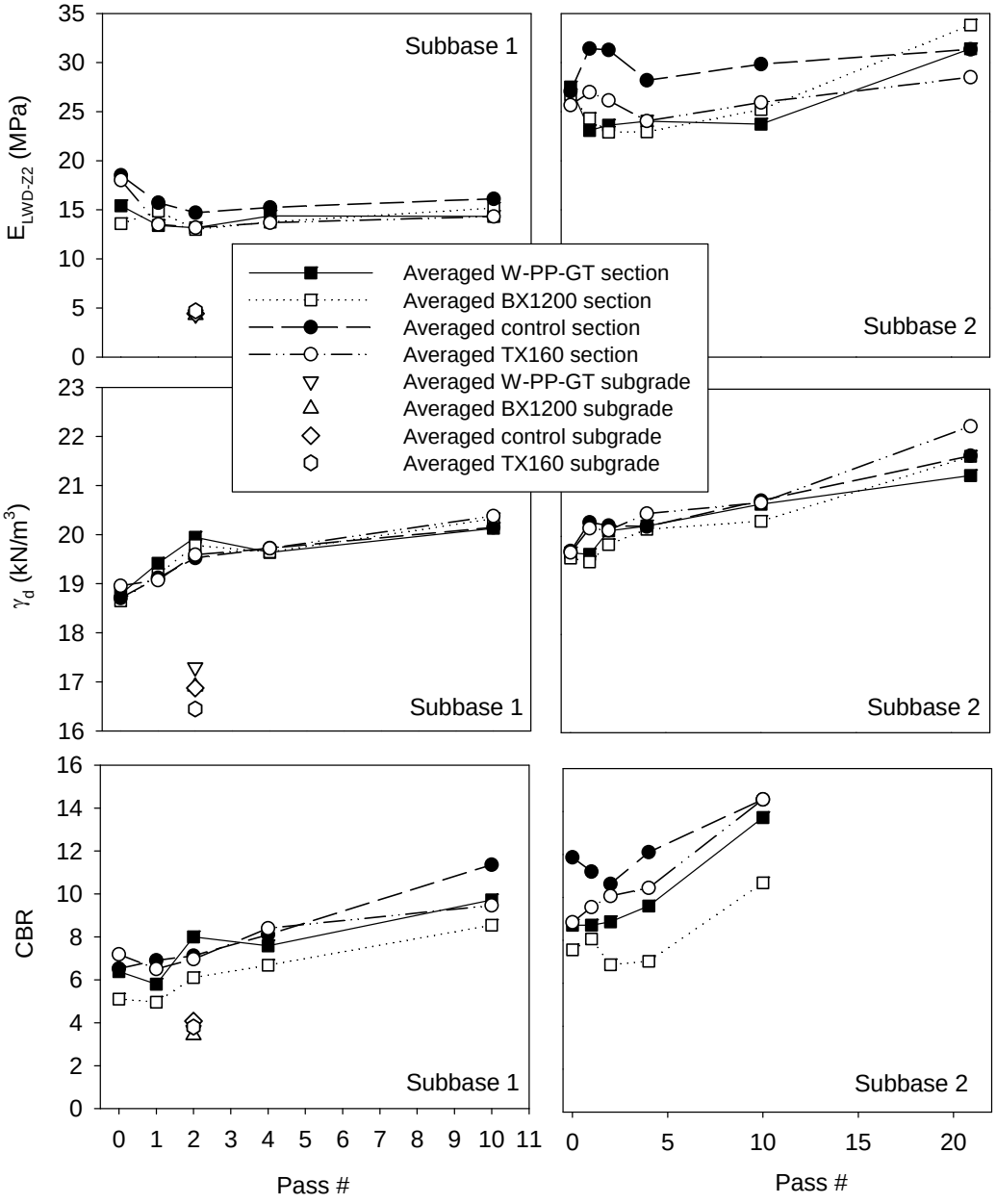

Figure 68. Averaged E_{LWD}, γd and CBR compaction curves for each section

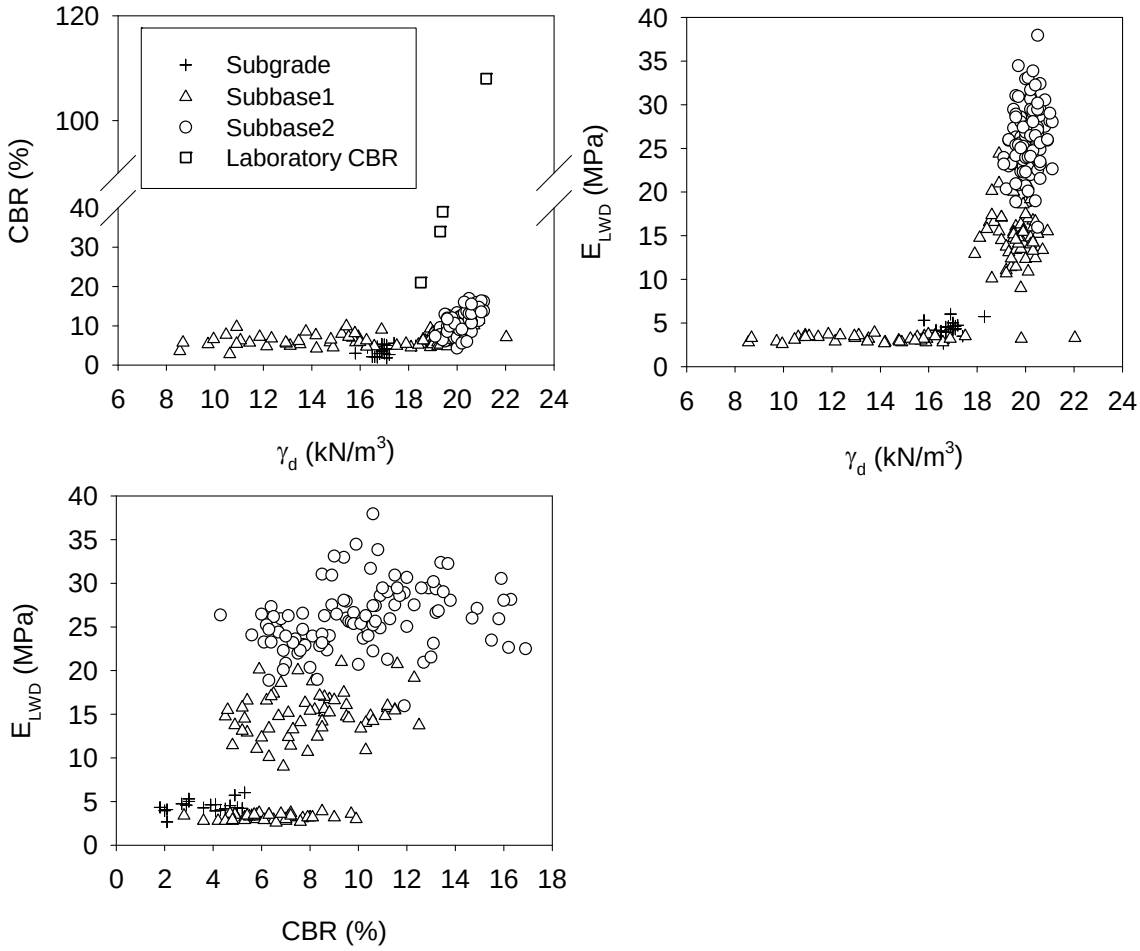

Figure 69. Comparison between CBR, γd and E_{LWD} of each layer

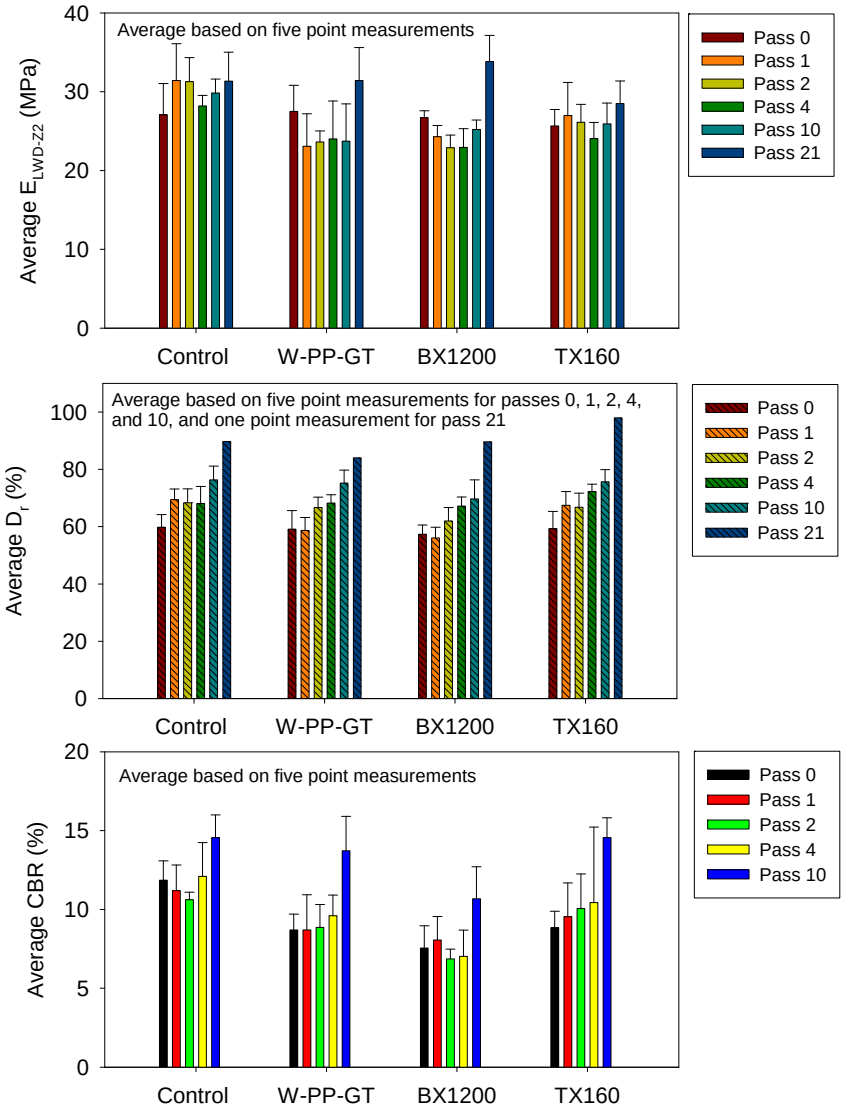

Figure 70. Average in-situ test measurements on subbase layer 2 after 0, 1, 2, 4, 10, and 21 roller passes (note data within 3 m from the start and end of each section not included)

Roller-Integrated Measurement Values

Table 11 and Table 12 summarize the pass numbers and machine operation parameters (i.e. vibration amplitude and vibration frequency for each of the four test section and all roller passes. Figure 71 through Figure 80 shows MVs as a function of distance or pass number for each test bed. Results are plotted for several roller passes for each of the layers tested – subgrade, subbase layer #1, and subbase layer #2. Key observations from this analysis are that the MVs show repeatability between passes and that often the first roller pass yield a higher MV than subsequent roller passes. Further, it is observed that in general the roller MVs are generally low and that might be in part due to the roller having a measurement influence depth on the order of 0.5 m to 1 m. Because the roller measurement influence depth in greater than the compacted layer thickness of the aggregate layers, the soft subgrade is being reflected in the roller MVs.

Table 11. Case/Ammann roller pass summary

Section	Pass Number	Amp (mm)	Freq (Hz)	Section	Pass Number	Amp (mm)	Freq (Hz)
Subgrade							
—	1	0.83	28	—	1	0.85	28
					2	0.83	28
					3	0.83	28
Subbase Layer 1							
W-PP-GT/ BX1200	1	0.69	30	Control/ TX160	1	0.64	30
	2	0.68	30		2	0.64	30
	3	0.68	30		3	0.64	30
	4	0.67	30		4	0.64	30
	5	0.67	30		5	0.63	30
	6	0.67	30		6	0.63	30
	7	0.67	30		7	0.63	31
	8	No Data			8	0.63	30
	9	0.67	30		9	0.63	31
	10	0.67	30		10	0.63	31
	11	0.67	30		11	0.62	30
	12	0.67	30		12	0.62	30
Subbase Layer 2							
W-PP-GT/ BX1200	1	0.64	31	Control/ TX160	1	0.62	30
	2	0.64	31		2	0.61	30
	3	0.63	30		3	0.61	30
	4	0.62	30		4	0.61	31
	5	0.63	30		5	1.47	30
	6	0.62	30		6	1.48	30
	7	0.62	30		7	0.36	31
	8	0.62	31		8	0.57	30
	9	0.62	30		9	0.71	31
	10	0.62	31		10	0.71	31
	11	0.63	31		11	0.62	31
	12	0.63	31		12	0.61	31
	13	0.99	30				
	14	1.29	23				
	15	0.64	24				

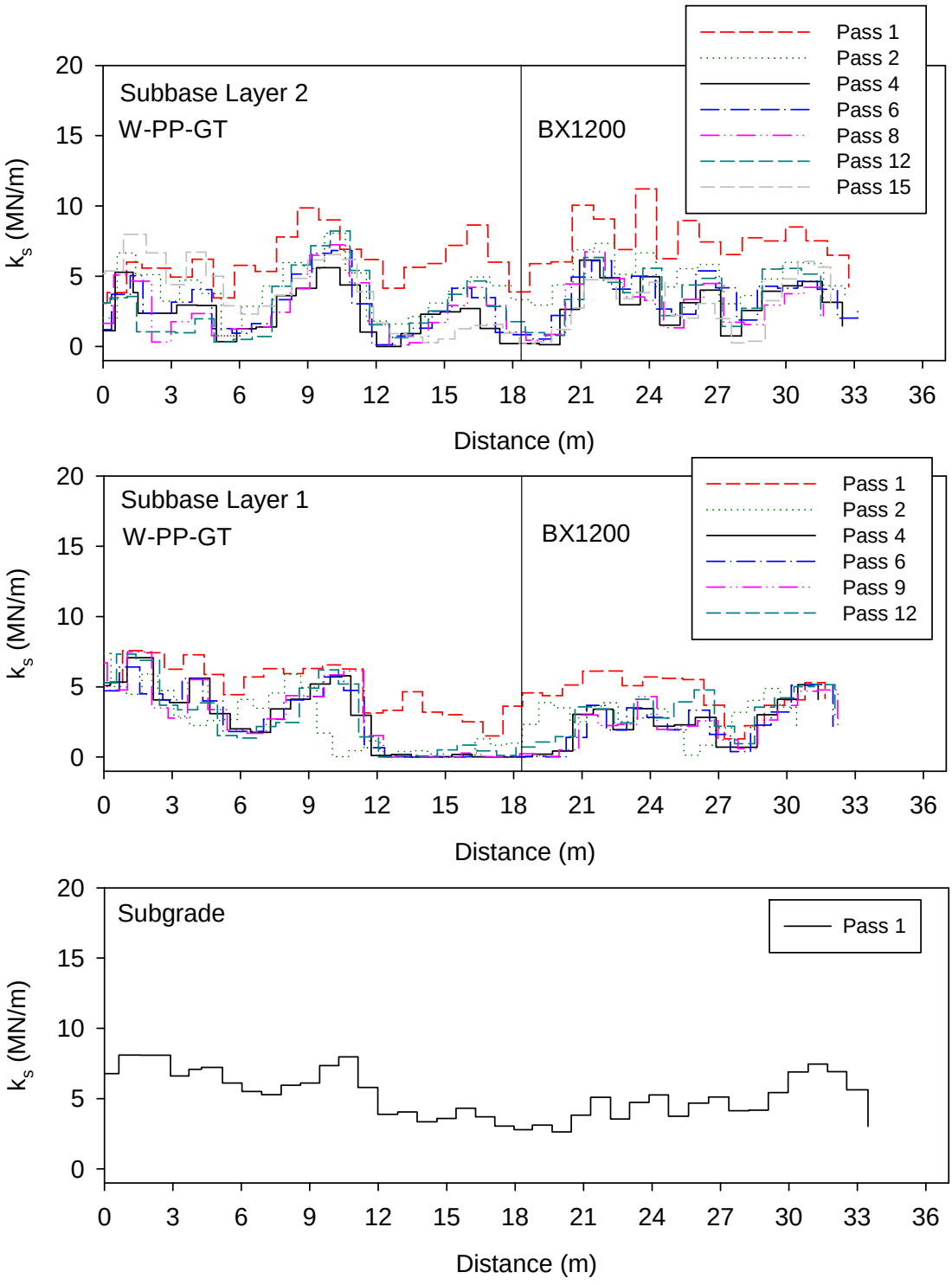

Figure 71. Case/Ammann k_s results for W-PP-GT and BX1200 sections

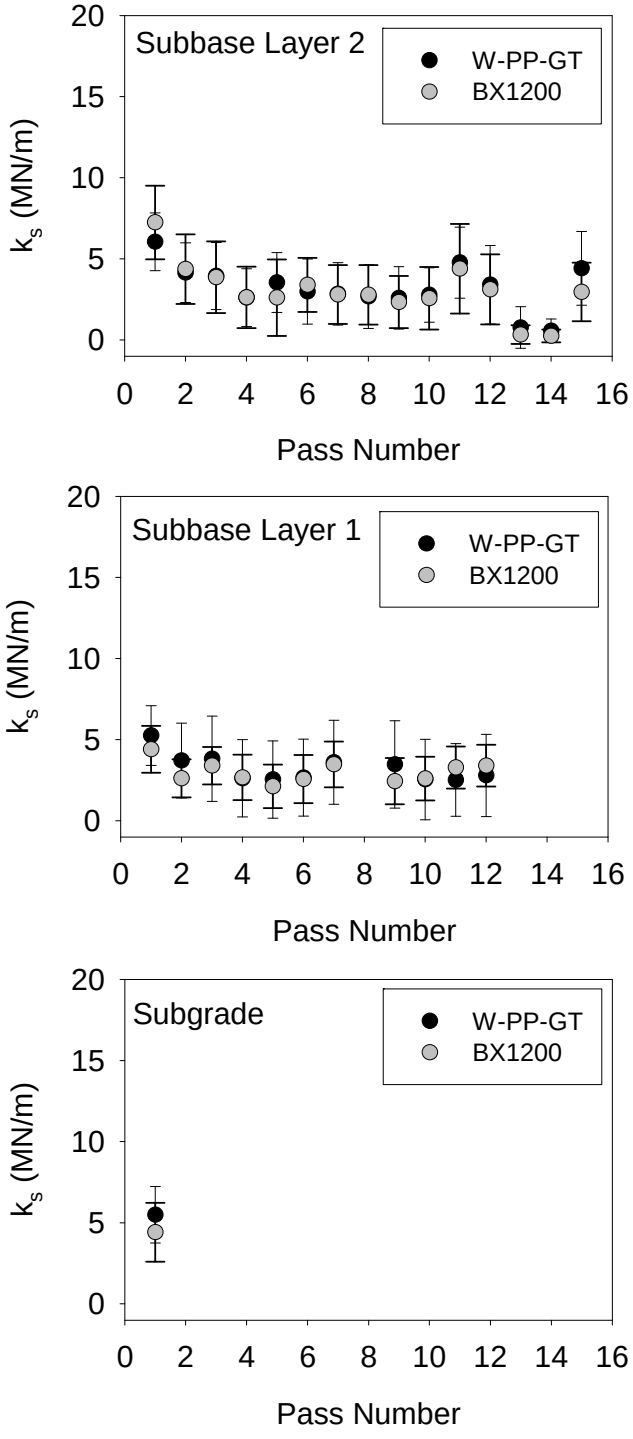

Figure 72. Case/Ammann average k_s (error bar indicates one standard deviation) compaction growth with increasing pass for W-PP-GT and BX1200 sections

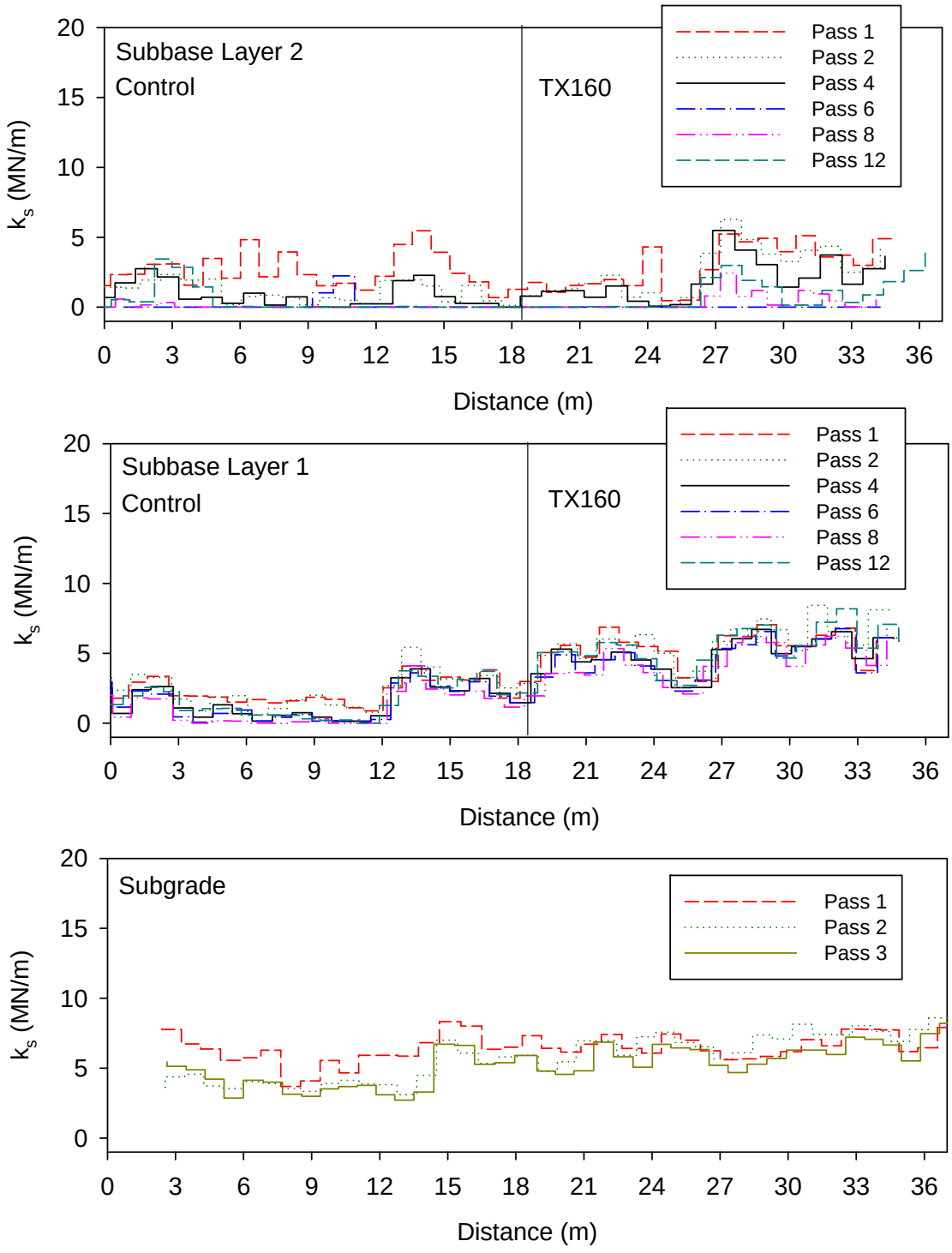

Figure 73. Case/Ammann k_s results for control and TX 160 sections

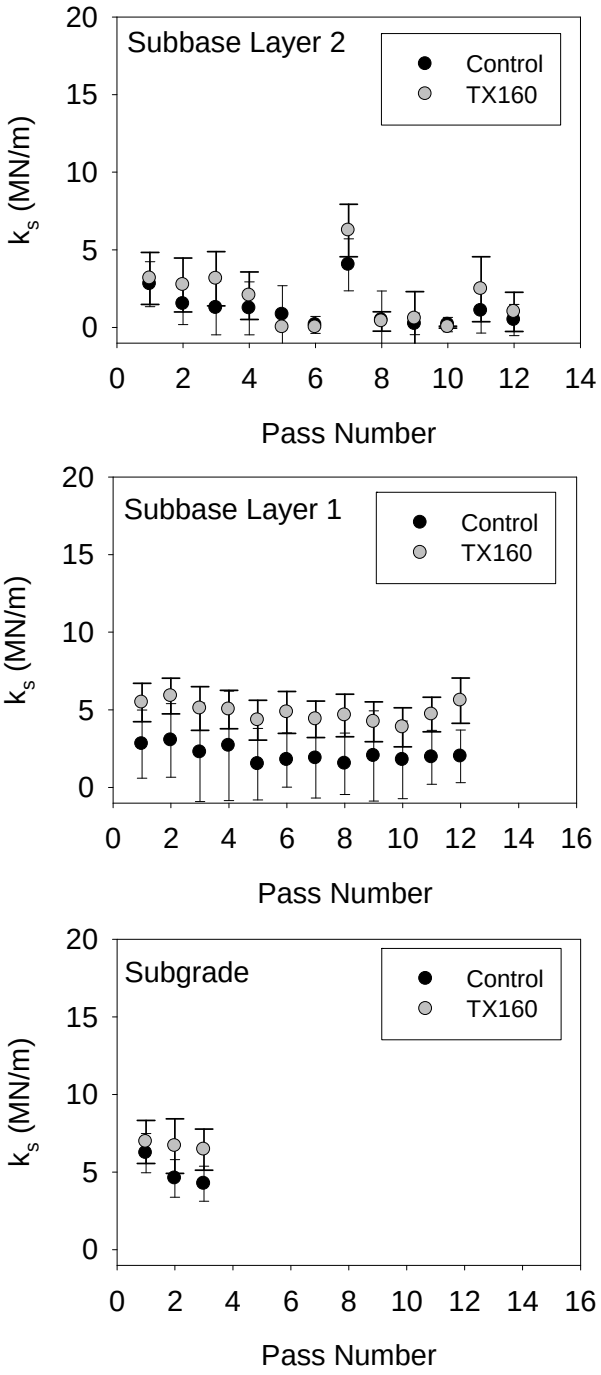

Figure 74. Case/Ammann average k_s (error bar indicates one standard deviation) compaction growth with increasing pass for control and TX160 sections

Table 12. Caterpillar roller pass summary

Section	Pass Number	Amp	Freq	Section	Pass Number	Amp	Freq
Subbase Layer 1							
W-PP-GT/ BX1200	1	0.85	31	Control/ TX160	1*	0.85	31
	2	0.85	31		2**	No Data	
Subbase Layer 2							
W-PP-GT/ BX1200	1	0.85	31	Control/ TX160	1	0.85	31
	2	1.70	31		2	0.85	31
	3	1.70	31		3	1.70	31
	4	0.85	31		4	1.70	31
	5	1.70	31		5	0.85	31
	6	0.85	31		6	0.85	31
					7	1.70	31
					8	1.70	31
					9	0.85	31

*Low GPS accuracy over half of the strip; **Low GPS accuracy

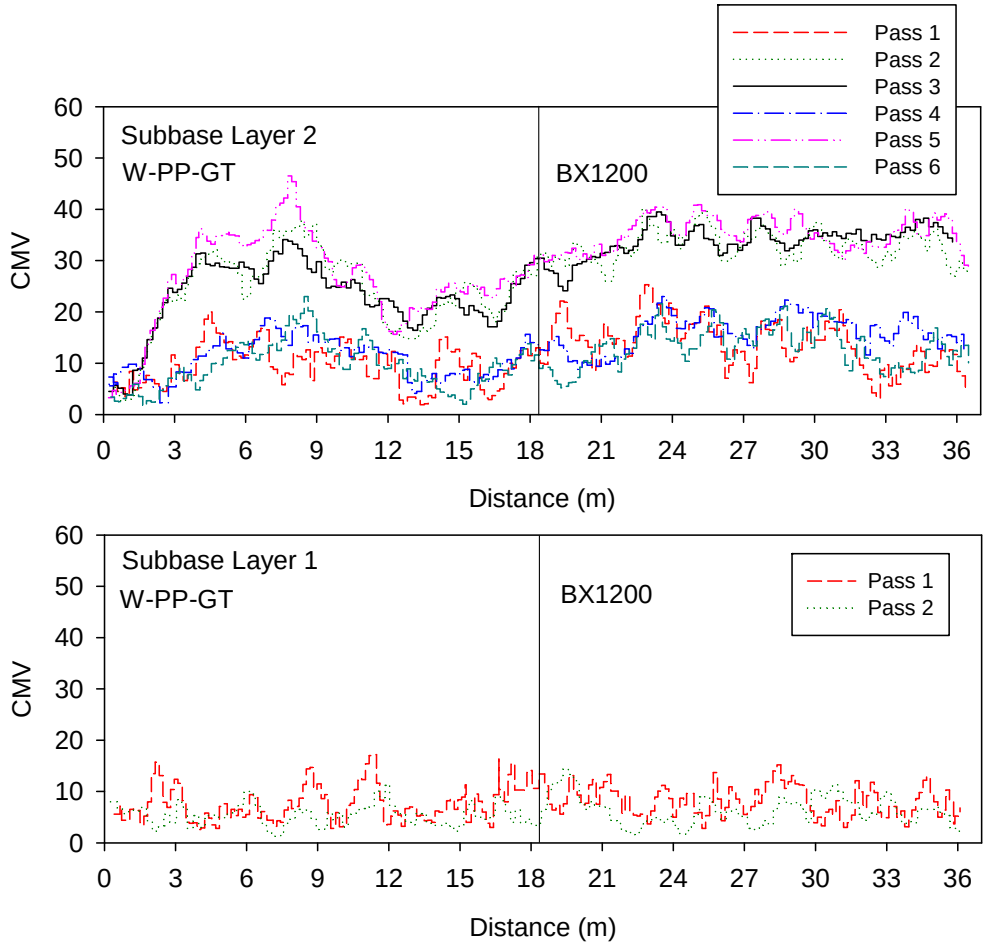

Figure 75. Caterpillar CMV results for W-PP-GT and BX1200 sections

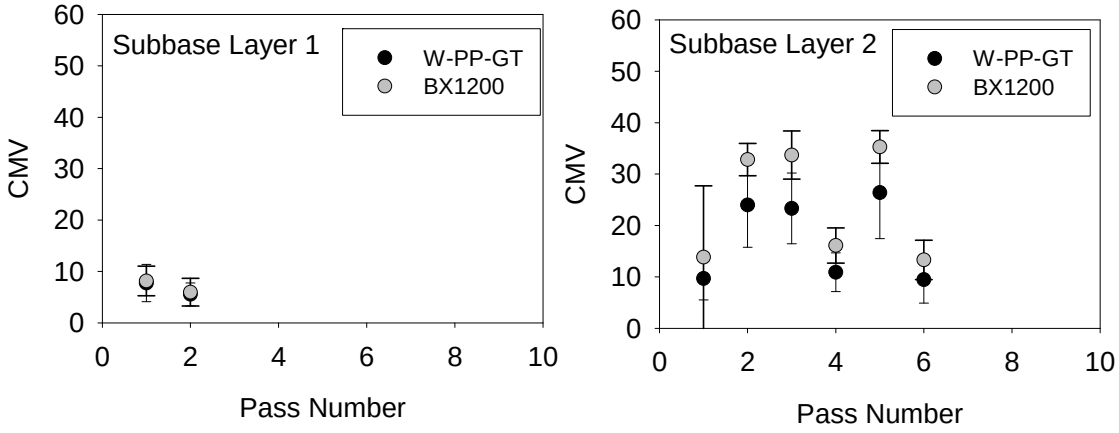

Figure 76. Caterpillar average CMV (average value shown as circle and error bar indicates one standard deviation) compaction growth with increasing pass for W-PP-GT and TX160

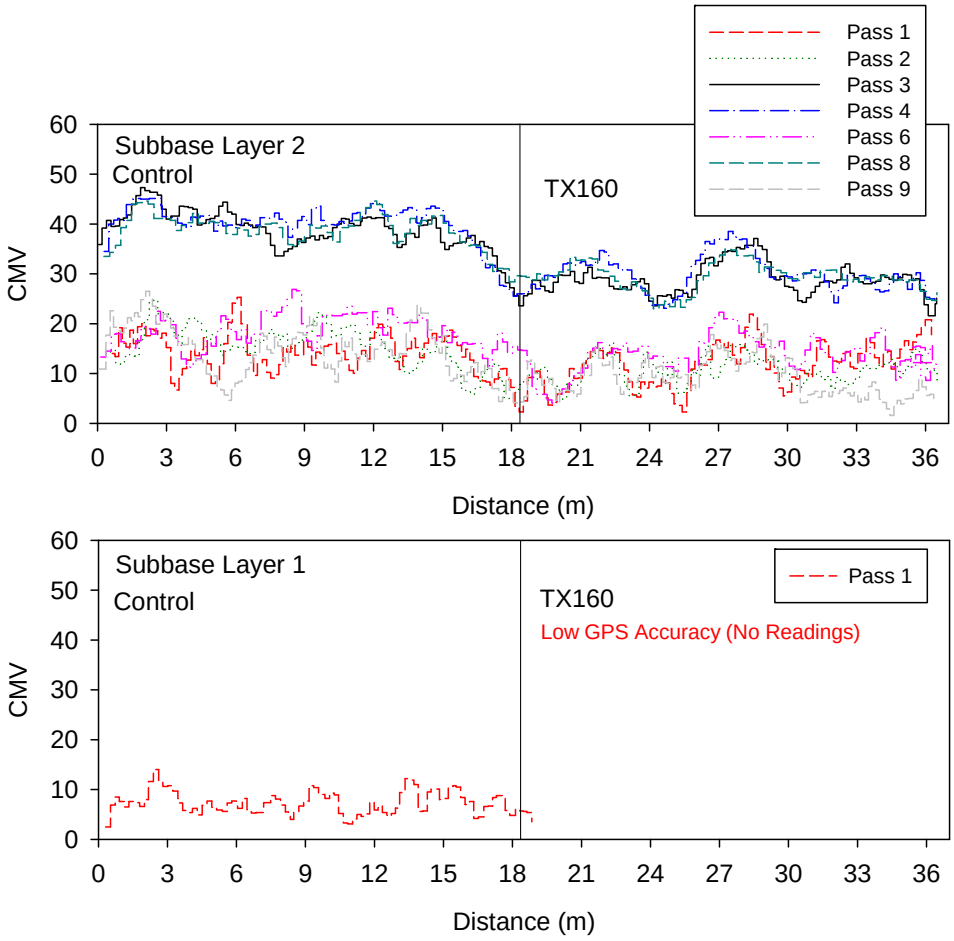

Figure 77. Caterpillar CMV results for W-PP-GT and TX160 sections

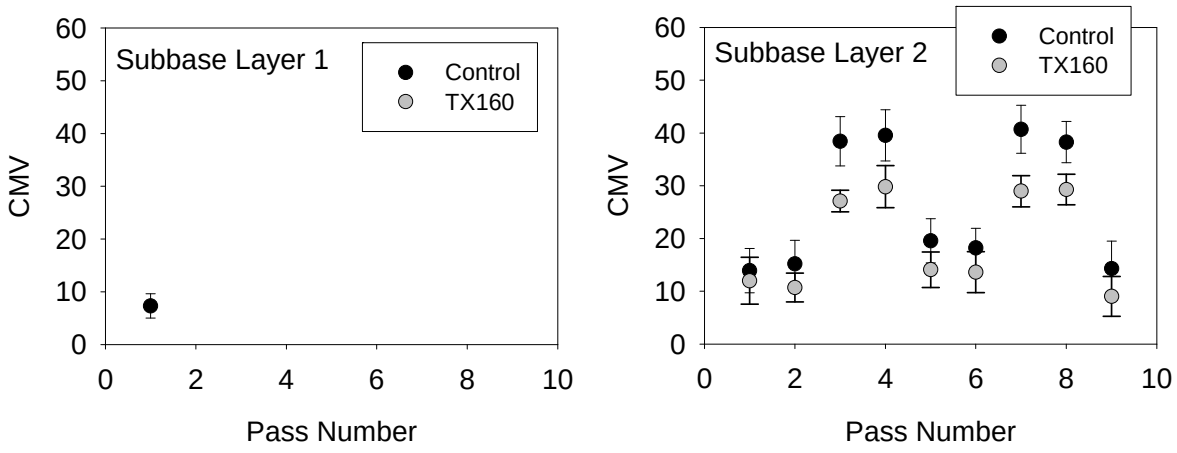

Figure 78. Caterpillar average CMV (average value shown as circle and error bar indicates one standard deviation) compaction growth with increasing pass for W-PP-GT and TX160 sections

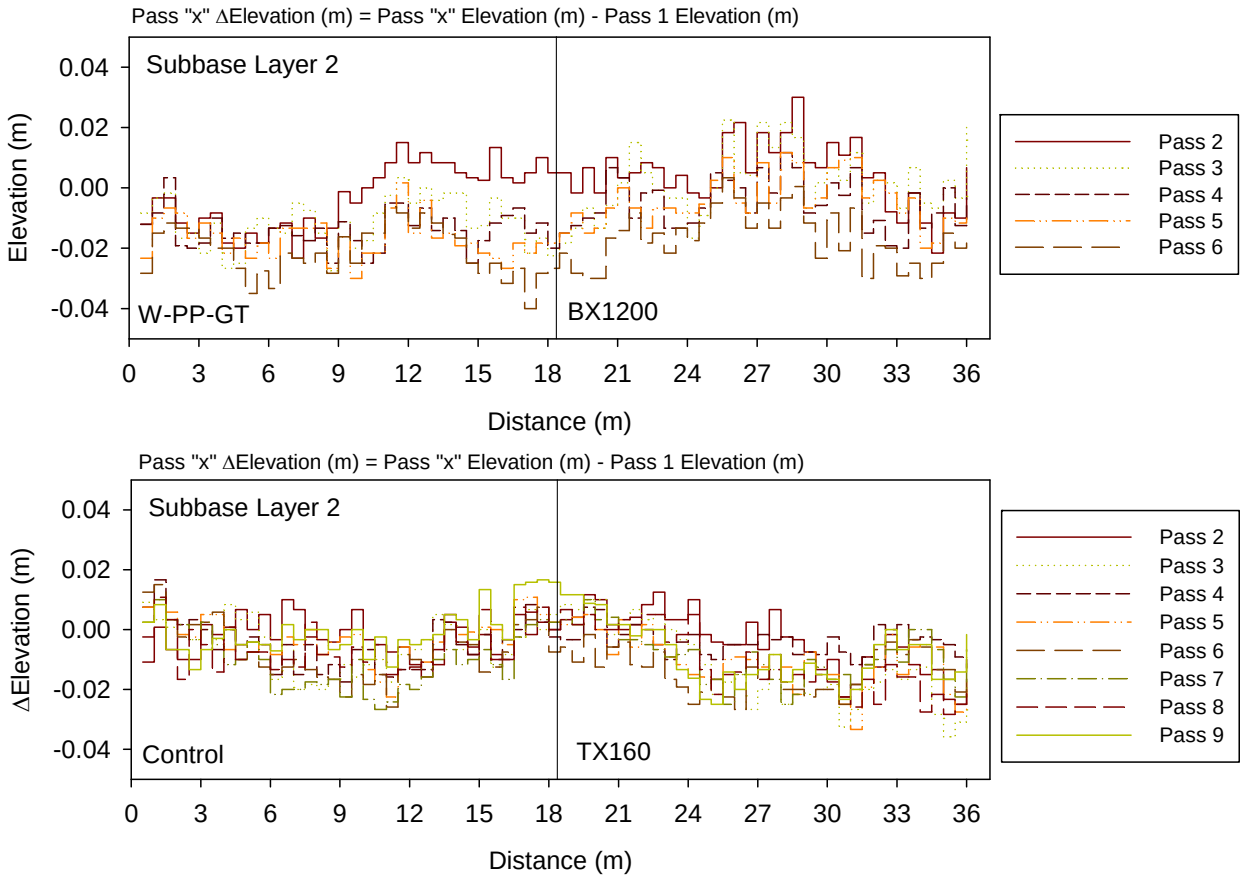

Figure 79. Change in elevation during compaction passes on subbase layer 2 relative to pass 1 (note: negative Δelevation means settlement and +ve Δelevation means heave)

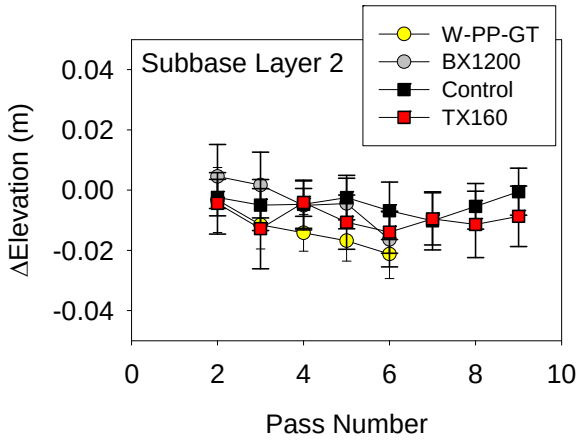

Figure 80. Average change in elevation during compaction on subbase layer 2 (with one standard deviation error bars) relative to pass 1 for different sections (note: negative Δelevation means settlement and +ve Δelevation means heave)

Rut Depth Measurements

Longitudinal rut depth profiles along W-PP-GT and BX1200 sections on subbase layer 1 after 4 truck passes are presented in Figure 81. Longitudinal rut depth profiles on all four sections on subbase layer 2 after 75 and 150 trafficking passes are presented in Figure 82 and Figure 83. Also presented in Figure 82 and Figure 83 are the thickness of the subbase layers and CBR of the subgrade layers to interpret the influence of the variability support conditions on the surface rut depths. Subgrade CBR values are presented as an average of the top 300 mm of the subgrade layer (denoted as CBR0-300) and CBR of the weakest zone that is at least 50 to 100 mm thick within in the top 300 mm of the subgrade (denoted as CBR*). Rut depth variability is primarily attributed to spatial variation in the subgrade moisture content and CBR values.

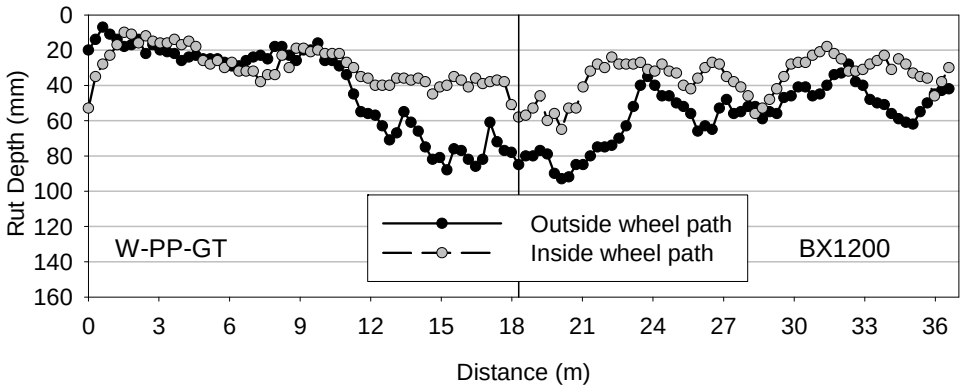

Figure 81. W-PP-GT and BX1200 section subbase 1 longitudinal rut depth after 4 trafficking passes

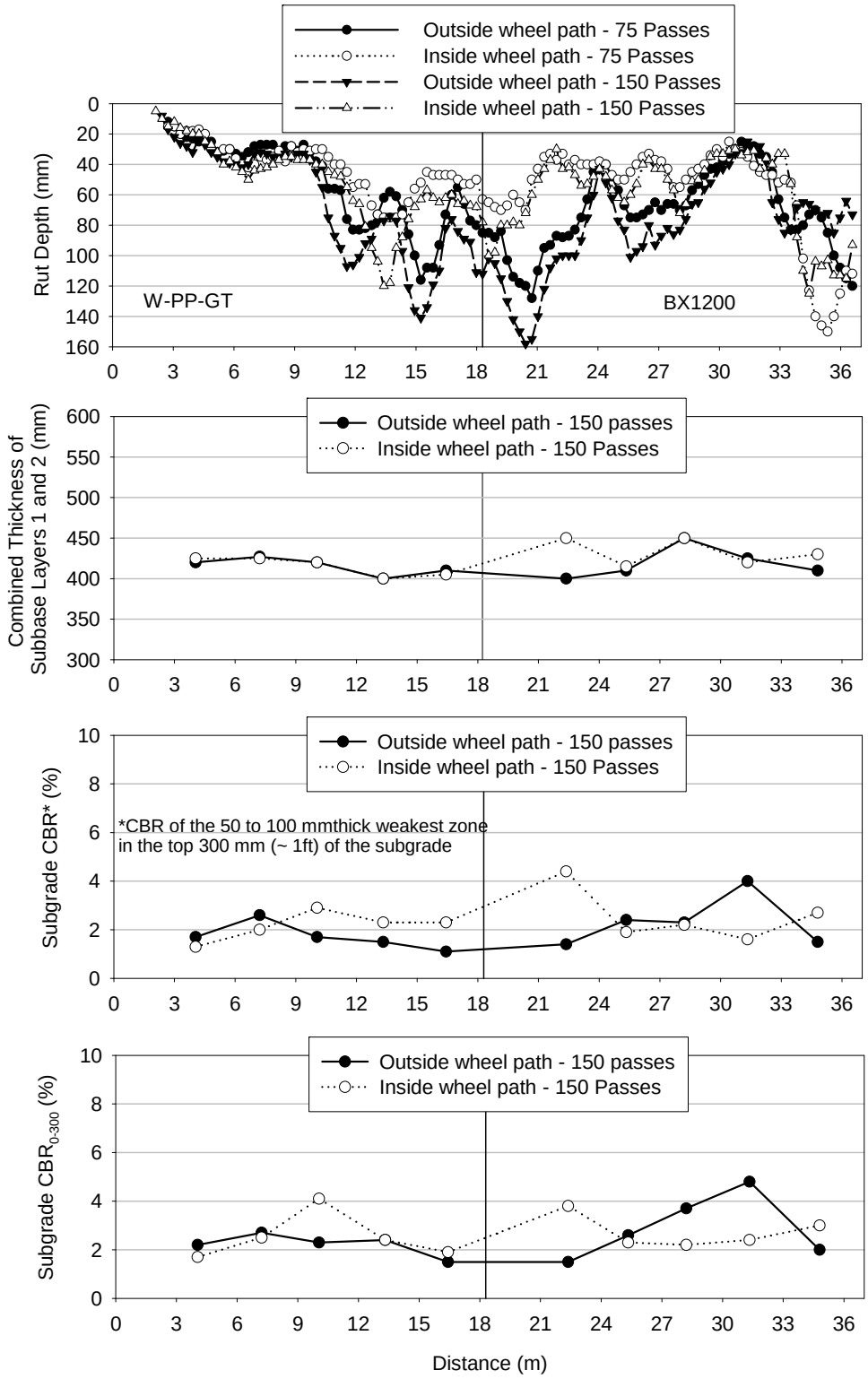

Figure 82. W-PP-GT and BX1200 sections subbase 2 longitudinal rut depth after 75 and 150 truck passes, subbase layer depths (interpreted from DCP profiles) after 150 trafficking passes, and CBR of the subgrade layer

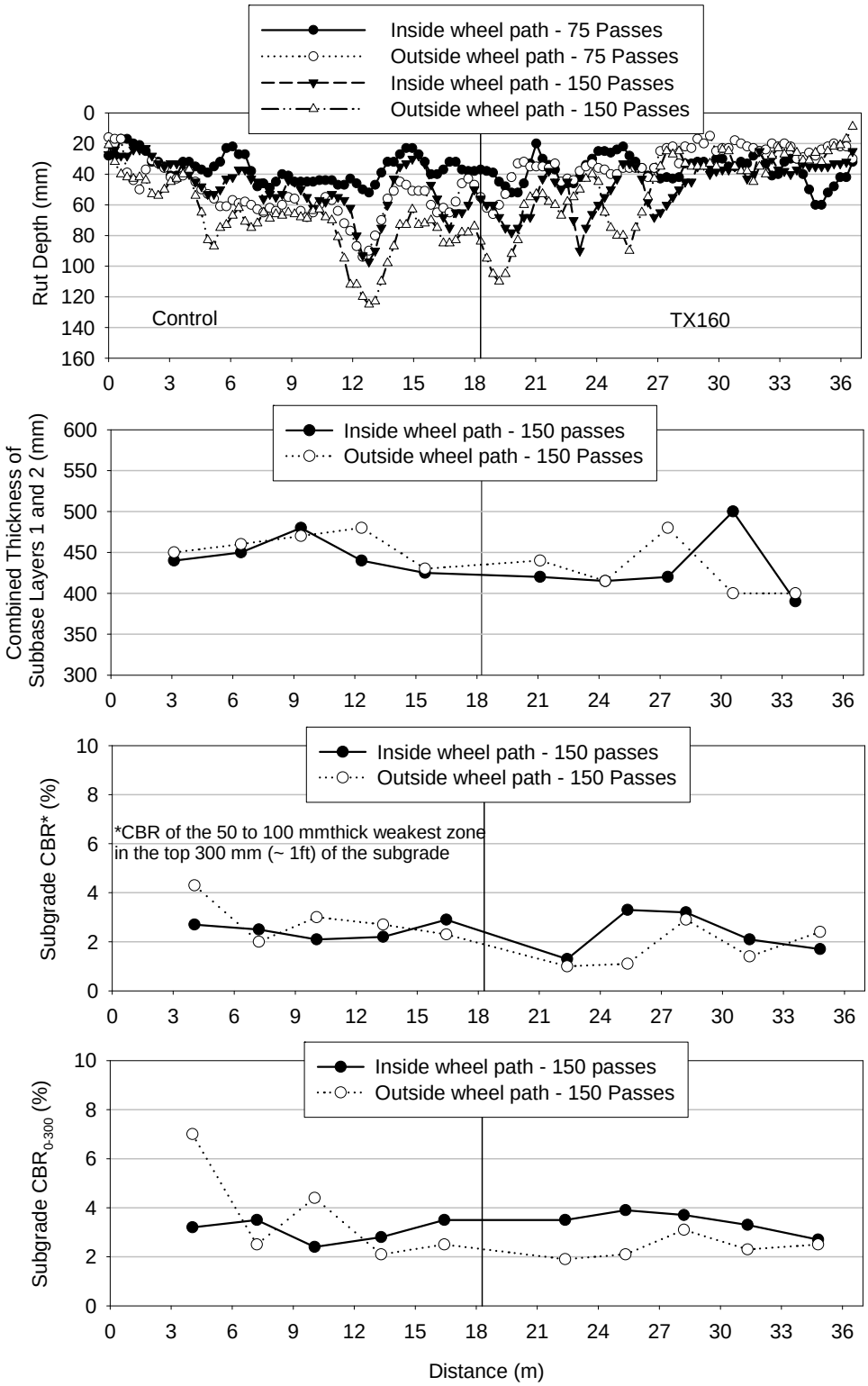

Figure 83. Control and TX160 sections subbase 2 longitudinal rut depth after 75 and 150 truck passes and subbase layer depths (interpreted from DCP profiles) after 150 trafficking passes, and CBR of the subgrade layer

Bar charts of average rut depth measurements obtained on subbase layer 2 after 75 and 150 trafficking passes are presented in Figure 84. The average rut depth was calculated based on measurements obtained from each test section on outside and inside wheel paths. The results are presented herein as an average given the variability of the measurements within individual test sections and between the outside and inside wheel paths. The number of test measurement locations for each test section varied from 66 to 71. Average D_r of the subbase material (based on five measurements per test section) after the final compaction pass on each test section is also presented on Figure 84. The average rut depth was comparatively higher in the control section and lower in the TX160 test section. Compaction measurements show that the average D_r was 98% for the TX160 section and 90% for the control and BX1200 sections at the completion of testing. The relative density was lowest for the W-PP-GT section at 84%, while the BX1200 section was similar to the control section at 90%.

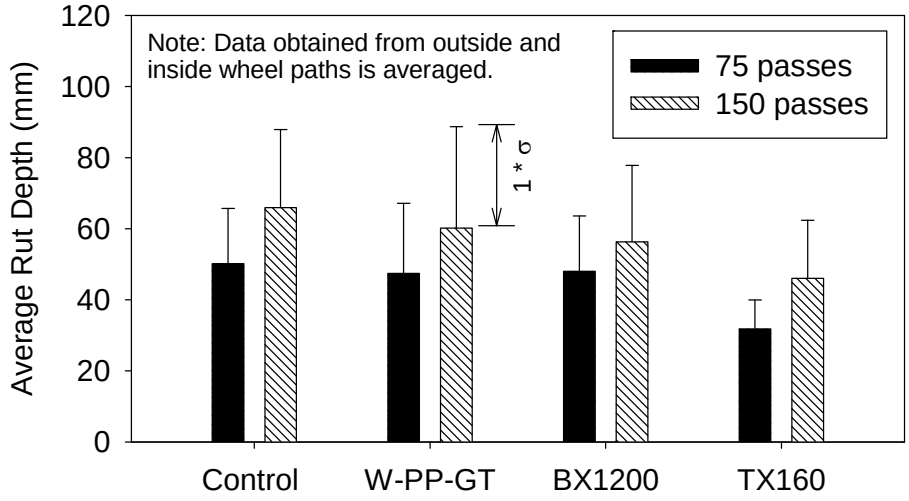

Figure 84. Bar chart comparing average longitudinal rut depth after 75 and 150 truck passes on subbase layer 2

Earth Pressure Cell Measurements

An example of dynamic vertical and horizontal total stress measurements obtained from the TX160 test section under a trafficking pass on subbase layer 2 is presented in Figure 93 through Figure 97. The stresses as presented represent the change in ground stresses minus the initial geostatic (overburden) stresses. In Figure 97 two peaks are observed under the trafficking pass due to the influence of front and rear tires. As expected, higher stresses are recorded under the dual rear-tire loaded axle. Stress measurements in Figure 86 indicate that the stresses before and after the trafficking pass were in the range of 15 to 20 kPa. These stresses are a result of "locked-in" stresses and principal stress rotation from prior compaction and trafficking passes. These "locked-in" stress values and the peak stress (under the rear tire) values were recorded for each roller and trafficking pass for each test section, and are presented in Figure 85 to Figure 90.

The results presented herein demonstrate performance differences between the four test sections from rut depth and compaction measurements, and that the inclusion of geosynthetic material at the interface of soft subgrade and subbase layers affects the development of the

"locked-in" horizontal stress following loading. Development of "locked-in" horizontal stresses in the subgrade and subbase layers gives a direct indication of the lateral restraint reinforcement mechanism.

Lateral stress ratio (K) (calculated as the ratio of total horizontal and total vertical stresses) plots for subgrade and subbase layers following roller and trafficking passes and for peak values under the roller and trafficking passes are presented in Figure 91 and Figure 92, respectively. The calculated K values from Figure 92 show that during trafficking (i.e., under peak loading), the K values are about 0.3 to 0.7 for the subgrade and 0.5 to 0.7 for the subbase for all test sections. However, the K values based on the "locked-in" stresses following trafficking passes from Figure 91 vary significantly between the different test sections. Table 12 summarizes the K values after 75 trafficking passes on subbase layer 2 (i.e., after 112 cumulative roller + truck passes). Results show buildup of horizontal stresses with relatively high K values in the control section subgrade layer compared to the geogrid (i.e., BX1200 and TX160) reinforced sections. The K values in the subbase were comparatively higher in the TX160 section compared to the control and BX1200 sections. The W-PP-GT section produced the highest K values in the subgrade and subbase layers.

Further examination of horizontal stress measurements and rut depth measurements show that the ratio of the "locked-in" horizontal stress in the subgrade to the "locked-in" horizontal stress in the subbase (lateral reinforcement ratio) provides an indication of the performance of the section. As shown in Table 12, rut depth measurements generally decreased as the reinforcement ratio increases. This approach although limited to these site conditions and materials, suggests that the reinforcement ratio value could be a useful indicator to performance and warrants further study. For the site and material conditions in this study, the results also suggest that the TX160 with its unique equilateral triangular shaped apertures provides comparatively higher reinforcement ratio than the other geosynthetics used in this study.

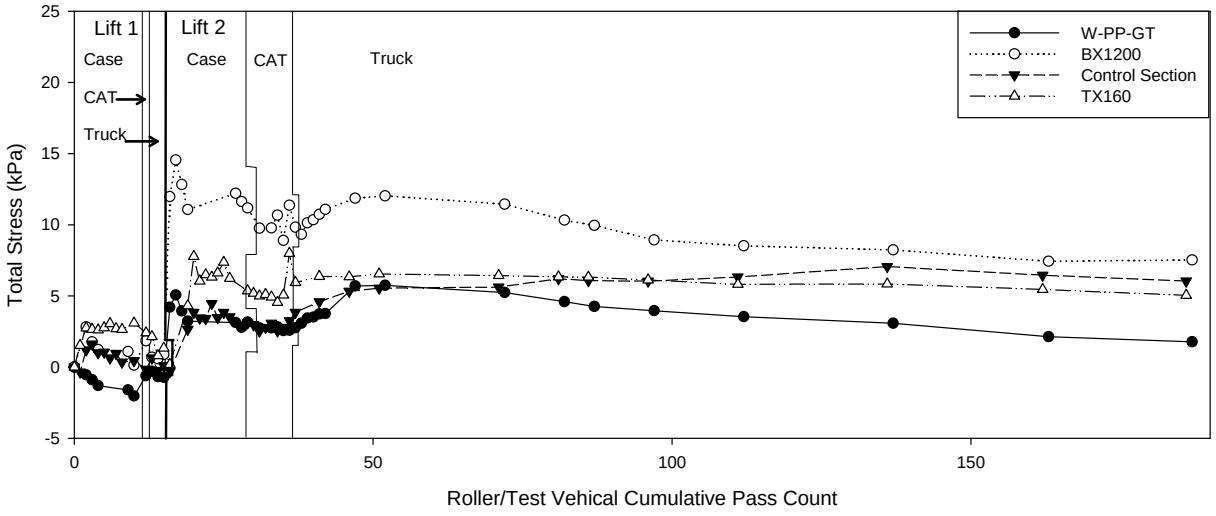

Figure 85. Total vertical stress at interface between geosynthetic and subgrade after roller compaction and test vehicle passes

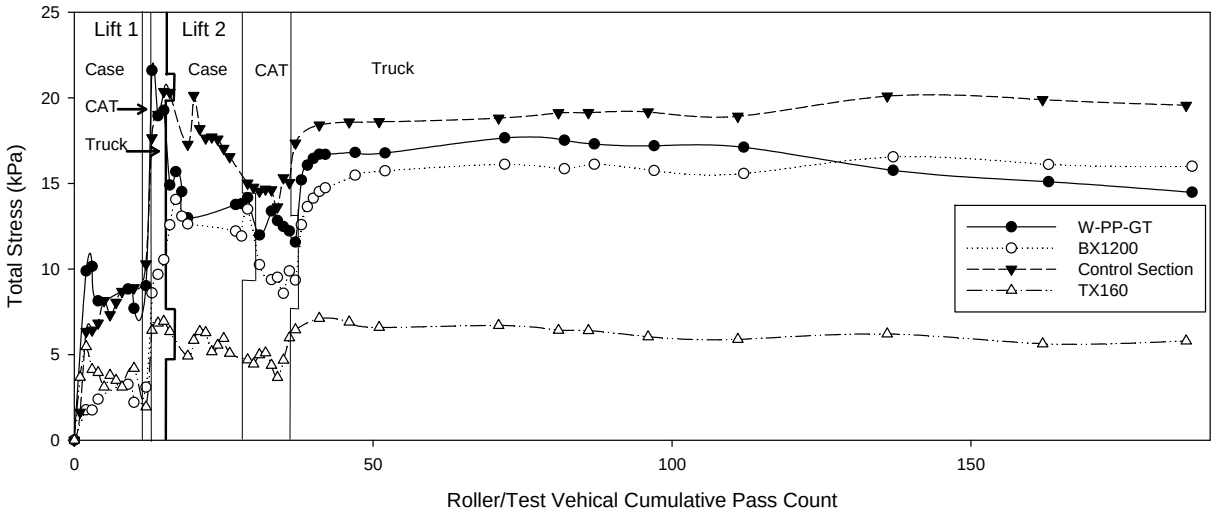

Figure 86. Total horizontal stress below geosynthetic in subgrade layer after roller compaction and test vehicle passes

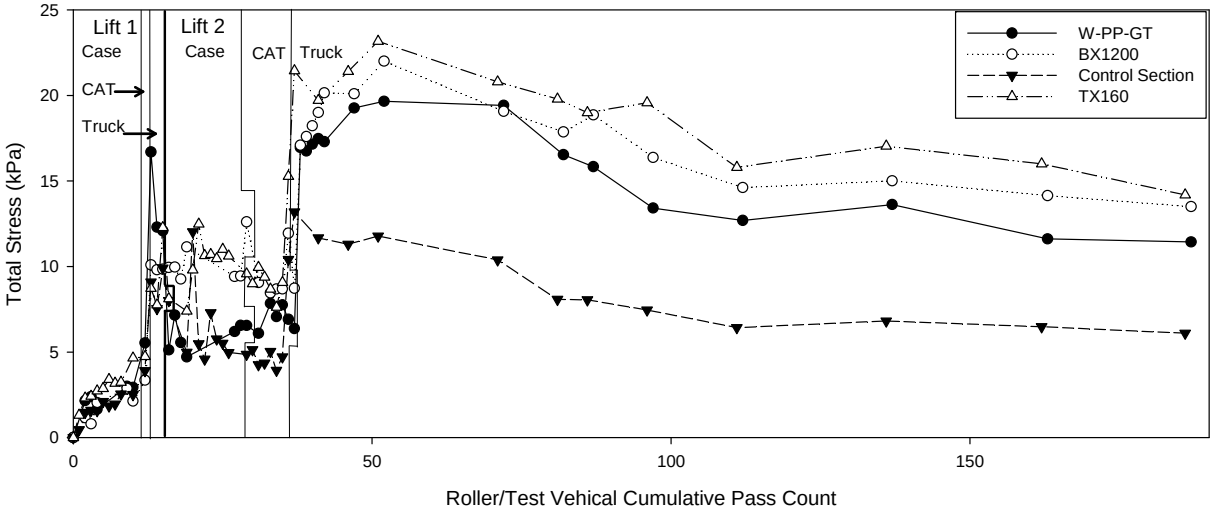

Figure 87. Total horizontal stress above geosynthetic in subbase layer after roller compaction and test vehicle passes

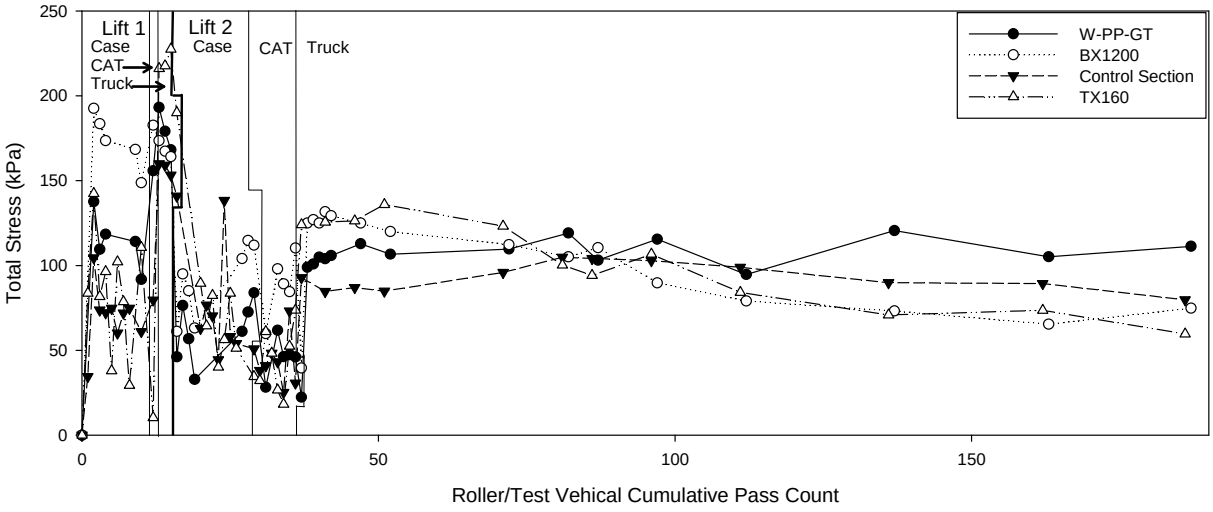

Figure 88. Maximum total vertical stress at interface between geosynthetic and subgrade during roller compaction and test vehicle passes

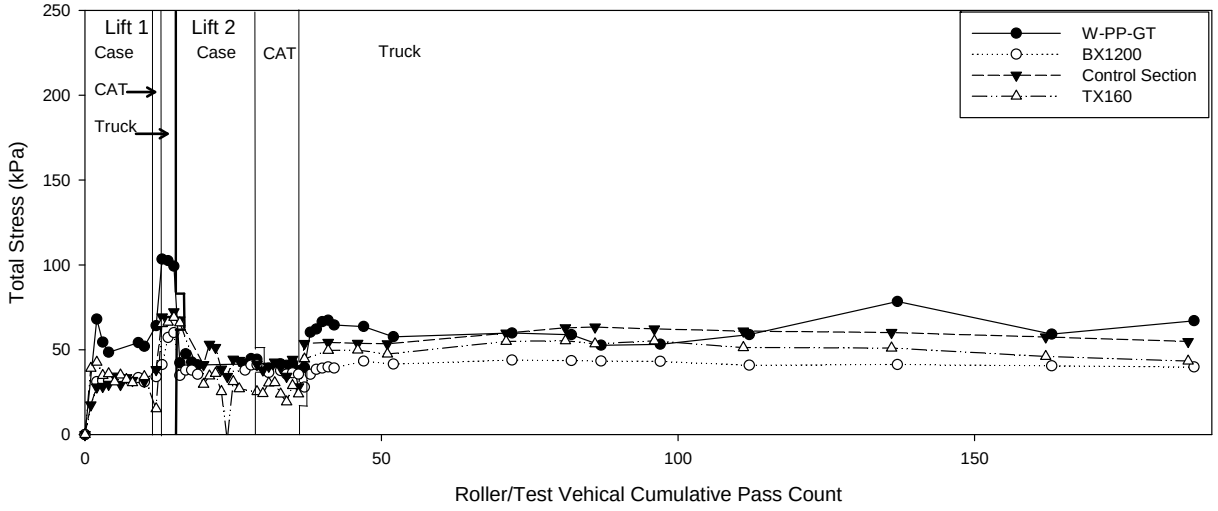

Figure 89. Maximum total horizontal stress below geosynthetic in <u>subgrade</u> layer during roller compaction and test vehicle passes

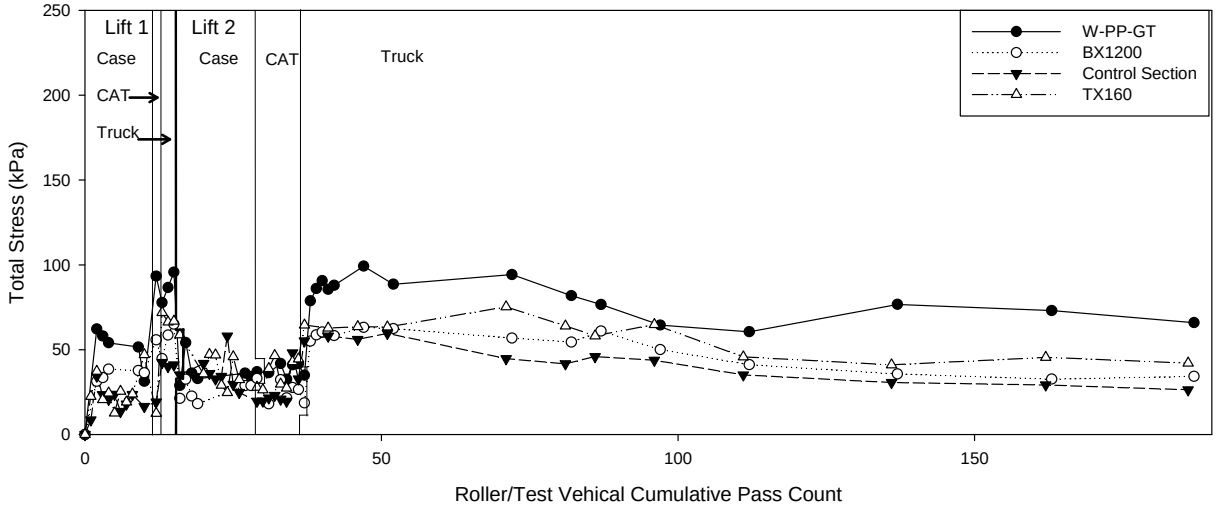

Figure 90. Maximum total horizontal stress above geosynthetic in <u>subbase</u> layer during roller compaction and test vehicle passes

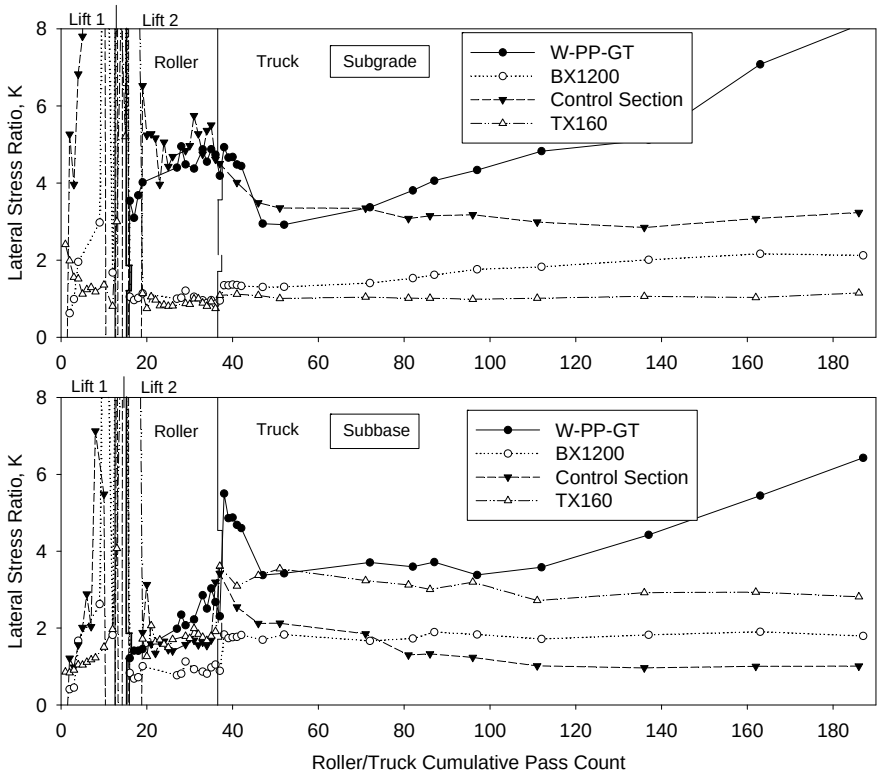

Figure 91. Lateral stress ratio (ratio of horizontal and vertical stresses) in subgrade and subbase layers after roller and test truck trafficking passes

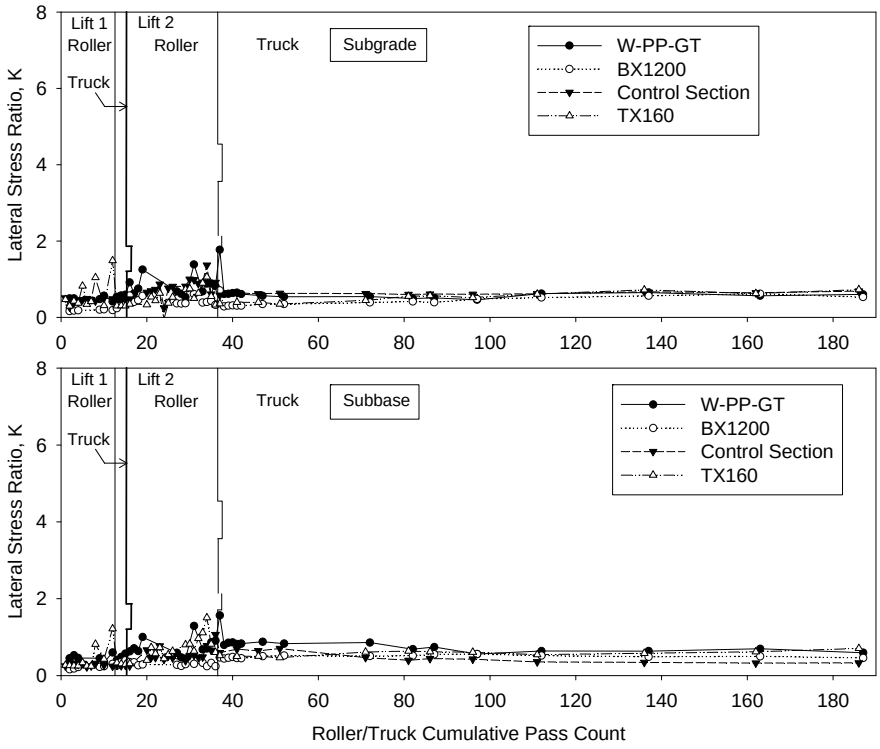

Figure 92. Lateral stress ratio (ratio of horizontal and vertical stresses) under roller drum and test truck wheel loading in subgrade and subbase layers

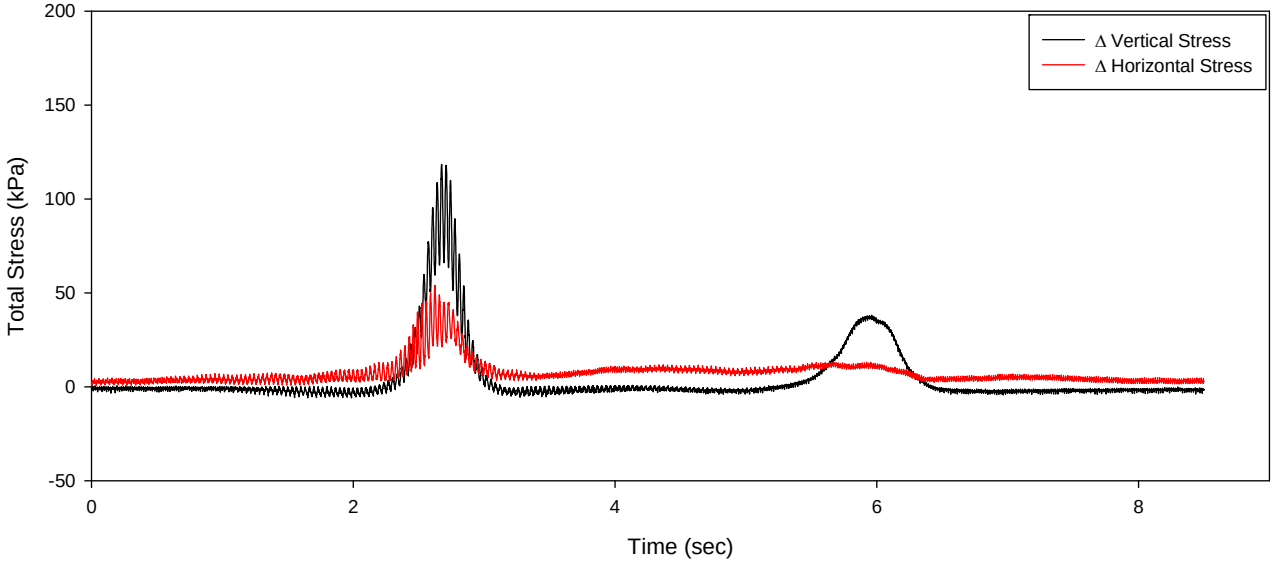

Figure 93. Total stress at interface between geosynthetic and subgrade and horizontal stress in subbase during Case roller pass number 4 (W-PP-GT treatment)

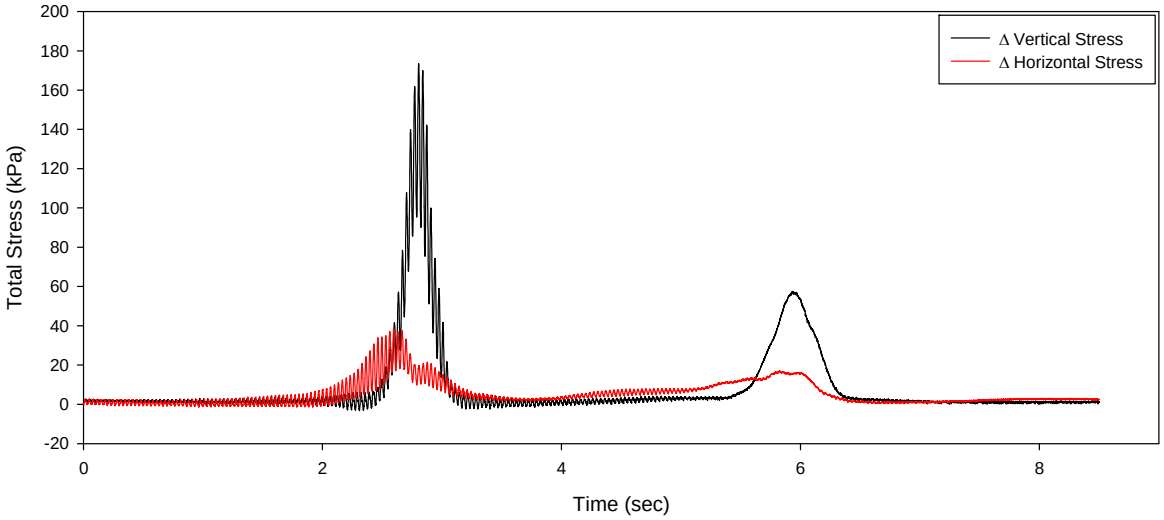

Figure 94. Total stress at interface between geosynthetic and subgrade and horizontal stress in subbase during Case roller pass number 4 (BX1200 treatment)

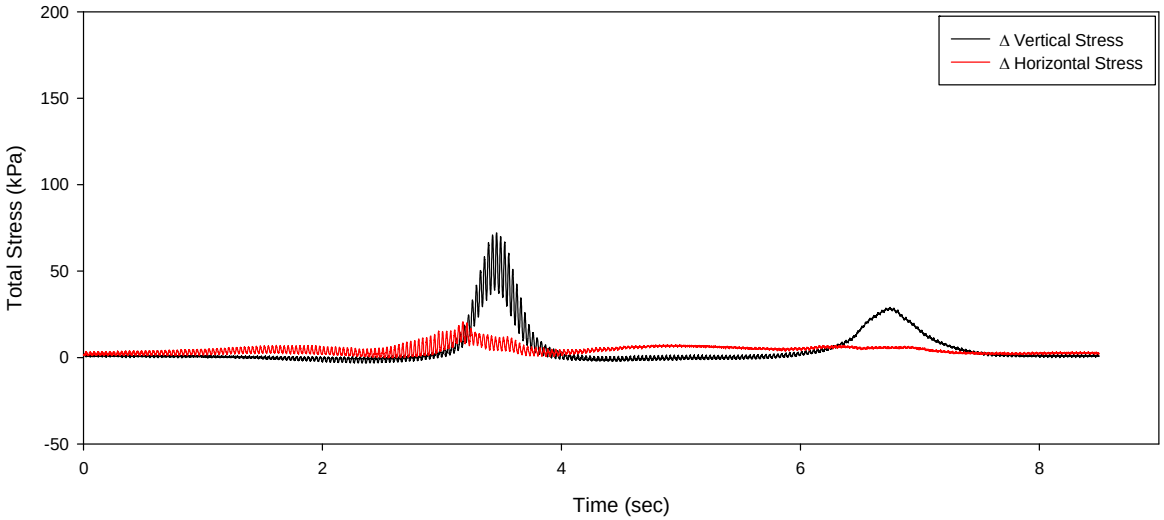

Figure 95. Total stress at interface between geosynthetic and subgrade and horizontal stress in subbase during Case roller pass number 4 (Control treatment)

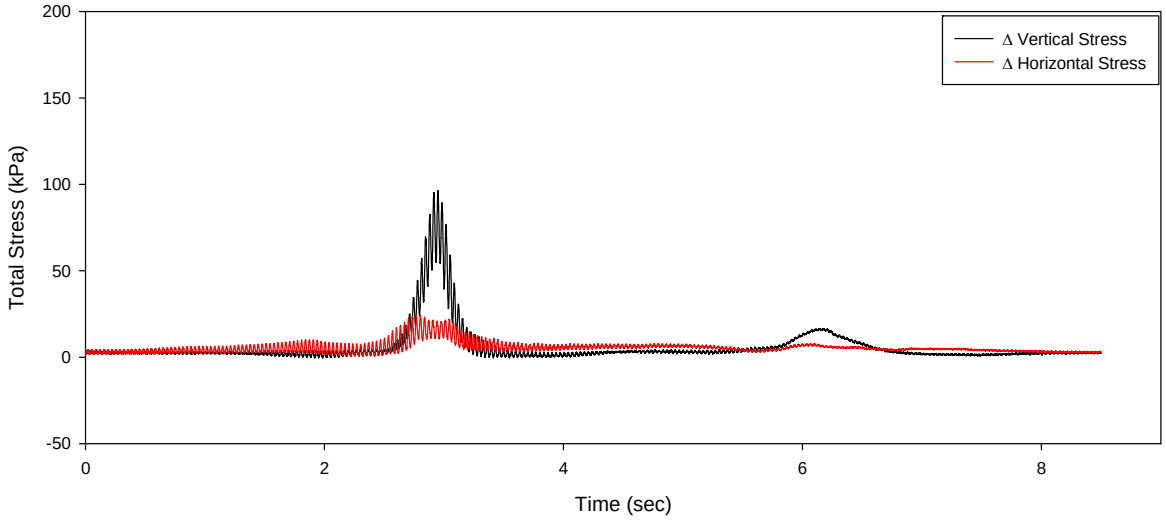

Figure 96. Total stress at interface between geosynthetic and subgrade and horizontal stress in subbase during Case roller pass number 4 (TX160 treatment)

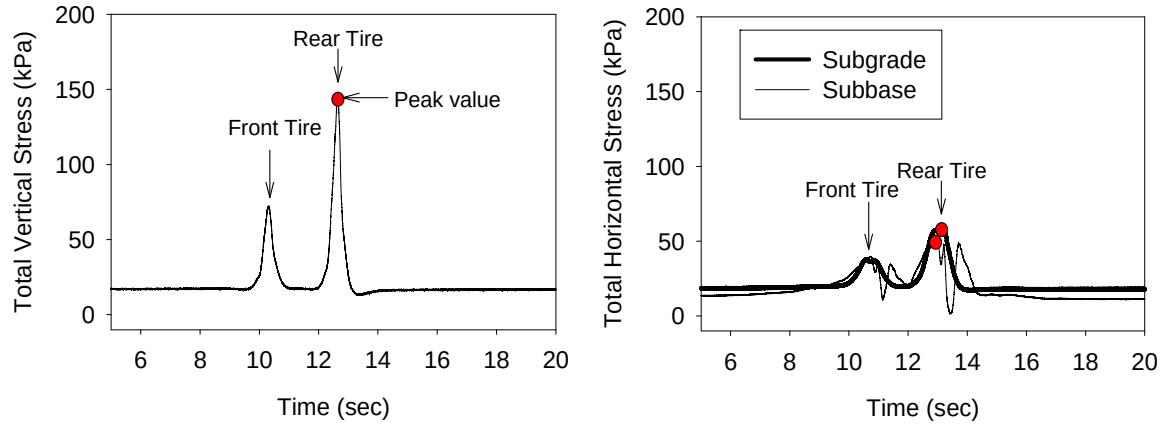

Figure 97. Example dynamic EPC measurements on TX160 section (under a trafficking pass on subbase layer 2)

Table 13. Performance comparison between test sections

Section	$K_{Subgrade}$	$K_{Subbase}$	Reinforcement Ratio*	Average Rut Depth after 75 trafficking passes on subbase layer 2 (mm)
Control	3.2	1.2	0.4	50
W-PP-GT	4.3	3.7	0.8	47
BX1200	1.8	1.8	1.0	48
TX160	1	3.2	3.3	32

*calculated as the ratio of horizontal "locked-in" stresses in subbase and subgrade

SUMMARY AND CONCLUSIONS

Results from a controlled field study comparing performance of three geosynthetic materials (TX160 geogrid, BX1200 geogrid, and W-PP-GT woven geotextile) and a control section with no reinforcement are described in this report. The geosynthetic materials were placed on top of the soft clay subgrade layer prior to compacting two overlying layers of crushed limestone. Rut depth measurements under trafficking from a heavy vehicle, compaction measurements on the subbase layer, and in-ground stress measurements under compaction and trafficking passes provide information on the reinforcing effects provided by the different geosynthetics. Results between the different test sections were compared to document differences in performance. Key findings from this study are as follows:

- Average CBR values for the subgrade, subbase layer 1, and subbase layer 2, were 2, 10, and 45, respectively. Comparison of CBR values between the different test sections was variable. Laboratory test showed that the CBR values were sensitive to moisture content.
- Average elastic modulus values from LWD measurements showed that the modulus values initially decreased for the first few roller passes and then increase thereafter. Modulus values increased by a factor of about two between the first subbase layer and the second subbase layer. This increase was more that for CBR or dry unit weight.
- Roller-integrated compaction measurement values showed that results were repeatable between passes, but primarily reflected the conditions of the underlying weak subgrade due to the high compaction stresses and the one-dimensional nature of the test strips. Future application for this technology should focus on large test areas.
- Rut depth and compaction measurements were variably within test sections, but showed less overall rutting in the TX160 geogrid section compared to other test sections.
- In-ground stress cell measurements showed that the “locked-in” horizontal stress in the subgrade after trafficking was lower in the TX160 section compared to other test sections.
- Higher “locked-in” horizontal stresses were measured in subbase layer of the TX160 section compared to the other test sections.
- The reinforcement ratio calculated as the ratio of horizontal “locked-in” stresses in the subbase and subgrade layers provides an indication of rut performance and warrants further research.

REFERENCES

Al-Qadi, I. L., Morian, D. A.; Stoffels, S. M., Elseifi, M., Chehab, G., and Stark, T. (2008). *Synthesis on Use of Geosynthetics in Pavements and Development of a Roadmap to Geosynthetically-Modified Pavements* – DRAFT REPORT. Federal Highway Administration.

Anderegg, R. (1998). *Nichtlineare Schwingungen bei dynamischen Bodenverdichtern.* Ph.D. Dissertation, Eidgenossische Technische Hochschule Zurich (in German).

Anderegg, R., and Kaufmann, K. (2004). "Intelligent compaction with vibratory rollers." *Transp. Res. Rec.*, 1868, Journal of the Transportation Research Board, Washington D.C., 124–134.

Berg, R. R., Christopher, B. R., and Perkins, S. (2000). *Geosynthetic reinforcement of the aggregate base/subbase courses of pavement structures*. Geosynthetics Materials Association.

Fannin, R. J., and Sigurdsson, O. (1996). "Field observations on stabilization of unpaved roads with geosynthetics." Journal of Geotechnical Engineering, 544-553.

Giroud, J. P, and Han, J. (2004a). "Design method for geogrid-reinforced unpaved roads. I. Development of design method." Journal of Geotechnical and Geoenvironmental Engineering, 130(8), 775-786.

Giroud, J. P, and Han, J. (2004b). "Design method for geogrid-reinforced unpaved roads. II. Calibration and applications." Journal of Geotechnical and Geoenvironmental Engineering, 130(8), 787-797.

Giroud, J. P., and Noiray, L. (1981). "Geotextile-reinforced unpaved road design." Journal of the Geotechnical Engineering Division, Proceedings of the American Society of Civil Engineers, 107(GT9), 1233-1254.

Holtz, R. D., Christopher, B. R., and Berg, R. R. (2008). *Geosynthetic Design and Construction Guidelines*. National Highway Institute, FHWA, FHWA-NHI-07-092. Washington, D.C. August 2008.

Kwon, J. and Tutumluer, E. (2009). "Geogrid base reinforcement with aggregate interlock and modeling of the associated stiffness enhancement in mechanistic pavement analysis." 88th Meeting of the Transportation Research Record, Manuscript 09-2079, Washington, D.C. January 2009.

Milligan, G. W. E., Jewell, R A., Houlsby, G. T., and Burd, H. J. (1989). "A new approach to the design of unpaved roads-part I." Ground Engineering, April 1989, Volume 22, No. 3, 25-29.

Milligan, G. W. E., Jewell, R A., Houlsby, G. T., and Burd, H. J. (1989). "A new approach to the design of unpaved roads-part II." Ground Engineering, November 1989, Volume 22, No. 8, 37-42.

Powell, W., Keller, G.R., and Brunette, B. (1999). "Application for geosynthetics on forest service low-volume roads." Transportation Research Record, 1652, 113-120.

Sandström Å., and Pettersson, C. B., (2004). "Intelligent systems for QA/QC in soil compaction", *Proc. TRB 2004 Annual Meeting* (CD-ROM), Transportation Research Board, Washington, D. C.

Tensar Earth technologies, Inc. (1996). "Design guideline for flexible pavements with Tensar geogrid base layers." Tensar Technical Note, TTN:BR96.

Thurner, H. and A. Sandstrom. 1980. A new device for instant compaction control. In *Proceedings of the International Conference on Compaction*. Volume 2. Paris, 611–614.

U.S. Army Corps of Engineers. (2003). "Use of geogrids in pavement construction." Technical Letter No. 1110-1-189.

White, D. W., Mekkawy, M., Jahren, C., Smith, D., and Suleiman, M. (2007). *Effective Shoulder Design and Maintenance*. Iowa Highway Research Board, Ames, Iowa, June 2007.

Yoo, T., Selig. E. (1980). "New concepts of vibratory compaction of soil," *Proc. of Intl. Conf. on Compaction*, Vol. II, Paris, pp. 703–707.

Zorn, G. (2003). *Operating manual: Light drop-weight tester ZFG2000*, Zorn Stendal, Germany.

APPENDIX A. IN-SITU DATA

Table 14. Summary of point test data – subgrade

Section	Roller Passes	Nuclear Density		E_{Z200} (MPa)	E_{V1} (MPa)	E_{V2} (MPa)	CBR (%)
		γ_{dry} (kN/m^3)	Moisture (%)				
Initial Test	---	17.2	20.4	3.49	---	---	
Initial Test	---	17.6	18.6	3.91	---	---	
W-PP-GT	2	17.7	18.5	5.41	---	---	
	2	17.6	18.7	5.78	---	---	
	2	16.6	20.2	4.99	---	---	
	2	17.5	19.2	3.90	---	---	
	2	17.0	20.5	4.09	---	---	
BX1200	2	17.3	19.1	4.97	---	---	
	2	16.9	19.6	4.53	---	---	
	2	17.0	19.7	4.34	---	---	
	2	17.2	19.4	4.38	---	---	
	2	16.5	20.7	4.95	---	---	
Sections W-PP-GT and BX1200 moisture conditioned, processed and recompacted with two passes							
W-PP-GT	2	17.0	20.3	5.02	---	---	3.0
	2	18.3	15.8	5.74	---	---	4.9
	2	17.2	20.2	4.73	---	---	2.7
	2	17.4	20.8	3.50	---	---	5.6
	2	16.6	22.4	2.67	---	---	2.1
BX1200	2	17.1	19.8	4.33	---	---	1.8
	2	16.7	19.8	3.95	---	---	2.0
	2	16.9	20.8	4.28	---	---	3.6
	2	16.7	19.9	4.54	---	---	4.7
	2	17.1	19.4	4.29	---	---	5.0

Table 15. Summary of point test data – subbase 1

Section	Roller Passes	Nuclear Density		E_{Z200} (MPa)	E_{V1} (MPa)	E_{V2} (MPa)	CBR (%)
		γ_{dry} (kN/m^3)	Moisture (%)				
W-PP-GT	0	18.4	3.2	15.92		---	7.2
	0	19.1	3.3	22.03		---	7.1
	0	19.1	2.8	15.88		---	7.0
	0	19.2	3.2	13.51		---	5.3
	0	18.2	2.9	9.72		---	5.3
BX1200	0	18.4	3.6	13.11		---	4.9
	0	18.5	3.7	11.85		---	7.2
	0	19.1	2.8	16.58		---	4.8
	0	17.8	3.4	10.61		---	2.8
	0	19.5	3.5	15.82		---	5.8
W-PP-GT	1	19.4	3.0	15.68		---	7.0
	1	19.7	3.5	17.51		---	4.9
	1	19.7	3.0	14.76		---	5.8
	1	19.7	3.1	10.46		---	7.7
	1	18.6	2.8	8.55		---	3.6
BX1200	1	19.1	3.3	12.95		---	5.5
	1	19.0	3.6	16.26		---	4.7
	1	19.3	2.8	14.20		---	4.2
	1	19.1	2.8	14.88		---	4.5
	1	19.5	3.7	15.98		---	5.9
W-PP-GT	2	19.9	3.2	16.88		---	9.0
	2	20.1	3.2	15.24		---	8.0
	2	20.2	2.7	14.17		---	7.6
	2	19.9	3.6	10.90		---	9.7
	2	19.6	3.3	8.68		---	5.7
BX1200	2	19.6	2.9	12.14		---	4.8
	2	19.9	3.4	11.43		---	5.7
	2	19.9	3.5	11.06		---	6.3
	2	19.3	2.9	14.79		---	6.5
	2	20.2	3.4	15.52		---	7.2
W-PP-GT	4	19.0	3.2	19.82		---	7.9
	4	19.9	3.2	15.78		---	8.1
	4	20.1	3.0	15.43		---	9.9
	4	19.9	3.4	10.90		---	5.4
	4	19.3	2.6	9.95		---	6.6
BX1200	4	19.7	2.9	13.46		---	6.1
	4	19.5	3.6	12.34		---	6.8
	4	19.2	3.5	12.93		---	5.7
	4	19.6	3.5	16.26		---	6.3
	4	20.2	3.9	13.76		---	8.5

Table 15. Summary of point test data – subbase 1 (Cont.)

Section	Roller Passes	Nuclear Density		E_{Z200} (MPa)	E_{V1} (MPa)	E_{V2} (MPa)	CBR (%)
		γ_{dry} (kN/m^3)	Moisture (%)				
W-PP-GT	10	20.1	3.1	20.75	---	---	11.6
	10	20.4	2.8	15.72	19.4	56.9	11.2
	10	20.3	3.2	15.21	17.5	50.8	8.6
	10	20.1	3.4	10.90	10.4	31.5	10.3
	10	19.8	2.5	9.01	---	---	6.9
BX1200	10	20.0	3.0	12.34	---	---	6.0
	10	20.0	3.1	18.78	---	---	8.1
	10	20.4	3.1	12.44	---	---	8.3
	10	20.3	3.2	16.73	---	---	8.8
	10	20.9	4.0	15.52	---	---	11.5

Table 16. Summary of point test data – subbase 2

Section	Roller Passes	Nuclear Density		E_{Z200} (MPa)	E_{V1} (MPa)	E_{V2} (MPa)	CBR base2
		γ_{dry} (kN/m^3)	Moisture (%)				
W-PP-GT	0	19.1	3.0	23.93	---	---	8.1
	0	19.6	3.6	31.04	---	---	8.5
	0	19.7	4.1	30.92	---	---	8.9
	0	20.1	3.4	25.04	---	---	10.3
	0	19.9	3.3	26.55	---	---	7.7
BX1200	0	19.3	3.8	25.91	---	---	6.8
	0	19.7	3.2	27.93	---	---	9.5
	0	19.5	3.8	27.32	---	---	6.4
	0	19.7	3.7	26.18	---	---	6.5
	0	19.6	3.6	26.27	---	---	8.6
W-PP-GT	1	19.2	3.5	20.36	---	---	8.0
	1	19.8	3.8	26.27	---	---	7.1
	1	19.8	3.8	28.57	---	---	10.9
	1	19.9	3.7	21.28	---	---	11.2
	1	19.6	3.5	18.88	---	---	6.3
BX1200	1	19.3	3.8	26.00	---	---	9.5
	1	19.5	3.7	23.26	---	---	6.1
	1	19.3	3.6	22.97	---	---	7.7
	1	19.8	3.5	25.64	---	---	9.6
	1	19.5	4.2	23.62	---	---	7.4
W-PP-GT	2	19.8	3.6	22.36	---	---	8.7
	2	20.2	4.1	24.39	---	---	6.7
	2	20.0	3.7	25.55	---	---	9.7
	2	20.3	3.7	22.23	---	---	10.6
	2	20.3	4.2	23.55	---	---	8.6
BX1200	2	19.7	3.3	20.81	---	---	7.0
	2	20.2	3.4	25.21	---	---	6.2
	2	19.9	3.4	22.90	---	---	7.8
	2	19.4	4.0	23.26	---	---	6.4
	2	19.9	3.3	22.29	---	---	6.9
W-PP-GT	4	20.2	3.6	30.92	---	---	11.5
	4	20.3	3.7	26.64	---	---	9.8
	4	20.1	3.4	22.83	---	---	8.4
	4	20.0	3.7	20.70	---	---	10.0
	4	20.4	3.1	18.97	---	---	8.3
BX1200	4	20.1	3.3	20.09	---	---	6.9
	4	20.2	3.6	21.97	---	---	7.5
	4	20.4	3.3	24.00	---	---	8.8
	4	20.0	3.7	26.36	---	---	4.3
	4	20.0	4.0	22.29	---	---	7.6

Table 16. Summary of point test data – subbase 2 (Cont.)

Section	Roller Passes	Nuclear Density		E_{Z200} (MPa)	E_{V1} (MPa)	E_{V2} (MPa)	CBR base 2
		γ_{dry} (kN/m^3)	Moisture (%)				
W-PP-GT	10	20.5	3.8	26.64	---	---	13.2
	10	20.8	4.0	27.52	---	---	11.5
	10	20.4	3.5	25.91	---	---	15.8
	10	21.1	3.9	22.63	---	---	16.2
	10	20.5	3.9	15.95	---	---	11.9
BX1200	10	20.2	3.4	24.71	---	---	7.7
	10	19.9	4.3	23.70	---	---	10.2
	10	20.9	3.4	25.91	---	---	11.3
	10	20.0	3.6	26.83	---	---	13.3
	10	20.6	3.6	24.88	---	---	10.9
W-PP-GT	21	---	---	35.27	71.7	137.8	---
	21	---	---	34.46	54.4	120.3	---
	21	21.2	3.3	33.54	61.1	123.9	---
	21	---	---	27.42	31.2	65.7	---
	21	---	---	26.36	25.6	57.4	---
BX1200	21	---	---	30.05	27.9	56.7	---
	21	---	---	34.15	37.4	77.1	---
	21	21.6	3.2	32.81	43.0	93.1	---
	21	---	---	39.13	78.9	142.7	---
	21	---	---	32.95	---	---	---

Table 17. Summary of point test data – subgrade

Section	Roller Passes	Nuclear Density		E_{Z200} (MPa)	E_{V1} (MPa)	E_{V2} (MPa)	CBR (%)
		γ_{dry} (kN/m^3)	Moisture (%)				
Initial Test	---	16.2	21.3	5.42	---	---	
Initial Test	---	16.3	23.2	4.24	---	---	
Control	2	16.8	21.5	4.59	6.4	19.1	2.9
	2	16.5	21.3	4.03	3.6	12.2	4.3
	2	17.0	20.9	4.24	---	---	5.2
	2	17.1	19.7	4.65	---	---	4.1
	2	17.0	19.9	4.63	---	---	3.9
TX160	2	16.9	18.6	6.02	---	---	5.3
	2	16.7	21.8	3.94	---	---	4.1
	2	16.5	20.8	4.07	---	---	2.1
	2	15.8	24.0	5.31	---	---	3.0
	2	16.3	20.8	4.18	---	---	4.5

Table 18. Summary of point test data – subbase 1

Section	Roller Passes	Nuclear Density		E_{Z200} (MPa)	E_{V1} (MPa)	E_{V2} (MPa)	CBR (%)
		γ_{dry} (kN/m^3)	Moisture (%)				
Control	0	19.5	3.1	20.03	---	---	7.5
	0	18.9	3.1	20.99	---	---	9.3
	0	18.6	2.9	20.14	---	---	5.9
	0	18.5	2.9	16.58	---	---	5.4
	0	18.1	2.3	14.76	---	---	4.5
TX160	0	18.7	2.6	16.58	---	---	6.2
	0	18.4	3.2	15.78	---	---	5.2
	0	18.6	2.3	17.35	---	---	6.5
	0	18.9	3.3	24.39	---	---	6.8
	0	20.3	2.8	15.95	---	---	11.2
Control	1	20.1	3.0	17.00	---	---	8.6
	1	19.6	3.0	16.05	---	---	9.5
	1	19.0	2.5	17.07	---	---	6.4
	1	18.9	3.1	15.49	---	---	4.6
	1	17.9	2.5	12.91	---	---	5.4
TX160	1	19.0	3.0	14.50	---	---	5.3
	1	18.6	2.6	10.11	---	---	6.3
	1	19.2	2.9	11.03	---	---	5.8
	1	19.0	3.3	17.11	---	---	8.4
	1	19.6	2.8	14.79	---	---	6.7
Control	2	19.5	3.2	14.73	---	---	9.5
	2	19.7	3.1	15.52	---	---	8.2
	2	19.8	2.4	16.30	---	---	7.8
	2	19.2	2.8	13.76	---	---	4.9
	2	19.3	2.1	13.11	---	---	5.2
TX160	2	19.6	3.0	13.37	---	---	6.3
	2	19.4	3.1	11.42	---	---	7.2
	2	19.6	2.7	11.45	---	---	4.8
	2	19.5	3.2	15.39	---	---	8.0
	2	19.9	3.5	14.17	---	---	8.5
Control	4	19.8	3.0	13.49	---	---	8.5
	4	19.9	3.1	18.60	---	---	6.8
	4	19.7	3.0	14.82	---	---	10.5
	4	19.5	2.8	15.15	---	---	7.1
	4	19.7	2.5	14.10	---	---	7.6
TX160	4	19.6	3.3	14.53	---	---	9.6
	4	19.4	3.2	12.40	---	---	7.1
	4	19.2	2.2	10.69	---	---	7.9
	4	19.9	3.0	15.59	---	---	8.6
	4	20.5	3.0	15.21	---	---	8.8

Table 18. Summary of point test data – subbase 1 (Cont.)

Section	Roller Passes	Nuclear Density		E_{Z200} (MPa)	E_{V1} (MPa)	E_{V2} (MPa)	CBR (%)
		γ_{dry} (kN/m^3)	Moisture (%)				
Control	10	20.4	3.0	13.73	15.3	43.8	12.5
	10	20.2	2.7	19.17	15.4	44.7	12.3
	10	20.0	2.8	17.47	11.3	38.7	9.4
	10	19.9	3.2	15.43	10.9	71.1	11.5
	10	20.2	2.2	14.79	14.4	44.2	11.1
TX160	10	20.2	3.0	14.02	22.3	55.8	10.3
	10	20.7	2.9	13.37	19.2	46.7	10.1
	10	20.3	2.9	13.27	15.3	33.6	7.3
	10	20.4	3.0	16.62	28.9	65.5	9.0
	10	20.3	3.3	14.23	---	---	10.6

Table 19. Summary of point test data – subbase 2

Section	Roller Passes	Nuclear Density		E_{Z200} (MPa)	E_{V1} (MPa)	E_{V2} (MPa)	CBR base 2
		γ_{dry} (kN/m^3)	Moisture (%)				
Control	0	20.2	3.5	30.66	---	---	12.0
	0	19.6	3.8	20.93	---	---	12.7
	0	19.5	3.7	29.46	---	---	12.9
	0	19.6	3.9	28.89	---	---	11.9
	0	19.6	3.8	25.38	---	---	9.8
TX160	0	19.1	4.1	23.19	---	---	7.3
	0	19.7	4.6	25.38	---	---	10.1
	0	19.8	4.3	28.03	---	---	9.4
	0	19.6	4.0	24.16	---	---	8.5
	0	20.1	4.2	27.52	---	---	8.9
Control	1	20.1	3.7	27.52	---	---	12.3
	1	20.3	3.3	26.27	---	---	10.3
	1	20.6	3.6	32.38	---	---	13.4
	1	20.5	3.3	37.94	---	---	10.6
	1	20.0	3.3	32.95	---	---	9.4
TX160	1	20.0	3.7	23.93	---	---	7.0
	1	20.6	4.2	23.19	---	---	8.5
	1	19.9	3.6	25.21	---	---	10.6
	1	20.1	4.1	33.10	---	---	9.0
	1	20.2	4.3	29.46	---	---	12.6
Control	2	20.3	3.8	33.84	---	---	10.8
	2	20.5	3.2	27.42	---	---	10.7
	2	19.7	3.7	34.46	---	---	9.9
	2	20.3	3.5	29.01	---	---	11.2
	2	20.2	3.0	31.70	---	---	10.5
TX160	2	19.8	3.8	25.04	---	---	12.0
	2	20.3	3.7	24.71	---	---	6.3
	2	20.1	3.4	24.00	---	---	10.4
	2	20.6	3.6	29.46	---	---	11.0
	2	19.9	4.4	27.42	---	---	10.6
Control	4	20.2	3.9	26.45	---	---	9.1
	4	20.3	3.4	29.35	---	---	13.2
	4	19.6	3.8	28.57	---	---	11.7
	4	20.5	3.4	29.46	---	---	11.6
	4	20.5	3.3	27.12	---	---	14.9
TX160	4	20.2	3.8	24.08	---	---	5.6
	4	20.5	3.8	22.49	---	---	16.9
	4	20.6	3.4	21.53	---	---	13.0
	4	20.4	4.0	26.45	---	---	6.0
	4	20.6	4.2	25.64	---	---	10.7

Table 19. Summary of point test data – subbase 2 (Cont.)

Section	Roller Passes	Nuclear Density		E_{Z200} (MPa)	E_{V1} (MPa)	E_{V2} (MPa)	CBR base 2
		γ_{dry} (kN/m^3)	Moisture (%)				
Control	10	20.8	4.2	30.54	---	---	15.9
	10	20.4	3.3	32.24	---	---	13.7
	10	20.5	3.8	30.17	---	---	13.1
	10	21.0	3.4	28.14	---	---	16.3
	10	21.1	3.4	28.03	---	---	13.8
TX160	10	20.3	3.9	28.03	---	---	16.0
	10	20.6	3.7	23.12	---	---	13.1
	10	20.9	3.6	26.00	---	---	14.7
	10	21.0	3.6	29.01	---	---	13.5
	10	20.6	4.1	23.48	---	---	15.5
Control	21	---	---	34.15	51.0	119.4	---
	21	---	---	34.30	41.4	101.8	---
	21	21.6	2.9	31.97	37.3	95.5	---
	21	---	---	25.30	26.9	83.0	---
	21	---	---	30.92	40.6	91.2	---
TX160	21	---	---	31.83	46.9	103.0	---
	21	---	---	26.18	46.3	91.5	---
	21	22.2	4.0	31.30	37.3	86.2	---
	21	---	---	27.42	60.8	131.2	---
	21	---	---	25.73	54.1	112.8	---

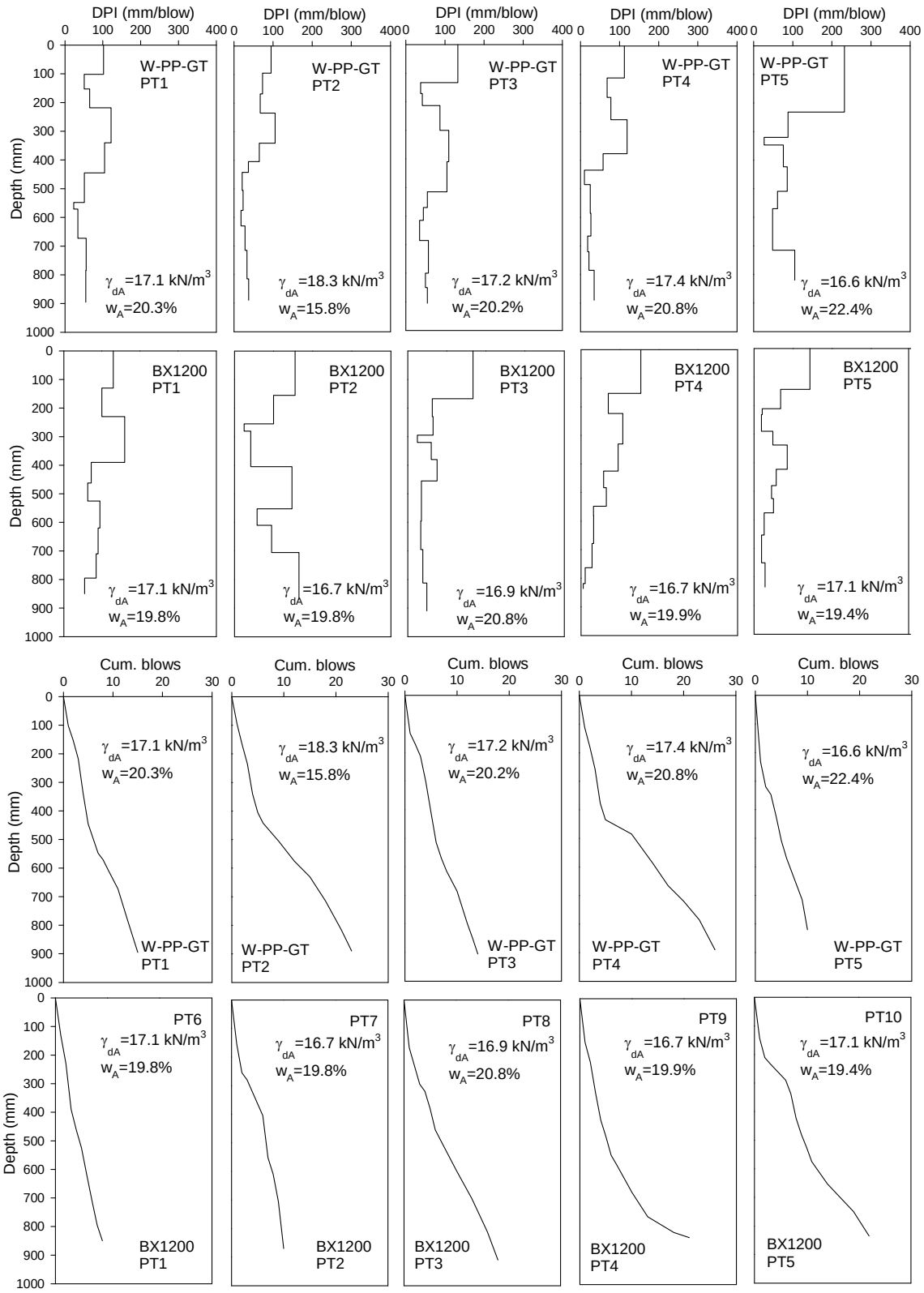

Figure 98. DCP profiles for W-PP-GT and BX1200 sections

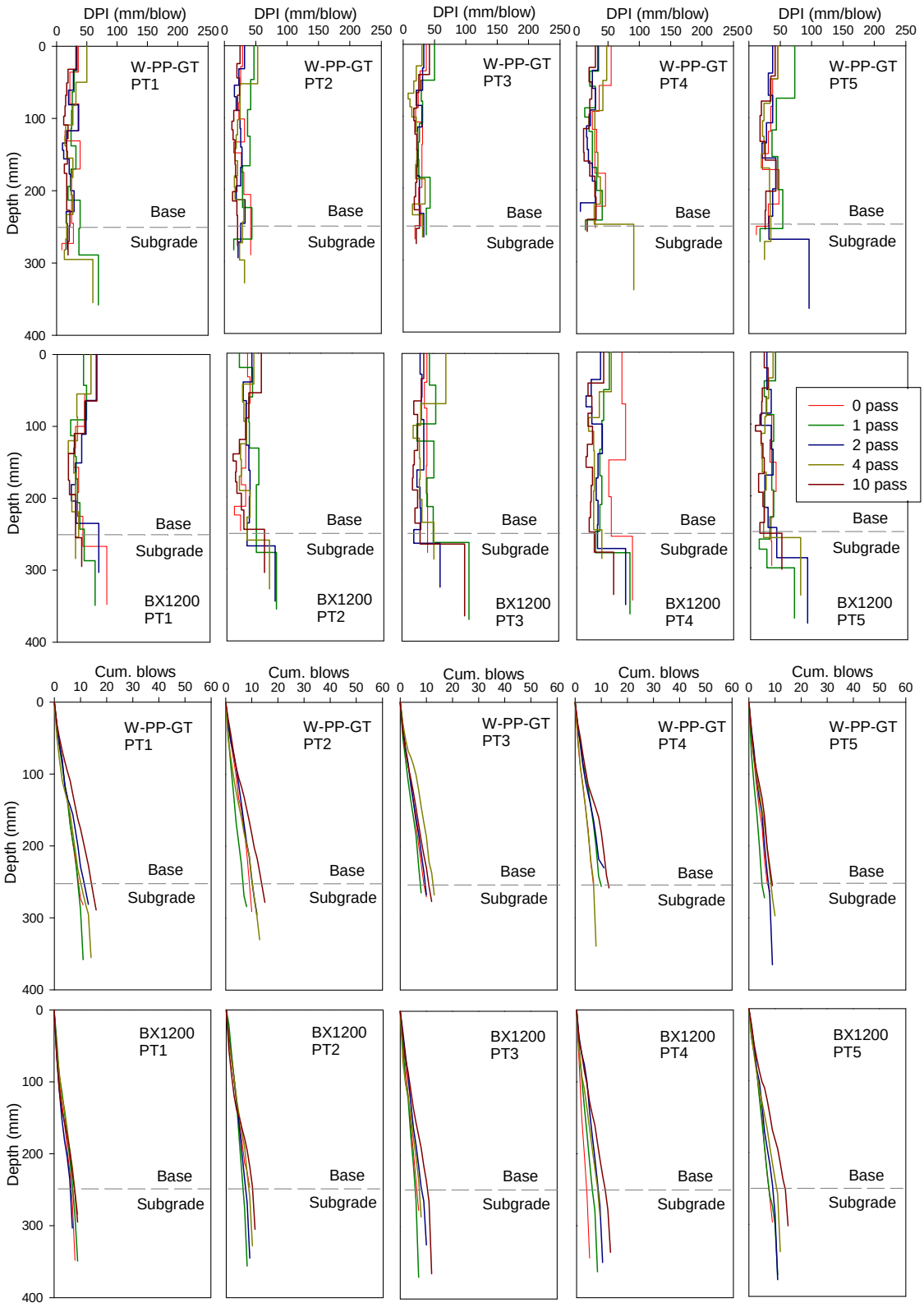

Figure 99. DCP profiles for W-PP-GT and BX1200 sections – subbase layer 1

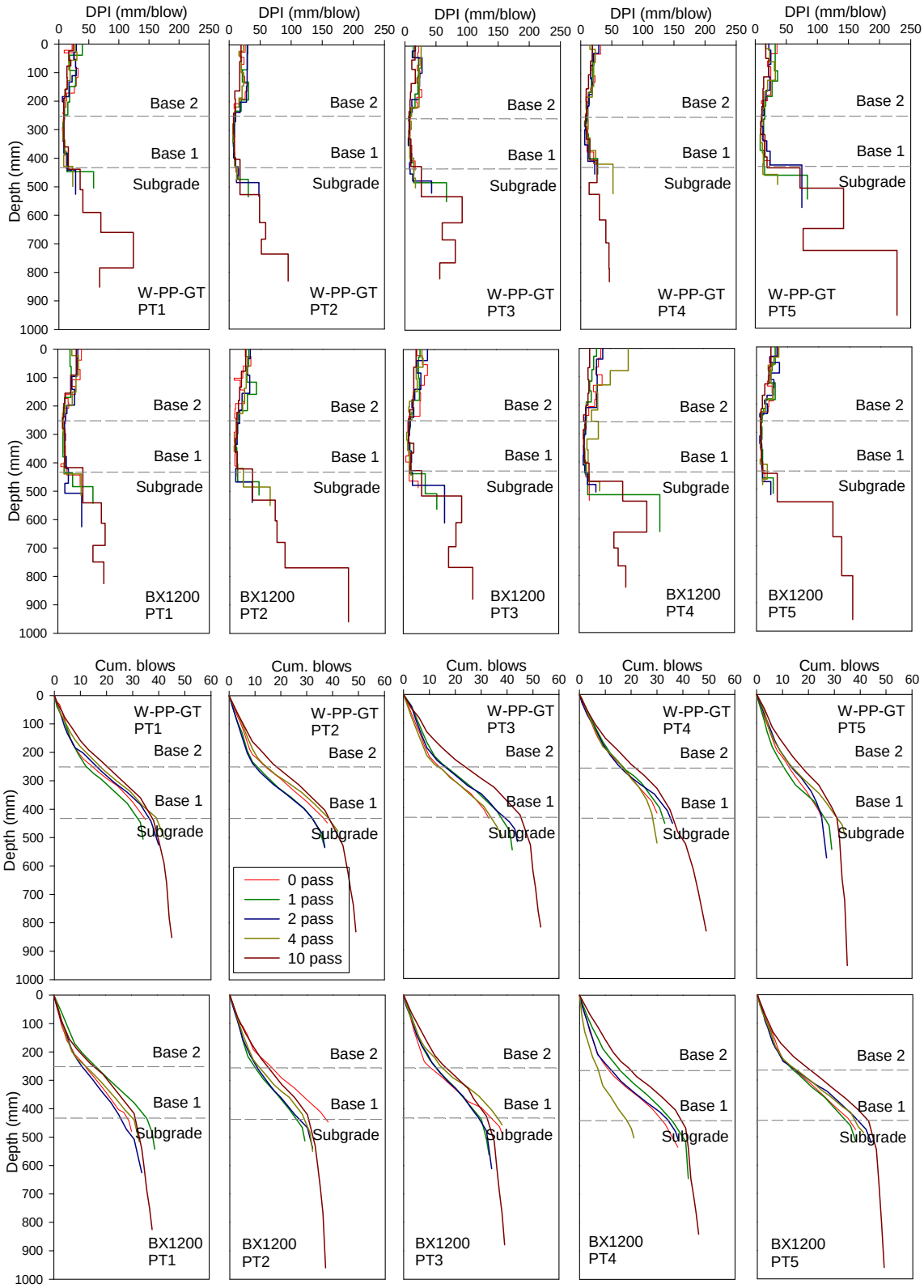

Figure 100. DCP profiles for W-PP-GT and BX1200 section – subbase layer 2

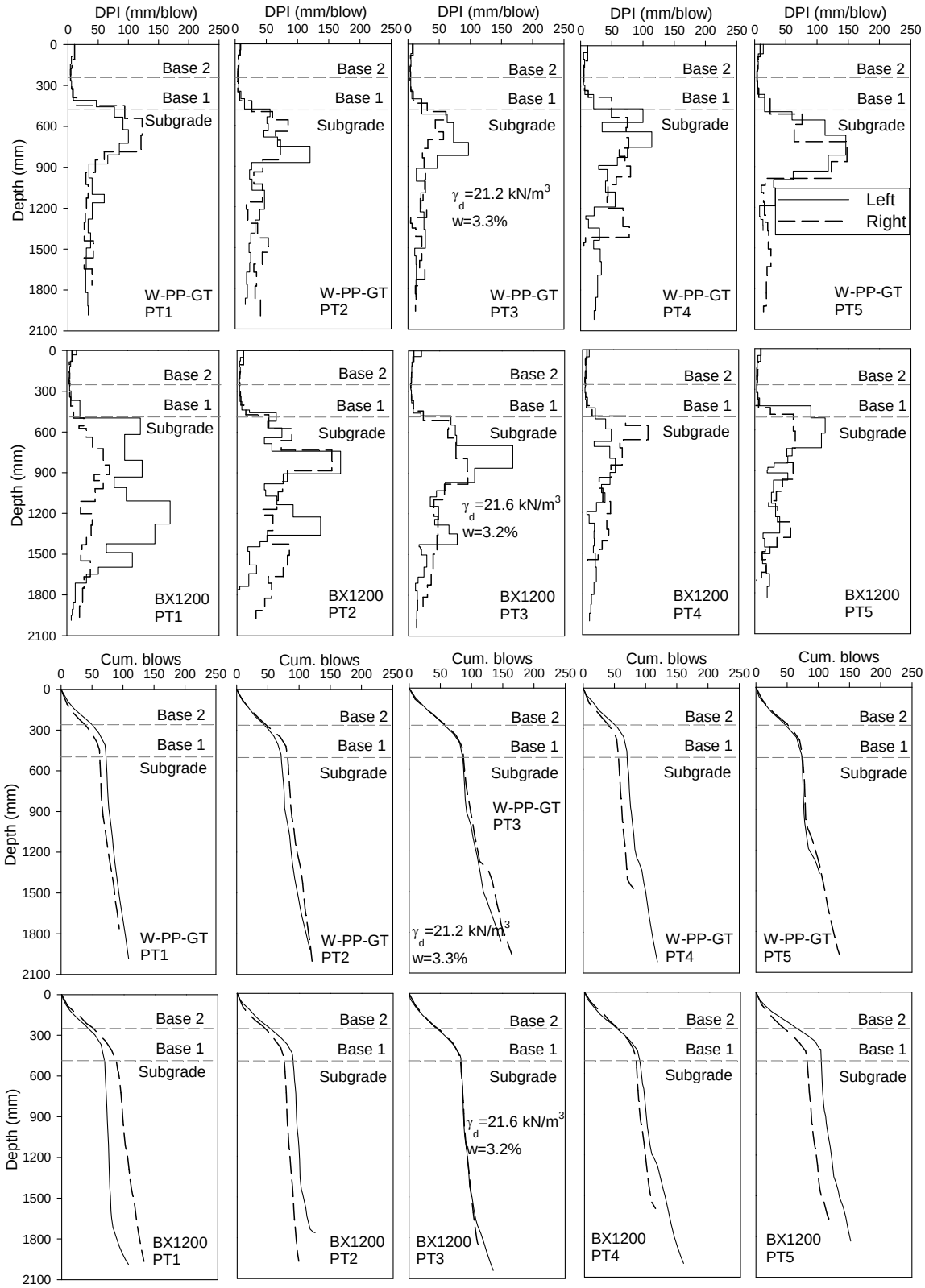

Figure 101. DCP profiles for W-PP-GT and BX1200 sections – final full depth test

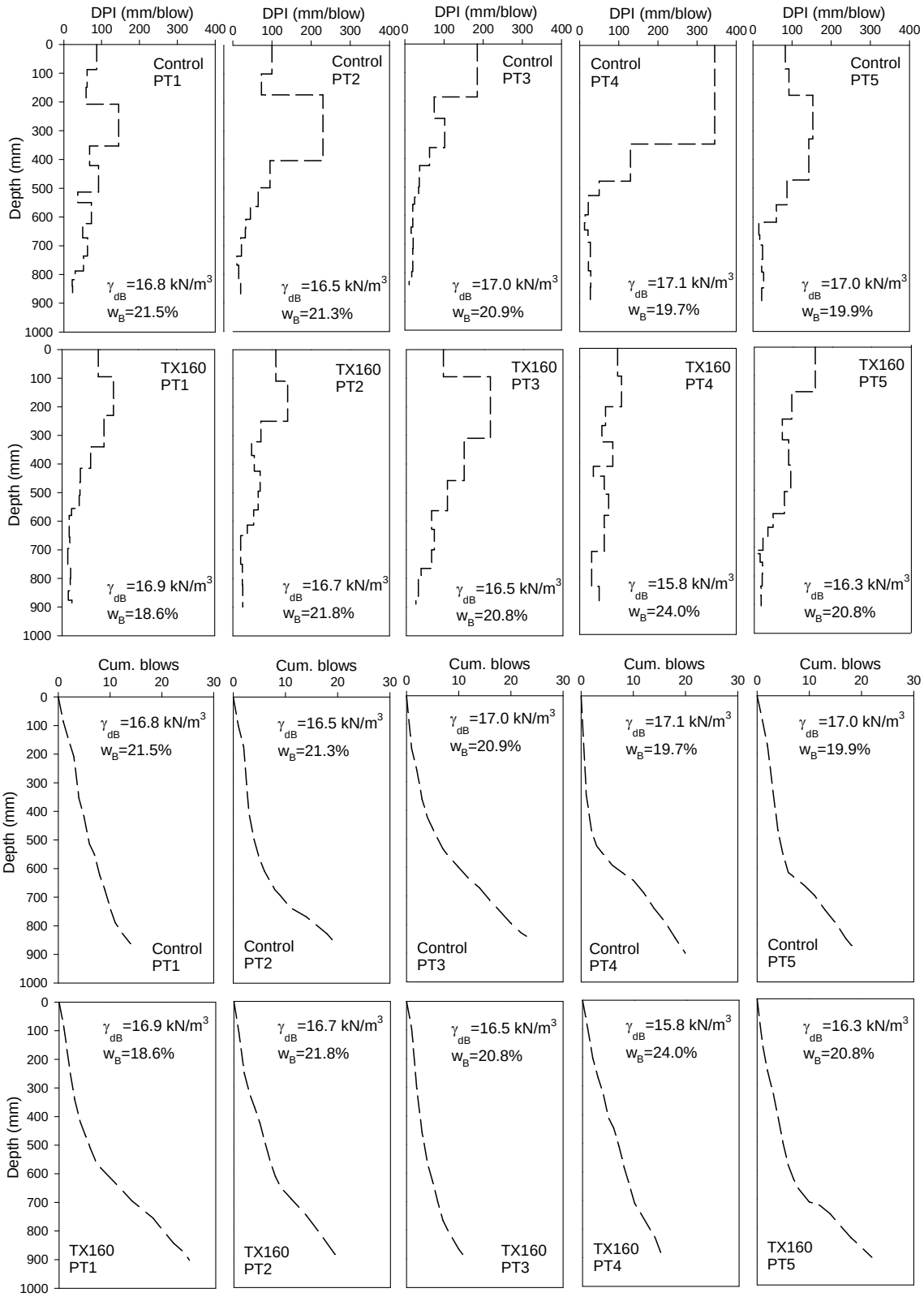

Figure 102. DCP profiles for control and TX160 sections

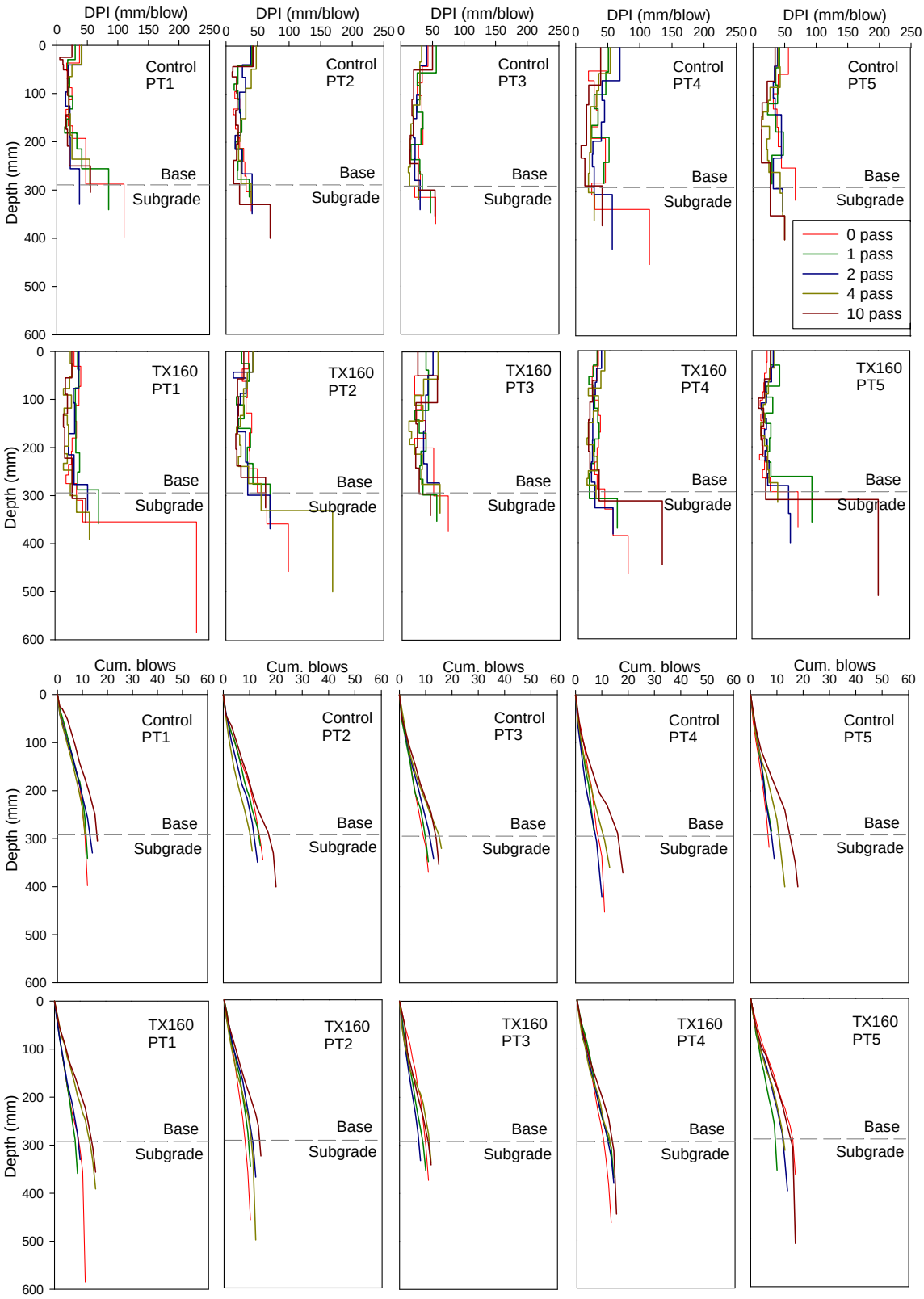

Figure 103. DCP profiles for control and TX160 sections – subbase layer 1

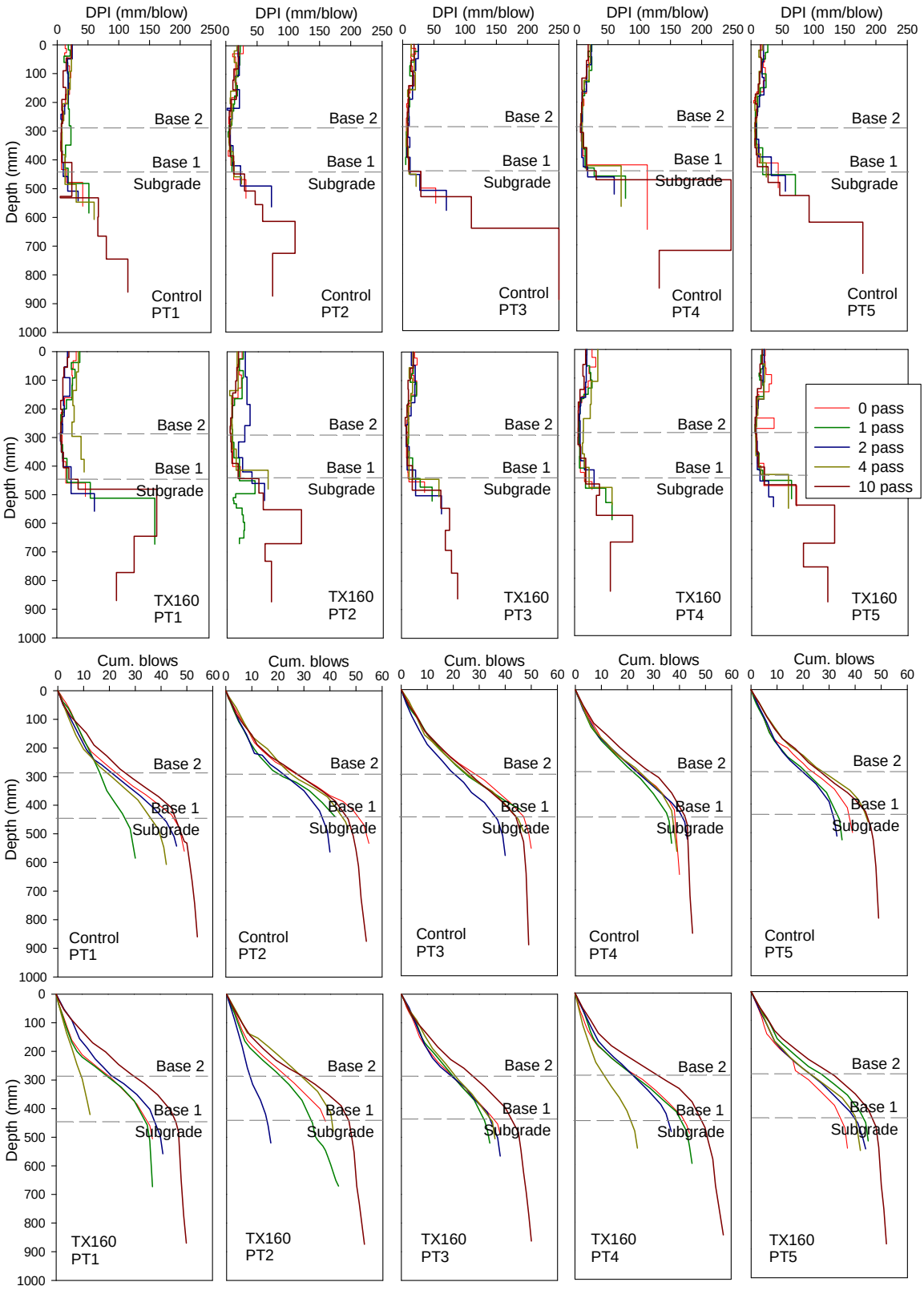

Figure 104. DCP profiles for control and TX160 sections – subbase layer 2

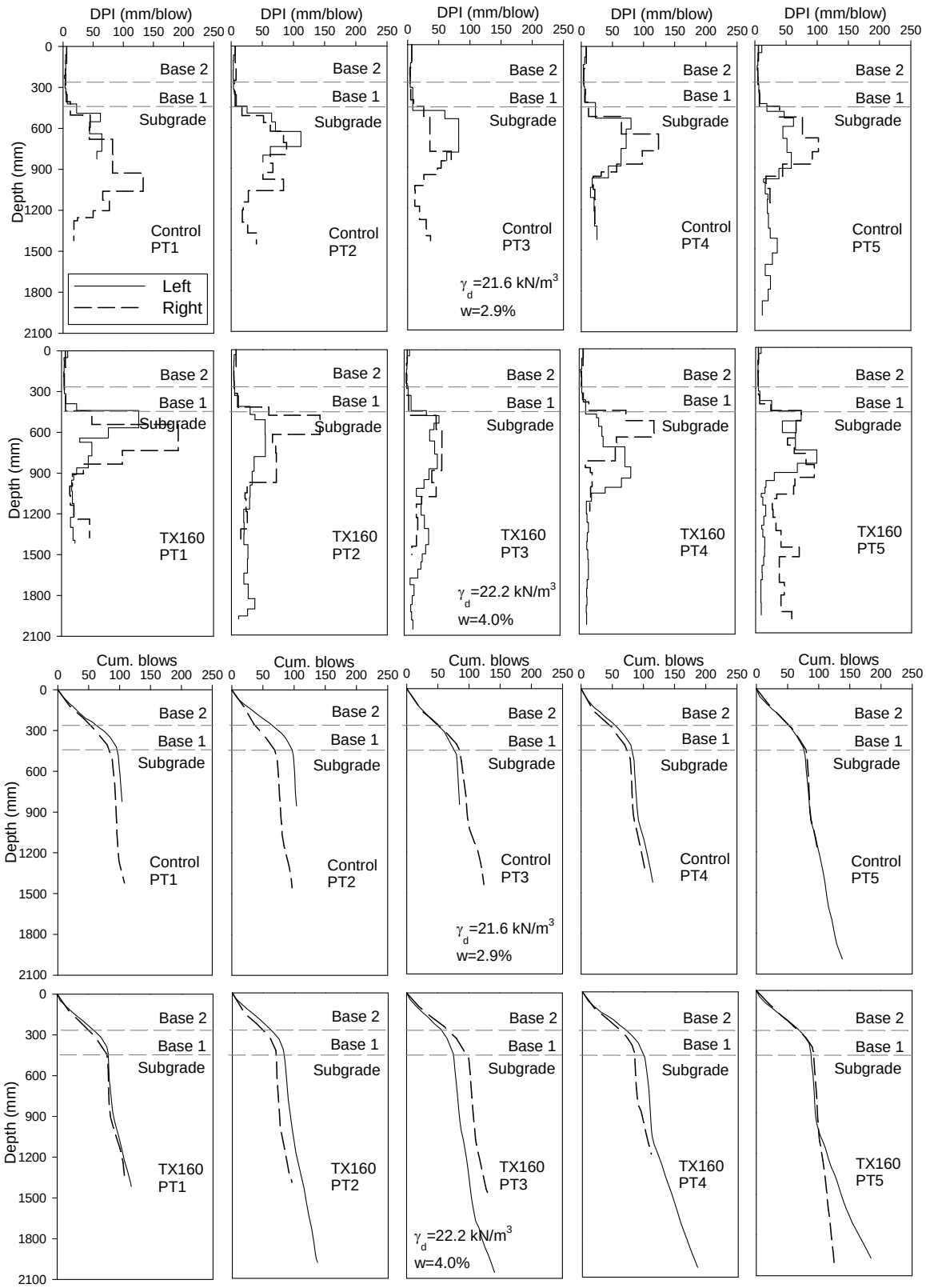

Figure 105. DCP profiles for control and TX160 sections – final full depth test

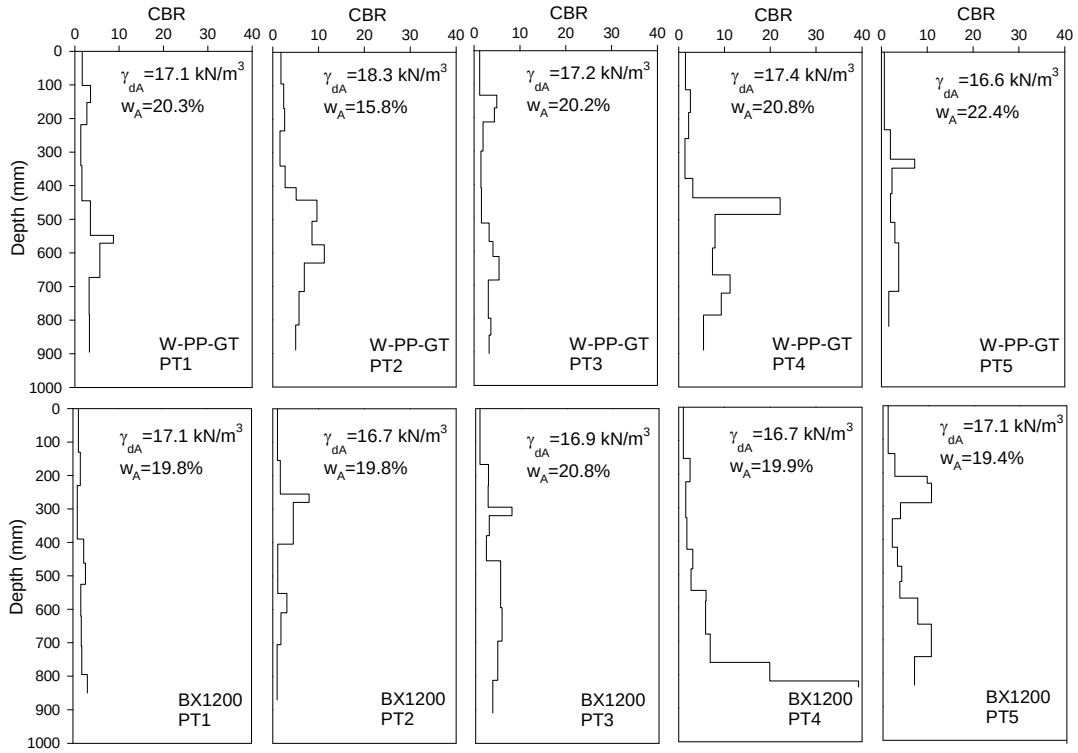

Figure 106. CBR profiles for subgrade layer for W-PP-GT and BX1200 sections

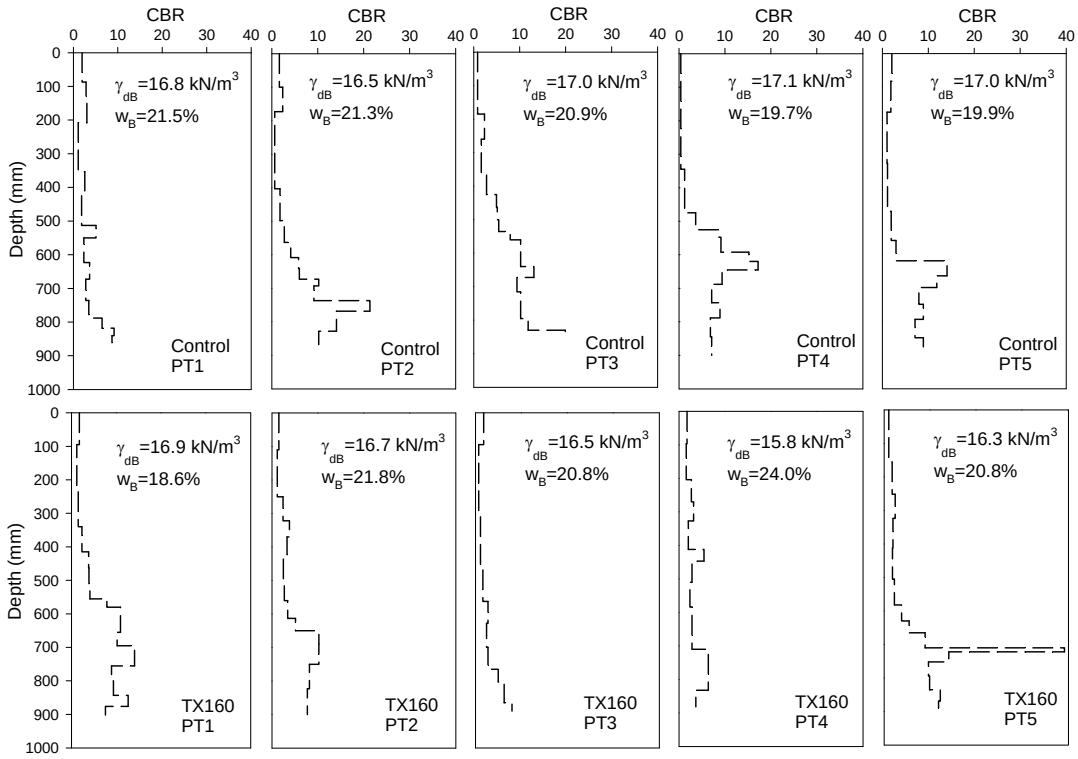

Figure 107. CBR profiles for subgrade layer for control and TX160 sections

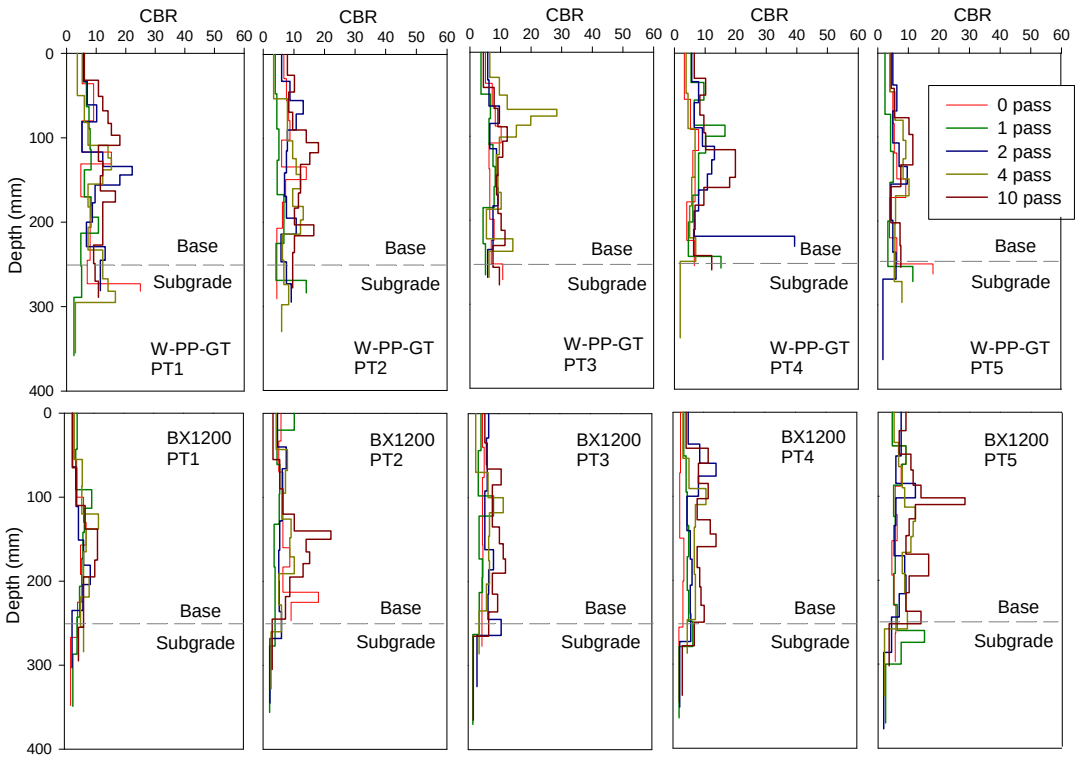

Figure 108. CBR profiles for W-PP-GT and BX1200 sections – subbase layer 1

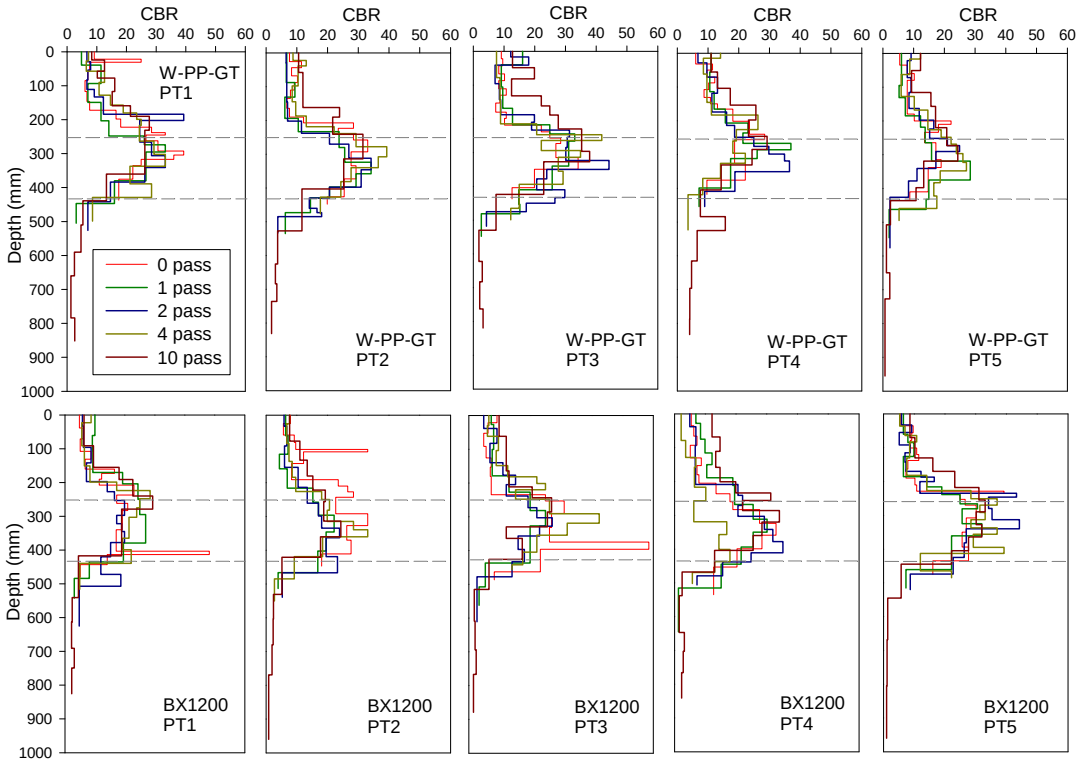

Figure 109. CBR profiles for W-PP-GT and BX1200 sections – subbase layer 2

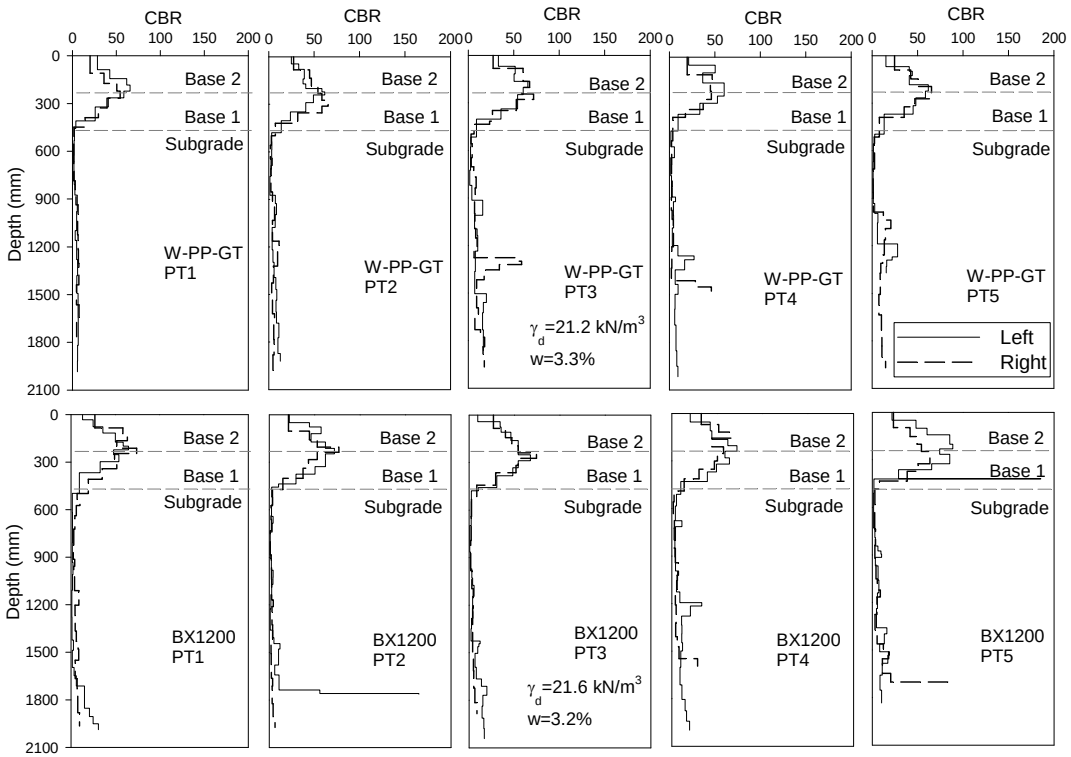

Figure 110. CBR profiles for W-PP-GT and BX1200 sections – final full depth test

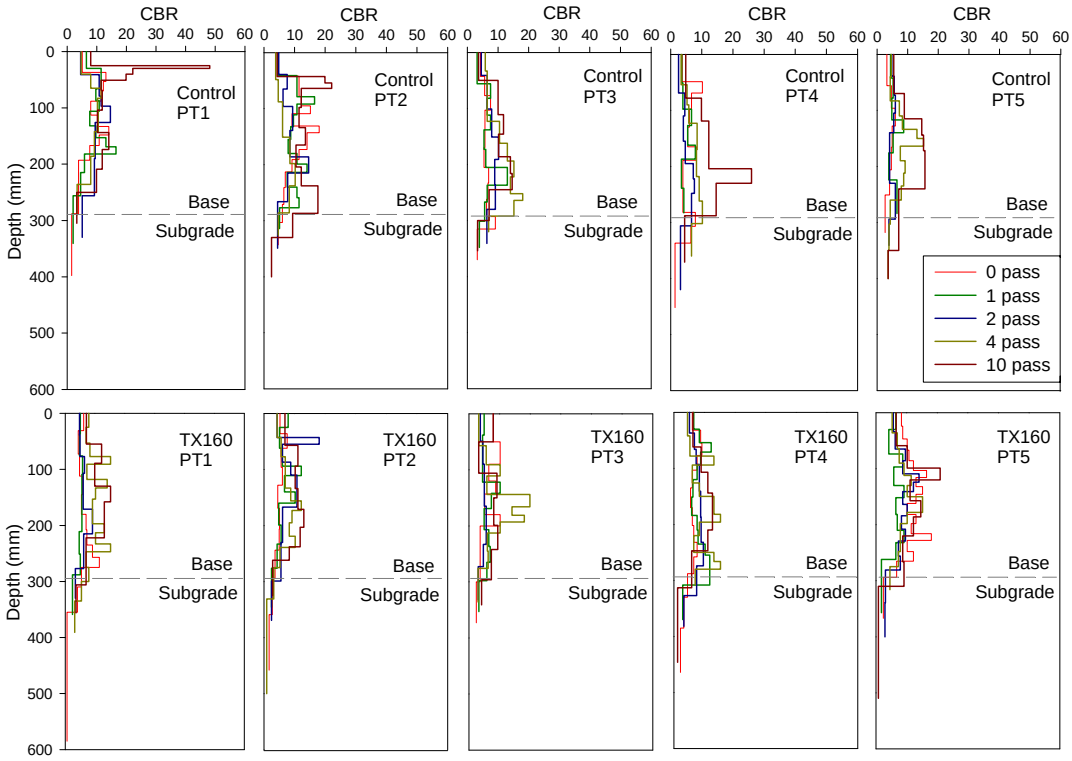

Figure 111. CBR profiles for control and TX160 sections – subbase layer 1

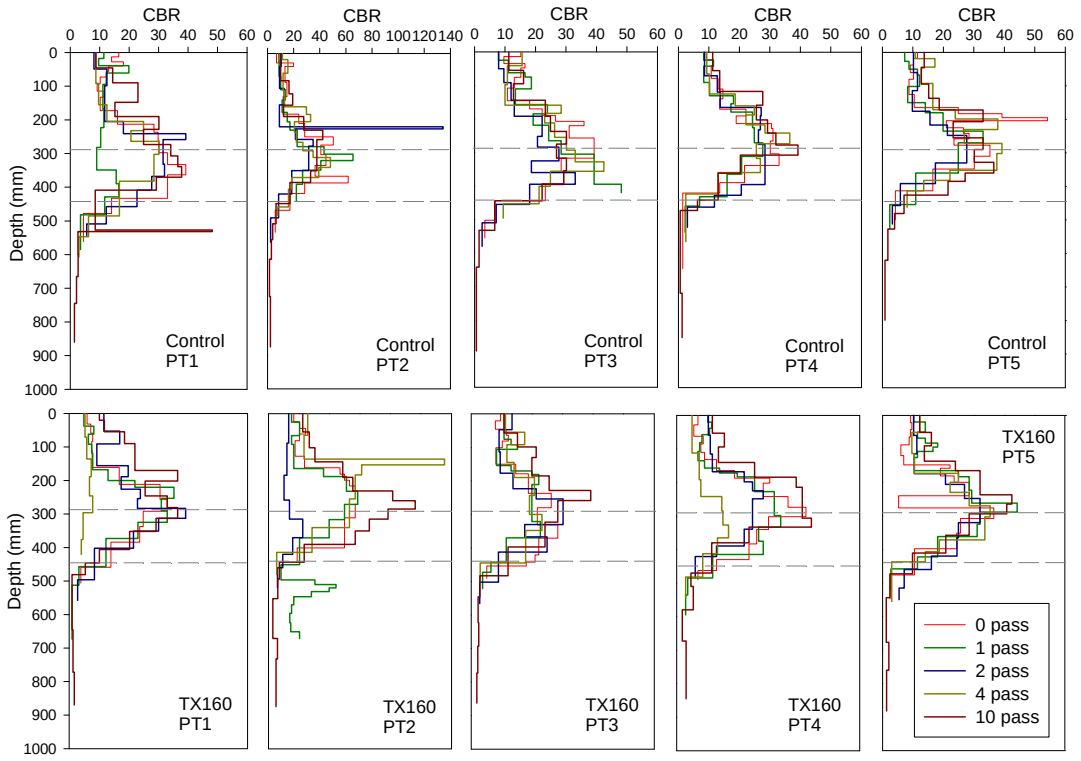

Figure 112. CBR profiles for control and TX160 sections – subbase layer 2

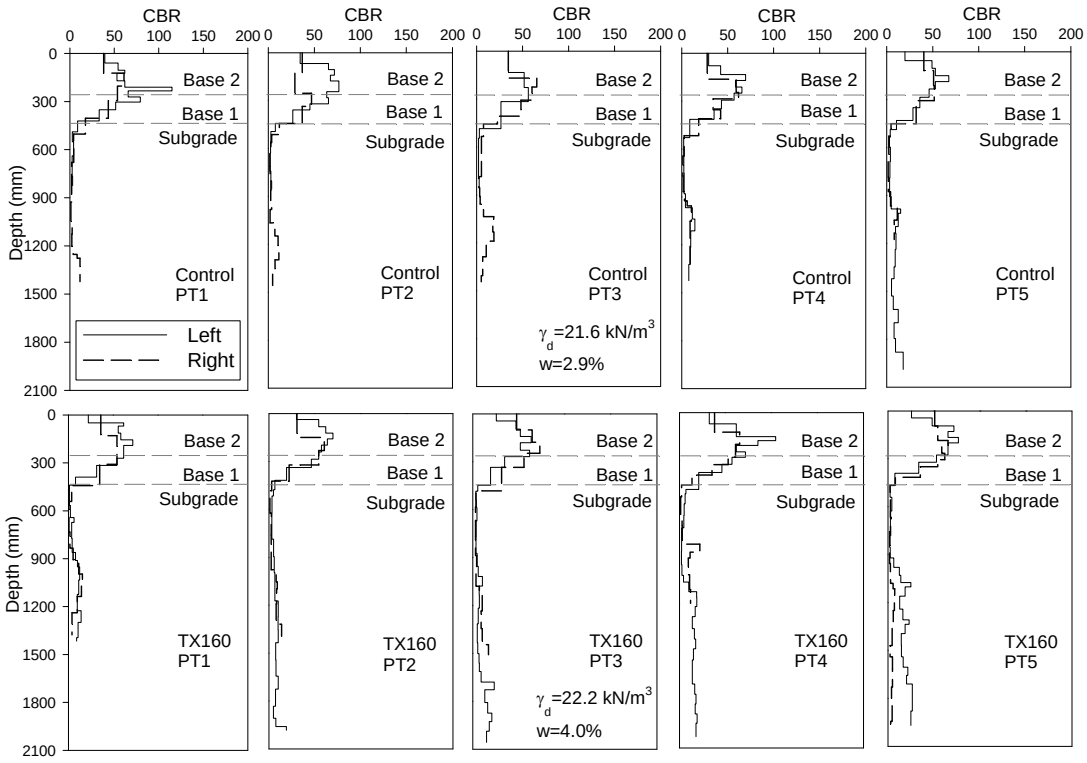

Figure 113. CBR profiles for control and TX160 sections – final full depth test

Table 20. Summary of DCP testing on subgrade

Section	Point	Material	Depth Range (mm)	DPI	CBR
W-PP-GT	1	Subgrade	0 – 571	71.4	2.5
W-PP-GT	2	Subgrade	0 – 442	73.7	2.4
W-PP-GT	3	Subgrade	0 – 615	76.9	2.3
W-PP-GT	4	Subgrade	0 – 435	87.0	2.0
W-PP-GT	5	Subgrade	0 – 570	95.0	1.8
BX1200	1	Subgrade	0 – 620	103.3	1.6
BX1200	2	Subgrade	0 – 552	78.9	2.2
BX1200	3	Subgrade	0 – 490	70.0	2.5
BX1200	4	Subgrade	0 – 580	82.9	2.1
BX1200	5	Subgrade	0 – 575	52.3	3.6
Control	1	Subgrade	0 – 623	77.9	2.2
Control	2	Subgrade	0 – 641	91.6	1.9
Control	3	Subgrade	0 – 535	76.4	2.3
Control	4	Subgrade	0 – 592	98.7	1.7
Control	5	Subgrade	0 – 633	90.4	1.9
TX160	1	Subgrade	0 – 580	72.5	2.4
TX160	2	Subgrade	0 – 613	76.6	2.3
TX160	3	Subgrade	0 – 628	125.6	1.3
TX160	4	Subgrade	0 – 584	73.0	2.4
TX160	5	Subgrade	0 – 582	97.0	1.7

Table 21. Summary of DCP testing on subbase 1

Section	Point	Material	Depth Range (mm)	DPI	CBR
W-PP-GT	1	Subbase 1	0 – 193	17.5	11.8
W-PP-GT	2	Subbase 1	0 – 203	18.5	11.2
W-PP-GT	3	Subbase 1	0 – 212	23.6	8.5
W-PP-GT	4	Subbase 1	0 – 210	19.1	10.7
W-PP-GT	5	Subbase 1	0 – 202	28.9	6.8
BX1200	1	Subbase 1	0 – 225	32.1	6.0
BX1200	2	Subbase 1	0 – 218	24.2	8.2
BX1200	3	Subbase 1	0 – 215	23.9	8.4
BX1200	4	Subbase 1	0 – 208	23.1	8.7
BX1200	5	Subbase 1	0 – 215	17.9	11.5
Control	1	Subbase 1	0 – 209	16.1	13.0
Control	2	Subbase 1	0 – 204	18.5	11.1
Control	3	Subbase 1	0 – 216	21.6	9.3
Control	4	Subbase 1	0 – 204	22.7	8.9
Control	5	Subbase 1	0 – 240	18.5	11.1
TX160	1	Subbase 1	0 – 222	18.5	11.1
TX160	2	Subbase 1	0 – 203	20.3	10.0
TX160	3	Subbase 1	0 – 199	28.4	6.9
TX160	4	Subbase 1	0 – 210	21.0	9.6
TX160	5	Subbase 1	0 – 220	18.3	11.2

Table 22. Summary of DCP testing on W-PP-GT and BX sections after trafficking subbase 2

Section	Point	Material	Depth Range (mm)	DPI	CBR
W-PP-GT	1L	Subbase[1]	0 – 409	5.8	41.1
		Subgrade	409 – 875	77.7	2.2
W-PP-GT	1R	Subbase[1]	0 – 389	6.7	34.6
		Subgrade	448 – 846	99.5	1.7
W-PP-GT	2L	Subbase[1]	0 – 404	6.1	38.4
		Subgrade	480 – 874	65.7	2.7
W-PP-GT	2R	Subbase[1]	0 – 419	5.3	45.1
		Subgrade	499 – 854	71.0	2.5
W-PP-GT	3L	Subbase[1]	0 – 403	5.0	48.4
		Subgrade	515 – 821	76.5	2.3
W-PP-GT	3R	Subbase[1]	0 – 416	5.0	48.0
		Subgrade	497 – 767	45.0	4.1
W-PP-GT	4L	Subbase[1]	0 – 361	5.6	42.8
		Subgrade	466 – 824	71.6	2.4
W-PP-GT	4R	Subbase[1]	0 – 331	6.6	35.2
		Subgrade	529 – 887	71.6	2.4
W-PP-GT	5L	Subbase[1]	0 – 369	5.7	41.8
		Subgrade	496 – 933	109.3	1.5
W-PP-GT	5R	Subbase[1]	0 – 389	5.6	42.8
		Subgrade	513 – 864	87.8	1.9
BX1200	1L	Subbase[1]	0 – 367	5.8	40.6
		Subgrade	497 – 932	108.8	1.5
BX1200	1R	Subbase[1]	0 – 408	5.1	47.1
		Subgrade	574 – 958	48.0	3.8
BX1200	2L	Subbase[1]	0 – 375	4.7	51.8
		Subgrade	437 – 907	67.1	2.6
BX1200	2R	Subbase[1]	0 – 401	5.7	41.3
		Subgrade	574 – 885	90.5	2.3
BX1200	3L	Subbase[1]	0 – 383	5.3	44.9
		Subgrade	478 – 865	81.4	3.7
BX1200	3R	Subbase[1]	0 – 365	5.2	45.9
		Subgrade	641 – 982	82.0	2.2
BX1200	4L	Subbase[1]	0 – 429	5.0	47.6
		Subgrade	511 – 906	39.5	4.8
BX1200	4R	Subbase[1]	0 – 413	5.3	45.2
		Subgrade	490 – 851	72.2	2.4
BX1200	5L	Subbase[1]	0 – 363	3.8	65.1
		Subgrade	421 – 844	84.6	2.0
BX1200	5R	Subbase[1]	0 – 434	5.4	43.9
		Subgrade	484 – 963	59.9	3.0

[1] Subbase includes subbase 1 and subbase 2 as included in depth ranges.

Table 23. Summary of DCP testing on control and TX sections after trafficking subbase 2

Section	Point	Material	Depth Range (mm)	DPI	CBR
Control	1L	Subbase[1]	0 – 421	4.4	55.1
		Subgrade	489 – 824	55.8	3.2
Control	1R	Subbase[1]	0 – 405	5.1	47.5
		Subgrade	503 – 927	45.8	7.0
Control	2L	Subbase[1]	0 – 442	4.6	53.4
		Subgrade	493 – 855	51.7	3.5
Control	2R	Subbase[1]	0 – 443	6.4	36.4
		Subgrade	512 – 930	69.7	2.5
Control	3L	Subbase[1]	0 – 485	6.1	38.8
		Subgrade	485 – 854	73.8	2.4
Control	3R	Subbase[1]	0 – 407	5.1	47.2
		Subgrade	534 – 957	42.3	4.4
Control	4L	Subbase[1]	0 – 414	5.2	46.3
		Subgrade	528 – 967	62.7	2.8
Control	4R	Subbase[1]	0 – 410	5.9	40.3
		Subgrade	516 – 924	81.6	2.1
Control	5L	Subbase[1]	0 – 430	5.7	41.3
		Subgrade	488 – 907	52.4	3.5
Control	5R	Subbase[1]	0 – 450	5.6	42.2
		Subgrade	529 – 876	86.8	2.0
TX160	1L	Subbase[1]	0 – 389	4.9	49.7
		Subgrade	439 – 911	52.4	3.5
TX160	1R	Subbase[1]	0 – 442	5.5	43.0
		Subgrade	542 – 906	91.0	1.9
TX160	2L	Subbase[1]	0 – 338	4.5	54.1
		Subgrade	516 – 896	47.5	3.9
TX160	2R	Subbase[1]	0 – 423	6.0	38.9
		Subgrade	483 – 978	82.5	2.1
TX160	3L	Subbase[1]	0 – 335	5.2	46.5
		Subgrade	484 – 875	48.9	3.7
TX160	3R	Subbase[1]	0 – 482	4.8	50.2
		Subgrade	482 – 888	58.0	3.1
TX160	4L	Subbase[1]	0 – 376	4.2	58.9
		Subgrade	572 – 952	54.3	3.3
TX160	4R	Subbase[1]	0 – 392	4.9	49.2
		Subgrade	454 – 825	74.2	2.3
TX160	5L	Subbase[1]	0 – 391	4.6	52.9
		Subgrade	468 – 920	64.6	2.7
TX160	5R	Subbase[1]	0 – 416	4.6	52.6
		Subgrade	465 - 956	70.1	2.5

[1] Subbase includes subbase 1 and subbase 2 as included in depth ranges.

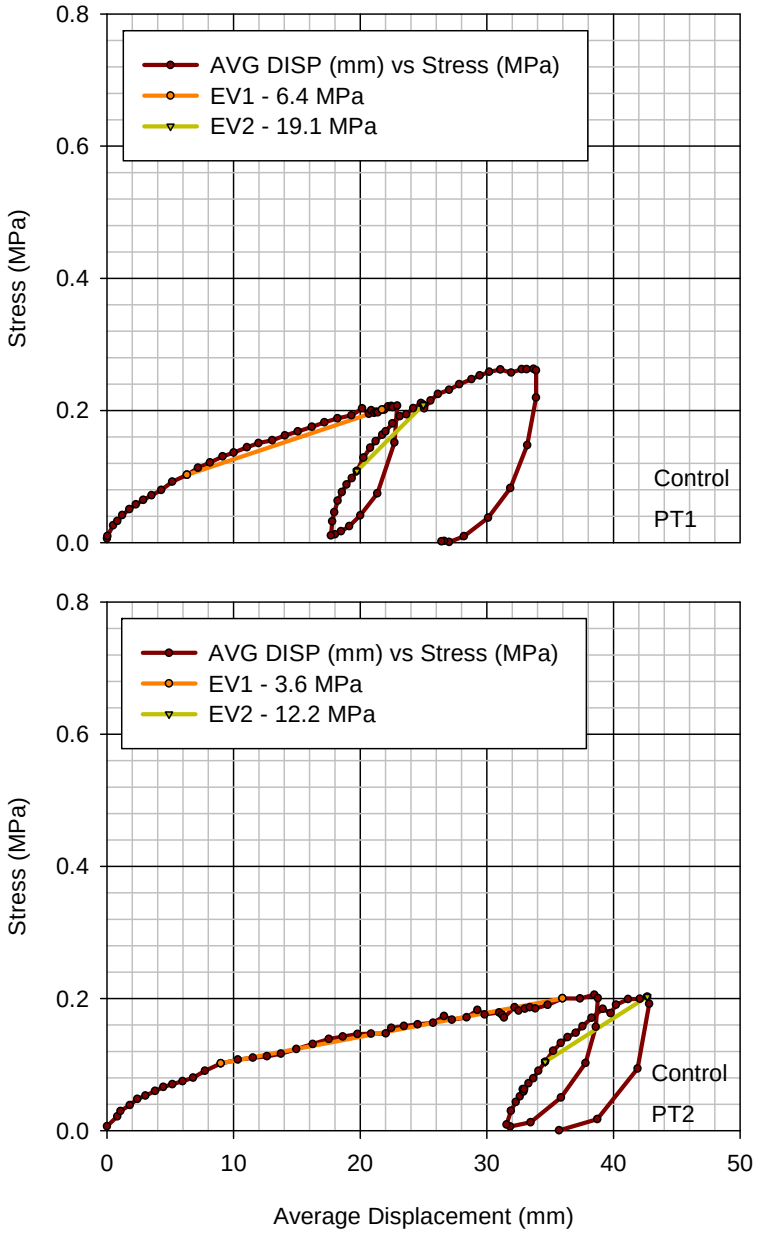

Figure 114. Plate load test results on control section – Subgrade

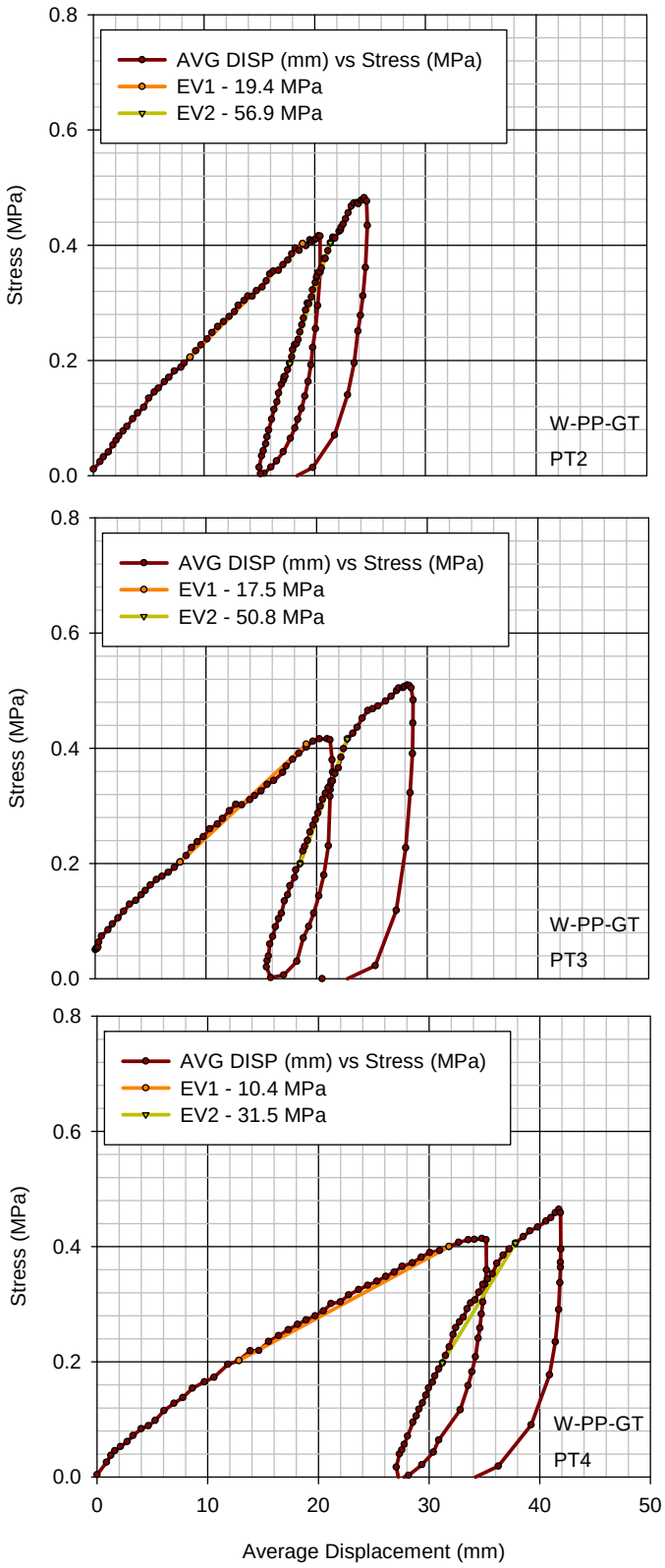

Figure 115. Plate load test results for section W-PP-GT – subbase 1

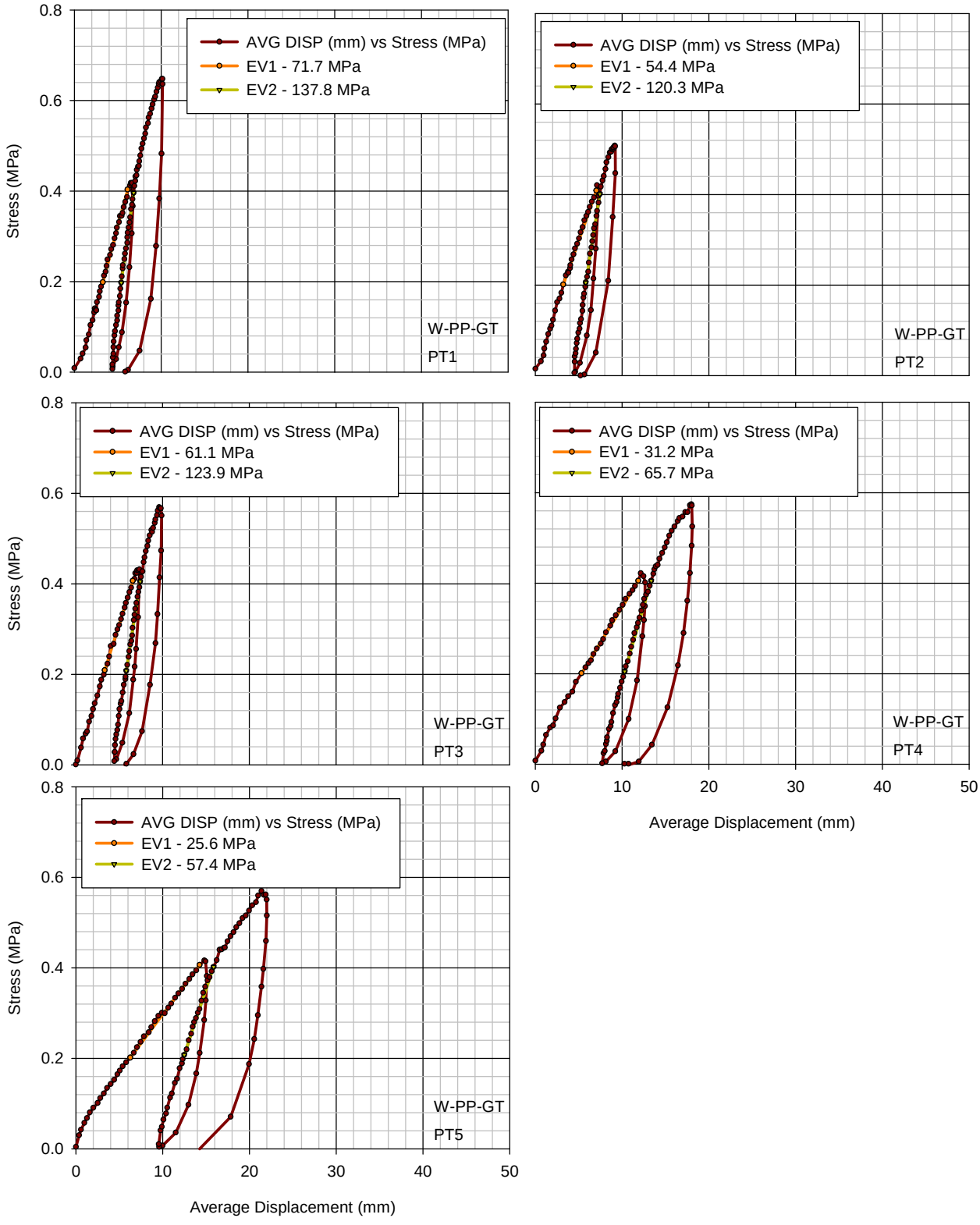

Figure 116. Plate load test results on section W-PP-GT – subbase 2

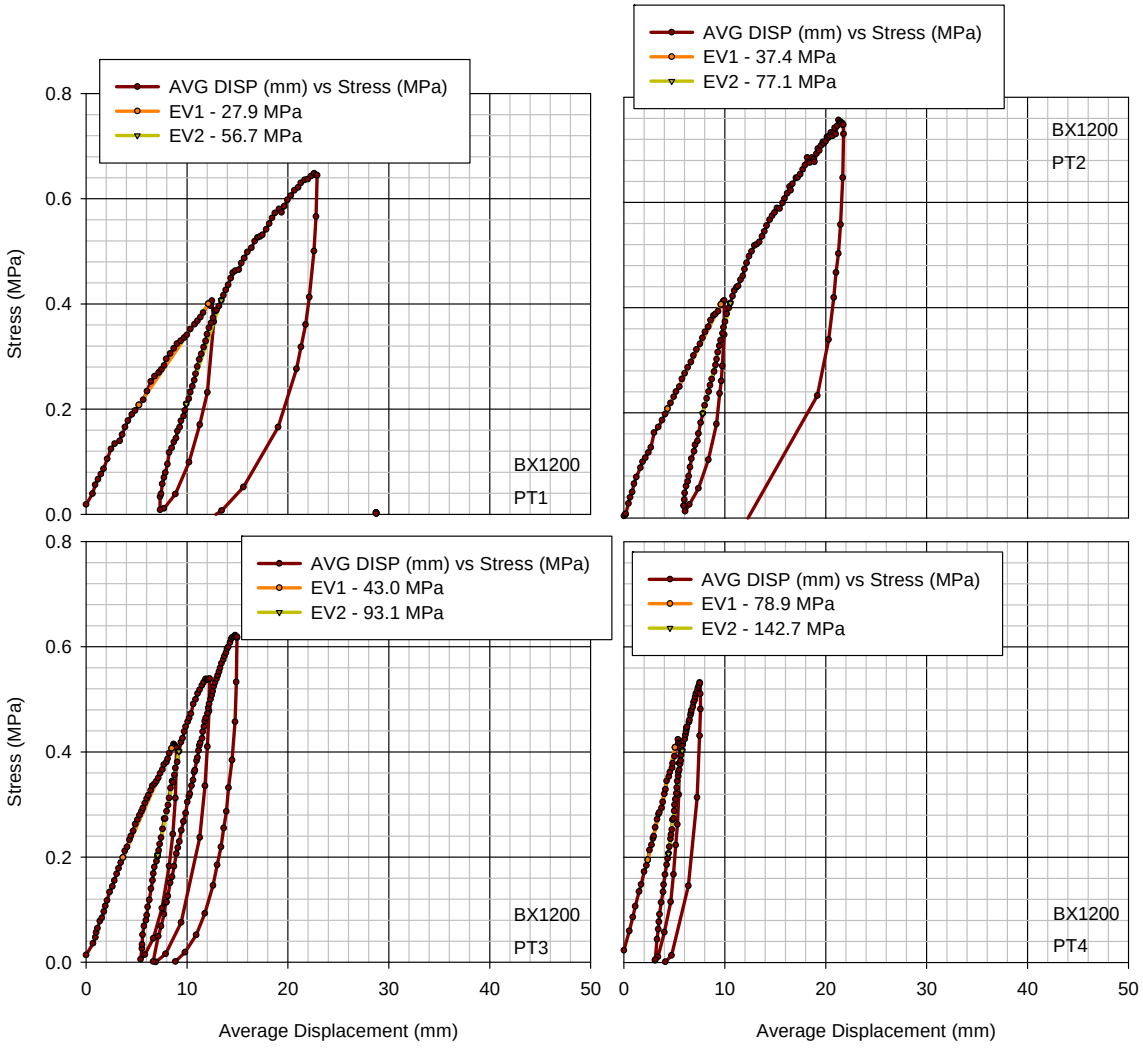

Figure 117. Plate load test results for BX1200 section – subbase 2

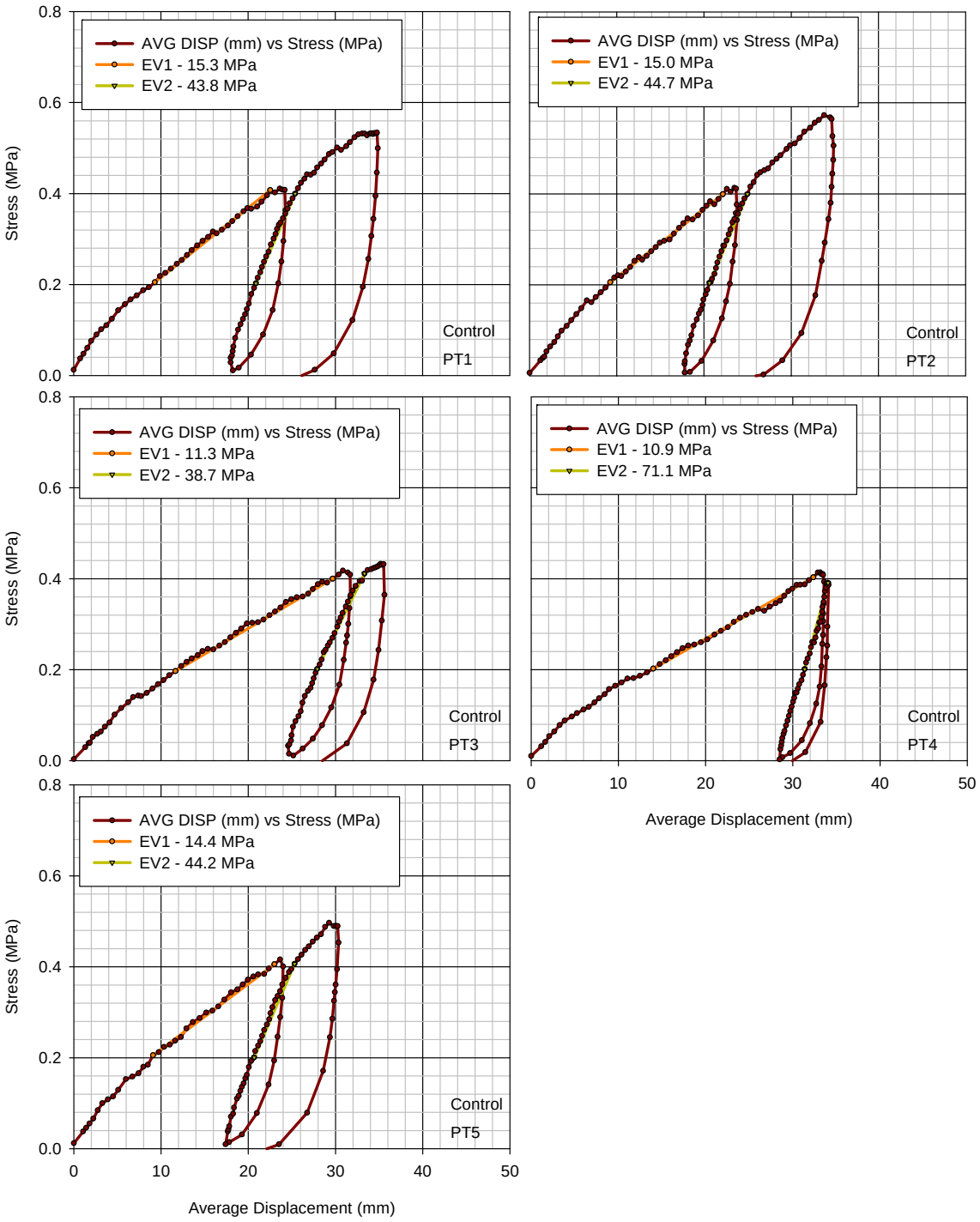

Figure 118. Plate load test results for control section – subbase 1

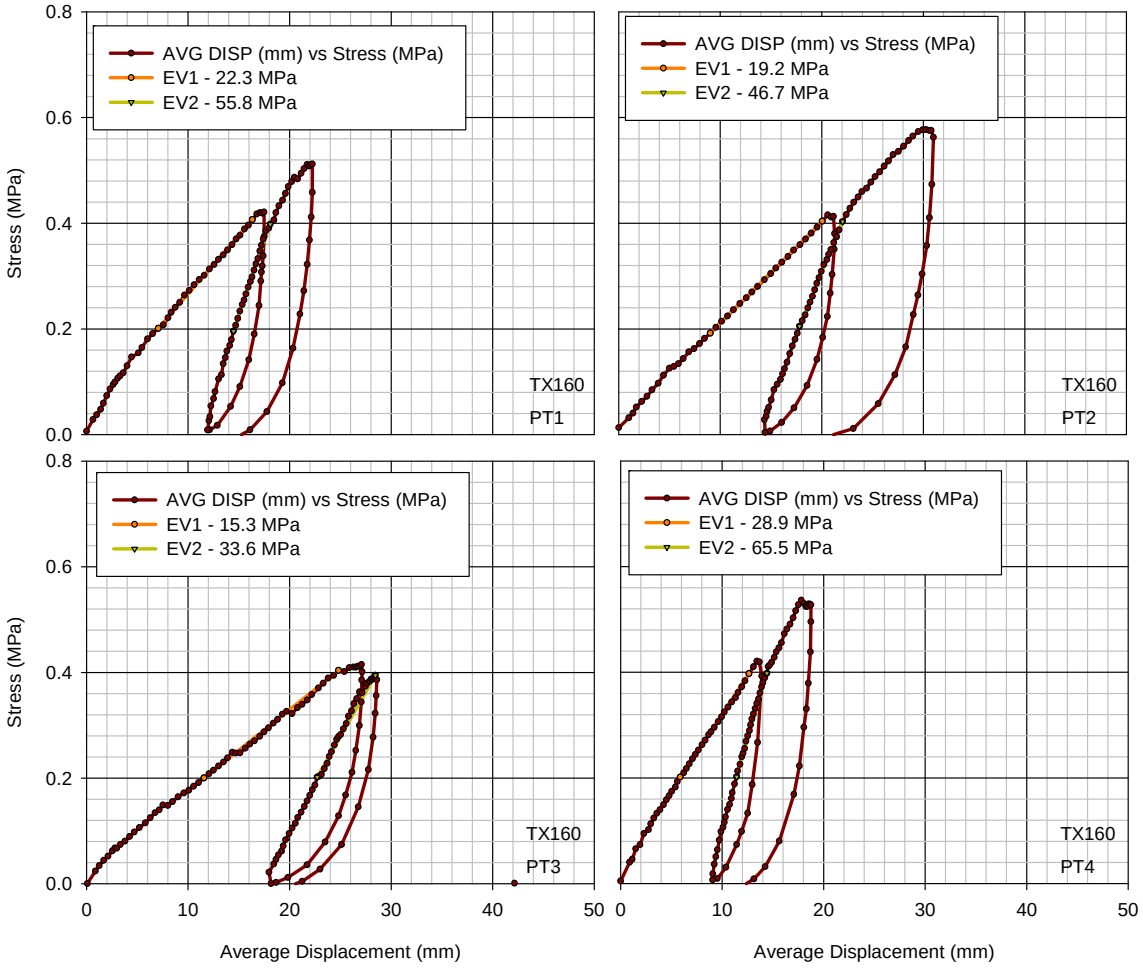

Figure 119. Plate load test results for TX160 section – subbase 1

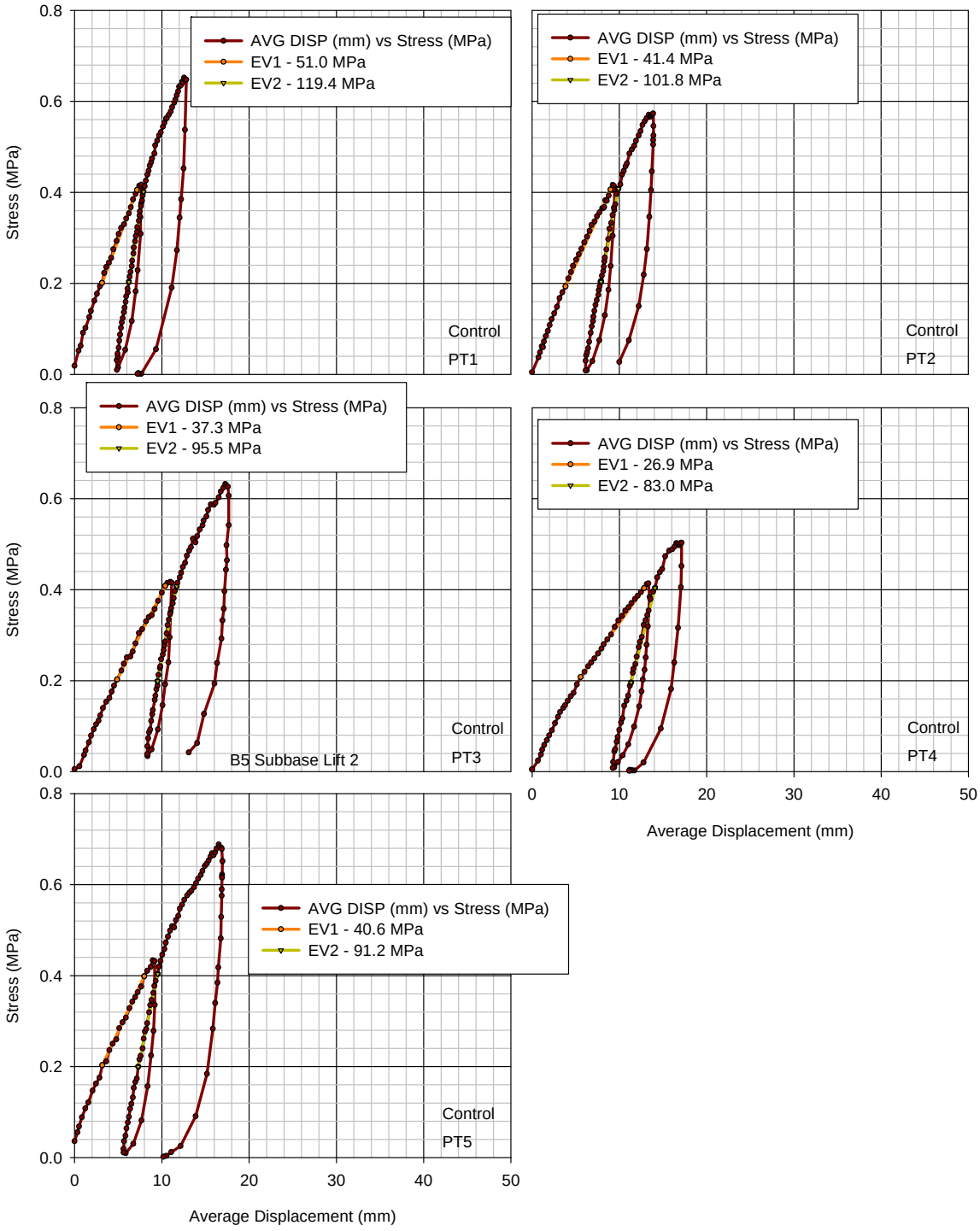

Figure 120. Plate load test results for control section – subbase 2

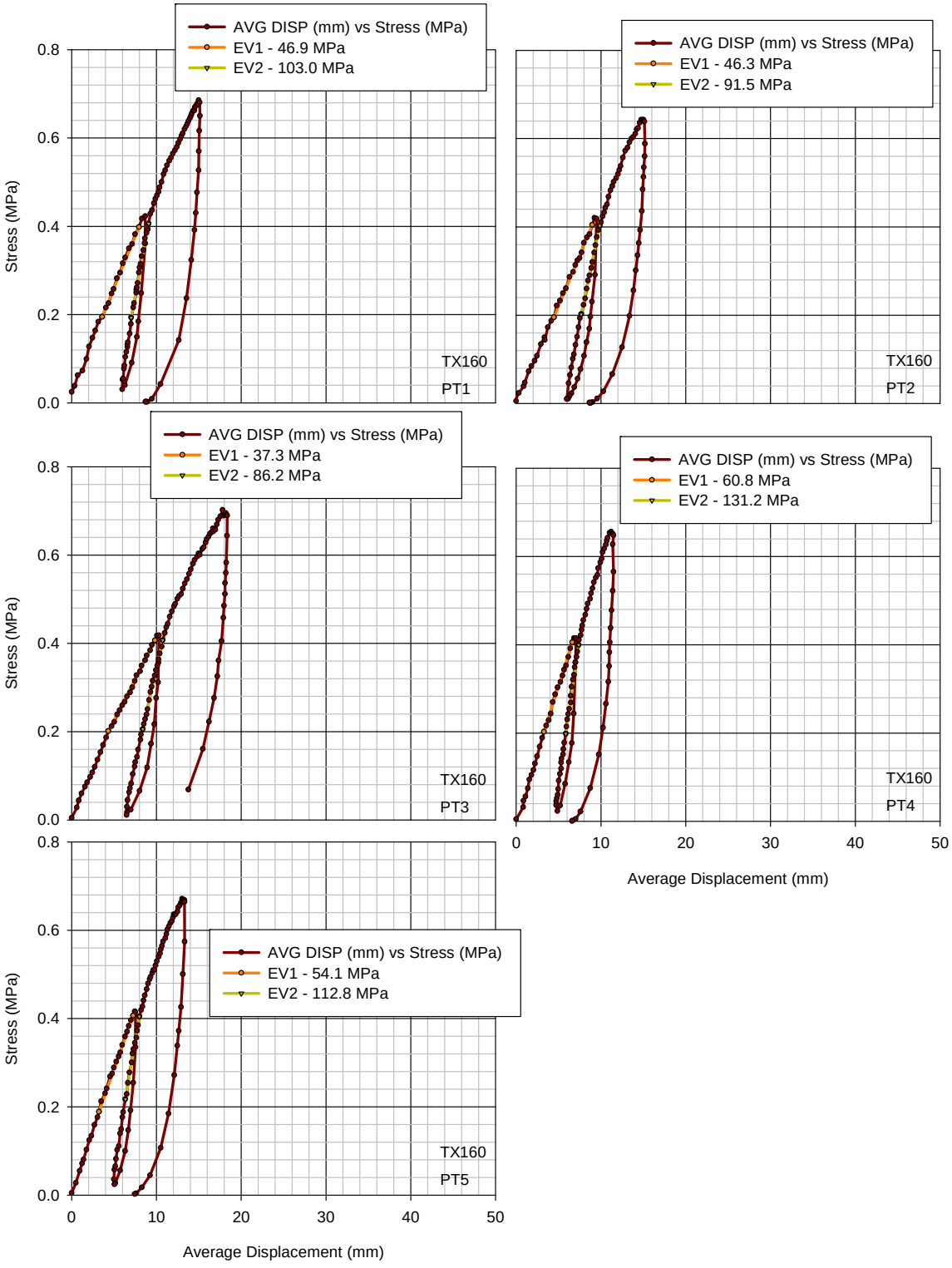

Figure 121. Plate load test results for TX160 section – subbase 2

Table 24. Summary of plate load tests results

Sections	Points	Subgrade		Subbase 1		Subbase 2	
		E_{V1} (MPa)	E_{V2} (MPa)	E_{V1} (MPa)	E_{V2} (MPa)	E_{V1} (MPa)	E_{V2} (MPa)
W-PP-GT	1	—	—	—	—	71.7	137.8
	2	—	—	19.4	56.9	54.4	120.3
	3	—	—	17.5	50.8	61.1	123.9
	4	—	—	10.4	31.5	31.2	65.7
	5	—	—	—	—	25.6	57.4
BX1200	1	—	—	—	—	27.9	56.7
	2	—	—	—	—	37.4	77.1
	3	—	—	—	—	43.0	93.1
	4	—	—	—	—	78.9	142.7
Control	1	6.4	19.1	15.3	43.8	51.0	119.4
	2	3.6	12.2	15.0	44.7	41.4	101.8
	3	—	—	11.3	38.7	37.3	95.5
	4	—	—	10.9	71.1	26.9	83.0
	5	—	—	14.4	44.2	40.6	91.2
TX160	1	—	—	22.3	55.8	46.9	103.0
	2	—	—	19.2	46.7	46.3	91.5
	3	—	—	15.3	33.6	37.3	86.2
	4	—	—	28.9	65.5	60.8	131.2
	5	—	—	—	—	54.1	112.8

APPENDIX B. EARTH PRESSURE CELL DATA

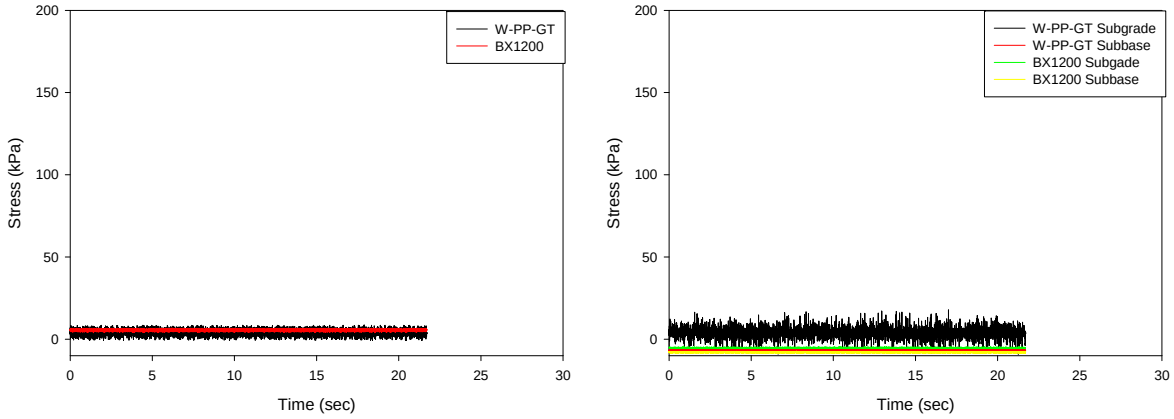

Figure 122. Earth pressure cell W-PP-GT and BX1200 sections layer 1 vertical (left) and horizontal (right) stress data at 0 passes

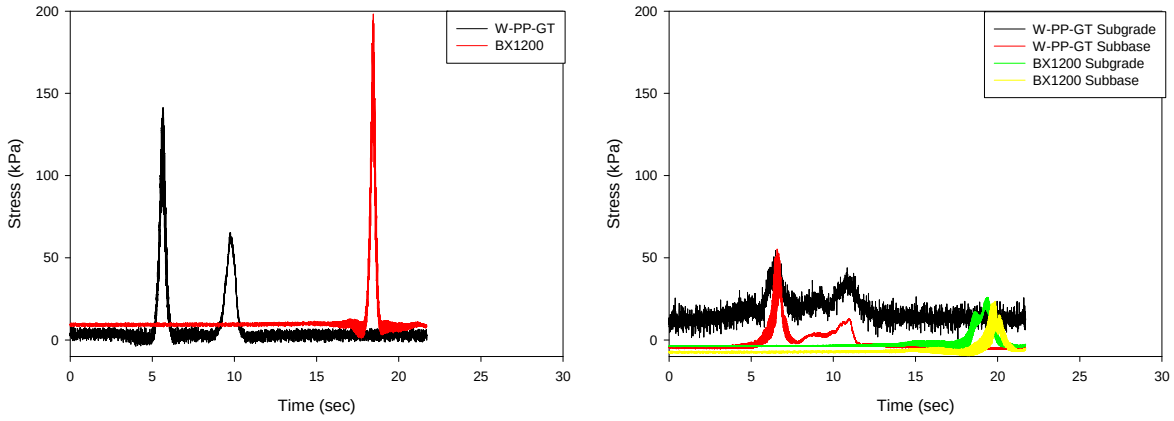

Figure 123. Earth pressure cell W-PP-GT and BX1200 sections layer 1 vertical (left) and horizontal (right) stress data Case roller pass 2

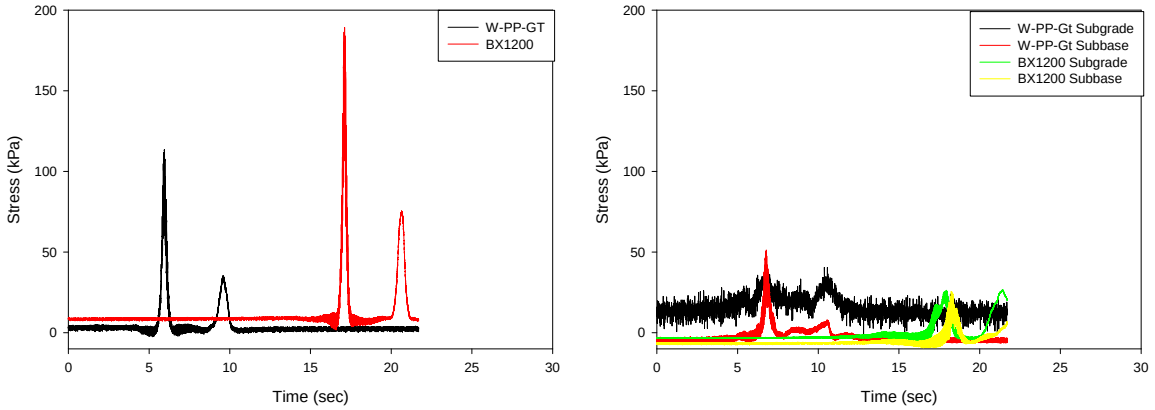

Figure 124. Earth pressure cell W-PP-GT and BX1200 sections layer 1 vertical (left) and horizontal (right) stress data Case roller pass 3

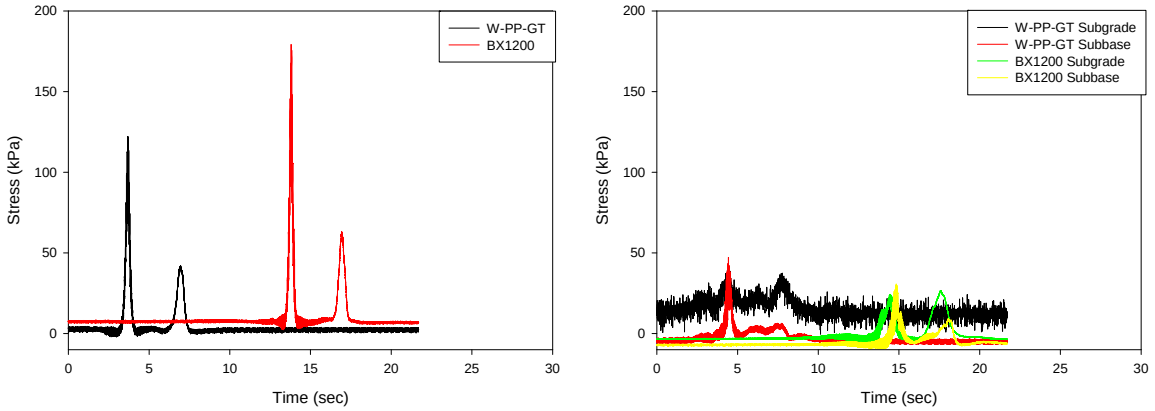

Figure 125. Earth pressure cell W-PP-GT and BX1200 sections layer 1 vertical (left) and horizontal (right) stress data Case roller pass 4

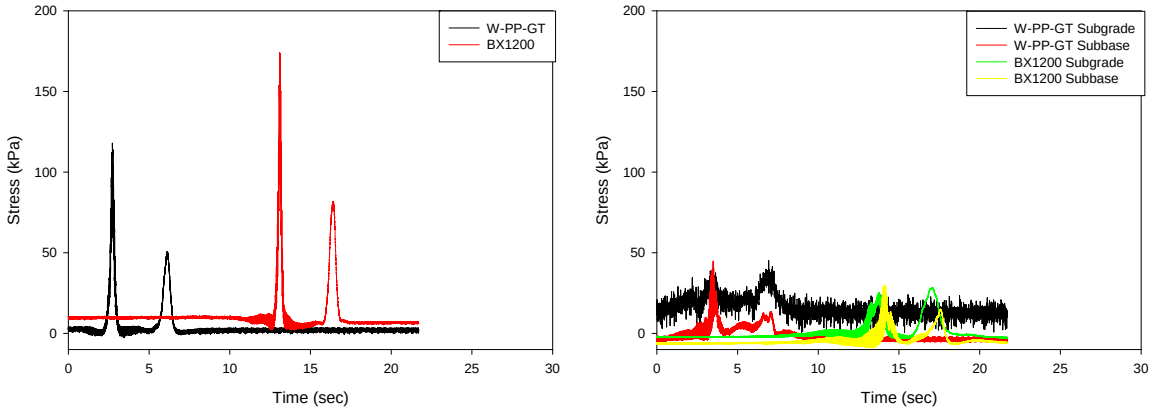

Figure 126. Earth pressure cell W-PP-GT and BX1200 sections layer 1 vertical (left) and horizontal (right) stress data Case roller pass

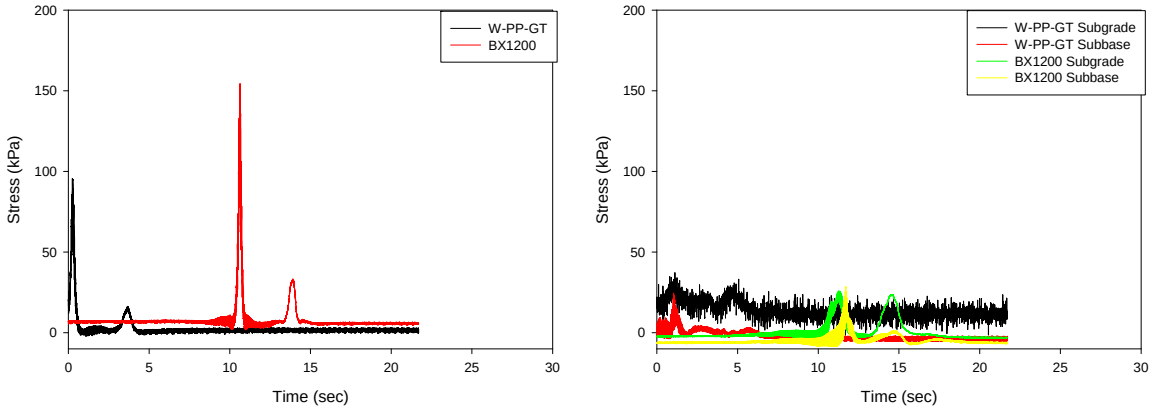

Figure 127. Earth pressure cell W-PP-GT and BX1200 sections layer 1 vertical (left) and horizontal (right) stress data Case roller 10

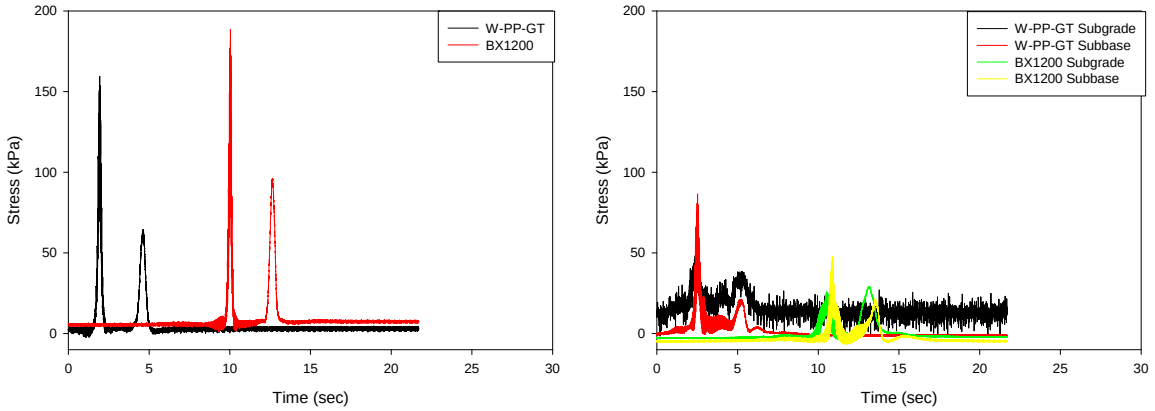

Figure 128. Earth pressure cell W-PP-GT and BX1200 sections layer 1 vertical (left) and horizontal (right) stress data Case roller 12

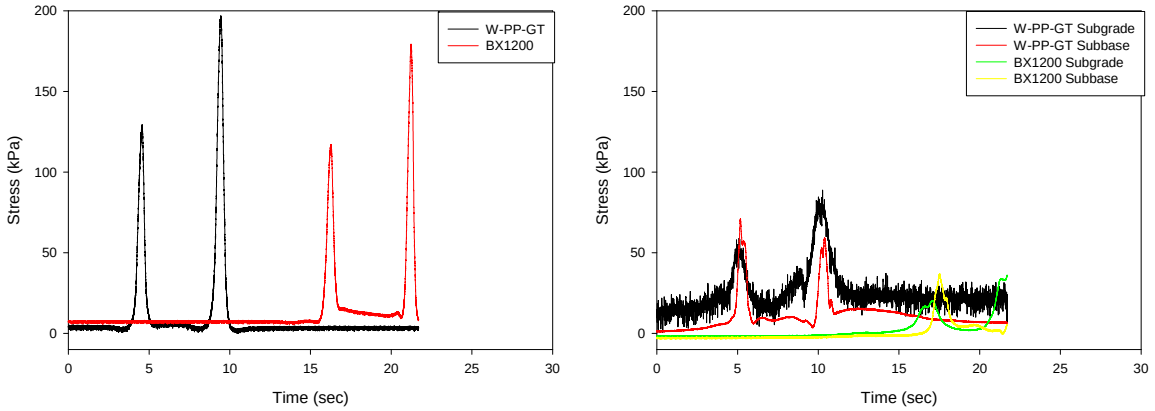

Figure 129. Earth pressure cell W-PP-GT and BX1200 sections layer 1 vertical (left) and horizontal (right) stress data truck traffic pass 1

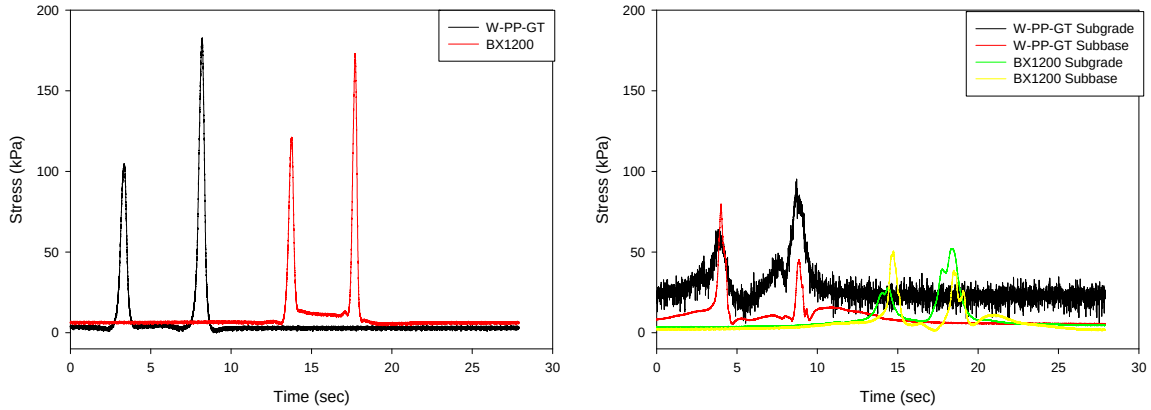

Figure 130. Earth pressure cell W-PP-GT and BX1200 sections layer 1 vertical (left) and horizontal (right) stress data truck traffic pass 2

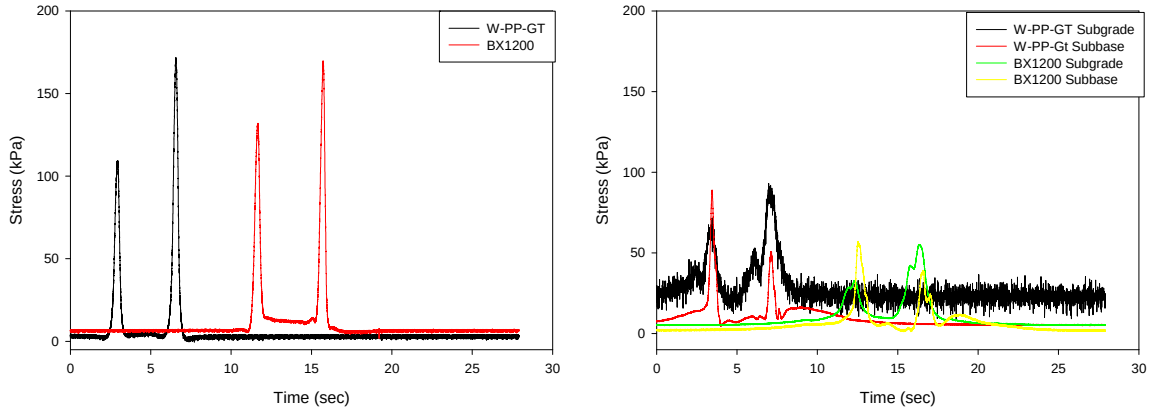

Figure 131. Earth pressure cell W-PP-GT and BX1200 sections layer 1 vertical (left) and horizontal (right) stress data truck traffic pass 3

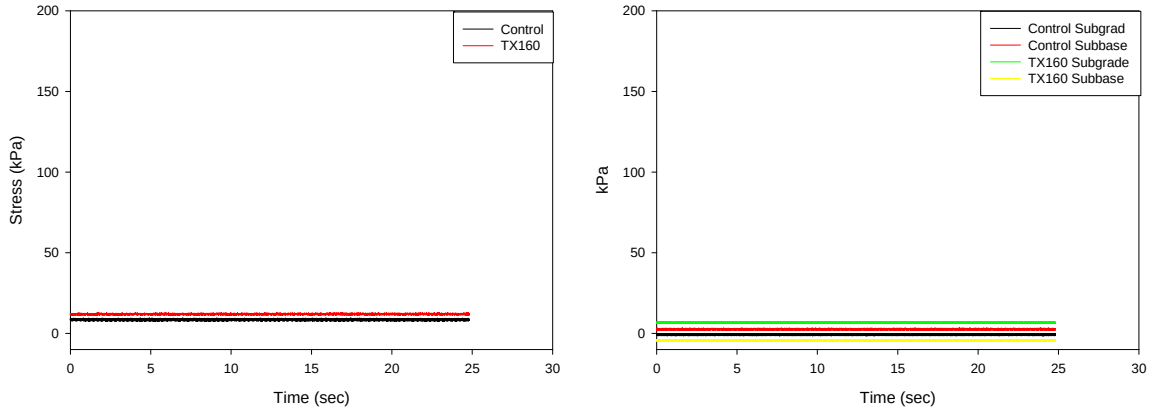

Figure 132. Earth pressure cell Control and TX160 sections layer 1 vertical (left) and horizontal (right) stress data pass 0

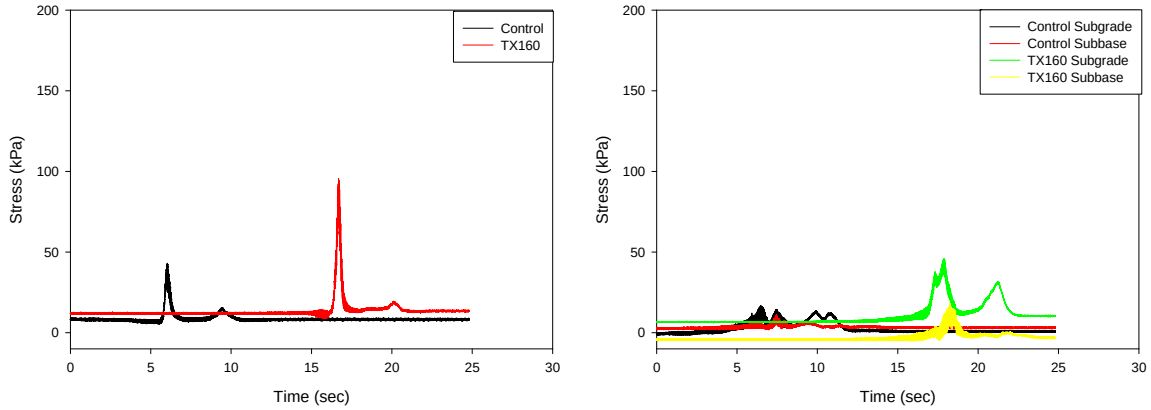

Figure 133. Earth pressure cell Control and TX160 sections layer 1 vertical (left) and horizontal (right) stress data Case roller pass 1

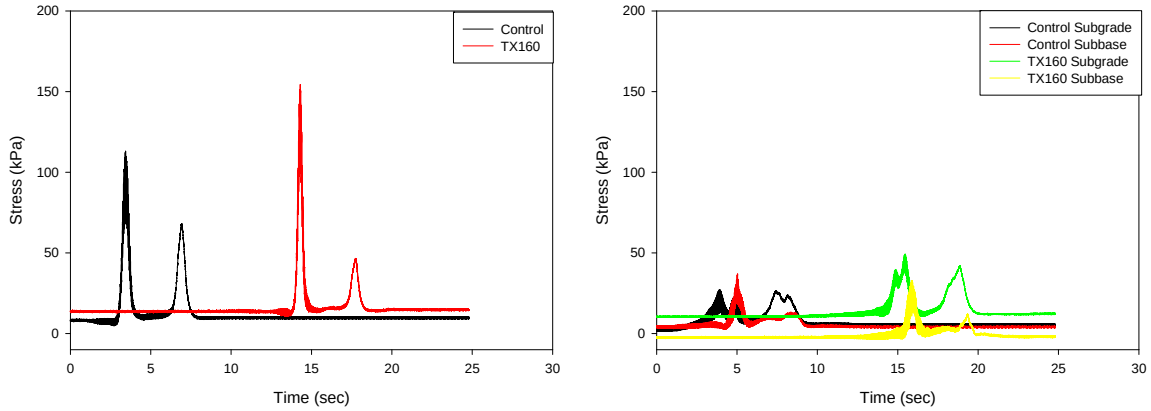

Figure 134. Earth pressure cell Control and TX160 sections layer 1 vertical (left) and horizontal (right) stress data Case roller pass 2

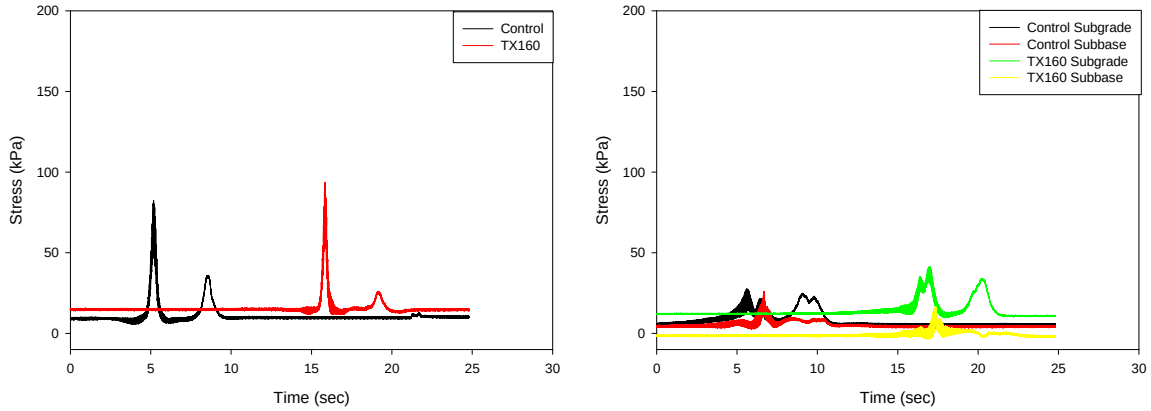

Figure 135. Earth pressure cell Control and TX160 sections layer 1 vertical (left) and horizontal (right) stress data Case roller pass 3

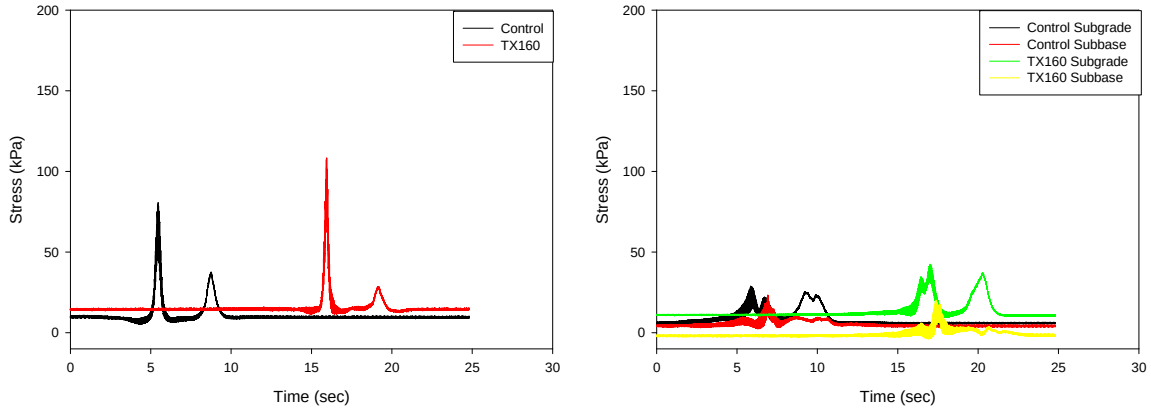

Figure 136. Earth pressure cell Control and TX160 sections layer 1 vertical (left) and horizontal (right) stress data Case roller pass 4

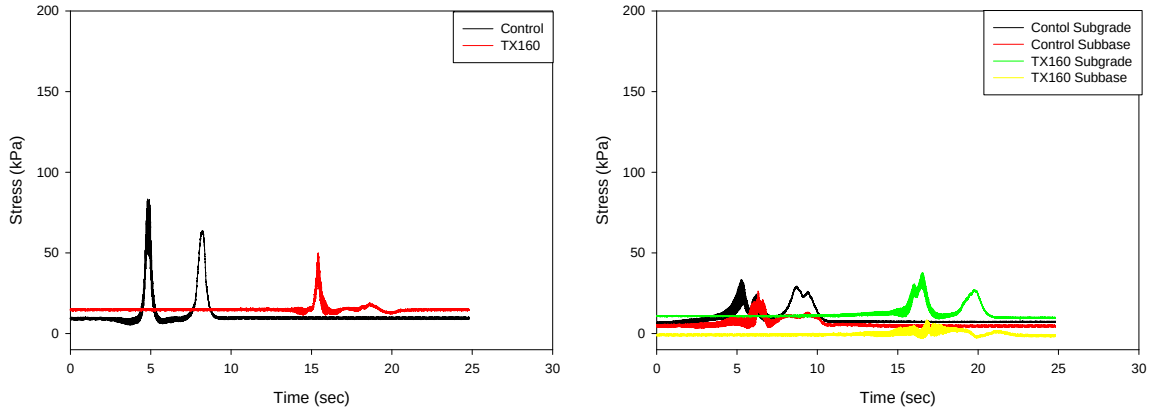

Figure 137. Earth pressure cell Control and TX160 sections layer 1 vertical (left) and horizontal (right) stress data Case roller pass 5

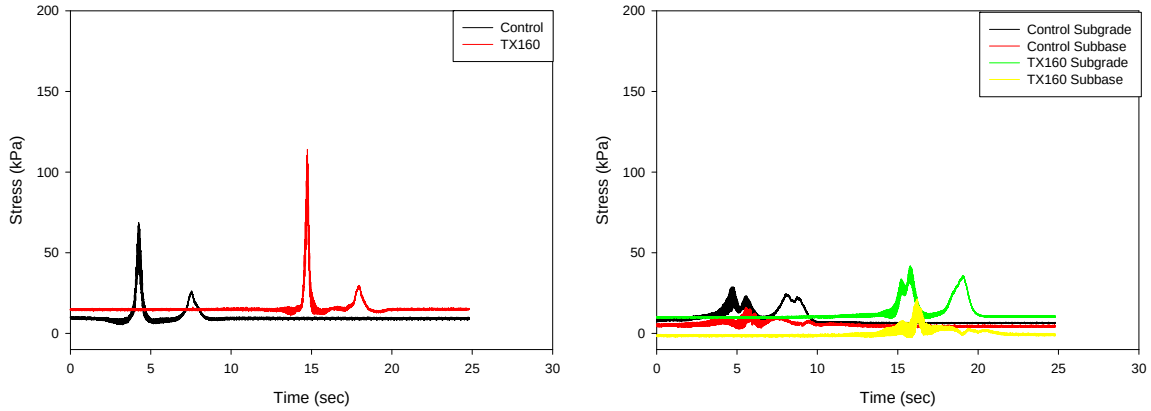

Figure 138. Earth pressure cell Control and TX160 sections layer 1 vertical (left) and horizontal (right) stress data Case roller pass 6

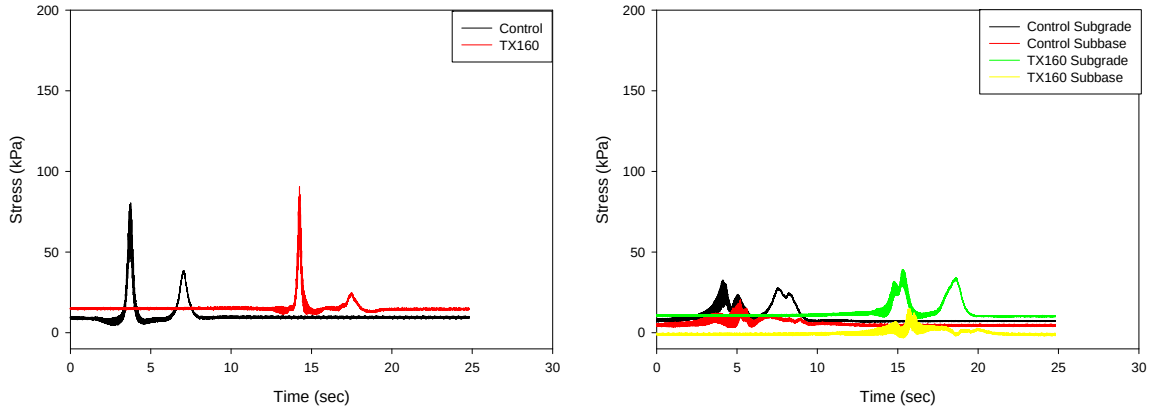

Figure 139. Earth pressure cell Control and TX160 sections layer 1 vertical (left) and horizontal (right) stress data Case roller pass 7

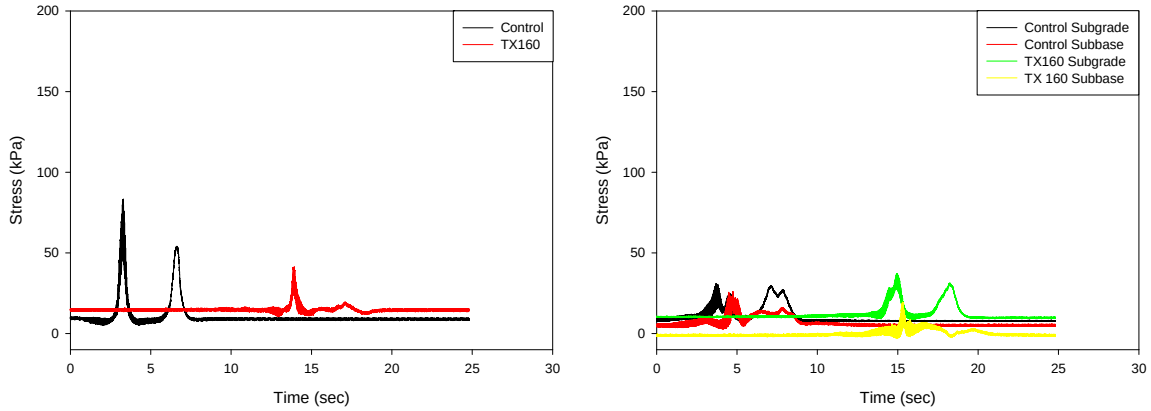

Figure 140. Earth pressure cell Control and TX160 sections layer 1 vertical (left) and horizontal (right) stress data Case roller pass 8

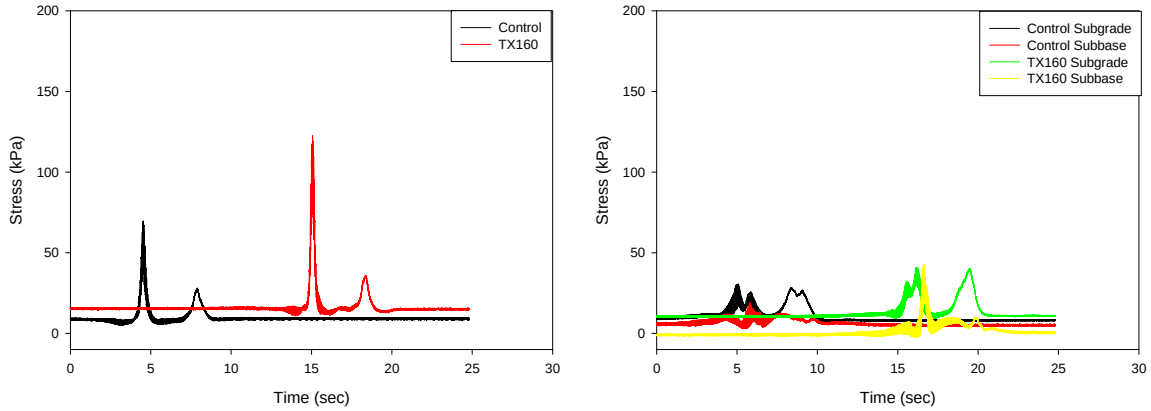

Figure 141. Earth pressure cell Control and TX160 sections layer 1 vertical (left) and horizontal (right) stress data Case roller pass 10

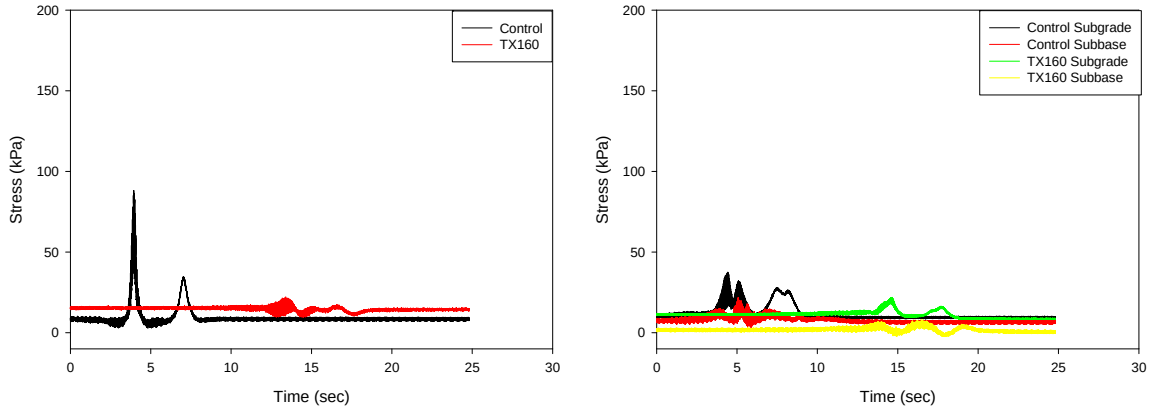

Figure 142. Earth pressure cell Control and TX160 sections layer 1 vertical (left) and horizontal (right) stress data CAT roller pass 12

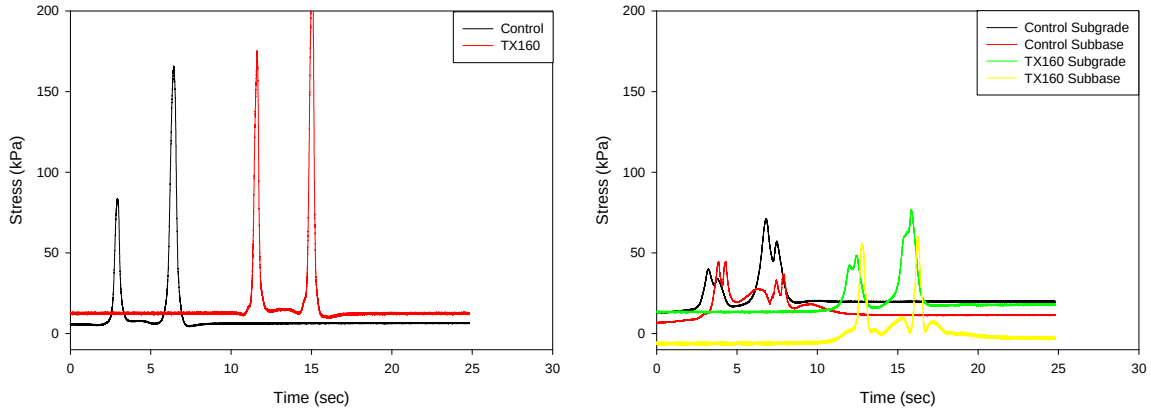

Figure 143. Earth pressure cell Control and TX160 sections layer 1 vertical (left) and horizontal (right) stress data truck traffic pass 1

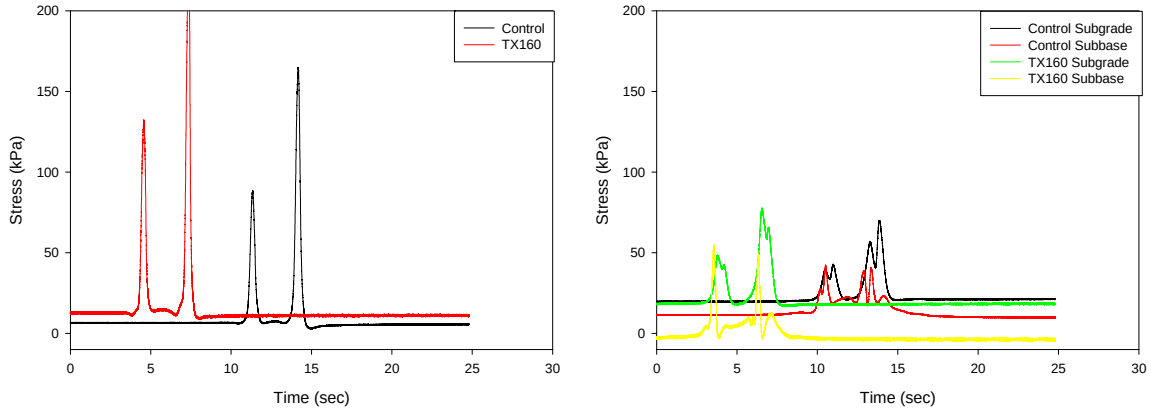

Figure 144. Earth pressure cell Control and TX160 sections layer 1 vertical (left) and horizontal (right) stress data truck traffic pass 2

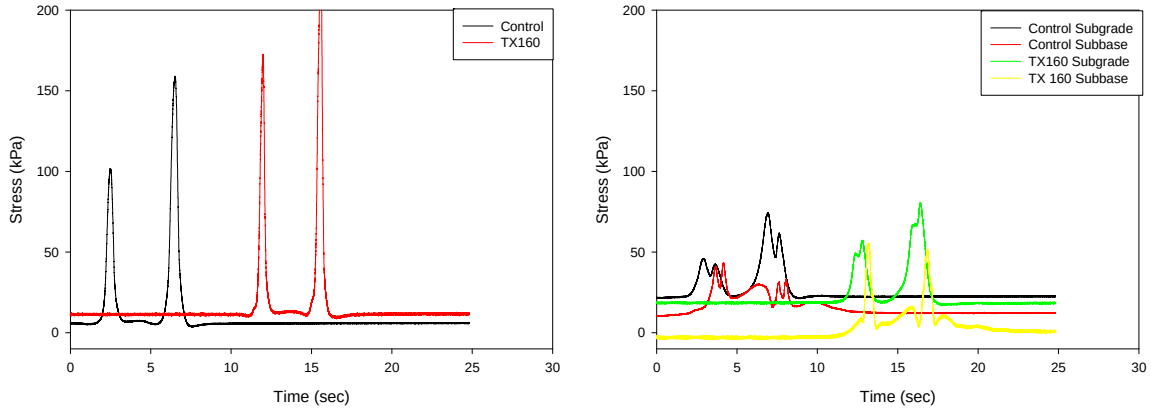

Figure 145. Earth pressure cell Control and TX160 sections layer 1 vertical (left) and horizontal (right) stress data truck traffic pass 3

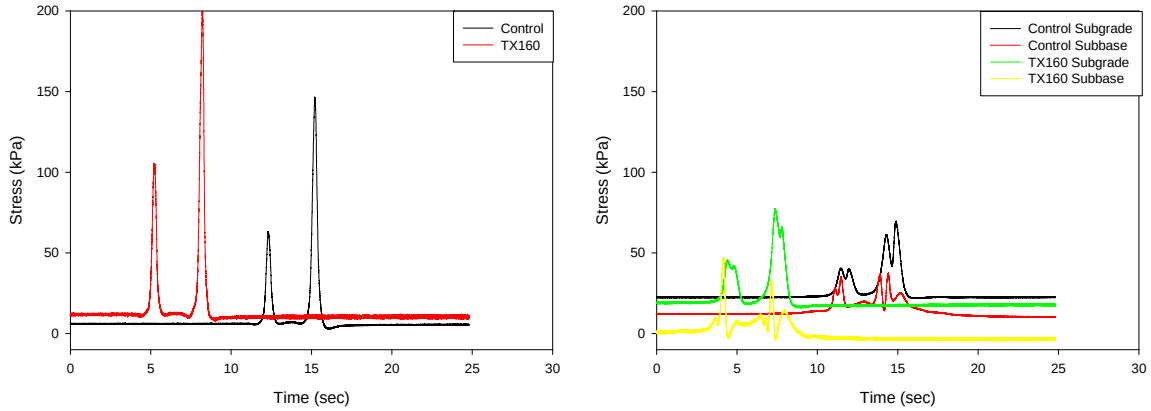

Figure 146. Earth pressure cell Control and TX160 sections layer 1 vertical (left) and horizontal (right) stress data truck traffic pass 4

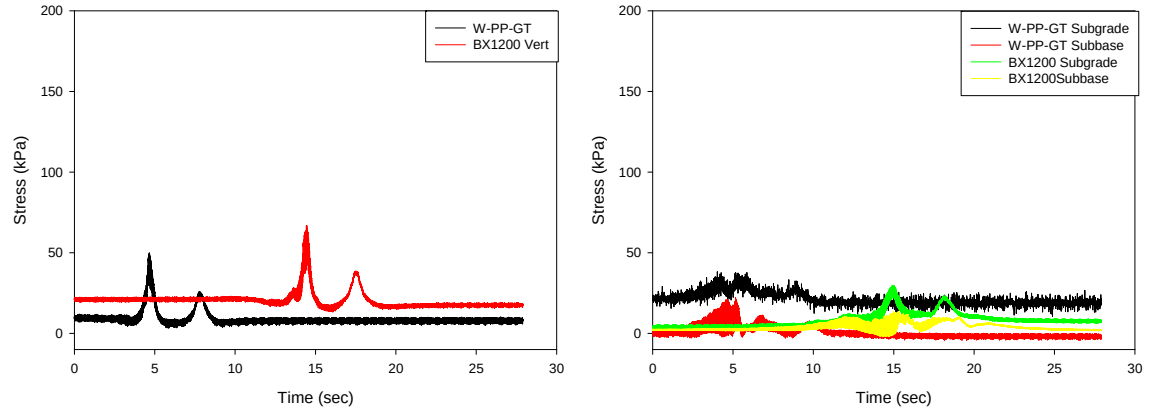

Figure 147. Earth pressure cell W-PP-GT and BX1200 sections layer 2 vertical (left) and horizontal (right) stress data Case roller pass 1

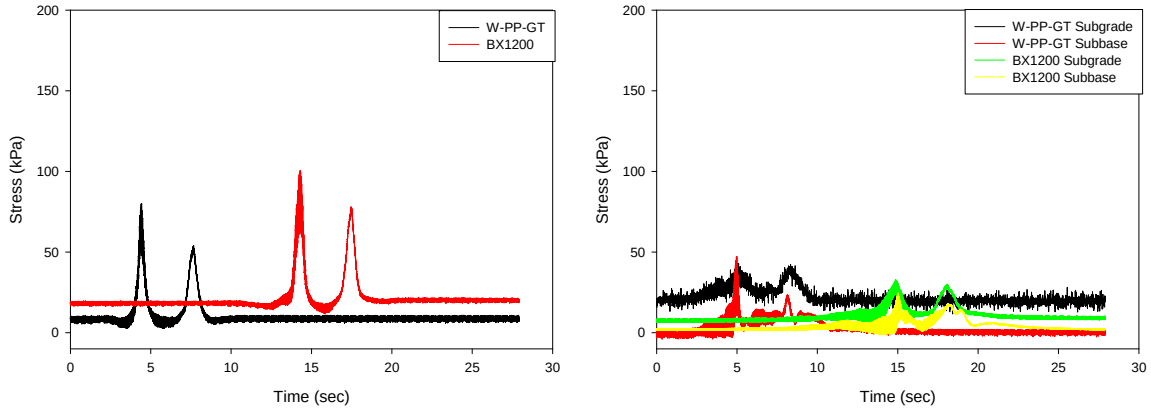

Figure 148. Earth pressure cell W-PP-GT and BX1200 sections layer 2 vertical (left) and horizontal (right) stress data Case roller pass 2

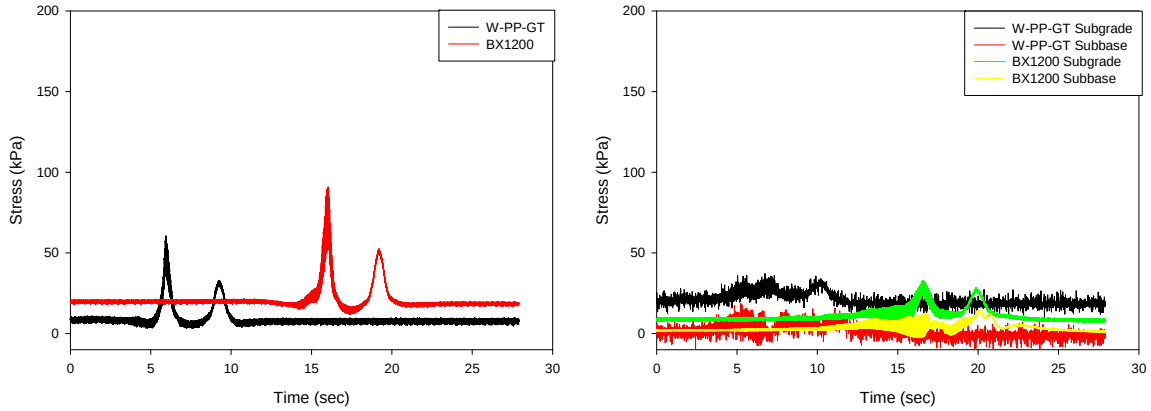

Figure 149. Earth pressure cell W-PP-GT and BX1200 sections layer 2 vertical (left) and horizontal (right) stress data Case roller pass 3

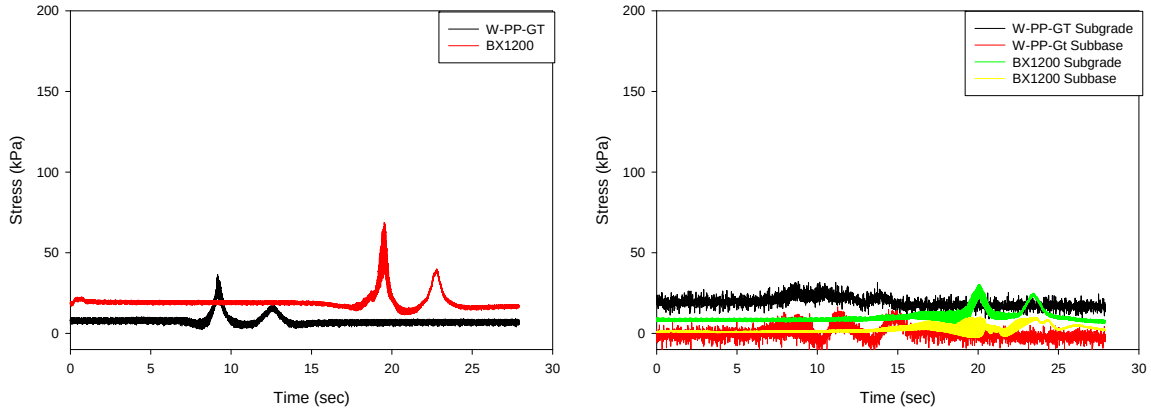

Figure 150. Earth pressure cell W-PP-GT and BX1200 sections layer 2 vertical (left) and horizontal (right) stress data Case roller pass 4

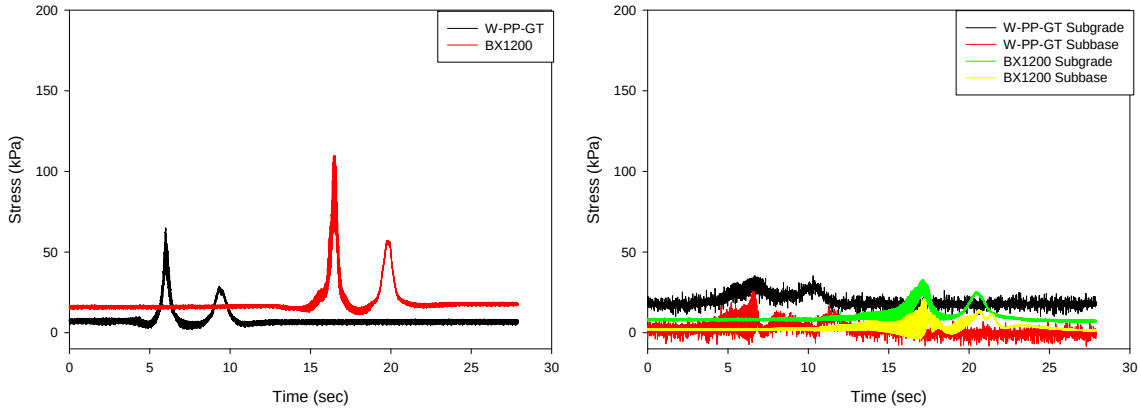

Figure 151. Earth pressure cell W-PP-GT and BX1200 sections layer 2 vertical (left) and horizontal (right) stress data Case roller pass 12

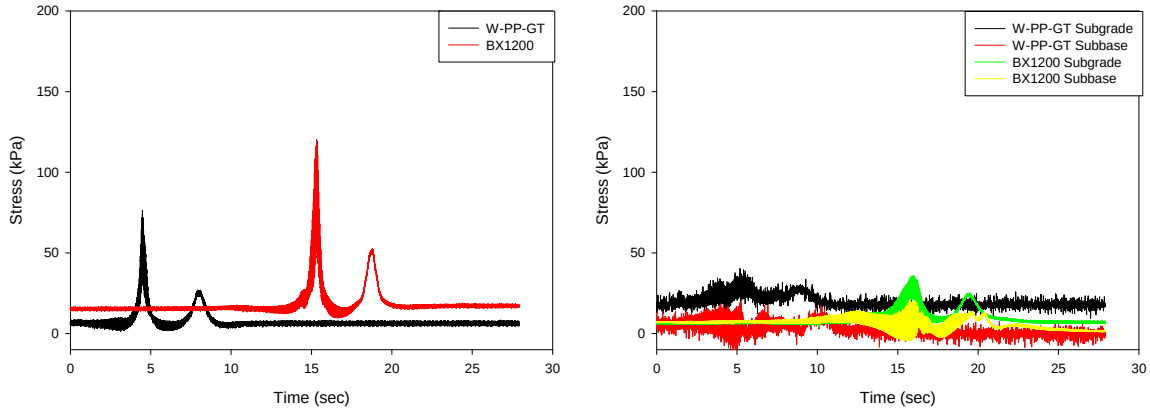

Figure 152. Earth pressure cell W-PP-GT and BX1200 sections layer 2 vertical (left) and horizontal (right) stress data Case roller high amplitude pass 13

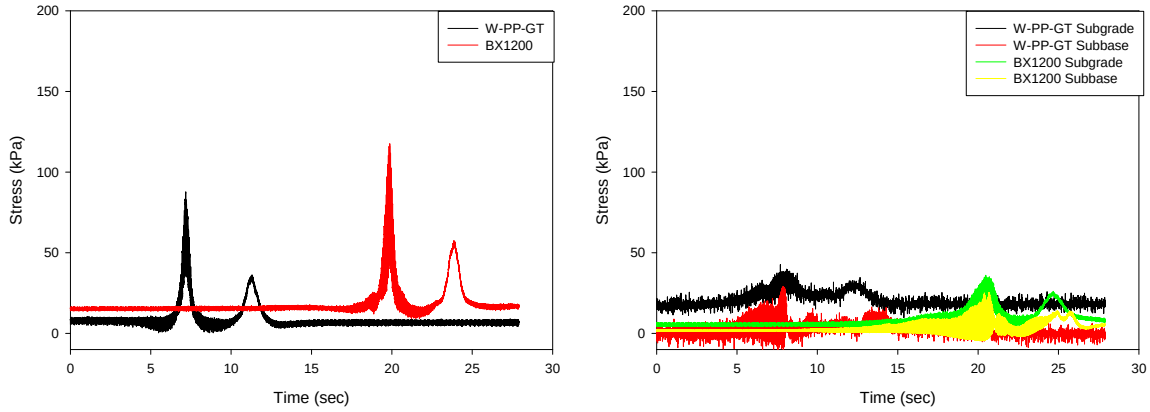

Figure 153. Earth pressure cell W-PP-GT and BX1200 sections layer 2 vertical (left) and horizontal (right) stress data Case roller high amplitude pass 14

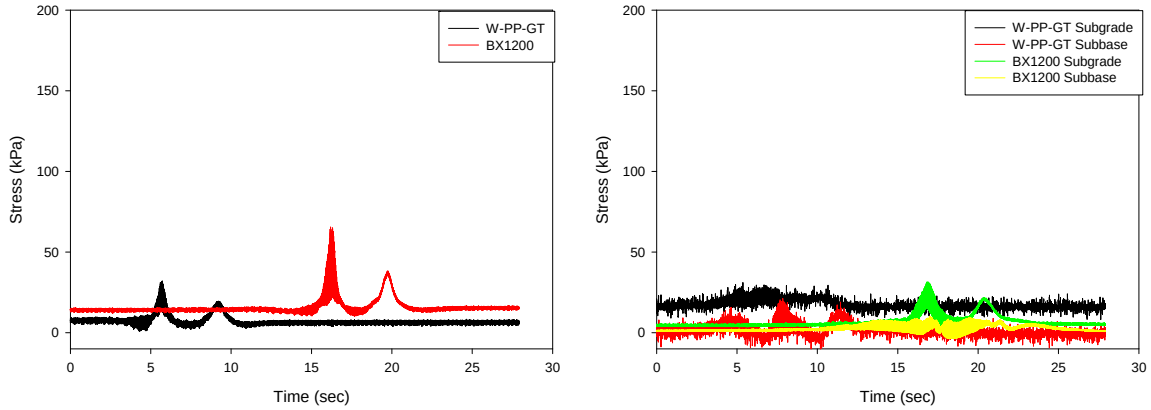

Figure 154. Earth pressure cell W-PP-GT and BX1200 sections layer 2 vertical (left) and horizontal (right) stress data CAT roller pass 16

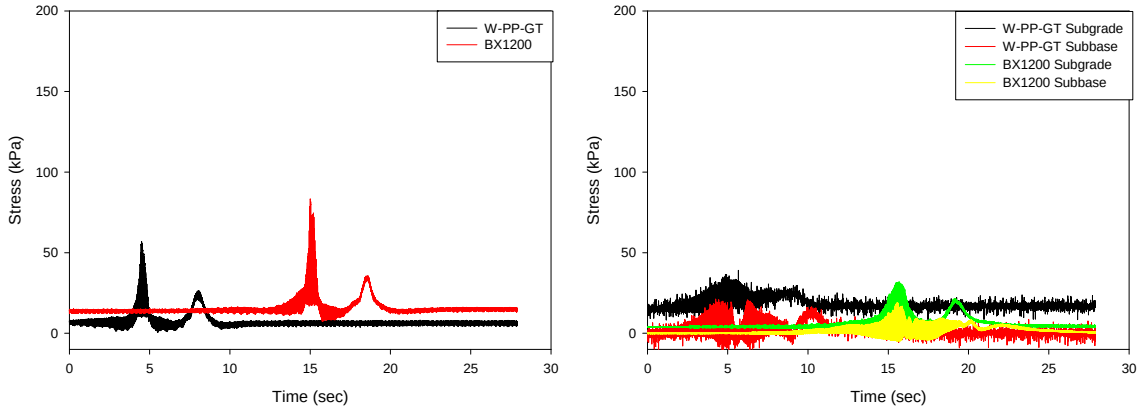

Figure 155. Earth pressure cell W-PP-GT and BX1200 sections layer 2 vertical (left) and horizontal (right) stress data CAT roller high amplitude pass 17

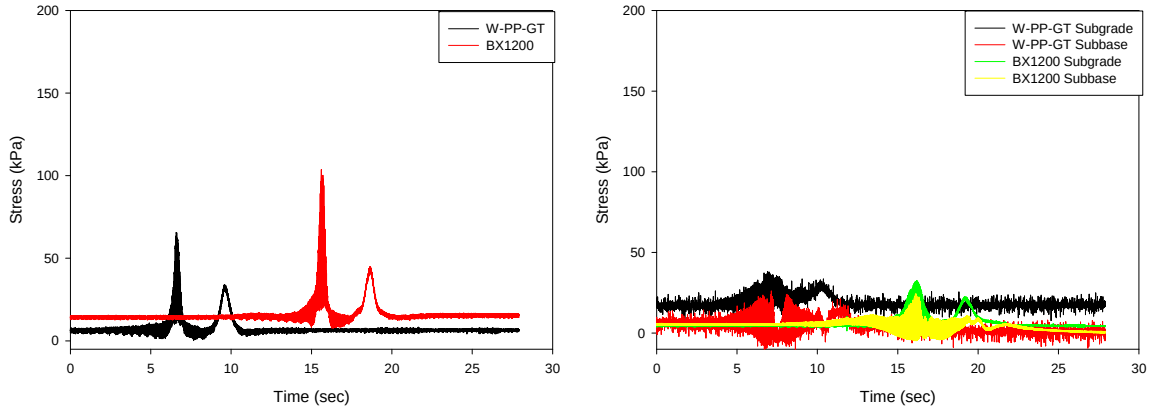

Figure 156. Earth pressure cell W-PP-GT and BX1200 sections layer 2 vertical (left) and horizontal (right) stress data CAT roller high amplitude pass 18

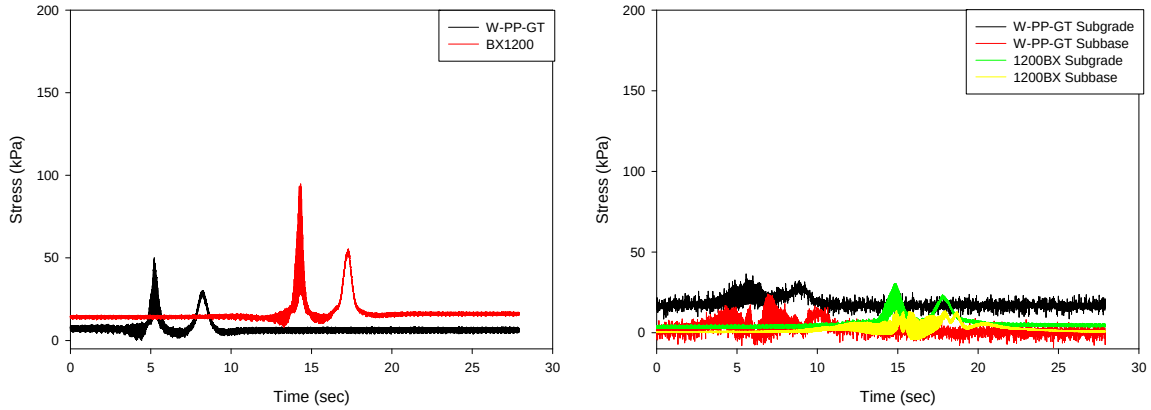

Figure 157. Earth pressure cell W-PP-GT and BX1200 sections layer 2 vertical (left) and horizontal (right) stress data CAT roller pass 19

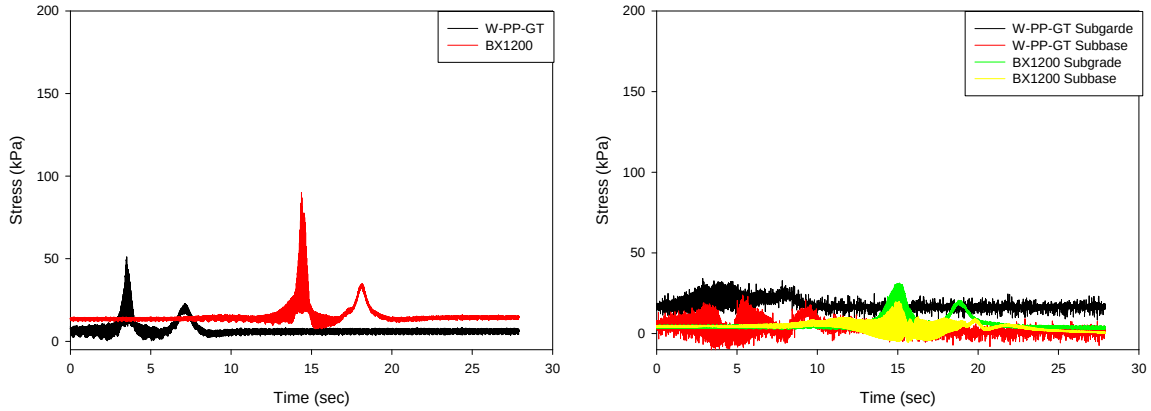

Figure 158. Earth pressure cell W-PP-GT and BX1200 sections layer 2 vertical (left) and horizontal (right) stress data CAT roller high amplitude pass 20

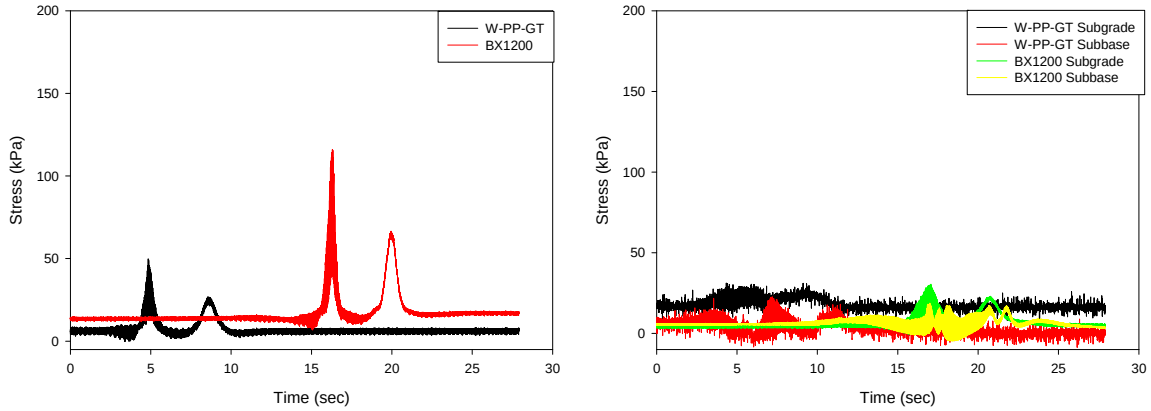

Figure 159. Earth pressure cell W-PP-GT and BX1200 sections layer 2 vertical (left) and horizontal (right) stress data CAT roller pass 21

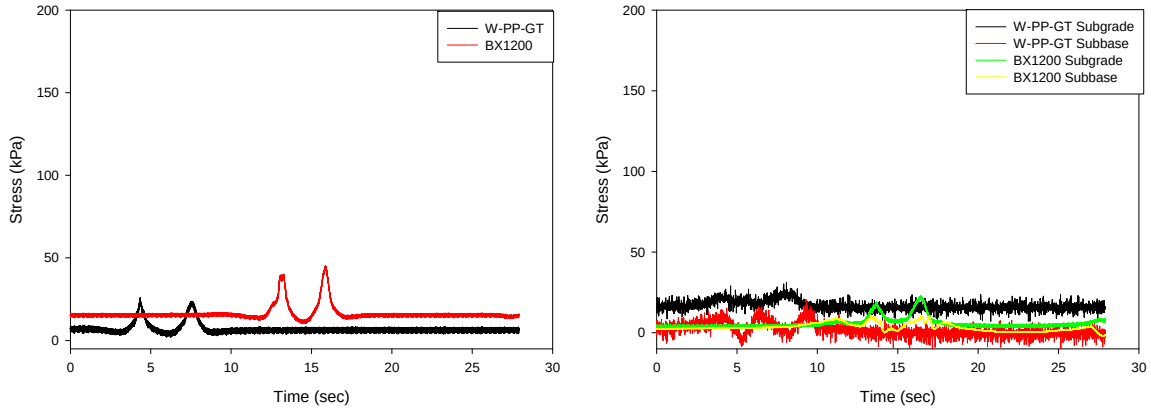

Figure 160. Earth pressure cell W-PP-GT and BX1200 sections layer 2 vertical (left) and horizontal (right) stress data CAT roller static pass 22

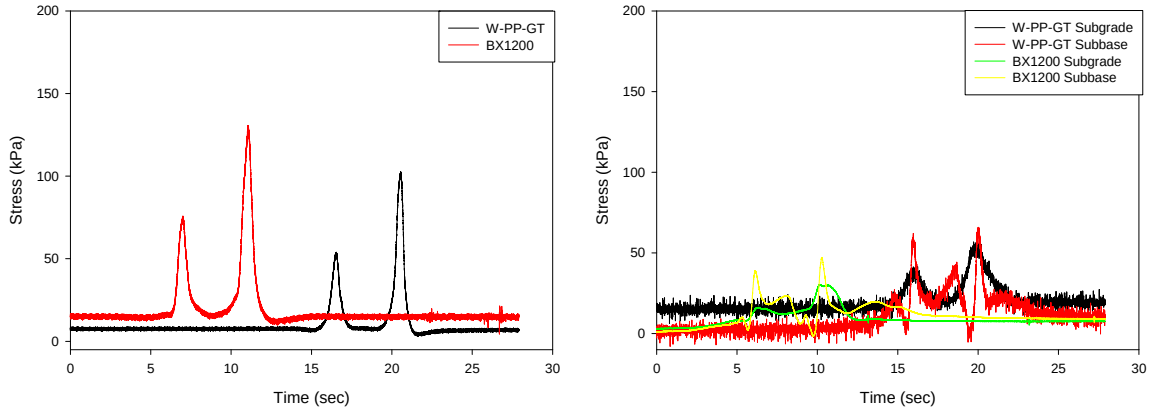

Figure 161. Earth pressure cell W-PP-GT and BX1200 sections layer 2 vertical (left) and horizontal (right) stress data truck traffic pass 1

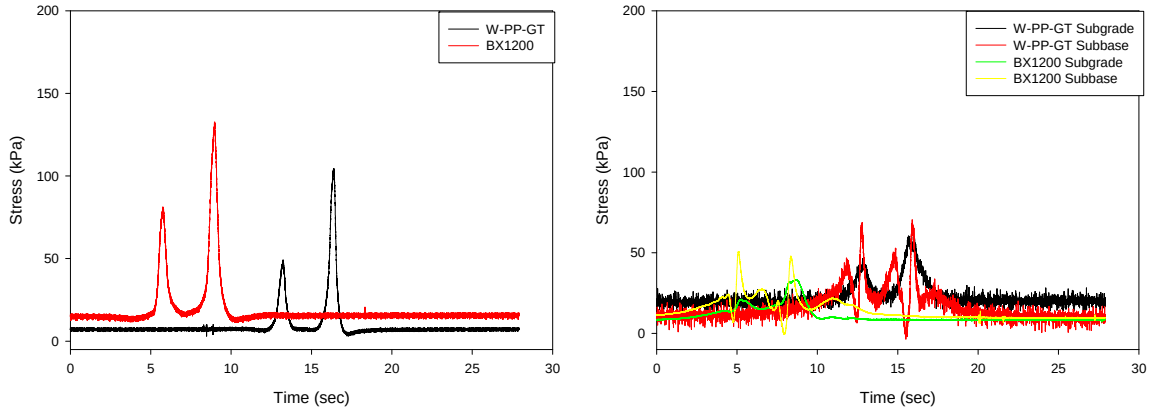

Figure 162. Earth pressure cell W-PP-GT and BX1200 sections layer 2 vertical (left) and horizontal (right) stress data truck traffic pass 2

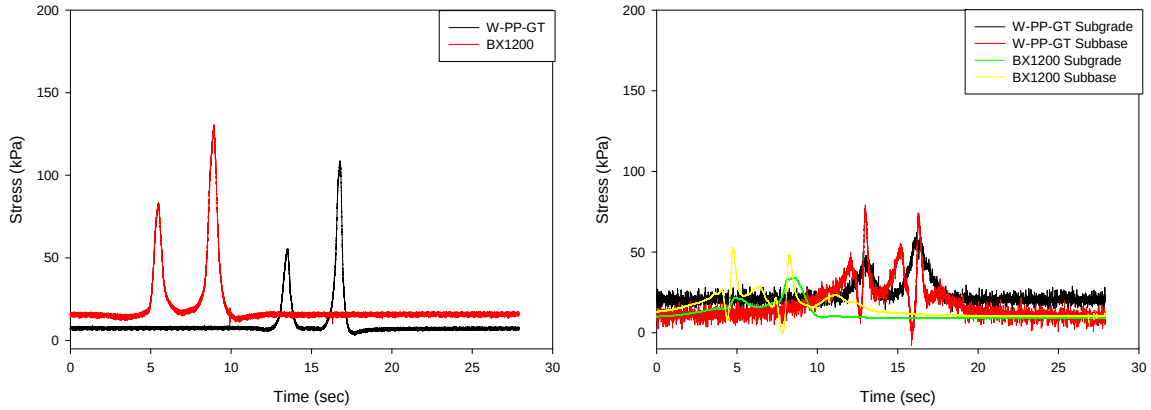

Figure 163. Earth pressure cell W-PP-GT and BX1200 sections layer 2 vertical (left) and horizontal (right) stress data truck traffic pass 3

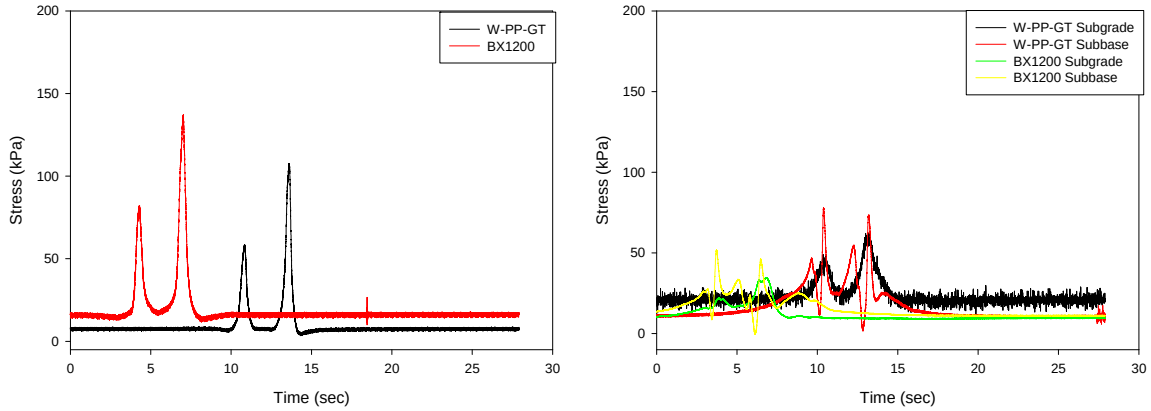

Figure 164. Earth pressure cell W-PP-GT and BX1200 sections layer 2 vertical (left) and horizontal (right) stress data truck traffic pass 4

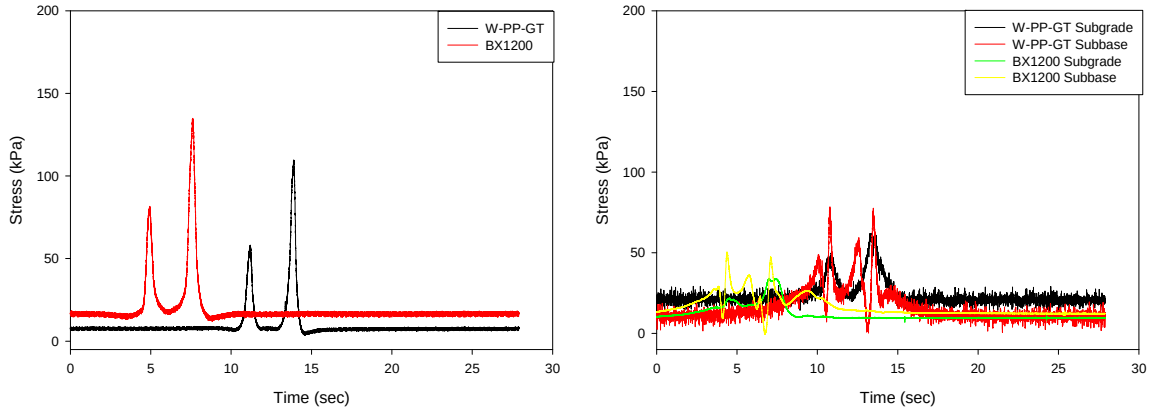

Figure 165. Earth pressure cell W-PP-GT and BX1200 sections layer 2 vertical (left) and horizontal (right) stress data truck traffic pass 5

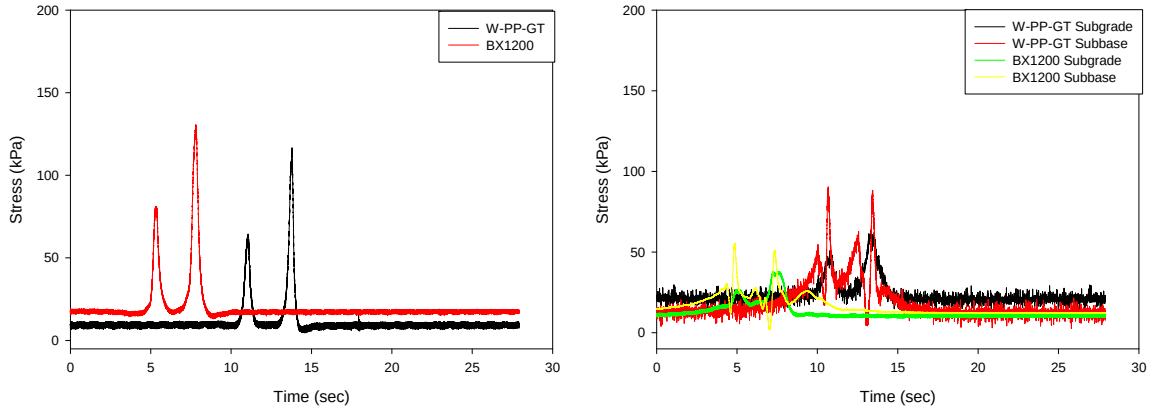

Figure 166. Earth pressure cell W-PP-GT and BX1200 sections layer 2 vertical (left) and horizontal (right) stress data truck traffic pass 10

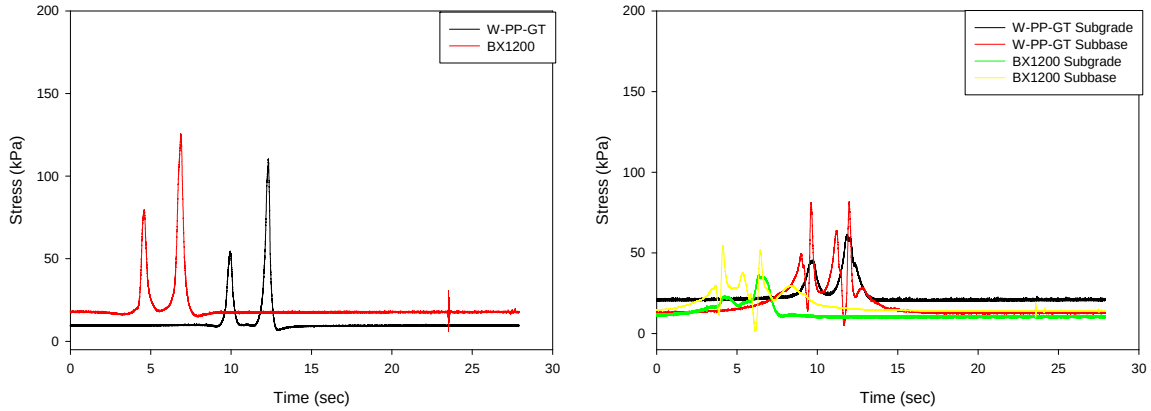

Figure 167. Earth pressure cell W-PP-GT and BX1200 sections layer 2 vertical (left) and horizontal (right) stress data truck traffic pass 15

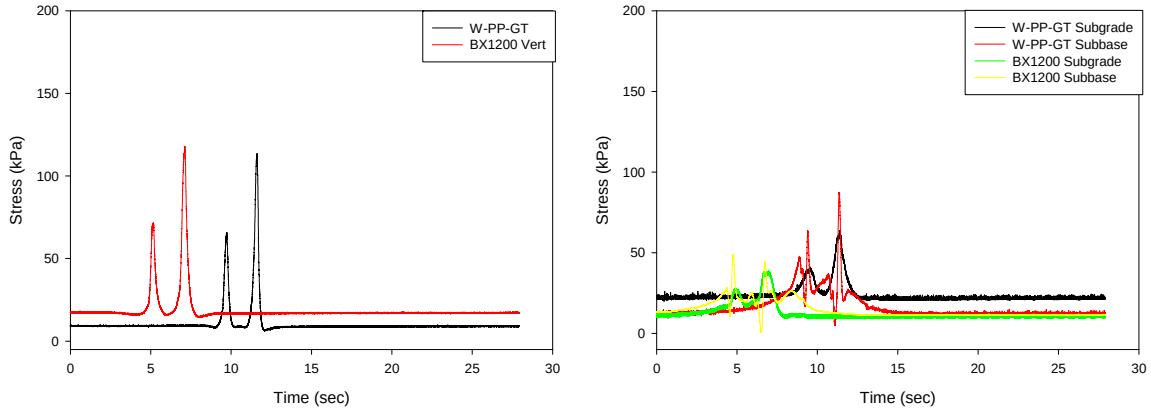

Figure 168. Earth pressure cell W-PP-GT and BX1200 sections layer 2 vertical (left) and horizontal (right) stress data truck traffic pass 35

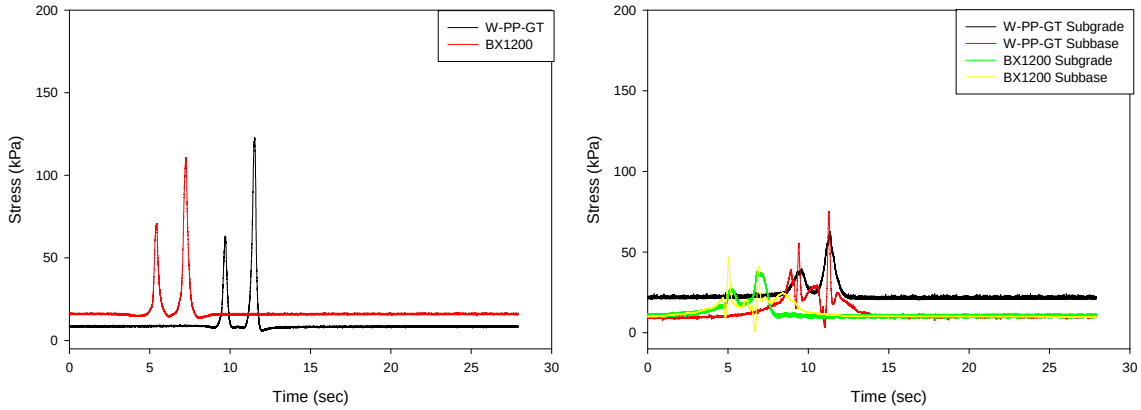

Figure 169. Earth pressure cell W-PP-GT and BX1200 sections layer 2 vertical (left) and horizontal (right) stress data truck traffic pass 45

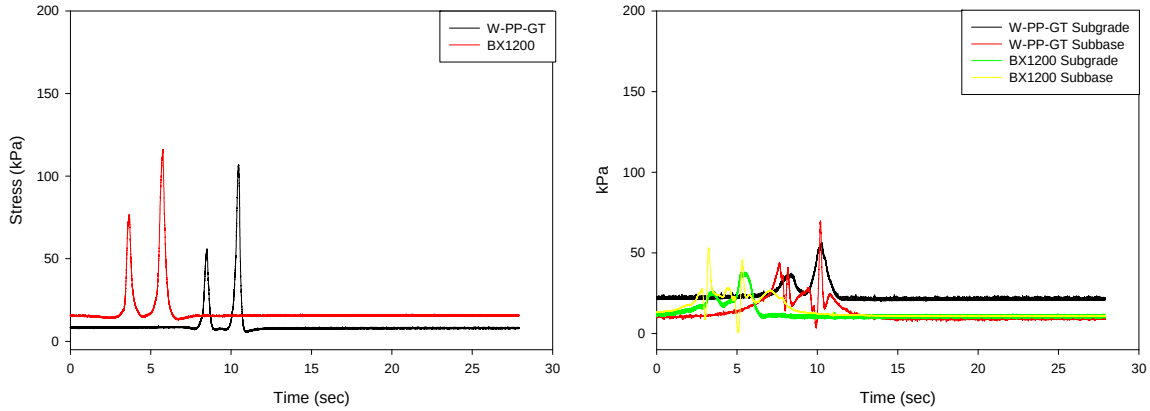

Figure 170. Earth pressure cell W-PP-GT and BX1200 sections layer 2 vertical (left) and horizontal (right) stress data truck traffic pass 50

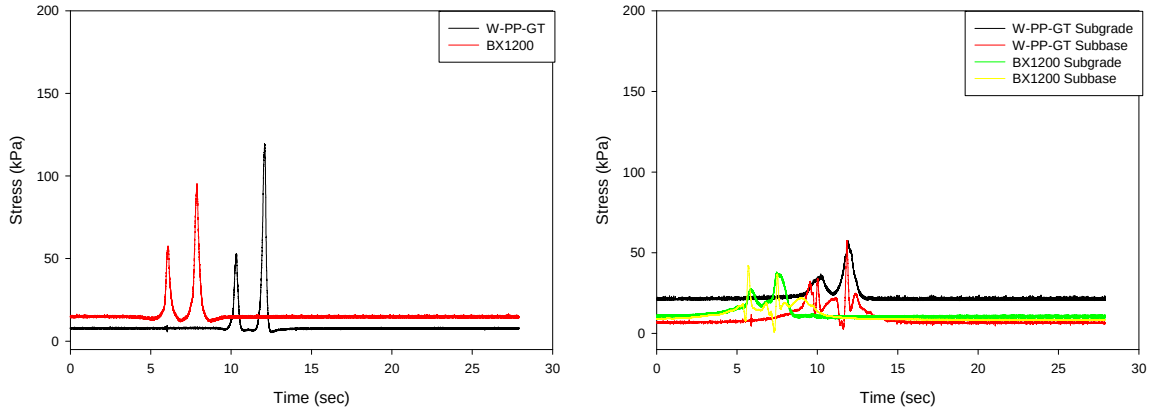

Figure 171. Earth pressure cell W-PP-GT and BX1200 sections layer 2 vertical (left) and horizontal (right) stress data truck traffic pass 60

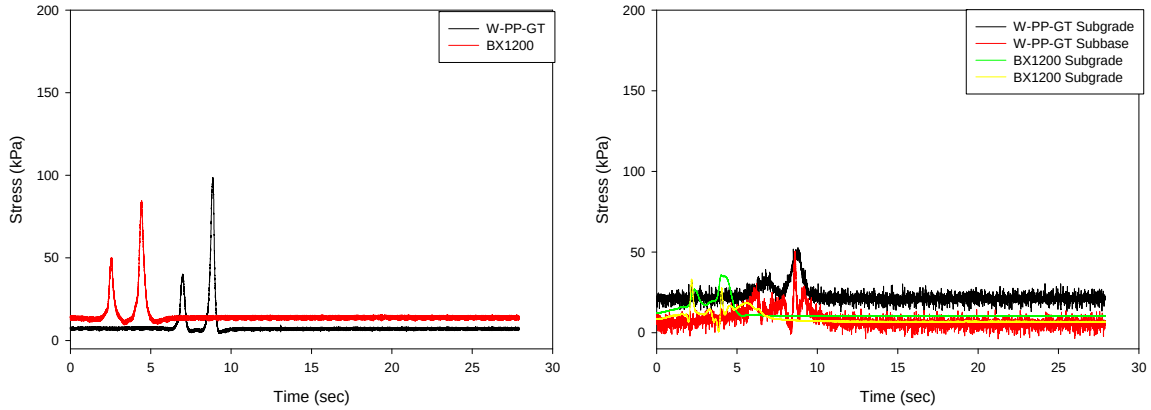

Figure 172. Earth pressure cell W-PP-GT and BX1200 sections layer 2 vertical (left) and horizontal (right) stress data truck traffic pass 75

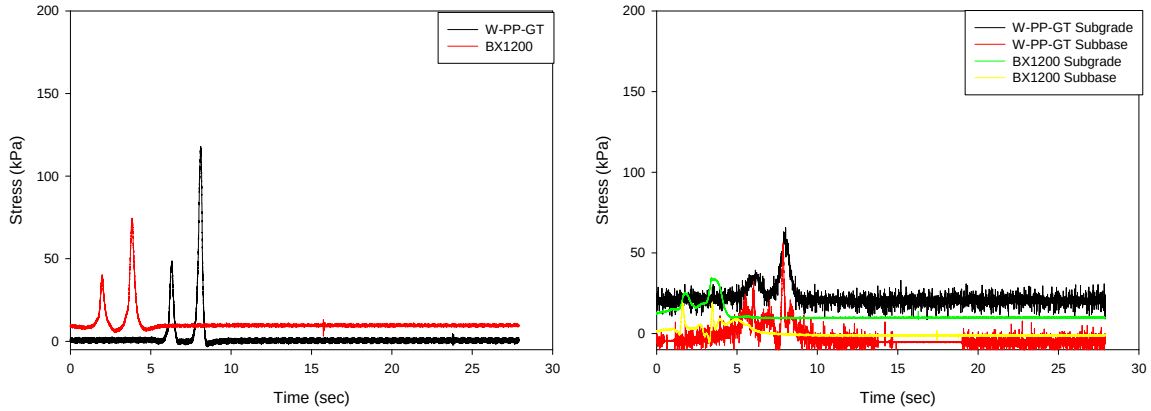

Figure 173. Earth pressure cell W-PP-GT and BX1200 sections layer 2 vertical (left) and horizontal (right) stress data truck traffic pass 100

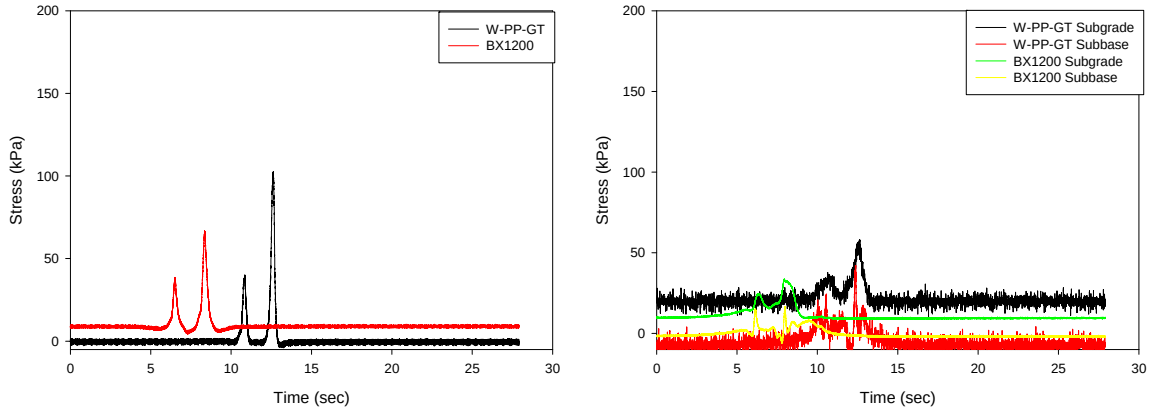

Figure 174. Earth pressure cell W-PP-GT and BX1200 sections layer 2 vertical (left) and horizontal (right) stress data truck traffic pass 126

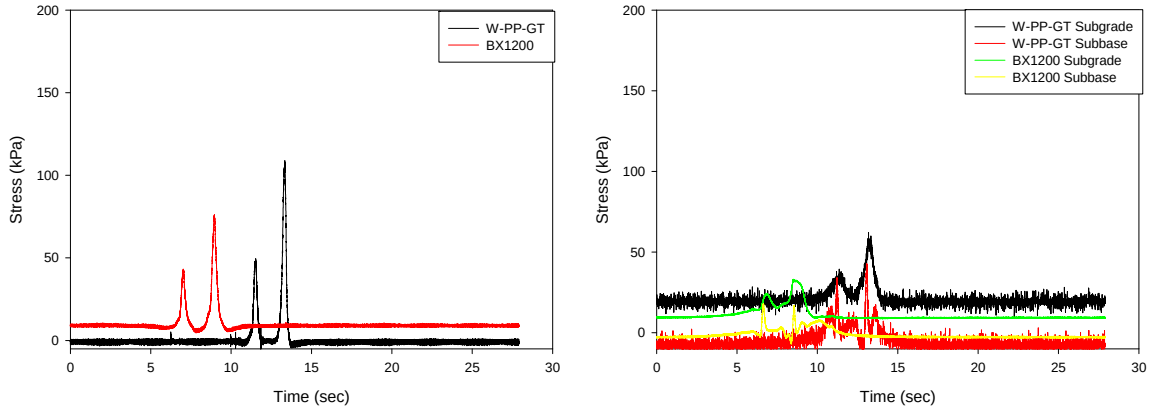

Figure 175. Earth pressure cell W-PP-GT and BX1200 sections layer 2 vertical (left) and horizontal (right) stress data truck traffic pass 150

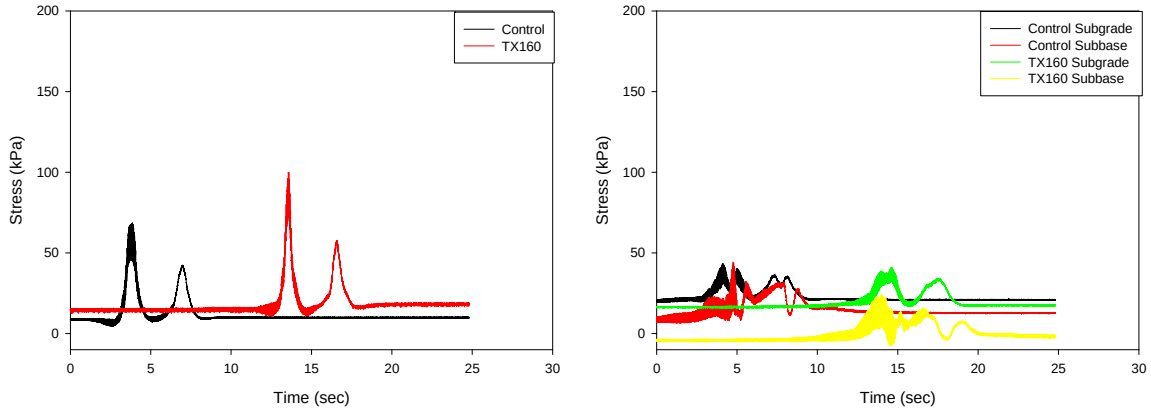

Figure 176. Earth pressure cell Control and TX160 sections layer 2 vertical (left) and horizontal (right) stress data Case roller pass 4

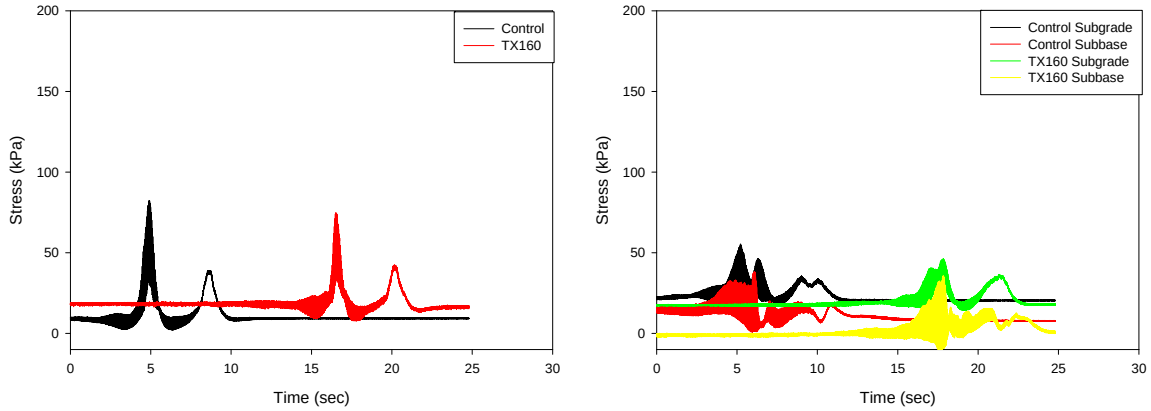

Figure 177. Earth pressure cell Control and TX160 sections layer 2 vertical (left) and horizontal (right) stress data Case roller high amplitude pass 5

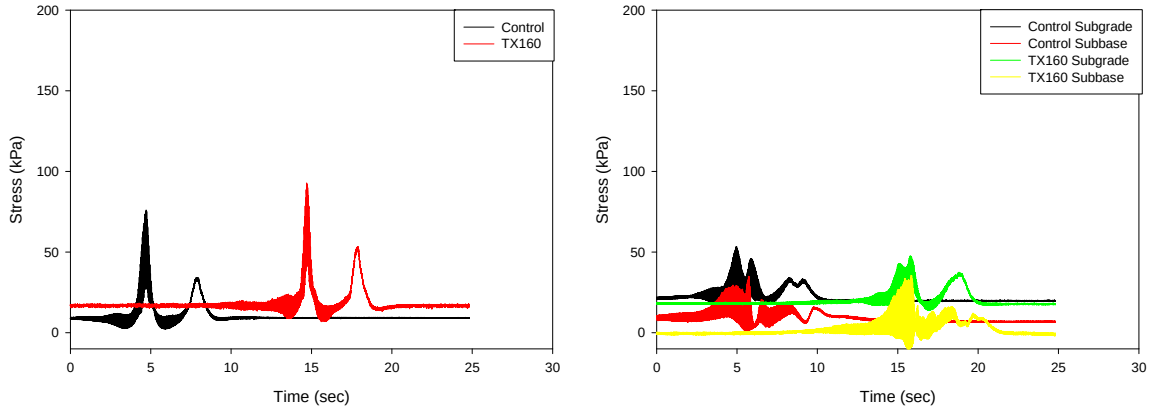

Figure 178. Earth pressure cell Control and TX160 sections layer 2 vertical (left) and horizontal (right) stress data Case roller high amplitude pass 6

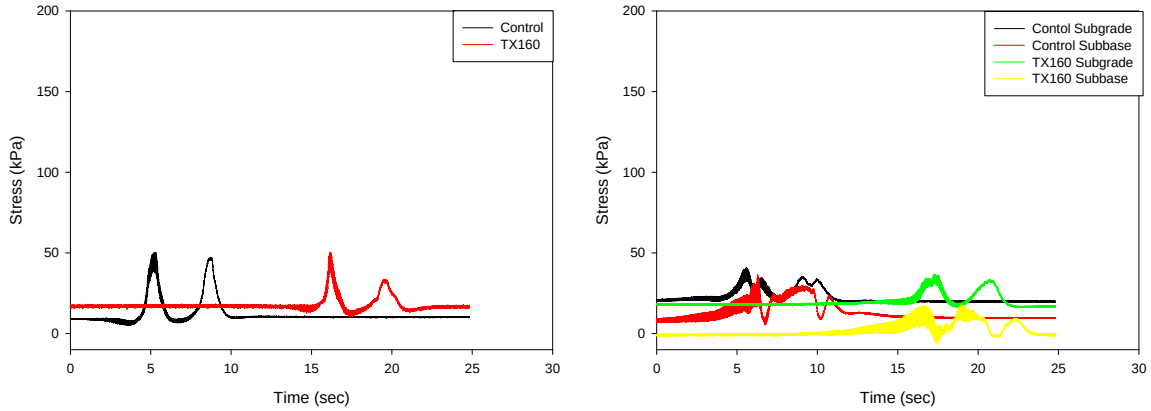

Figure 179. Earth pressure cell Control and TX160 sections layer 2 vertical (left) and horizontal (right) stress data Case roller pass 7

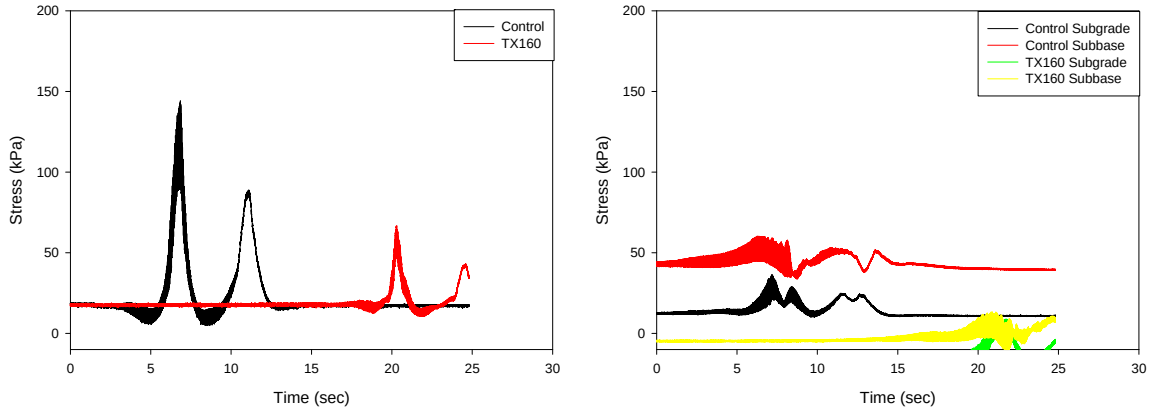

Figure 180. Earth pressure cell Control and TX160 sections layer 2 vertical (left) and horizontal (right) stress data Case roller pass 8

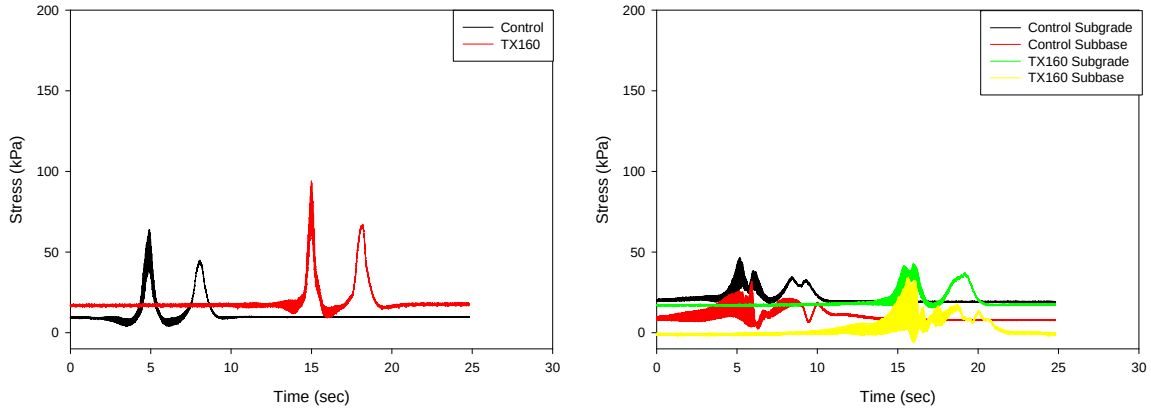

Figure 181. Earth pressure cell Control and TX160 sections layer 2 vertical (left) and horizontal (right) stress data Case roller pass 9

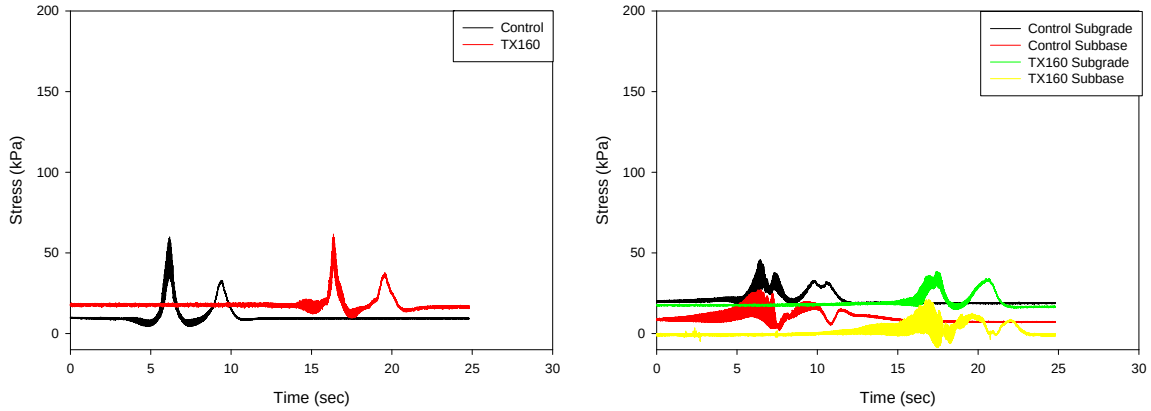

Figure 182. Earth pressure cell Control and TX160 sections layer 2 vertical (left) and horizontal (right) stress data Case roller pass 10

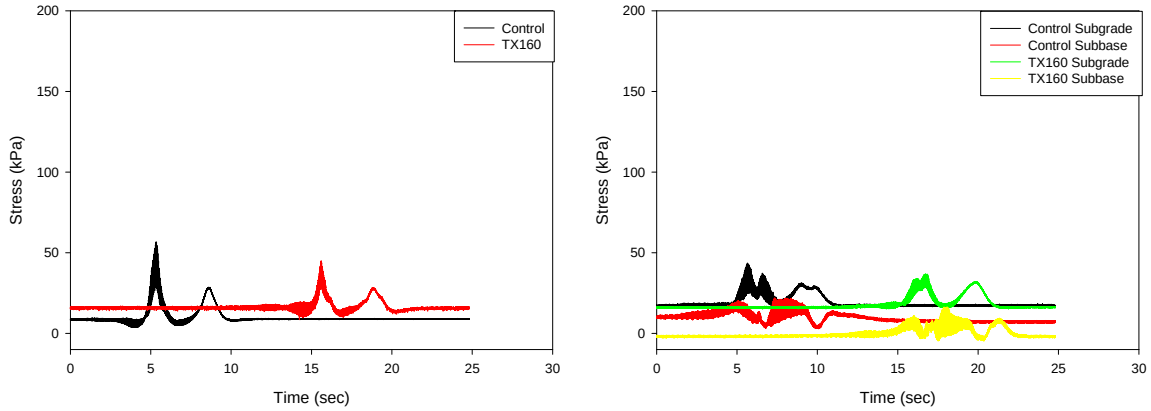

Figure 183. Earth pressure cell Control and TX160 sections layer 2 vertical (left) and horizontal (right) stress data CAT roller pass 13

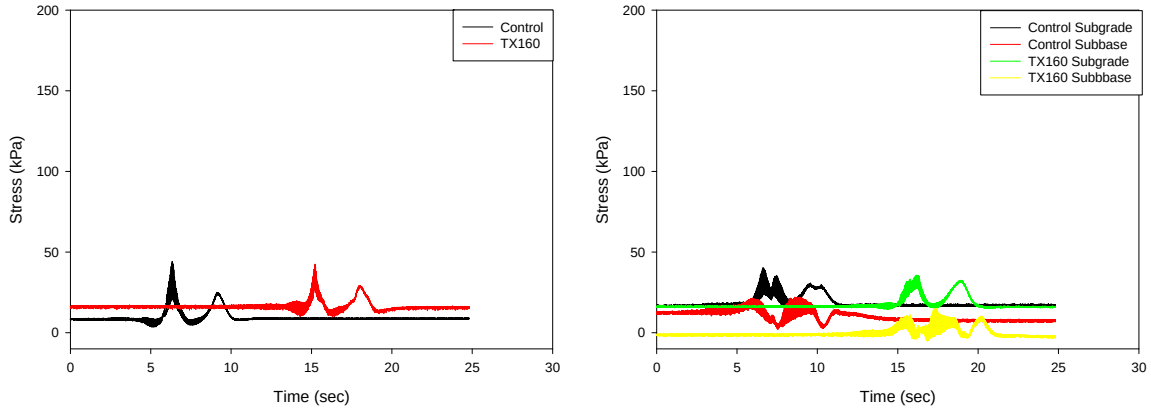

Figure 184. Earth pressure cell Control and TX160 sections layer 2 vertical (left) and horizontal (right) stress data CAT roller pass 14

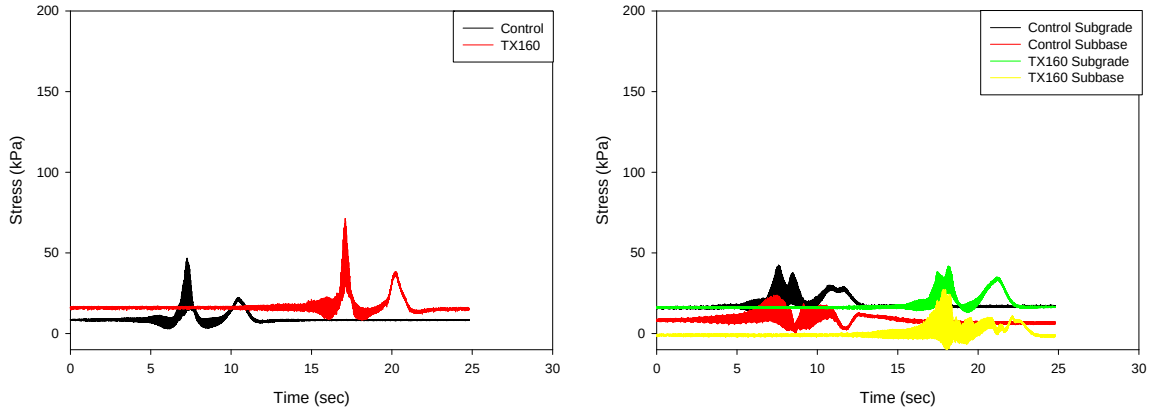

Figure 185. Earth pressure cell Control and TX160 sections layer 2 vertical (left) and horizontal (right) stress data CAT roller high amplitude pass 15

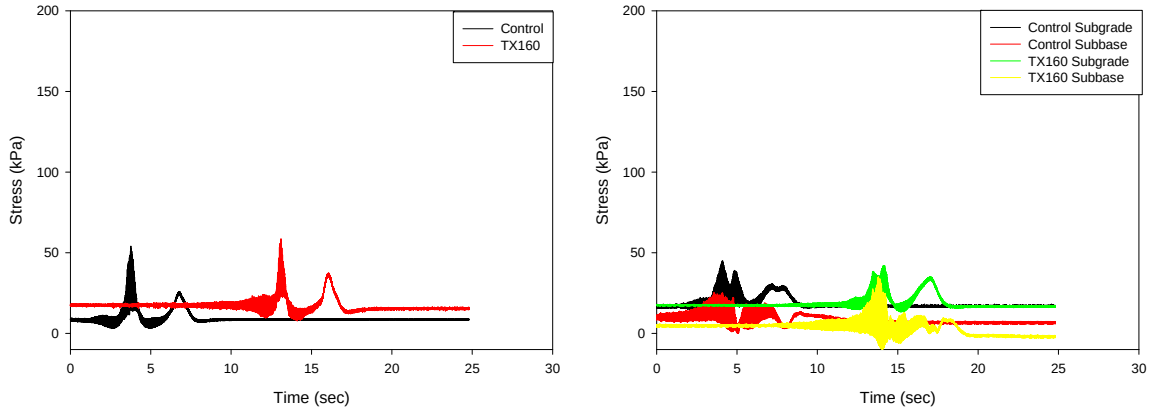

Figure 186. Earth pressure cell Control and TX160 sections layer 2 vertical (left) and horizontal (right) stress data CAT roller high amplitude pass 16

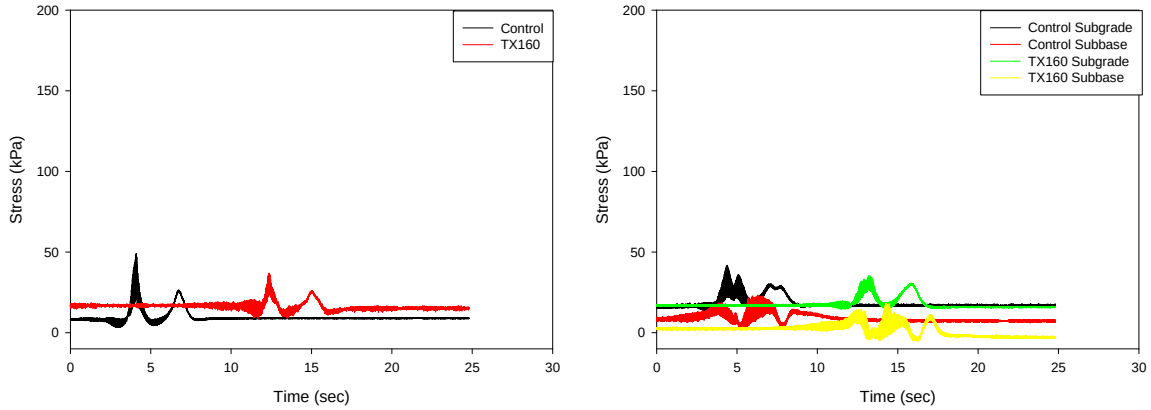

Figure 187. Earth pressure cell Control and TX160 sections layer 2 vertical (left) and horizontal (right) stress data CAT roller pass 17

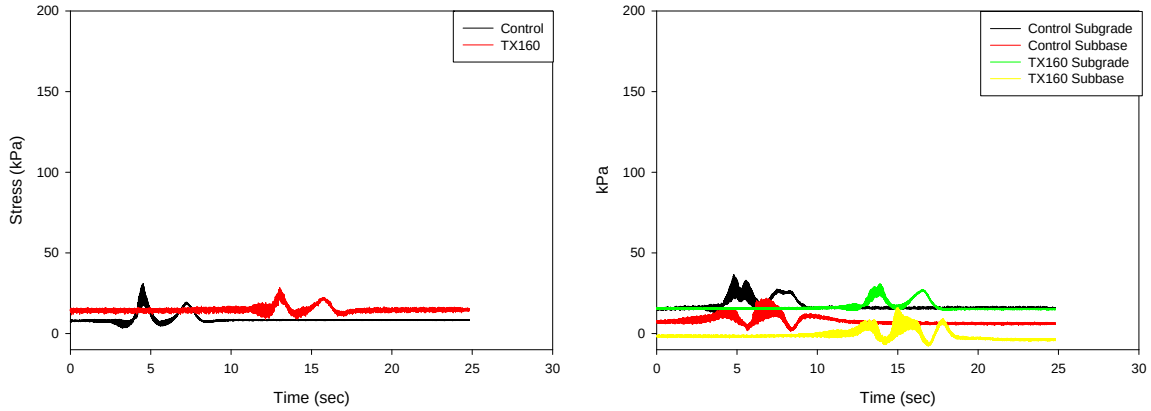

Figure 188. Earth pressure cell Control and TX160 sections layer 2 vertical (left) and horizontal (right) stress data CAT roller pass 18

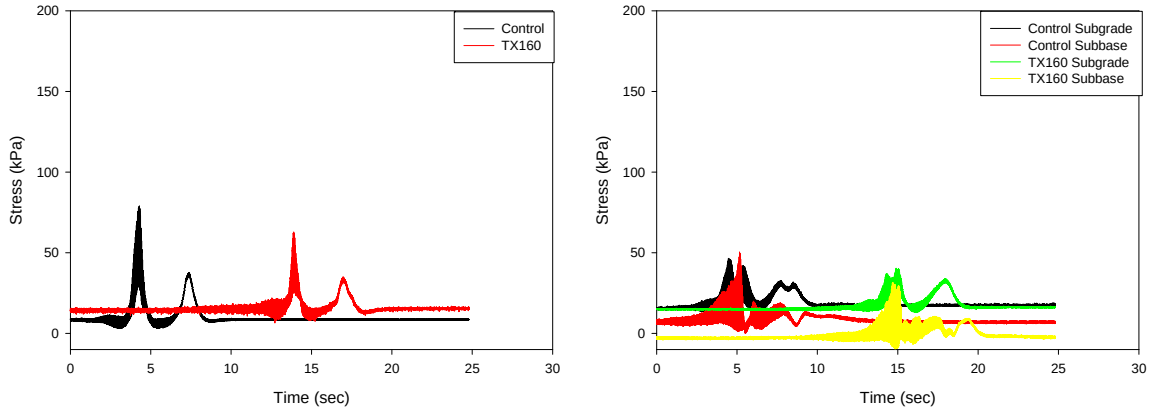

Figure 189. Earth pressure cell Control and TX160 sections layer 2 vertical (left) and horizontal (right) stress data CAT roller high amplitude pass 19

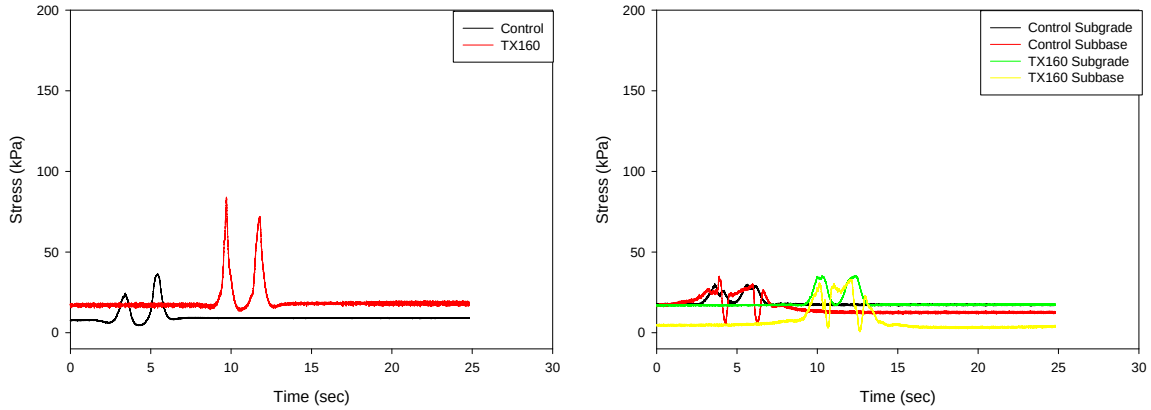

Figure 190. Earth pressure cell Control and TX160 sections layer 2 vertical (left) and horizontal (right) stress data CAT roller static pass 20

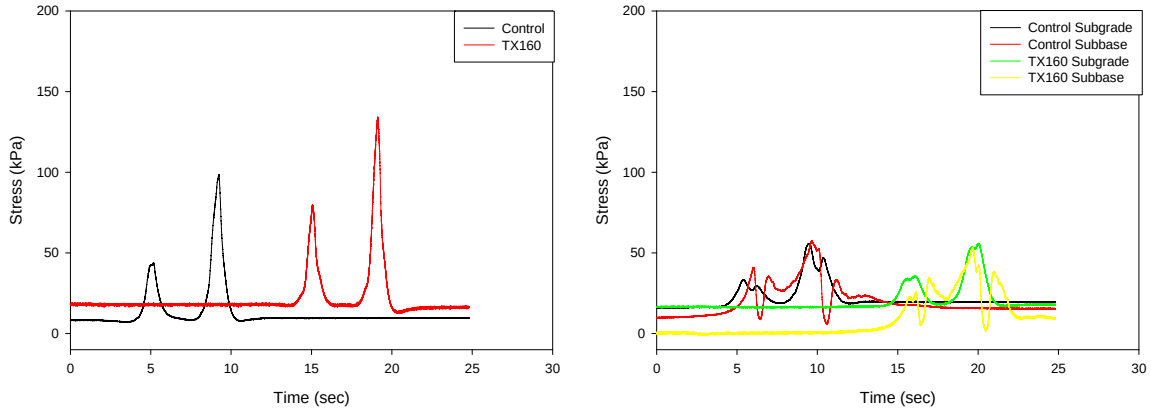

Figure 191. Earth pressure cell Control and TX160 sections layer 2 vertical (left) and horizontal (right) stress data truck traffic pass 1

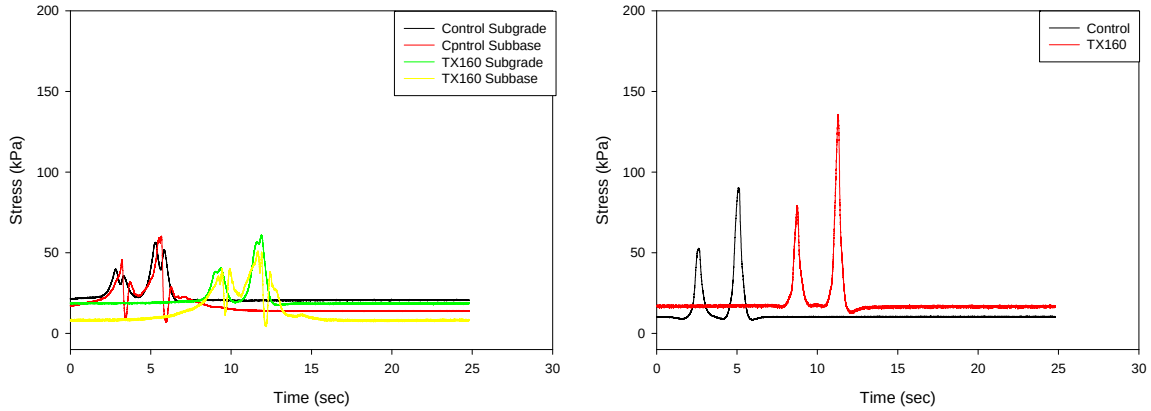

Figure 192. Earth pressure cell Control and TX160 sections layer 2 vertical (left) and horizontal (right) stress data truck traffic pass 5

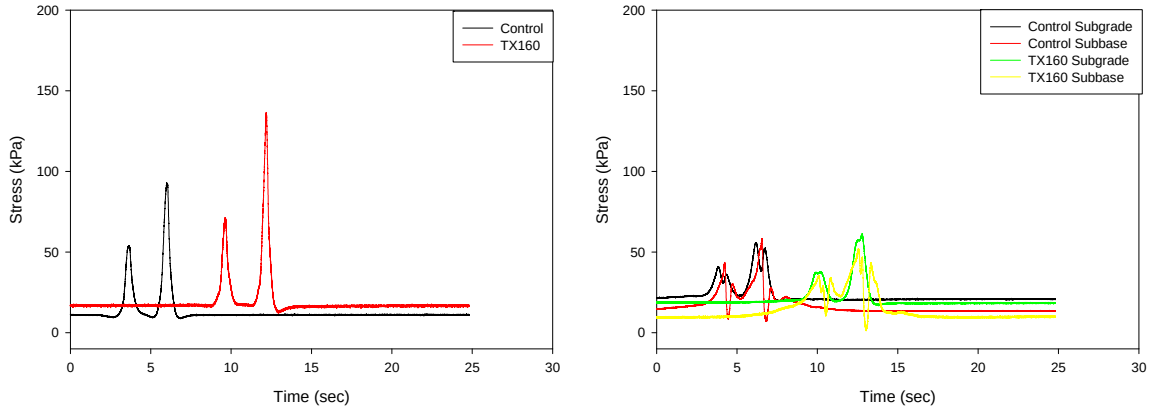

Figure 193. Earth pressure cell Control and TX160 sections layer 2 vertical (left) and horizontal (right) stress data truck traffic pass 10

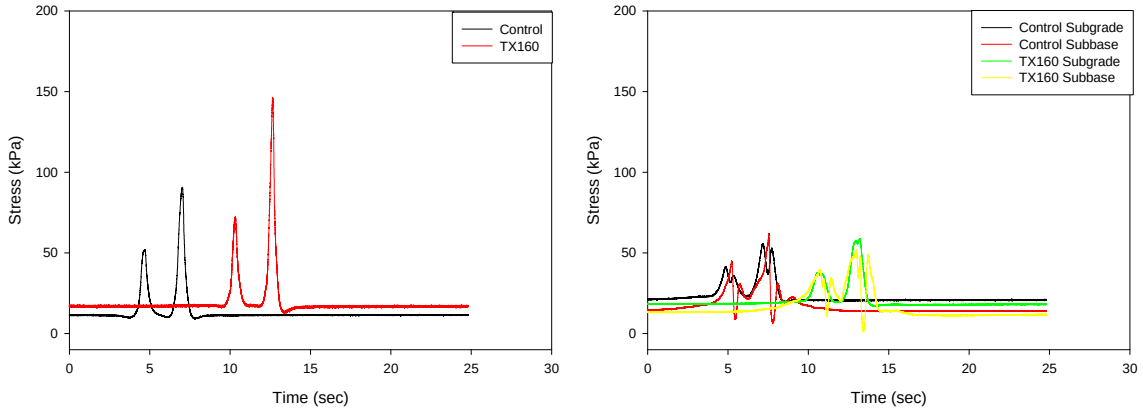

Figure 194. Earth pressure cell Control and TX160 sections layer 2 vertical (left) and horizontal (right) stress data truck traffic pass 15

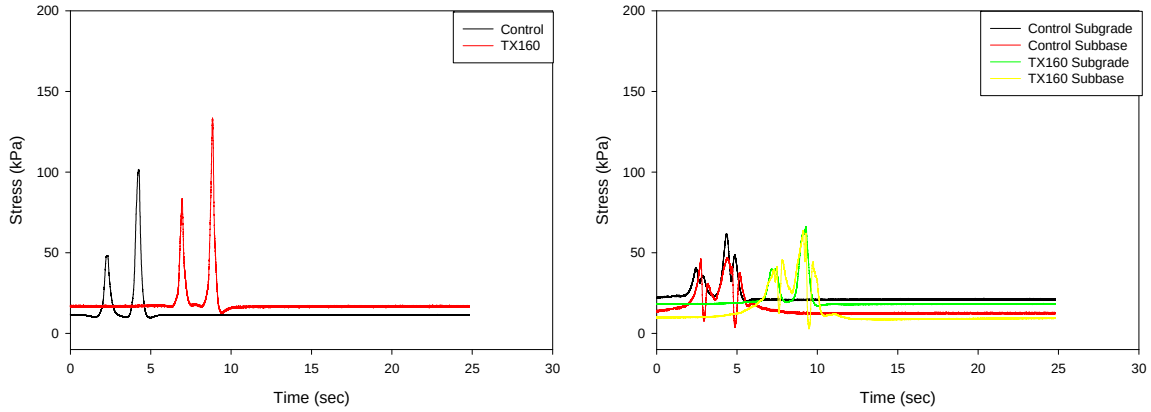

Figure 195. Earth pressure cell Control and TX160 sections layer 2 vertical (left) and horizontal (right) stress data truck traffic pass 35

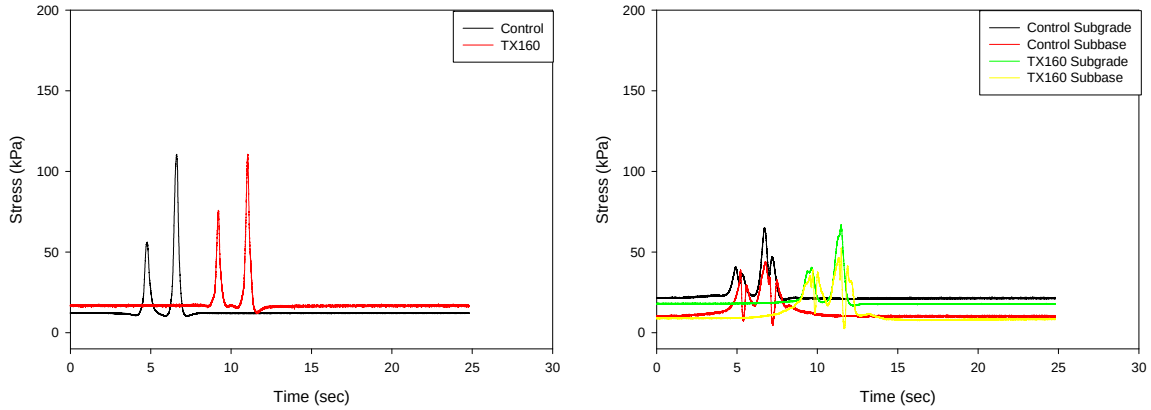

Figure 196. Earth pressure cell Control and TX160 sections layer 2 vertical (left) and horizontal (right) stress data truck traffic pass 45

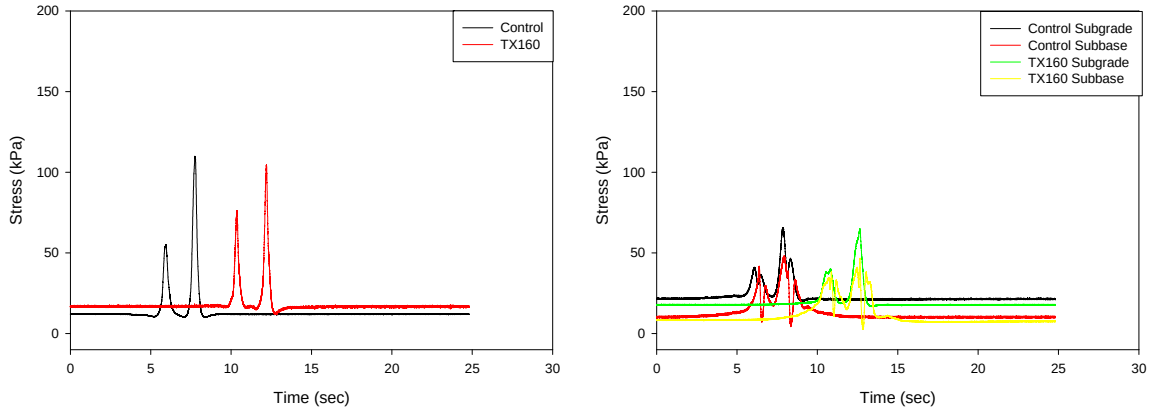

Figure 197. Earth pressure cell Control and TX160 sections layer 2 vertical (left) and horizontal (right) stress data truck traffic pass 50

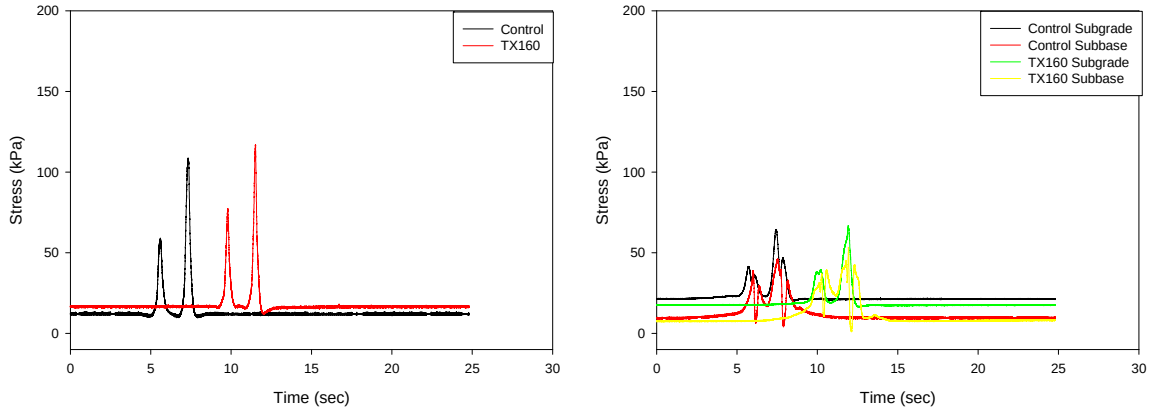

Figure 198. Earth pressure cell Control and TX160 sections layer 2 vertical (left) and horizontal (right) stress data truck traffic pass 60

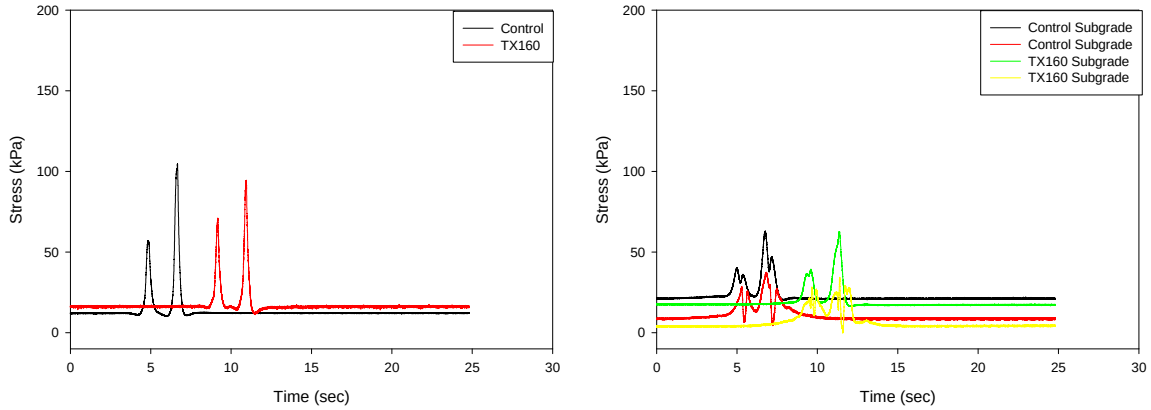

Figure 199. Earth pressure cell Control and TX160 sections layer 2 vertical (left) and horizontal (right) stress data truck traffic pass 75

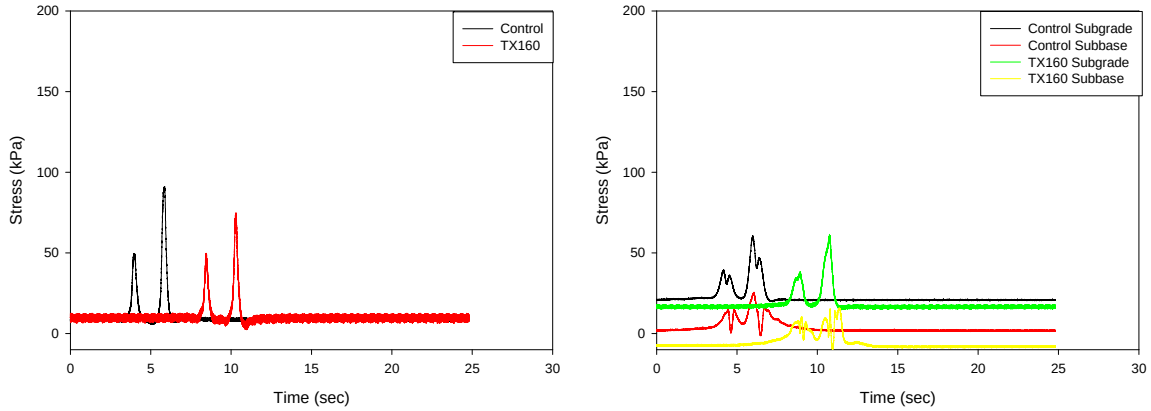

Figure 200. Earth pressure cell Control and TX160 sections layer 2 vertical (left) and horizontal (right) stress data truck traffic pass 100

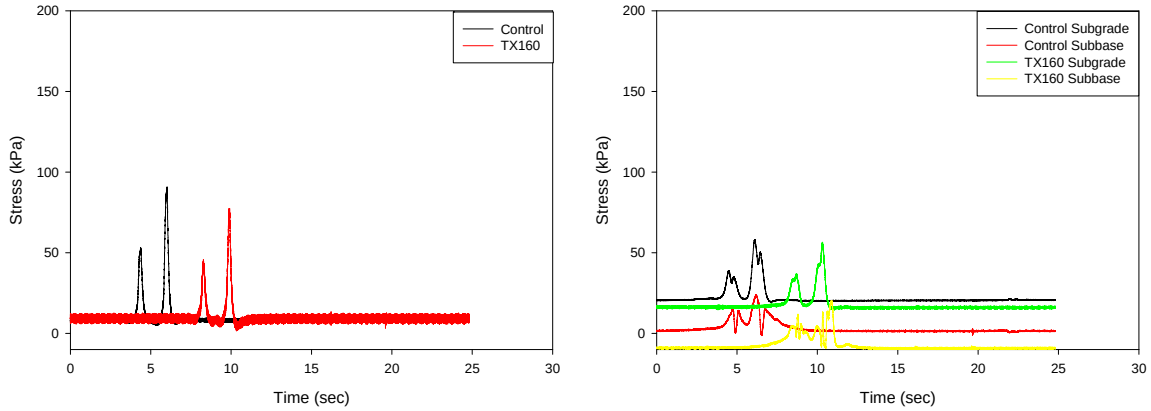

Figure 201. Earth pressure cell Control and TX160 sections layer 2 vertical (left) and horizontal (right) stress data truck traffic pass 126

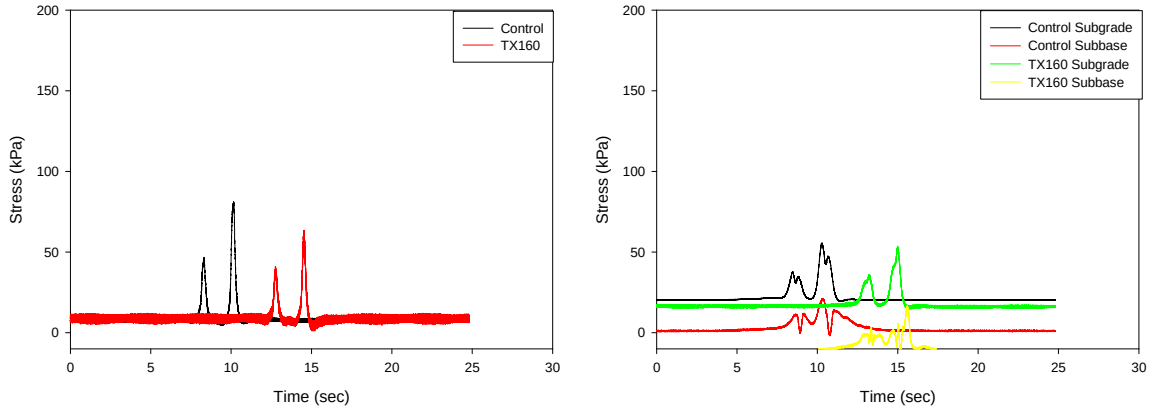

Figure 202. Earth pressure cell Control and TX160 sections layer 2 vertical (left) and horizontal (right) stress data truck traffic pass 150

APPENDIX C. INDIVIDUAL CROSS SECTIONS

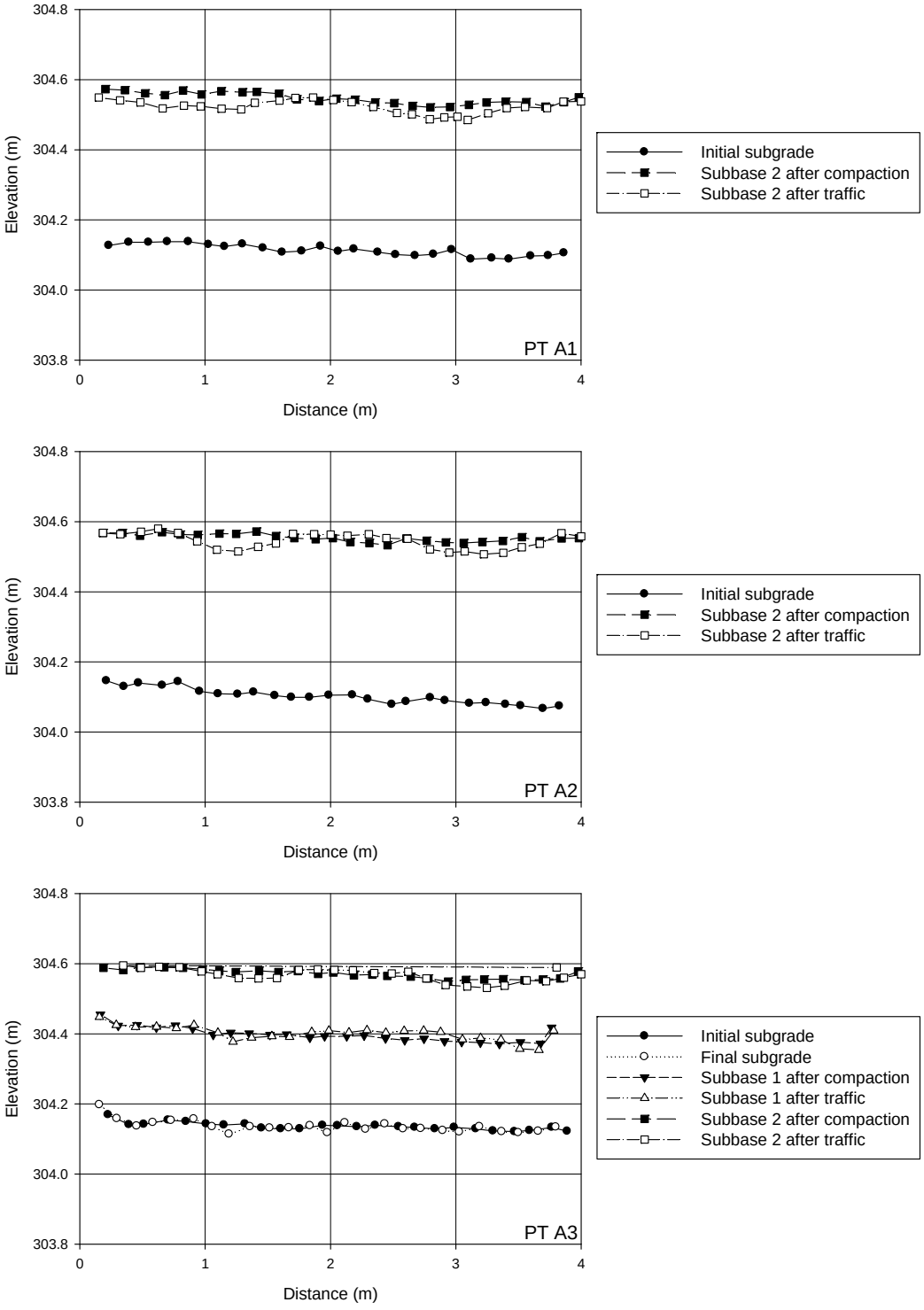

Figure 203. Cross section profiles, W-PP-GT section, points A1, A2 and A3

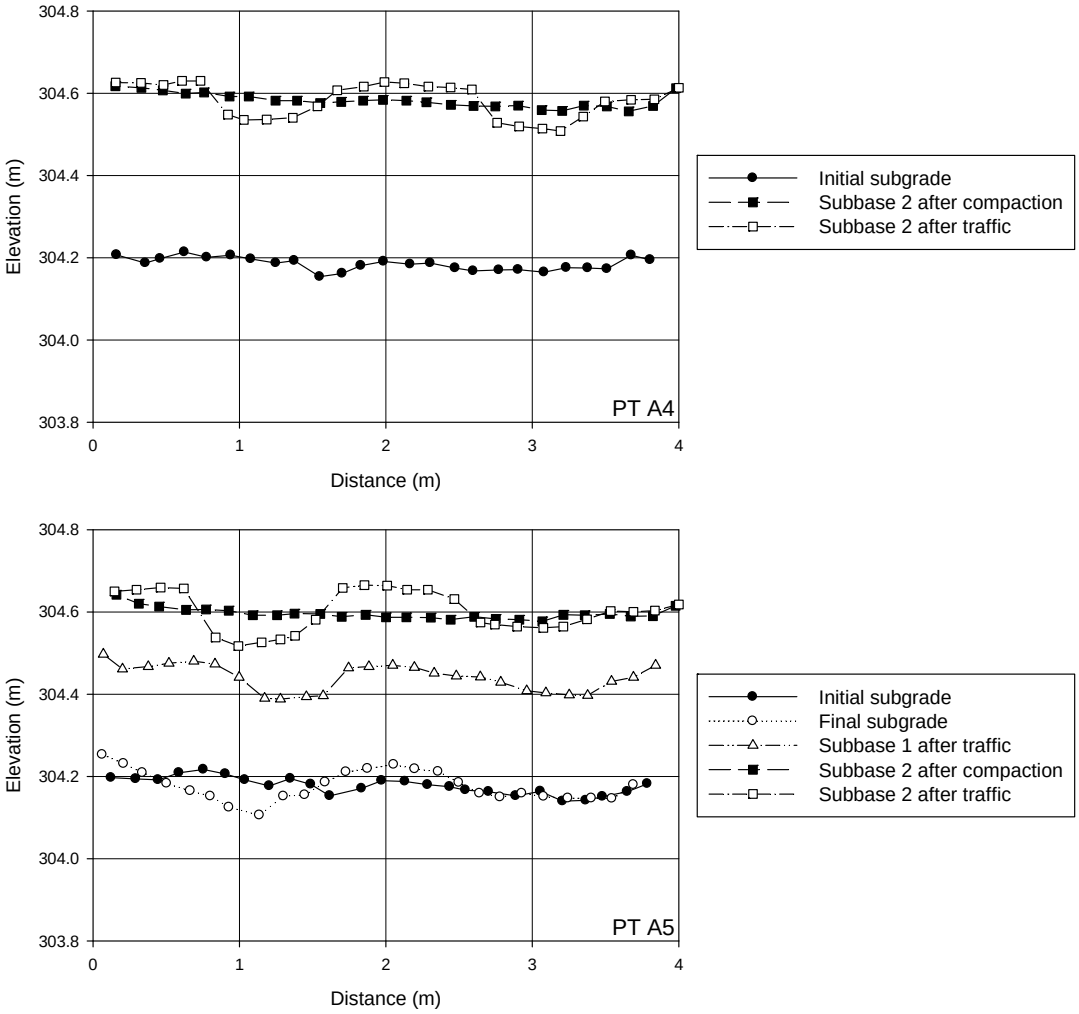

Figure 204. Cross section profiles W-PP-GT section, points A4 and A5

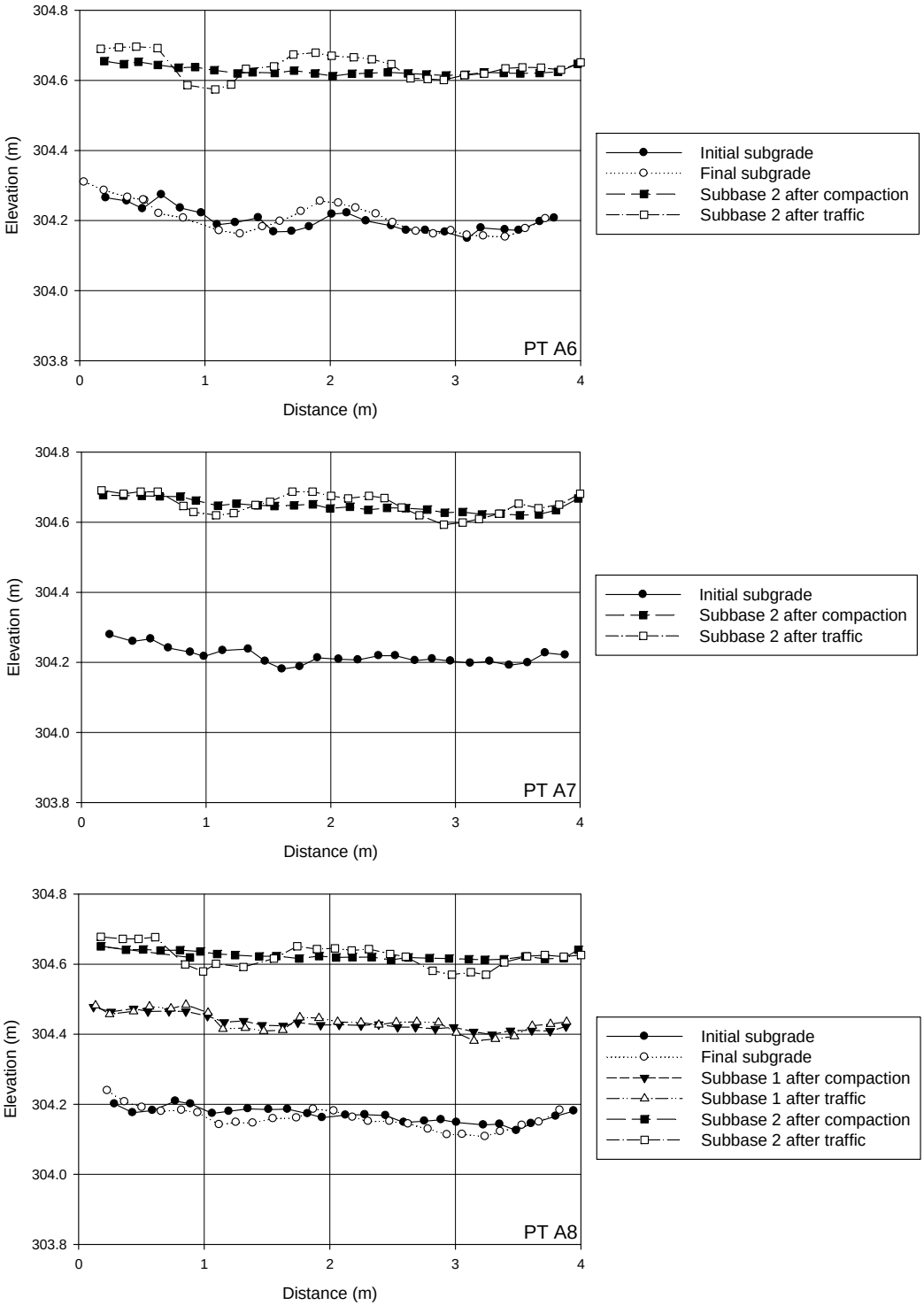

Figure 205. Cross section profiles BX1200 section, points A6, A7 and A8

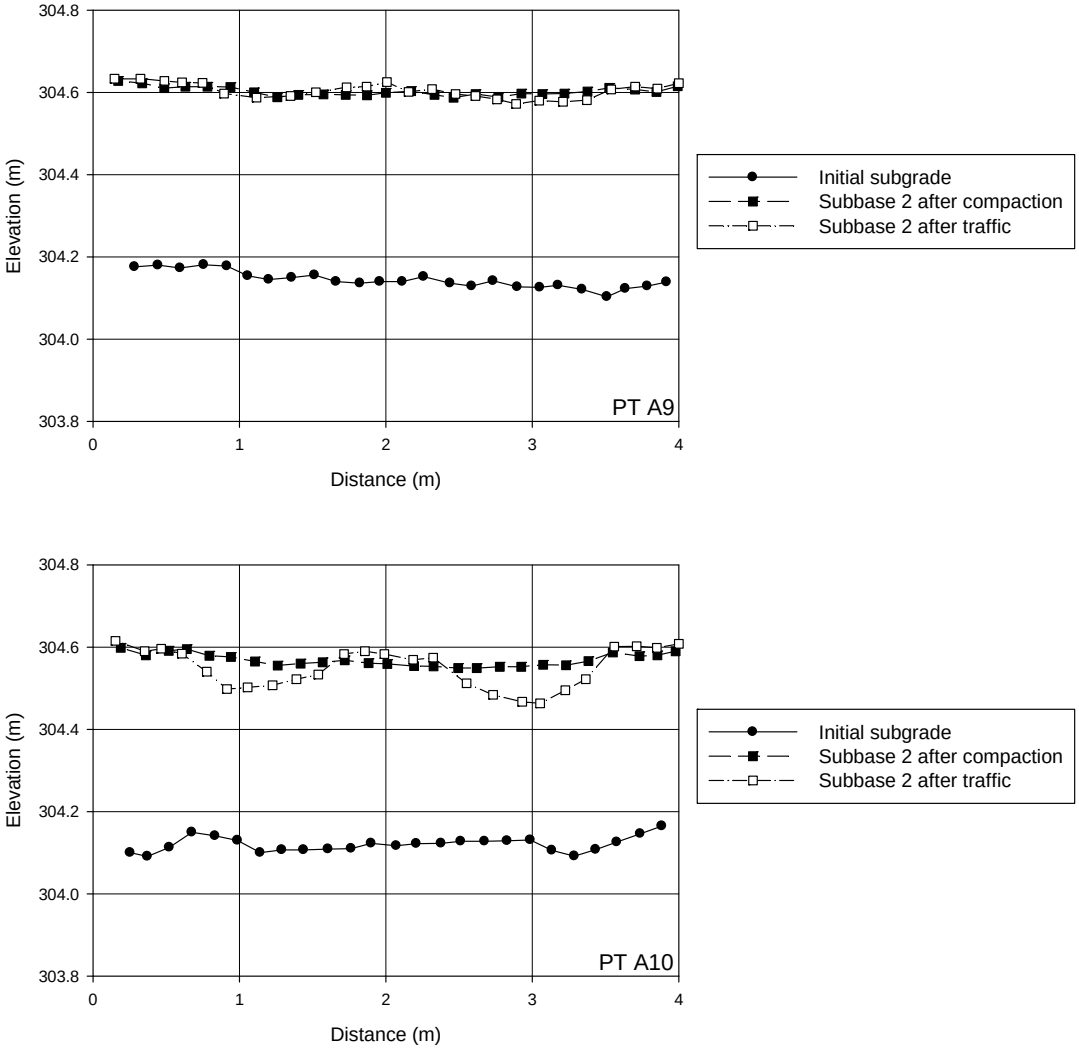

Figure 206. Cross section profiles BX1200 section, points A9 and A10

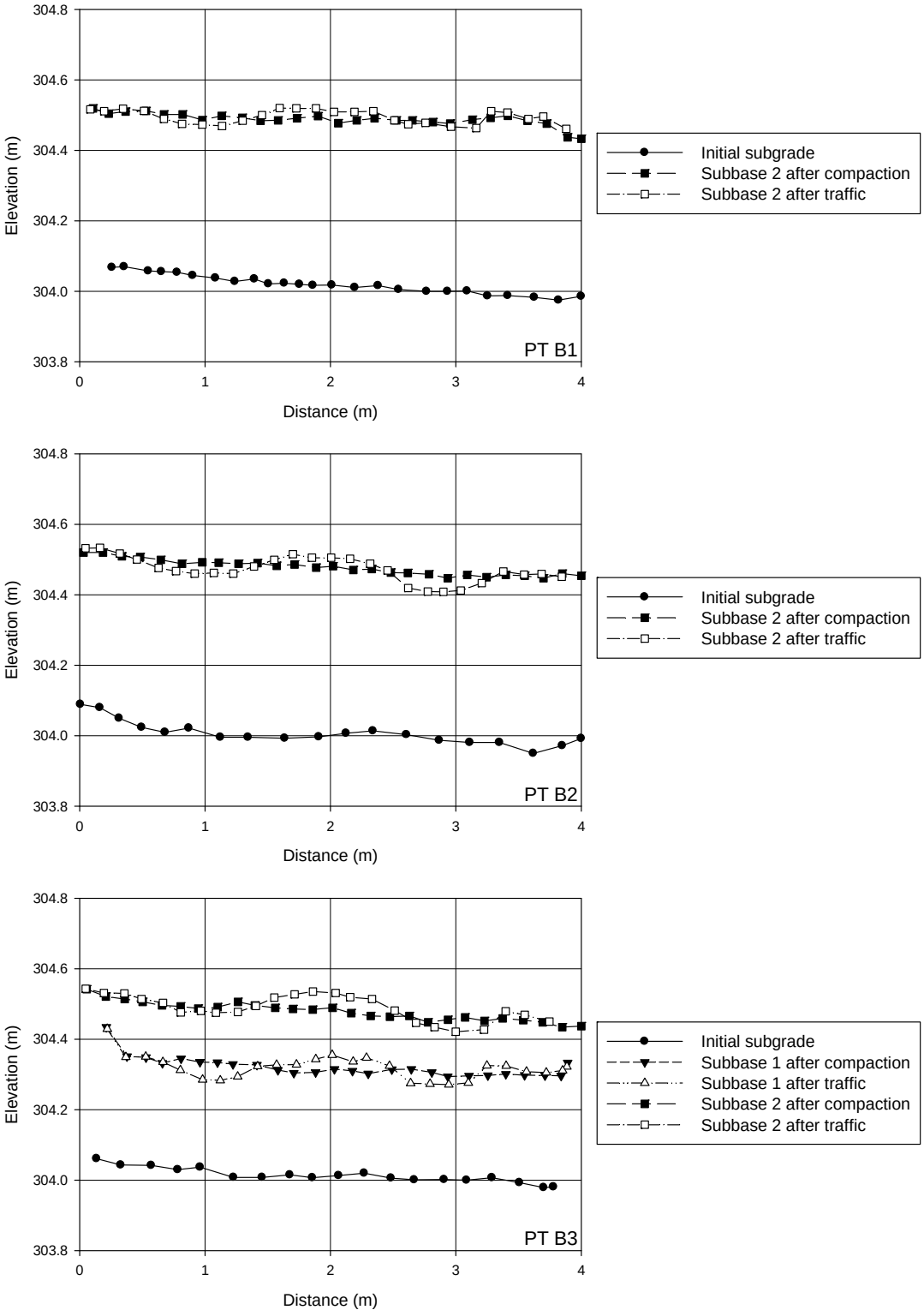

Figure 207. Cross section profiles control section, points B1, B2 and B3

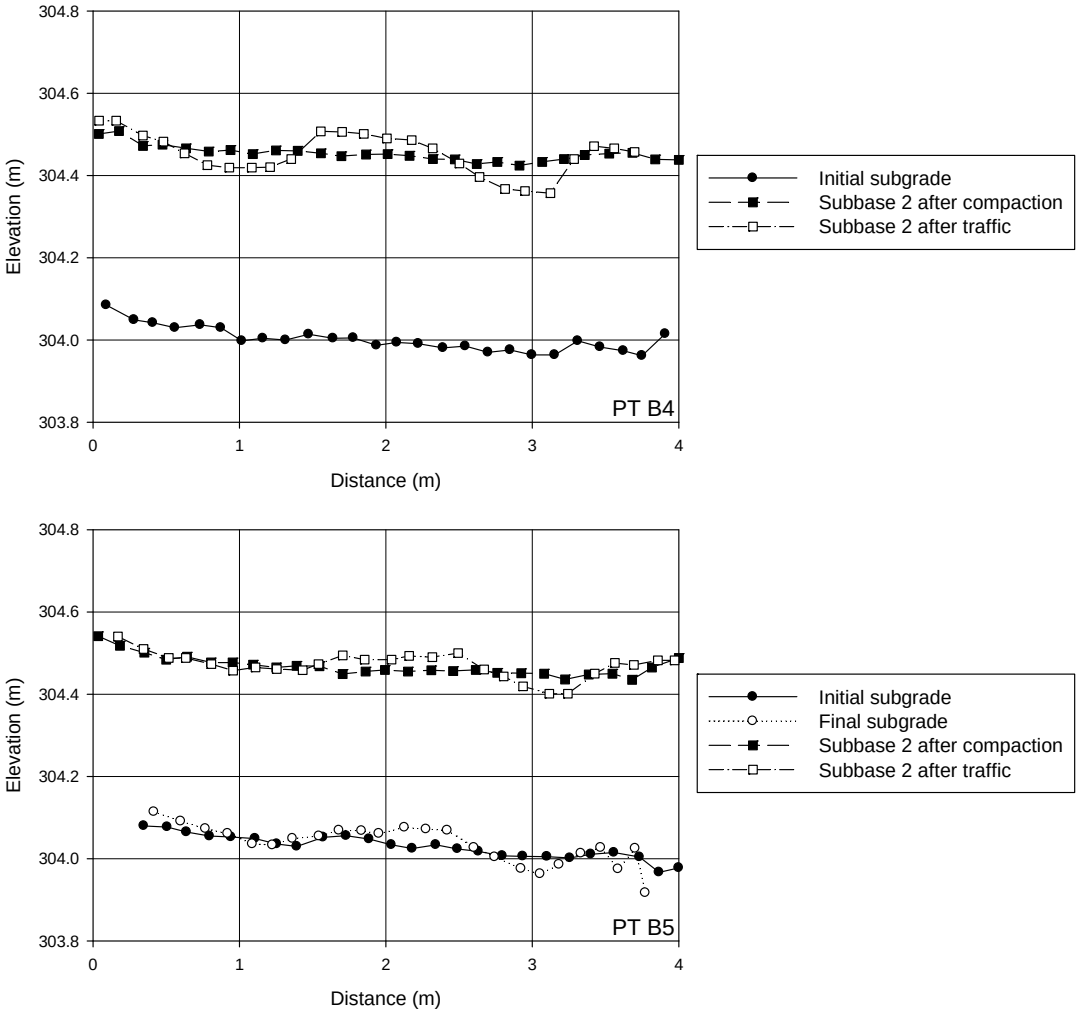

Figure 208. Cross section profiles control section, points B4 and B5

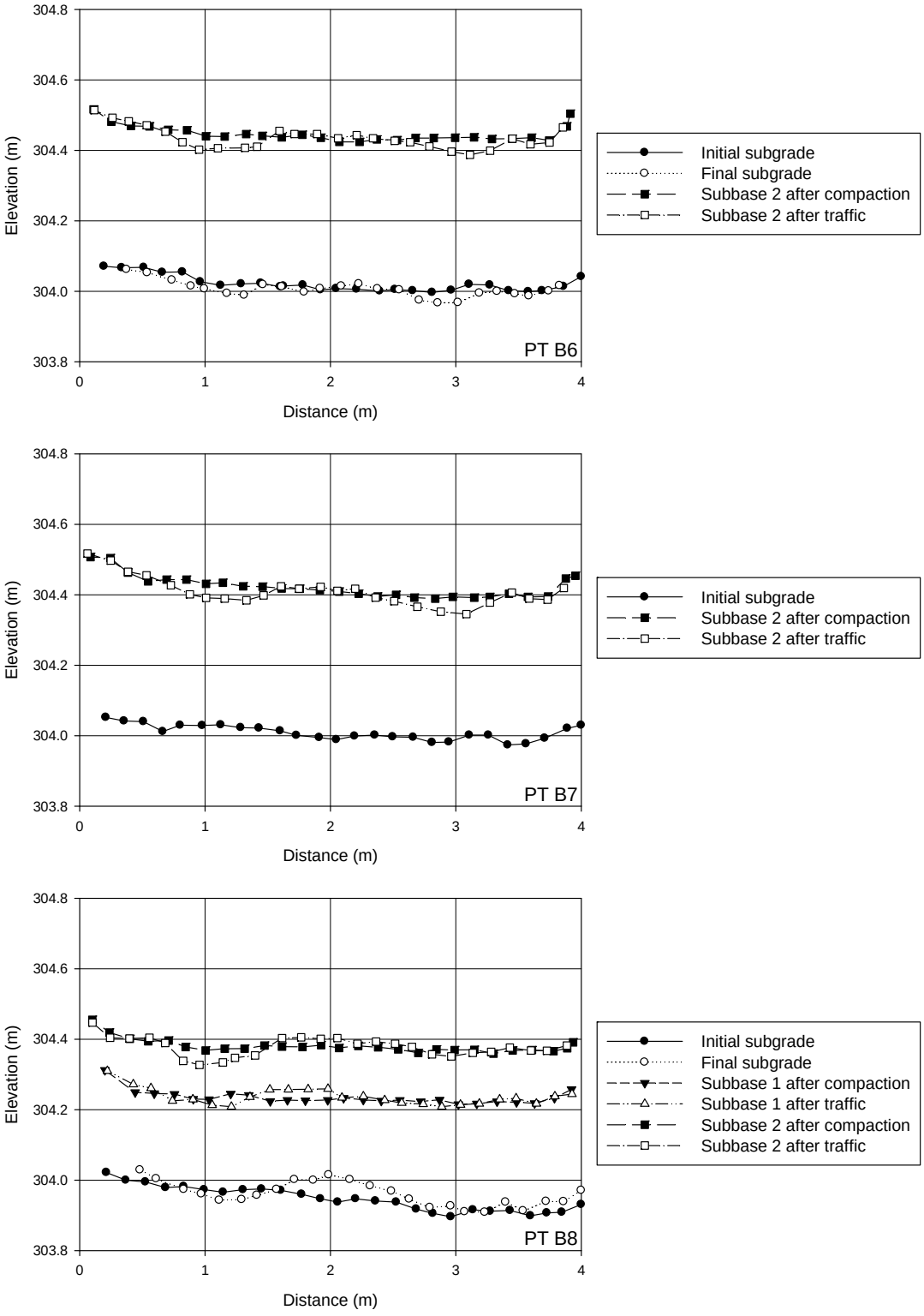

Figure 209. Cross section profiles TX160 section, points B6, B7 and B8

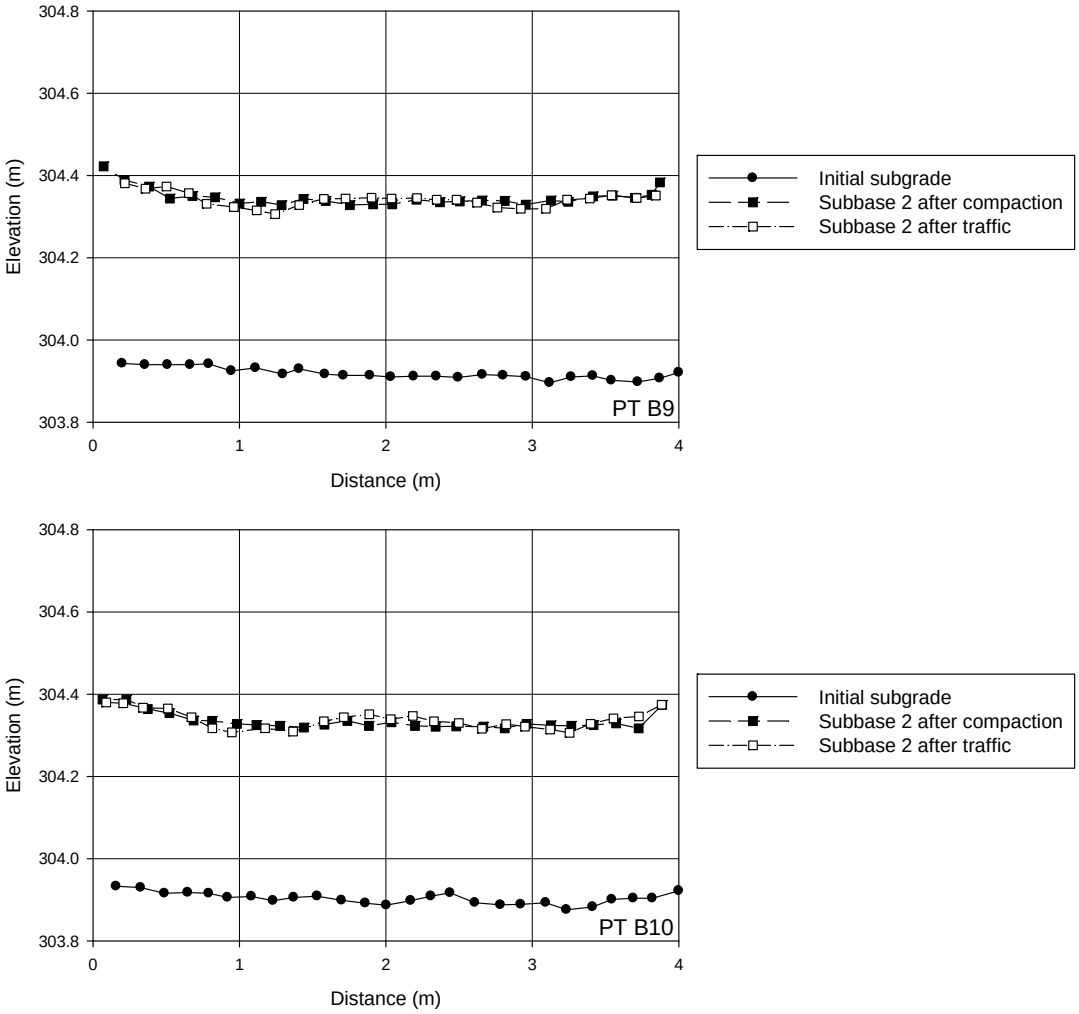

Figure 210. Cross section profiles TX160 section, points B9 and B10

APPENDIX D. HISTOGRAMS

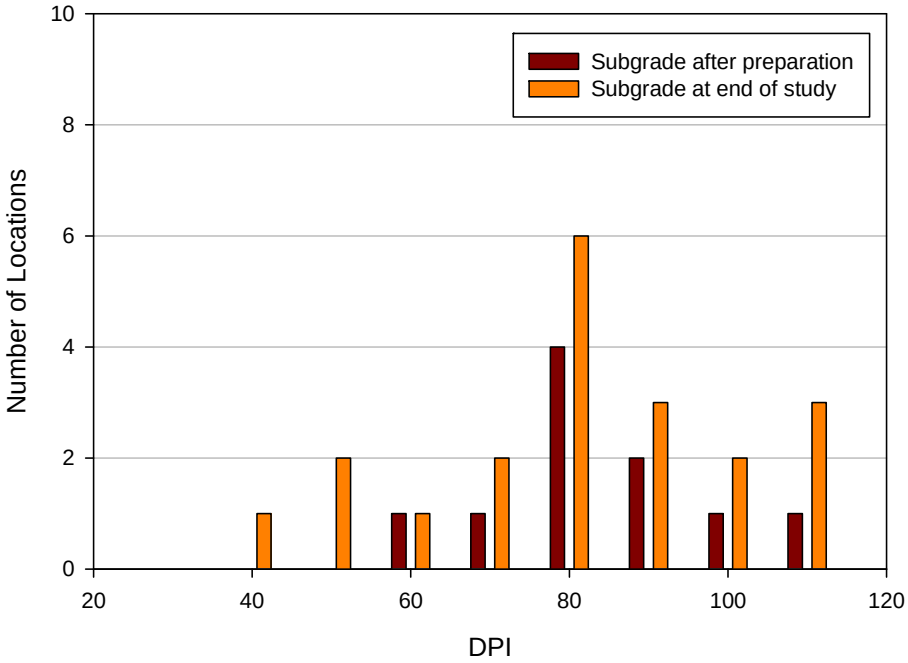

Figure 211. W-PP-GT and BX1200 sections subgrade DPI histogram

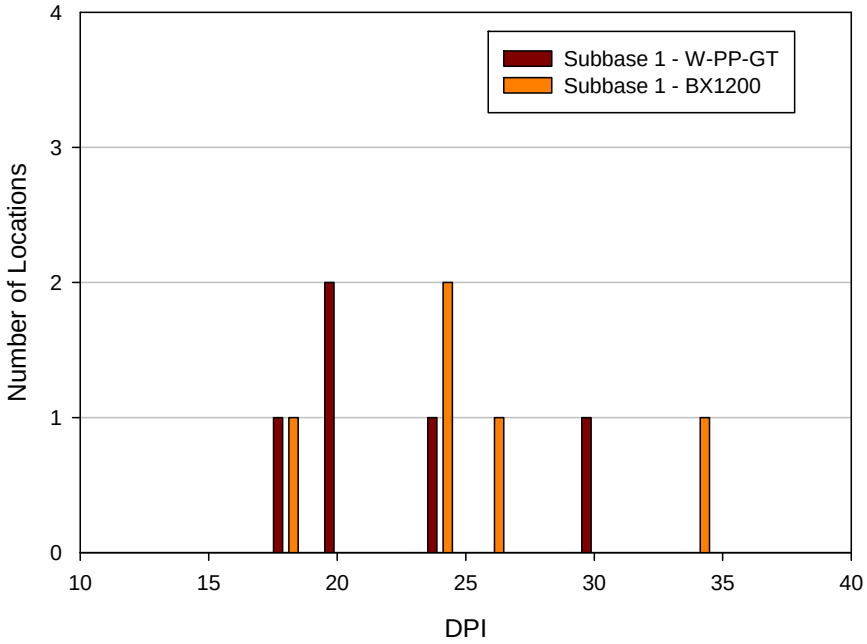

Figure 212. W-PP-GT and BX1200 sections subbase 1 DPI histogram

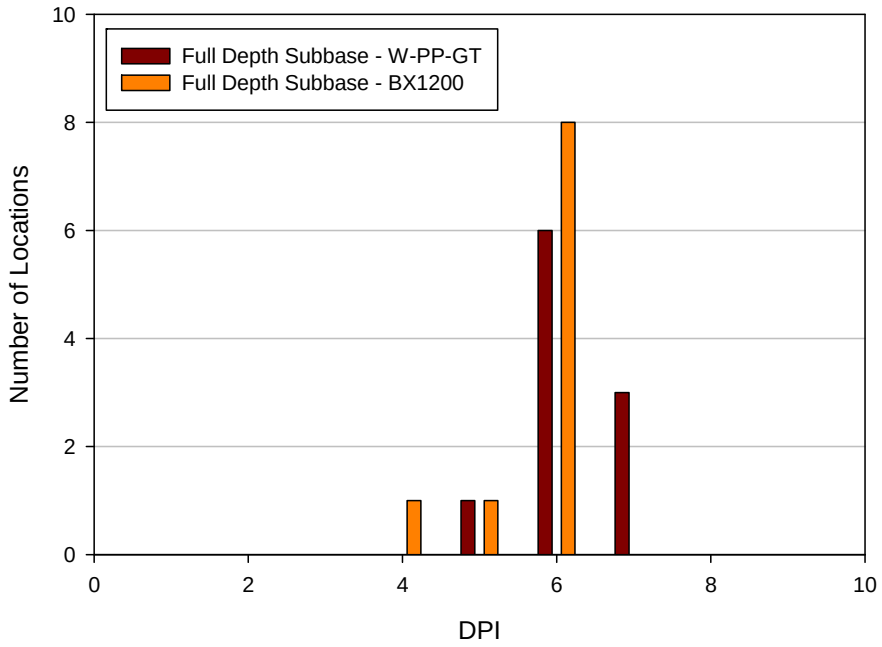

Figure 213. W-PP-GT and BX1200 sections subbase 2 DPI histogram

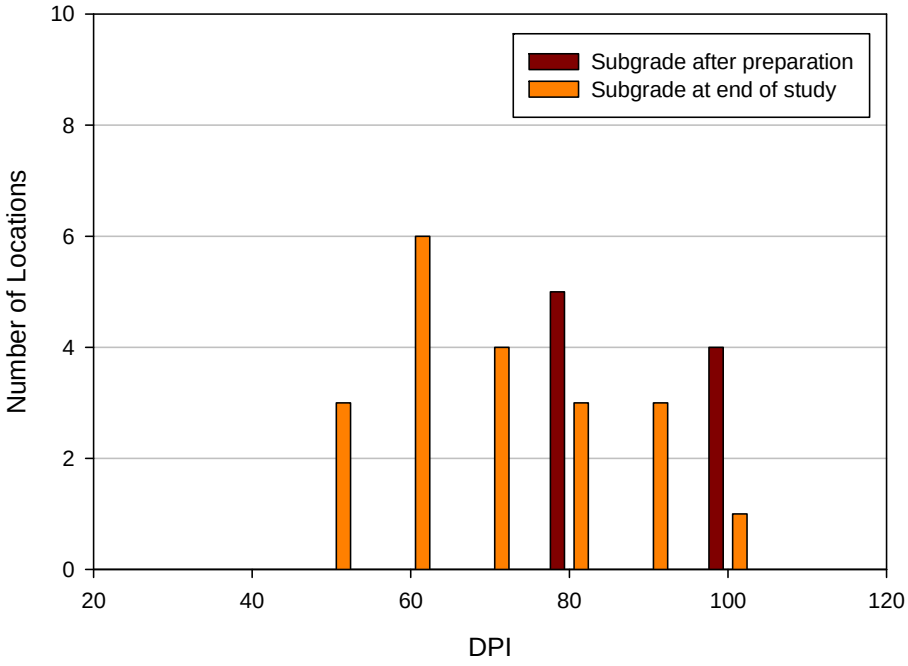

Figure 214. Control and TX160 sections subgrade DPI histogram

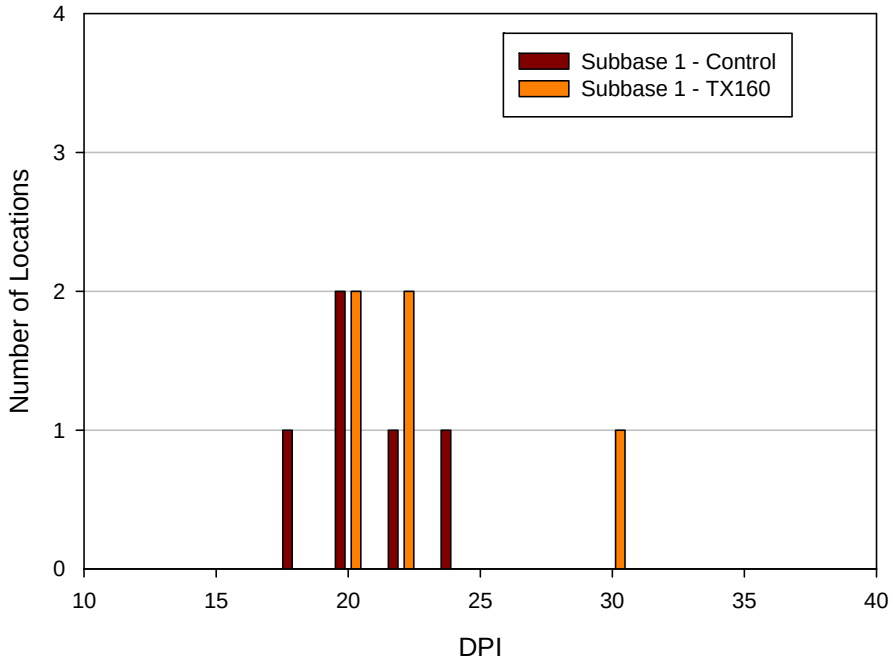

Figure 215. Control and TX160 sections subbase 1 DPI histogram

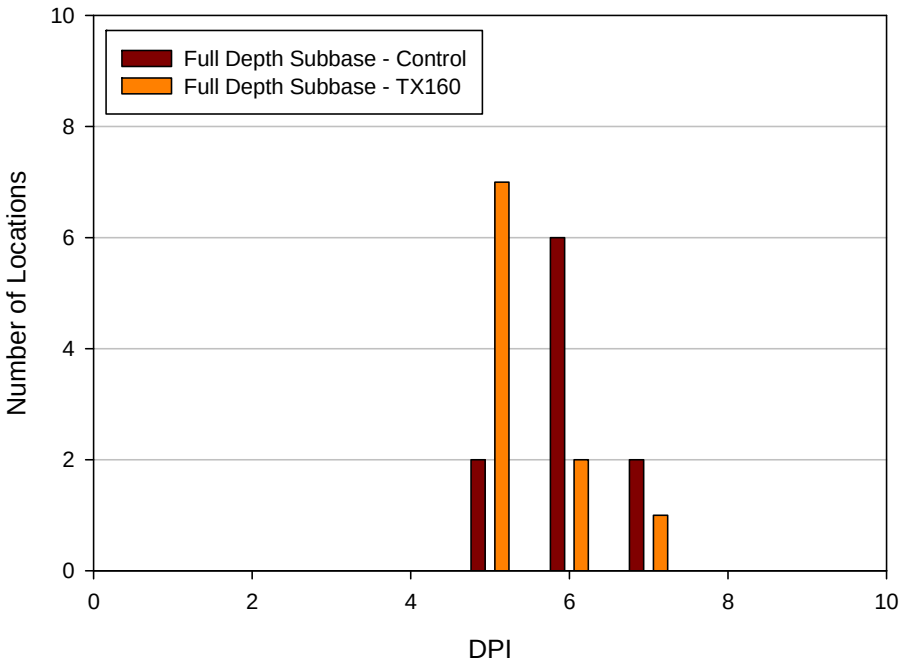

Figure 216. Control and TX160 sections subbase 2 DPI histogram

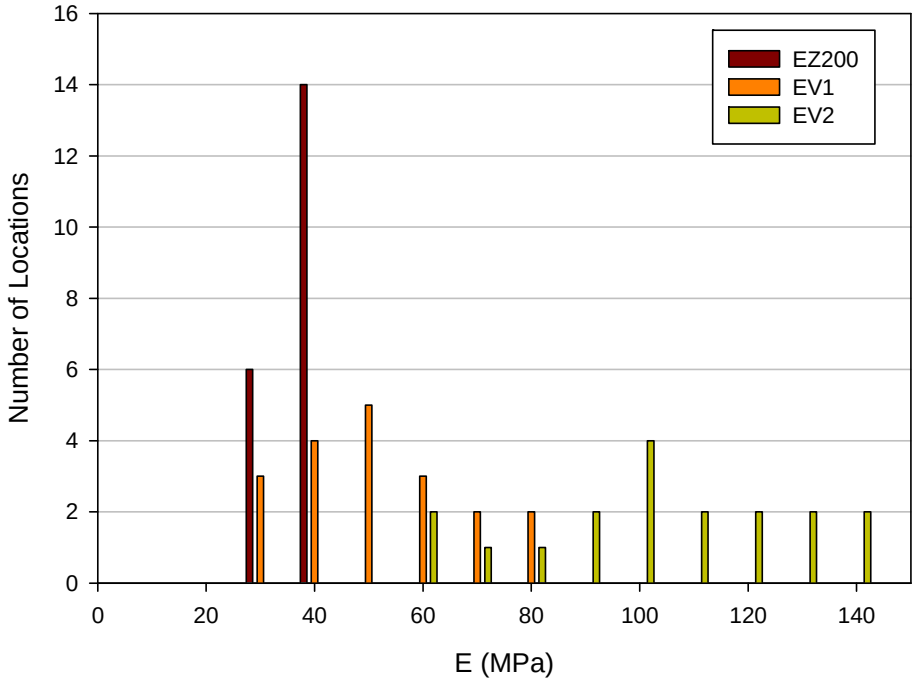

Figure 217. Combined sections subbase 2 modulus histogram